

**CONTROLLED DIFFUSION SOLIDIFICATION (CDS) OF
Al-7xxx WROUGHT ALLOYS**

**CONTROLLED DIFFUSION SOLIDIFICATION PROCESS (CDS) OF AL-
7XXX WROUGHT ALLOYS:
HEAT TREATMENT, MICROSTRUCTURE, AND MECHANICAL
PROPERTIES**

BY

S. REZA GHIAASIAAN, B.S.C. M.S.C.

A THESIS

SUBMITTED TO THE SCHOOL OF GRADUATE STUDIES

IN PARTIAL FULFILLMENT OF THE REQUIREMENTS

FOR THE DEGREE OF

DOCTOR OF PHILOSOPHY

MCMASTER UNIVERSITY

© COPYRIGHT BY SEYED REZA GHIAASIAAN, FEBRUARY 2015

ALL RIGHT RESERVED

DOCTOR OF PHILOSOPHY (2015)
(Mechanical Engineering)

McMaster University
Hamilton, Ontario

**TITLE: Controlled Diffusion Solidification Process (CDS) of Al-7xxx Wrought
Alloys: Heat Treatments, Microstructures and Mechanical Properties**

Author: Seyed Reza Ghiaasiaan
B.Sc. and M.Sc. (Materials Science and Engineering)
Sharif University of Technology, Tehran, Iran

Supervisor: Prof. Sumanth Shankar
Department of Mechanical Engineering
McMaster University, Hamilton, On, Canada

Number of Pages: xxi, 177

Abstract

Over the past decades, researchers in casting fields, especially in semi-solid metal state, have endeavored to find new ways to enable the Al wrought alloys of casting using the conventional casting processes; mainly in order to improve the product properties and decrease the product cost. The thixoforming and rheocasting processes have been presented as ways by which the microstructure of Al-base wrought alloys can be changed into non-dendritic, which in turn can lead to improvement to the mechanical properties. This can be because the effect of the non-dendritic microstructure on the mechanical properties of the material. Unfortunately, these processes have proved to be cost prohibitive and be a bit complicated for commercial applications. Further, conventional casting of Al-base wrought alloys along with their superior properties and performance have been a challenge for foundry industry due to the main disadvantage of hot tearing or hot cracking during solidification process. This can render the cast component ineffective. To overcome the disadvantages of thixoforming and rheocasting processes, Controlled Diffusion Solidification (CDS) process was innovated mainly to enable casting of aluminum wrought alloys with a non-dendritic morphology of the primary Al phase in the resultant cast microstructure and thus alleviating the problem of hot tearing and obtaining a cost effective product with improved mechanical properties. The CDS is a simple process involving mixing of two precursor alloys of different thermal masses (temperature and solute) and subsequently casting the resultant mixture of the desired solute composition and temperature as a near net shaped cast product. The process can easily be commercialized with a marginal capital cost required for set up such as the addition of an extra holding furnace. Further, the CDS process would prove itself to be unique in its ability to cast Al-based wrought alloys into near net shaped components without additional processes and cost.

The originality of this study is to present a viable casting process for the Al-7xxx wrought alloys (Al-Zn-Mg-Cu); by which the Al-7xxx family alloys are presented in cast condition to have an acceptable uniaxial property range that is comparable with their wrought counterparts.

This study presents the process and alloy parameters necessary for the casting of Al-7xxx wrought alloys (Al-Zn-Mg-Cu), by using the CDS process coupling with tilt pour gravity casting (TPGC) machine. The uniaxial tensile mechanical properties of several Al-7xxx CDS castings under various heat treatment conditions, namely, solutionizing (T4), peak aged (T6) and annealing (O), necessary for development of an ageing process on the material were investigated and presented. The tilt pour gravity casting process coupled with the CDS technology was employed to demonstrate the ability to cast Al-7xxx wrought alloys into high integrity components with high strength and ductility. The microstructure characterization was carried out by Electron Microscopy (TEM, SEM and EDS) and DSC test experiments for all the as cast (F), T4, T6 and anneals (O) conditions of the CDS cast components. Also, the predictive capabilities for the yield strength of Al 7xxx alloys CDS cast components was investigated using structural-properties modeling for the various strengthening effects that are recently proposed specifically for the Al-7xxx wrought counterparts.

The study has successfully led to a more in-depth understanding of the innovative CDS casting process by applying it to several compositions of Al-7xxx wrought alloys in an industrial scale CDS casting experiments, using tilt pour gravity casting (TPGC) machine. This will hopefully lead us to a clearer path towards commercializing the CDS process and obtaining a viable casting process for Al-base wrought alloys into near net shape components without much change to economics of the casting process.

Acknowledgements

I would like to express my deepest gratitude to my supervisor, Professor Sumanth Shankar whose consistent help and support have always been with me during my doctoral studies. Over the past five years, I have learned a lot under Dr. Shankar's invaluable assistance and guidance. Dr. Shankar's perpetual energy together with an open ocean of new ideas have always been a strong motivation for all his students, including me, which made my research life at McMaster University a rewarding period of my life.

My sincere gratefulness goes to the members of my supervisory committee: Professor Joe McDermid and Dr. Kumar Sadayappan. Their knowledge, assistance, patience and ingenious ideas have greatly helped me to overcome the unlimited amount of experimental and theoretical problems.

I would like to extend my deepest gratitude to faculty members of the Department of Material Science and Engineering, Prof. Tony Petric, David Wilkinson and Hatem Zurob for their time on discussions hours for my thesis; special thanks to Prof. Marek Niewczas for his pure commitment to Science as he patiently spent long discussion hours over several sessions to discuss very details of my thesis.

I would like to also thank my colleagues and research scientists working at the Light Metal Casting Research Centre (LMCRC): Dr. Jeyakumar Manickaraj; special thanks to Dr. Abbas Khalaf for all his help and insightful discussions and instructions; and also special thanks to Dr. Xiaochun Zeng for his great helps, especially in tough times of experimental failures. I am also thankful to technicians, and non-teaching staff in the Department of Mechanical Engineering at McMaster University for their help and support; special thanks to Mr. Ron Lodewyks for all his full commitment and patiently technical assistance in designing, machining and welding of components required for the project; and also special thanks to Ms. Connie Barry and Mr. Doug Cully from the Department of Materials Science and Engineering for technical training and assistance required to use the uniaxial tensile test machine and the metallography and chemical analysis device.

I am also thankful to the Government of Canada for providing the financial support for this project through the Natural Sciences and Engineering Research Council (NSERC) of Canada and the Discovery Grant program; and also I would like to thank the CANMET Materials for their the provision of their TEM facilities, including their senior TEM specialist: Dr. Babak Shalchi-Amirkhiz.

Also I would like to thank my friend, Mr. Tom Smith, here in Hamilton for all his moral and spiritual support; special thanks to my dear friend Dr. Peyman Ashtari whose technical support through long discussion hours was greatly help me, particularly over the last and toughest year of my studies at McMaster.

Last but not least, once again I am thankful to the Almighty God; and my beloved parents for all their endless support over the past five years, without this would be possible at all.

S. Reza Ghiaasiaan

ghiaassr@mcmaster.ca

McMaster University, Hamilton, ON, Canada,

August 14th, 2015

Table of Contents

Abstract	iv
Acknowledgements	v
Table of Contents	vi
List OF Figures	ix
List of Tables	xix
1 Introduction.....	1
2 Abbreviations and Nomenclature.....	10
3 Project objectives and Methodology	12
4 Prior-Art.....	15
4.1 Solidification in Al-Zn-Mg-Cu System	15
4.1.1 Shrinkage and Hot Tearing	15
4.1.2 CDS Technology: History and Mechanism	18
4.1.3 Al 7xxx Series wrought Alloys	23
4.2 Heat-treatments of Al-Zn-Mg-Cu system.....	25
4.2.1 Solutionizing of the Al-Zn-Mg-Cu alloys.....	27
4.2.2 Precipitate free zone (PFZ)	30
4.2.3 Precipitation age-hardening process of Al-Zn-Mg-Cu alloys	32
4.2.4 Rate of hardening during ageing process:.....	38
4.2.5 Effect of alloying elements on the ageing process:	39
4.3 Deformation in metals and Dislocation Interactions	40
4.3.1 Solid Solution Strengthening.....	41
4.3.2 Grain Boundary Strengthening	43
4.3.3 Strain Hardening Mechanisms	45
4.3.4 Strengthening from Fine-Scale Precipitates	48
4.3.5 A process model strengthening mechanism in the Aluminum alloys.....	50
4.4 Mechanical properties of Al-7xxx Alloys.....	65
4.4.1 Fractography of the Al-7xxx alloys under tension load.....	66
5 Experiment Procedures.....	70
5.1 Materials and Experimental equipment	70
5.2 Laboratory scale CDS experiments	71
5.3 The CDS casting experiments using (TPGC) machine	77
5.4 Microstructural Analysis.....	78
5.5 Transmission Electron Microscopy (TEM)	79
5.6 Image Analysis	79
5.7 Heat treatments procedures and equipment	84

5.8	Differential Scanning Calorimetry (DSC) Tests	85
5.9	Uniaxial Tensile Tests	86
5.10	Hardness Test	87
5.11	Density measurement test	87
6	Results and disucssion.....	91
6.1	The CDS Experiments using Tilt Pour Gravity Casting (TPGC)	91
6.2	Microstructure Characterization.....	92
6.2.1	Differential Scanning Calorimetry (DSC)	92
6.2.2	Scanning Electron Microscopy (SEM)	96
6.2.3	Transmission Electron Microscopy (TEM).....	112
6.3	Precipitation Hardening	119
6.4	Uniaxial Tensile Properties	126
6.4.1	Effect of heat treatment.....	127
6.4.2	Effect of alloying elements	131
6.4.3	Effect of grain size.....	134
6.4.4	Effect of eutectic phase	135
6.4.5	Effect of porosity content (%).....	136
6.4.6	Comparison of AA7050 in CDS Cast and Wrought Conditions.....	137
6.5	Fractography after Tensile Test.....	137
7	Strengthening model.....	143
7.1	Kinetics of Precipitation Strengthening.....	143
7.2	Activation Energy (Q_A): Al-7050 CDS cast samples and wrought product	147
7.3	Strengthening Model For Yield Strength Prediction	148
7.3.1	Intrinsic Strength	150
7.3.2	Solid Solution Strengthening.....	151
7.3.3	Precipitation Strengthening	152
7.3.4	Dislocation Strengthening	154
7.3.5	Grain Boundary Strengthening.....	154
7.3.6	Total Yield Strength Estimation.....	155
8	Conclusions.....	160
8.1	CDS Technology with Al 7xxx Alloys.....	161
8.2	Microstructure and Heat Treatment.....	161
8.3	Strengthening Models	162
8.4	Summary of Scientific Contributions in this Dissertation	163
9	APPENDICES	164
9.1	List of Publications.....	164

9.2	TEM micro-graphs of secondary phases in the Al-7xxx alloys in T6 temper	165
9.3	Details of the Strengthening Models	166
10	References.....	168

List OF Figures

FIGURE 1–1 SALES-WEIGHTED AVERAGE FUEL ECONOMY OF NEW U.S. LIGHT-DUTY PASSENGER VEHICLES [2].	1
FIGURE 1–2 MATERIAL BREAKDOWNS FOR AUTOMOTIVE LIGHT-WEIGHTING STRATEGY USING TWO SEPARATE TECHNOLOGICAL ROUTES: (A) HIGH STRENGTH STEEL INTENSIVE AND (B) ALUMINUM ALLOY INTENSIVE [2]. THE 0% SHOWN IN THE ABOVE GRAPHS REPRESENTS THE AVERAGE MATERIAL BREAKDOWN AND CURB WEIGHT FOR A LIGHT DUTY AUTOMOBILE IN THE YEAR 2009.	2
FIGURE 1–3 TYPICAL STRAIN-STRESS CURVES OF A356.2 IN T4 CONDITION AND AA 7050 FORGINGS IN T6 CONDITION [5].	5
FIGURE 1–4 SCHEMATIC PROCESS PLOTS OF THE TEMPERATURE VERSUS TIME FOR (A) RHEOCASTING [25] AND (B) THIXOCASTING SEMI-SOLID METAL PROCESSES [26].	6
FIGURE 1–5: TRACE OF SOLID FRACTION (F_s) AS A FUNCTION OF TEMPERATURE FOR (A) AA7050 WROUGHT ALLOY AND (B) AL-7SI CASTING ALLOY TO SHOW THE TEMPERATURE DROP TO OBTAIN SEMI-SOLID SLURRY OF ABOUT 0.3 SOLID FRACTIONS [6].	7
FIGURE 1–6 PHOTOGRAPHS OF TYPICAL SHRINKAGE AND HOT TEARING DEFECTS IN CASTINGS OF AL ALLOYS (A) SHRINKAGE IN B206 (AL-4.7CU) ALLOY, (B) HOT TEARING IN RING CASTING OF AL-MG-CU (AA2014) ALLOY [40], RESPECTIVELY.	8
FIGURE 3–1. FLOW CHART OUTLINING THE METHODOLOGY USED IN THIS PROJECT.	14
FIGURE 4–1 A SCHEMATIC OF THE SOLIDIFICATION OF THE MUSHY ZONE HIGHLIGHTING (A) DENDRITIC NETWORK OF THE DENDRITIC PRIMARY PHASE ALONG WITH THE INITIATION OF A HOT TEAR AT THE REGION DEMARKED AS <i>LOCALIZED STRAIN</i> (B) THE PRESSURE GRAIENT [46].	16
FIGURE 4–2 SCHEMATIC OF A TYPICAL BINARY HYPOEUTECTIC ALLOY SHOWING THE VARIOUS THERMAL REGIMES IN THE MUSHY ZONE ALONG WITH THE SCHEMATIC OF THE ANTICIPATED DISTRIBUTION OF THE SOLID AND LIQUID PHASES IN THESE THERMAL REGIMES AND THE HOT CRACKING SUSCEPTIBILITY OF THESE REGIMES AS A FUNCTION OF SOLUTE COMPOSITION SCHEMATIC DIAGRAM OF TEMPERATURE-HOT TEARING SUSCEPTIBILITY IN ALUMINUM ALLOYS ALONG WITH ILLUSTRATIVE GRAIN GROWTH COHERENCY DURING SOLIDIFICATION PROCESS, CORRELATING THE PHASE DIAGRAM AND HOT TEARING SUSCEPTIBILITY. THE SCHEMATIC COMPOSITE SHOWN HERE WAS COMPOSED FROM TWO DIFFERENT REFERENCES IN THE PRIOR-ART [18, 48].	17
FIGURE 4–3 THE UNIAXIAL TENSILE AND FATIGUE TEST BARS OF AA 7050 CAST BY TILT POUR GRAVITY CASTING (TPGC) MACHINE ALONG WITH THEIR OPTICAL MICROGRAPHS: (A) AND (B) SHOWS THE HOT TEARING DEFECTS IN CONVENTIONALLY CAST PARTS IN MACRO- AND MICRO-SCALE IMAGES, RESPECTIVELY; (C) AND (D) SHOWS THE SOUND AND FLAWLESS CDS CASTINGS.	18
FIGURE 4–4 MECHANISM OF DIFFUSION SOLIDIFICATION (A) BINARY ALLOY PHASE DIAGRAM AND (B) MECHANISM OF DIFFUSION SOLIDIFICATION [50].	20
FIGURE 4–5 THE THREE STAGES IN THE MECHANISM OF THE CDS TECHNOLOGY. (A) SCHEMATIC OF THE TYPICAL THERMAL PROFILE OBSERVED IN THE CDS PROCESS WITH THREE DISTINCT STAGES STARTING WITH MIXING OF ALLOYS AT POINT A, AND (B) THE THREE MORPHOLOGIES OF THE PRIMARY AL PHASE WHICH ARE ASSOCIATED WITH THE THREE STAGES SHOWN IN (A) FOR THE AL-4.5CU ALLOY [40].	20
FIGURE 4–6: (A) A TYPICAL AL-ZN BINARY PHASE DIAGRAM SCHEMATICALLY SHOWING THE ALLOY CONSTITUENTS OF THE CDS PROCESS TECHNOLOGY; (B) ACTUAL THERMAL CURVES OBTAINED WHILE CASTING AA7050 ALLOY WITH THE CDS TECHNOLOGY; (C) OPERATIONAL STAGES IN A TYPICAL CONTROLLED DIFFUSION SOLIDIFICATION (CDS) PROCESS; (D) AND (E) SAMPLE PRODUCTS MANUFACTURED VIA CDS TECHNOLOGY COUPLED WITH TPGC AND SAND CASTING PROCESSES, RESPECTIVELY [].	21
FIGURE 4–7 COMPARATIVE SCHEMATIC SOLUTE AND TEMPERATURE REDISTRIBUTION REGIMES AHEAD OF THE SOLIDIFYING SOLID-LIQUID INTERFACE ARE PRESENTED FOR (A) THE CDS PROCESS AND (B) CONVENTIONAL SOLIDIFICATION [40].	22
FIGURE 4–8 BASIC ALUMINUM WROUGHT ALLOY FAMILY CLASSIFICATION AND HEAT TREATMENTS [5,31].	23

- FIGURE 4–9: SECTIONS AT DIFFERENT ZINC AND COPPER CONTENT IN THE AL-ZN-MG-CU SYSTEM [66]. 25
- FIGURE 4–10 ISOPLETH OF SIMULATED EQUILIBRIUM PHASE DIAGRAM OF THE AL-ZN-MG-CU SYSTEM SHOWING AL-2MG-2CU ALLOY WITH VARYING COMPOSITION OF ZN IN THE ALLOY. THE TYPICAL TEMPERATURE REGIMES USED FOR THE VARIOUS HEAT TREATMENT PROCEDURES ARE SHADED IN THE PHASE DIAGRAM. 26
- FIGURE 4–11 TYPICAL THERMAL DATA FROM A DTA EXPERIMENT OF AA7075 ALLOY CARRIED OUT AT A HEATING RATE OF 20° C/MIN (36° F/MIN). HOMOGENIZED IN THE FIGURE REFERS TO SOLUTIONIZING. THE ARROWS INDICATE THE START OF A MELTING PROCESS. SIGNIFICANT INFLECTIONS ON THE CURVES ARE MARKED AS (1) PRECIPITATION FROM SATURATED SOLID SOLUTION, (2) RE-SOLUTION OF PRECIPITATED PHASE(S), AND (3) MELTING AREA; EQUILIBRIUM SOLIDUS MELTING FOR THE ALLOY IS SHOWN BY (3B) AND NONEQUILIBRIUM INCIPIENT MELTING BY (3C), WHICH IS THE MELTING POINT OF S-PHASE [5]. 28
- FIGURE 4–12 CALCULATED EQUILIBRIUM PHASE FRACTION FOR DIRECT CHILLED CAST 7050 INGOTS; H CORRESPONDS TO THE SOLUTIONIZING (HOMOGENIZATION) TEMPERATURE (753K). HOWEVER, THE CALCULATION IS LIMITED TO EQUILIBRIUM THEREFORE IT DOES NOT ALLOW THE EFFECT OF METASTABLE PRECIPITATION TO BE EXPLORED [72]. 28
- FIGURE 4–13 DSC CURVES IN THREE CONSECUTIVE RUNS WITH HEATING RATE OF 10°C/MIN FOR AL-6.1ZN-2.3 MG- 2.6CU (WT.%) ALLOY IN ARTIFICIALLY OVER-AGED CONDITION (T7=16 HR @ 172°C); A= DISSOLUTION OF η' -PHASE; B= FORMATION OF η -PHASE; C= DISSOLUTION OF η -PHASE; D AND E= DISSOLUTION AND FORMATION OF S-PHASE; T AND G= MELTING OF T AND S PHASES; THE IDENTIFICATION OF THESE PHASES ARE LISTED IN TABLE 4–5 [73]. 29
- FIGURE 4–14: TYPICAL PRECIPITATE FREE ZONES (PFZ) NEAR GRAIN BOUNDARIES IN AL-5.9ZN-2.9MG (WT.%) ALLOY: (A) WATER QUENCHED FROM 465°C AND THEN AGED FOR 12 HOURS AT 180°C, AND (B) OIL QUENCHED FROM 465°C AND THEN AGED FOR 3 HOURS AT 180°C. NOTE THE EFFECT OF QUENCHING RATE ON THE WIDTH OF THE ZONE AND THE DISPERSION OF PRECIPITATES WITHIN THE GRAINS. MAGNIFICATION OF BOTH (A) AND (B) IS X27,000 [75]. 31
- FIGURE 4–15: A COMPARISON OF THE VACANCY CONCENTRATION PROFILES FOR VARIOUS SOLUTION TREATMENTS TEMPERATURE, QUENCHING CONDITIONS OF AL-5.9ZN-2.9MG (WT.%) ALLOY. THE PRECIPITATE FREE ZONE WIDTHS DEPICTED ARE (A) SOLUTION AT 510°C, WATER QUENCH, AGE AT 135°C, (B) SOLUTION AT 510°C, WATER QUENCH, AGED AT 180°C, (C) SOLUTION AT 465°C, WATER QUENCH, AGE AT 180°C AND (D) SOLUTION AT 465°C, OIL QUENCH, AGE AT 180° [75]. 31
- FIGURE 4–16 THE AL-2MG- (0~10) ZN ISOPLETH PHASE DIAGRAM SHOWING THE SCHEMATIC EQUILIBRIUM SOLVUS TEMPERATURE LINES FOR THE METASTABLE GP ZONES (GP-I AND GP-II), H' AND EQUILIBRIUM H-MGZN₂; NOTE THAT JUST FOR THE PURPOSE OF SIMPLICITY, THE COMPOSITION RANGE IN THE ISOPLETH PHASE DIAGRAM IS CHOSEN TO REPRESENT THE TERNARY AL-MG-ZN SYSTEM WITHIN THE COMPOSITIONAL RANGE THAT IS SELECTED FOR THIS STUDY. 32
- FIGURE 4–17 SCHEMATIC PRESENTATION OF TOTAL FREE ENERGY AS A FUNCTION OF TIME; NOTE THE DISTINCT REACTIONS FOR FORMATION OF H'-PRECIPITATES FROM GP ZONES TYPE I AND II [68]. 33
- FIGURE 4–18 THE SCHEMATIC PRESENTATION OF PRECIPITATION SEQUENCES IN AL-2MG-XZN ALLOYS: (A) THE METASTABLE SOLVUS LINES IN THE AL-2MG VS. ZN PHASE DIAGRAM; AND (B) RELATIVE TIME FOR THE START OF FORMATION OF EACH PRECIPITATION STAGE AT DIFFERENT TEMPERATURE FOR ALLOY WITH X COMPOSITION IN (A) [68]. 33
- FIGURE 4–19 SCHEMATIC PRESENTATION OF MOLAR FREE ENERGY FOR AL-ZN-MG-(CU) ALLOY SHOWING THE ACTIVATION ENERGY BARRIER TO NUCLEATION/FORMATION OF THE TRANSIENT PHASES ARE SMALLER THAN THAT OF DIRECT TRANSFORMATION FROM SUPERSATURATED SOLID SOLUTION (A₀) AL MATRIX TO THE EQUILIBRIUM H-MGZN₂ PRECIPITATES; THE SCHEMATIC DIAGRAMS WERE REVISED FROM THE ORIGINAL SCHEMATICS PRESENTED FOR AL-CU SYSTEM [68]. 34
- FIGURE 4–20 SELECTED AREA DIFFRACTION PATTERNS (SAED) FROM SAMPLES AGED TO AN (1) UNDER-AGED, (2) OPTIMAL AGE (T6) AND (3) OVER-AGE (T7) CONDITIONS OF AL7050 ALLOYS ARE SHOWN IN (A) THE [001]_{AL}-PROJECTION, (B) [112]_{AL}-PROJECTION, AND (C) [111]_{AL}-PROJECTION. PRECIPITATE SPOTS ARE

- FROM GP ZONES, H' AND H-PHASES. SHARP EXTRA SPOTS AT SIMPLE CUBIC POSITIONS 100_{AL} , ARE FROM THE Al_3Zr DISPERSOIDS [88]. 35
- FIGURE 4–21 (A) SCHEMATIC DIAGRAM OF THE SAED PATTERN FROM GP (II) ZONES; (B) TO (F) SAED PATTERN ALONG THE $[001]_{AL}$ ZONE AXIS FROM VARIOUS HEAT AFFECTED AREAS IN FSW OF AA 7050-T651; SHOWING THE PRECIPITATION EVOLUTION (GP (I)/H'-PHASES AND GP (II)/H-PHASES) BY MEANS OF THE REFLECTION SPOTS [89]. 36
- FIGURE 4–22 (A) SCHEMATIC DIAGRAM OF THE DIFFRACTION PATTERN FROM GP (I)/H'-PHASES AND GP (II)/H-PHASES IN THE $[111]_{AL}$ ZONE AXIS; AND (B)-(F) THE SAED PATTERNS ALONG THE $[111]_{AL}$ ZONE AXIS FROM VARIOUS HEAT AFFECTED AREAS CLOSE TO THE FRICTION STIR WELD (FSW) AREA OF AA 7050-T651, SHOWING THE PRECIPITATION FORMATION PROCEDURE BY EVOLUTION WITHIN THEIR SAED PATTERNS [89]. 36
- FIGURE 4–23 GRAPHS SUMMARIZES THE 1DAP RESULTS SHOWING THE CHANGES OF (A) AVERAGE PARTICLE SIZE AND (B) NUMBER OF DENSITY FOR THE PRECIPITATES IN TWO OF AL-ZN-MG-(CU)-ALLOY SAMPLES; THE DATA POINTS SHOWN BY CROSS SIGN (X) BELONG TO THE COPPER FREE SAMPLE (AL-2.3ZN-1.38MG (WT.%)); AND THE STAND-ALONE, ONE DATA POINT SHOWN BY EMPTY CIRCLE IS REPRESENTING THE COPPER SAMPLE (AL-2.3ZN-1.38MG-0.13CU (WT.%)) [92]. 38
- FIGURE 4–24 (A) TYPICAL EXPERIMENTAL DATA OF THE NUMBER DENSITY AND THE SIZE OF THE EARLY STAGE CLUSTERING (GP ZONES), EVOLVING DURING AGEING PROCESS AT 121 °C OF AA 7050 ALLOY, WHICH WERE MEASURED BY 3DAP FOR A DURATION OF 1440 MINUTES TIME PERIOD [90]. 38
- FIGURE 4–25: THE EFFECT OF EXCESS ALLOYING ELEMENTS SUCH AS MG AND ZN ON VARIOUS AGEING PROCESSES OF AL-ZN-MG ALLOYS: (A) AL-4ZN-1MG, (B) AL-4ZN-3MG, AND (C) AL-8ZN-2MG (WT.%) [66]. 39
- FIGURE 4–26 MACRO-HARDNESS CURVES OF THREE DISTINCT ALLOYS FROM AL-7XXX FAMILY CAST BY CDS PROCESSES USING TILT POUR GRAVITY CASTING MACHINE, SHOWING THE EFFECT OF ALLOYING ELEMENT EFFECT ON THE HARDNESS VALUE AND HARDENING RATE [95]. 40
- FIGURE 4–27 SCHEMATICS SHOWING THE TRANSITION FROM AN UNSLIPPED TO SLIPPED STATE. (A) VARIATION OF ENERGY FROM AN UNSLIPPED STATE TO SLIPPED STATE AND (B) INTERFACIAL REGION BETWEEN THE SLIPPED AND UNSLIPPED STATE WHICH IS A DISLOCATION CORE [96]. 40
- FIGURE 4–28 SCHEMATIC PRESENTATION DISLOCATION MOVEMENT AS A STEP DURING THE PLASTIC DEFORMATION BY MEANS OF THE SLIP MECHANISM: (A) ATOM MOVEMENT NEAR DISLOCATION IN SLIP; AND (B) MOVEMENT OF AN EDGE DISLOCATION [96]. 41
- FIGURE 4–29 THE SCHEMATIC PRESENTATION OF THE STRENGTHENING EFFECT OF ADDITION OF ALLOYING ELEMENTS AS SOLID SOLUTION ON THE STRESS STRAIN CURVE [96]. 42
- FIGURE 4–30 TYPICAL SINGLE-CRYSTAL STRESS-STRAIN CURVE FOR AL AND CU WITH FCC STRUCTURE AND MG AND ZN WITH HCP STRUCTURE; NOTE THE FCC STRUCTURE WITH HIGHER NUMBER SLIP SYSTEMS (12) SHOW HIGHER STRAIN HARDENING DUE TO POSSIBILITY OF DUPLEX OR MULTIPLE SLIPPING SYSTEMS; WHEREAS IN HCP STRUCTURES (MG AND ZN) WITH MERE ONE SLIP SYSTEM ARE NOT CAPABLE OF CREATING HIGH DEGREE OF DEFORMATION BY DISLOCATION MECHANISMS [96]. 42
- FIGURE 4–31 SCHEMATIC PRESENTATION OF CALCULATION OF THE CRITICALLY RESOLVED SHEAR STRESS (CRSS) IN A PRESUMABLY CYLINDRICAL SINGLE CRYSTAL UNDER UNIAXIAL TENSION. THE CRSS VALUE IS THE EQUIVALENT OF THE YIELD STRESS OF AN ORDINARY STRESS-STRAIN CURVE AND IT DEPENDS MAINLY ON THE COMPOSITION AND TEMPERATURE. IT IS NOTEWORTHY, THAT, IT IS VERY DIFFICULT TO DETERMINE THE CSRR VALUE, WHICH IS BASICALLY THE STRESS AT WHICH THE FIRST SLIP BANDS ARE FORMED; IN PRACTICE, FOR THE MOST CASES, THE CRSS VALUES ARE OBTAINED BY THE EXTRAPOLATION TECHNIQUE OF ELASTIC AND PLASTIC REGIONS OF THE STRESS-STRAIN CURVE [96]. 44
- FIGURE 4–32 FORMATION OF GLISSILE OR SESSILE DISLOCATIONS: (A) A JOG (J) BY A DISLOCATION THAT IS CUTTING THROUGH A SCREW DISLOCATION AS IT GLIDES FROM AB TO A'B'; (B) BY PART OF A SCREW DISLOCATION LINE AB CROSS SLIPPING FROM THE PRIMARY SLIP PLANE PQ INTO THE PLANE RS [115]. 46

- FIGURE 4–33 TYPICAL FLOW CURVE FOR FCC SINGLE CRYSTAL, INDICATING DIFFERENT STAGES OF DISLOCATION INTERACTIONS: I) EASY GLIDE OF DISLOCATIONS; II) PILED-UP MECHANISM OF DISLOCATION GROUPS; AND III) CROSS SLIPPING AND INTERSECTION OF FORESTS OF DISLOCATIONS [96]. 46
- FIGURE 4–34 TYPICAL ELECTRON TRANSMISSION MICROGRAPHS OF THE DISLOCATION TANGLES FORMING DURING THE DEFORMATION PROCESS (IN THE LATE STAGE I AND II, SHOWN FIGURE 4–33) IN THE FCC SINGLE CRYSTALS: (A) AND (B) $\langle 111 \rangle$ ALUMINUM SPECIMEN AFTER COMPRESSION TO 59 MPA WITH RECOVERY AT 453K; AND (C) AND (D) TEM FOILS OF COPPER POLYCRYSTALS DEFORMED AT ROOM TEMPERATURE WITH THE FLOW STRESS LEVELS OF (C) 28 MPA; AND (D) 69 MPA []. 47
- FIGURE 4–35 SCHEMATIC PRESENTATION OF AGE HARDENING PROCESS AFTER SOLUTION TREATMENT BETWEEN AMBIENT AND AN ELEVATED TEMPERATURES DESCRIBED AS NATURAL AND ARTIFICIAL AGEING, RESPECTIVELY. 48
- FIGURE 4–36 DISLOCATION PASSING PRECIPITATES BY (A) SHEARING OR CUTTING THROUGH THE STRENGTHENING PARTICLES; OR (B) BOWING BETWEEN THEM; AND (C) SCHEMATIC COMPARATIVE PRESENTATIONS OF STRENGTHENING EFFECT OF THESE TWO MECHANISMS: SHEARING AND BYPASSING THE STRENGTHENING PARTICLES [31]. 49
- FIGURE 4–37 SCHEMATIC PRESENTATION OF DIFFERENT STAGES OF A DISLOCATION MOVEMENT BETWEEN WIDELY SEPARATED OBSTACLES IN A MATRIX; BASED ON OROWAN’S MECHANISM OF DISPERSION HARDENING FOR NONE-SHEARABLE AND INCOHERENT PRECIPITATES [96]. 50
- FIGURE 4–38 THE SCHEMATIC PRESENTATION OF THE RELATIVE CONTRIBUTIONS OF VARIOUS FACTORS TO THE INTRINSIC YIELD STRESS OF THE MATERIAL. THE FACTORS ARE SUCH AS SOLID SOLUTION STRENGTHENING, PRECIPITATION HARDENING DUE TO SHEARABLE AND NONE-SHEARABLE PARTICLES [122]. 52
- FIGURE 4–39 (A) DEFINITION OF THE CRITICAL PARTICLE SIZE (D_c) FOR THE TRANSITION FROM SHEARING TO BYPASSING IN ALUMINUM ALLOYS WITH 1% VOLUME FRACTION OF PARTICLES AS PER BELOW TABLE; (B) SCHEMATIC PRESENTATION OF CONSEQUENT EFFECT OF PARTICLE SIZE ON THE STRAIN LOCALIZATION [125]. 53
- FIGURE 4–40 DEFINITION OF THE ORIENTATIONAL ANGLES THAT ARE DETERMINED WITH RESPECT TO THE ROLLING DIRECTION (L) AND THE UNIAXIAL TENSILE AXIS. THE ANGLE Φ IS DEFINED AS THE ANGLE BETWEEN THE UNIAXIAL TENSILE AXIS AND THE ITS PROJECTION ON THE LONGITUDINAL-TRANSVERSE (L-T) PLANE; AND THE ANGLE ϕ IS DEFINED MAINLY ON THE L-T PLANE BETWEEN THE PROJECTION OF THE UNIAXIAL TENSILE AXIS AND THE TEXTURE DIRECTION THAT ARE THE WORKING OR ROLLING DIRECTION [137]. 59
- FIGURE 4–41 DIRECTION DEPENDANCY OF ORIENTATIONAL FACTOR (M) FOR THE EIGHT (8) ZR-CONTAINING ALLOYS. THE SOLID BLACK LINE IS A PRESENTATION OF AVERAGE M VALUE FOR ALL THE EIGHT ALLOYS; WHEREAS THE DOTTED LINES PRESENTS THE AVERAGE M VALUE FOR THE CASES WITH THREE AND FOUR ACTIVE SLIP SYSTEMS [137]. 60
- FIGURE 4–42 SCHEMATIC REPRESENTATION OF: (A) THE STRESS FIELD IN AN ELLIPTICAL CENTRAL CRACK [96]; (B) THE CRACK GROWTH MECHANISM BY INFLUENCE OF EXTERNAL FORCES AND INTER-ATOMIC FORCES AT ITS TIP; (C) BREAKING OF INTER ATOMIC BONDS WITHOUT PLASTIC DEFORMATION OR MICRO-CRACKING AHEAD OF CRACK; (D) PLASTIC FLOW AT THE CRACK TIP BY THE FORMATION OF THE SHEAR STRAIN BANDS; AND (E) THE FORMATION OF MICRO-CRACKS IN THE SHEAR STRAIN BANDS AHEAD OF CRACK TIP (VOID SHEETS) [162]. 66
- FIGURE 4–43 SCHEMATIC REPRESENTING TYPICAL DUCTILE FRACTURE UNDER THE UNIAXIAL TENSION LOAD TEST, WHERE THE VOID COALESCENCE IS THE DOMINATE MECHANISM LEADING TO FORMATION OF THE EQUIAXED DIMPLES ON THE FRACTURE SURFACE: (A) RANDOM PLANAR ARRAY OF PARTICLES AS INITIATION SITED FOR MICROCRACKS; (B) GROWTH OF THE MICROVOIDS IN THE FORM OF WEBS AND COLUMNS, (C) CROSS-SECTIONAL APPEARANCE OF “DIMPLES” AS A HOLE-JOINING MECHANISM FOR DUCTILE FRACTURE; (D) POLISHED OPTICAL MICROGRAPHS OF THE POLISHED CROSS-SECTION IN LOW MAGNIFICATION OF A POLYCRYSTALLINE COPPER ALLOY FRACTURED UNDER THE UNIAXIAL TENSION TEST AT AN ELEVATED TEMPERATURE [162]. 67

- FIGURE 4–44 EFFECT OF VOLUME FRACTION OF INTERMETALLIC PARTICLES AND COMPOSITION OF AL-MATRIX ON THE FRACTION STRAIN OF 6MM (2IN.) TENSILE SPECIMEN OF AL-ZN ALLOYS [5] 68
- FIGURE 4–45 TYPICAL SEM MICROGRAPHS OF FRACTURE SURFACES OF REFINED AL-12ZN-3MG-2.5CU-0.1TI IN PEAK AGE (T6) CONDITION: (A) LOW AND (B) HIGH MAGNIFICATION MICROGRAPHS OF THE MICROVOIDS NUCLEATED HETEROGENEOUSLY ON SECONDARY PHASE PARTICLES AT GRAIN BOUNDARY FORMING MICRO CRACK AT GRAIN BOUNDARY WITH ITS PROPAGATION PATHS ALONG THE GRAIN BOUNDARY AREAS [163]. 68
- FIGURE 4–46 TYPICAL HIGH MAGNIFICATION SEM MICROGRAPHS OF FRACTURE SURFACE OF REFINED AL-12ZN-3MG-2.5CU-0.1TI IN SOLUTION HEAT TREATMENT (T4) CONDITION, SHOWING (A) SHRINKAGE POROSITIES WITH FREE SURFACE AS THE HETEROGENEOUS INITIATION SITES FOR THE NUCLEATION OF MICROVOIDS; AND (B) THE PREFERRED INITIATION PATHS AT THE GRAIN BOUNDARY AREAS [163]. 69
- FIGURE 5–1 PHASE DIAGRAM ISOPLETH OF (A) BINARY AL-MG PHASE DIAGRAM (ALLOY1); AND (B) AL-ZN-CU TERNARY PHASE DIAGRAM (ALLOY2); BOTH OF WHICH ARE DESIGNED FOR THE CDS PROCESS OF THE AL-7050 ALLOY AS THE RESULTANT ALLOY (ALLOY3) OF WHICH THE QUATERNARY AL-ZN-MG-CU PHASE DIAGRAM ISOPLETH IS SHOWN IN (C). 72
- FIGURE 5–2 ACTUAL THERMAL CURVES FOR THE PRECURSOR ALLOYS (ALLOY1, ALLOY2 AND ALLOY3) DESIGNED FOR THE LAB SCALE CDS EXPERIMENTS OF THE AA-7050 THAT ARE OBTAINED EXPERIMENTALLY BY A SLOW COOLING RATE OF ABOUT $0.1\text{ }^{\circ}\text{C}\cdot\text{s}^{-1}$ INSIDE THE MELTING FURNACES. 73
- FIGURE 5–3 LABORATORY SCALE EXPERIMENTAL SET-UPS FOR CDS EXPERIMENTS: (A) THE SCHEMATIC AND (B) THE ACTUAL LAB SCALE EXPERIMENTAL SET-UPS: CRUCIBLES FOR PRECURSOR ALLOYS (ALLOY1 AND ALLOY2) AND THERMOCOUPLES USED FOR MONITORING THE TEMPERATURES DURING THE CDS EXPERIMENTS [54]. 73
- FIGURE 5–4 THE PHASE DIAGRAM ISOPLETH OF THE AL-7XXX ALLOYS SELECTED FOR THE CDS EXPERIMENTS IN THIS STUDY. 75
- FIGURE 5–5 TYPICAL SOLID FRACTION OF THE DESIRED RESULTANT ALLOYS FROM THE AL-7XXX ALLOYS THAT ARE SELECTED FOR THE CDS EXPERIMENTS IN THIS STUDY; IT IS NOTEWORTHY THAT THESE SOLID FRACTION PHASE DIAGRAM ISOPLETH WERE SIMULATED USING PANDA THERMODYNAMIC DATABASE. 77
- FIGURE 5–6 CASTING EQUIPMENT FOR THE STUDY OF THE CDS PROCESS THAT IS UTILIZED FOR THIS STUDY: (A) TILT POUR GRAVITY CASTING (TPGC) EQUIPMENT AND (B) COMPONENT PARTS LIST OF THE TPGC MACHINE [54]. 77
- FIGURE 5–7 CAVITY MOULD OF TILT POUR GRAVITY CASTING (TPGC) MACHINE WHICH CONSISTS OF TWO TENSILE TEST AND ONE FATIGUE TEST BARS, ACCORDING TO ASTM STANDARD NUMBERS ASTM B557 AND ASTM E466-96, RESPECTIVELY [54]. 78
- FIGURE 5–8 SAMPLING LOCATIONS FROM THE UNIAXIAL TENSILE BARS (A) FOR VARIOUS TESTS SUCH AS MICROSCOPY AND HARDNESS-TEST (WITHIN THE GAUGE LENGTH AREA); AND CHEMISTRY-TEST SPECIMENS (FROM BOTH ENDS OF THE TENSILE BARS); (B) DIMENSIONAL PRESENTATION OF THE MICROSCOPY AND HARDNESS-TEST SPECIMEN IN AS-POLISHED CONDITION. 79
- FIGURE 5–9 SCHEMATIC PRESENTATION OF IMAGE ANALYSIS PROCEDURE ON THE RELATIVELY HIGH MAGNIFICATION BRIGHT FIELD OPTICAL MICROGRAPHS FOR THE AREA MEASUREMENTS OF THE RELATIVELY LARGE PRECIPITATES DURING THE ANNEALING (O) PROCESS IN AL-7XXX ALLOYS. 81
- FIGURE 5–10 SCHEMATIC PRESENTATION OF IMAGE ANALYSIS PROCEDURE USING OPTICAL MICROGRAPHS FOR THE AREA FRACTION MEASUREMENTS OF THE RELATIVELY LARGE SECONDARY EUTECTIC PHASES FORMING DURING THE SOLIDIFICATION PROCESS AT GRAIN BOUNDARY AREAS IN (A) AND (B) FOR THE AL-5.8ZN-2.2MG-2.5CU ALLOY IN T4 HEAT TREATMENT CONDITION; AND IN (C) AND (D) FOR THE AL-3.6ZN-1.8MH-0CU ALLOY IN AS-CAST (F) TEMPER. 82
- FIGURE 5–11 SCHEMATIC PRESENTATION OF SPATIAL DISTRIBUTION OF NANO-SCALE PARTICLES WITHIN THE VOLUME OF THE TEM FOIL SAMPLE AND THE RESPECTIVE PROJECTION ON A 2-DIMENSIONAL IMAGE. THIS MAY AFFECT THE MEASUREMENTS OF THE ACTUAL INTER-PARTICLE SPACING WITH A SPATIAL

- DISTRIBUTION WITHIN THE VOLUME OF THE TEM SAMPLES AS COMPARED TO THE 1D (LINEAR) AND 2D (AREA) MEASUREMENTS ON THE TEM PROJECTED MICROGRAPHS. 83
- FIGURE 5–12 SCHEMATIC PRESENTATION OF IMAGE ANALYSIS PROCEDURE ON THE RELATIVELY LOW MAGNIFICATION BRIGHT FIELD TEM MICROGRAPHS FOR THE AREA MEASUREMENTS OF THE NANO-SIZED PARTICLES. 83
- FIGURE 5–13 TYPICAL HEAT-UP CURVES OBTAINED BY THE EMBEDDED THERMOCOUPLES INSIDE TENSILE BAR SAMPLES INSERTED INTO THE ELECTRIC RESISTANCE FURNACES FOR THE ISOTHERMAL SOLUTIONIZING TEMPERATURE AT 477°C FOR 24 HOURS: (A) THE THERMAL CURVE FOR THE LARGE SIZED FURNACE WITH FORCED AIR CONVECTION THAT IS EQUIPPED WITH INTERNAL FAN; AND (B) THERMAL CURVE FOR THE SMALL SIZED FURNACE WITH NATURAL AIR CONVECTION. 85
- FIGURE 5–14 SUB-SIZED TENSILE SPECIMEN, ACCORDING TO ASTM STANDARD NUMBER E8/E8M–(13A), USED FOR THE AA 7050 WROUGHT (ROLLED) PRODUCTS. 87
- FIGURE 5–15 THE SCHEMATIC PRESENTATION OF EXPERIMENTAL SET-UP FOR POROSITY MEASUREMENTS BASED ON ARCHIMEDES TEST METHOD [177], WHICH WAS USED FOR DENSITY MEASUREMENTS OF THE AL-7XXX CDS ALLOYS IN THIS STUDY. 87
- FIGURE 5–16 THE EFFECT OF CHEMISTRY VARIATION MEASURED BY GDOES FOR EACH ALLOYING ELEMENT IN THE ALLOY COMPOSITION OF EACH OF THE NINE ALLOYS ON THE THEORETICAL AND EXPERIMENTAL DENSITY. 90
- FIGURE 5–17 THE EFFECT OF CHEMISTRY VARIATION MEASURED BY GDOES FOR EACH ALLOYING ELEMENT IN THE ALLOY COMPOSITION OF EACH OF THE NINE ALLOYS ON POROSITY MEASUREMENTS. 90
- FIGURE 6–1 TYPICAL LIGHT OPTICAL MICROGRAPHS OF AS-CAST SAMPLES FOR AA7050 ALLOY CAST USING THE TPGC PROCESS WITH CDS TECHNOLOGY. (A) AND (B) SHOW TWO DIFFERENT IMAGE MAGNIFICATIONS. 91
- FIGURE 6–2 TYPICAL LIGHT OPTICAL MICROGRAPHS OF SOLUTION HEAT TREATED (T4 TEMPER) OF THE AA7050 CASTINGS SHOWN IN FIGURE 6–1. (A) AND (B) SHOW TWO DIFFERENT IMAGE MAGNIFICATIONS. 92
- FIGURE 6–3 DSC THERMAL DATA, OBTAINED DURING A HEAT-UP EXPERIMENT AT $0.17\text{ }^{\circ}\text{C}\cdot\text{s}^{-1}$, FOR TWO DIFFERENT AS-CAST (F) SAMPLES OF AA 7050 ALLOYS CAST BY THE CDS TECHNOLOGY USING TILT POUR GRAVITY CASTING (TPGC) MACHINE; NOTE THAT THE DSC SAMPLES WERE SELECTED FROM DIFFERENT CDS EXPERIMENT CAST-BATCHES. 93
- FIGURE 6–4 DSC THERMAL DATA, OBTAINED DURING A HEAT-UP EXPERIMENT AT $0.17\text{ }^{\circ}\text{C}\cdot\text{s}^{-1}$, FOR VARIOUS HEAT TREATMENT CONDITIONS OF AA 7050 CDS ALLOYS SUCH AS, AS-CAST (F), SOLUTIONIZED (T4) AND ANNEALED (F+O AND T4+O) HEAT TREATMENT SAMPLES; NOTE THAT THE DSC SAMPLES WERE SELECTED FROM DIFFERENT CDS EXPERIMENT CAST-BATCHES. 93
- FIGURE 6–5 TYPICAL THERMAL DATA FOR DSC EXPERIMENTS, OBTAINED DURING HEATING AT $0.17\text{ }^{\circ}\text{C}\cdot\text{s}^{-1}$, OF VARIOUS COMPOSITIONS OF AL-7XXX CDS ALLOYS SELECTED FOR THIS STUDY. THE DEMARCATED REGION SHOWS THE INCIPENT MELTING OF SECONDARY PHASES IN THE ALLOY AL-5.8ZN-2.2MG-2.5CU. 94
- FIGURE 6–6. DSC THERMAL DATA, OBTAINED DURING A HEAT-UP EXPERIMENT AT $0.17\text{ }^{\circ}\text{C}\cdot\text{s}^{-1}$ FOR VARIOUS HEAT TREATMENT CONDITIONS OF AA 7050 CDS ALLOYS SUCH AS, AS-CAST (F), SOLUTIONIZED (T4) AND ANNEALED (T4+O) HEAT TREATMENT SAMPLES; SAMPLES WERE SELECTED FROM RANDOM CDS EXPERIMENT CASTINGS. 95
- FIGURE 6–7 SECONDARY ELECTRON (SE) SEM IMAGE OF AA7050 ALLOY IN F TEMPER. (A) LOW MAGNIFICATION SHOWING TWO REGIONS OF SECONDARY PHASES EVOLVED DURING SOLIDIFICATION: A AND B; (B) IMAGE ALONG WITH THE (C) ELEMENTAL MAP OF MAGNIFIED SECTION OF PHASES IN REGION A OF (B) IMAGE AND ELEMENTAL MAP OF MAGNIFIED SECTION OF PHASES IN REGION B WHICH IS SOLIDIFIED FROM THE LAST REMAINING LIQUID DURING SOLIDIFICATION; FURTHER IN (D) AND (F) THE HIGH MAGNIFIED IMAGES FOR THE FE-BEARING INTERMETALLIC PHASES ARE SHOWN IN THE REGIONS

- SOLIDIFYING FROM THE LAST PART OF REMAINING LIQUID, ALONG WITH THE ELEMENTAL MAP OF MAGNIFIED SECTION OF PHASES. 98
- FIGURE 6–8 SEI FROM SEM OF EUTECTIC PHASES IN THE LAST DROP OF SOLIDIFIED LIQUID IN AA 7050 CDS IN THE F CONDITION SHOWING (A) AND (B) THE DIVORCED EUTECTIC-LIKE STRUCTURE OF S-/θ- AND SIGMA PHASES; ALONG WITH (C) THE ELEMENTAL LINE SCAN OBTAINED BY THE EDS DETECTOR FROM (B). 99
- FIGURE 6–9 BACKSCATTERED ELECTRON MICROGRAPHS OF A TYPICAL AS-CAST MICROSTRUCTURE OF AA7050 CDS CASTINGS (A); AND (B) THE CONCENTRATION PROFILES OF THE ALLOYING ELEMENTS (ZN, MG AND CU) PLOTTED FOR A PRIMARY AL-GRAIN DEMARCATED ON THE BSE IMAGE (A) BY MEANS OF EDS LINE SCAN RESULTS. 99
- FIGURE 6–10 SEI FROM SEM OF PHASES IN THE GRAIN BOUNDARY AREAS OF AA 7050 CDS IN THE T4 CONDITION SHOWING THE DOMINANT S-PHASE, PLATE LIKE IRON-CONTAINING INTERMETALLIC PHASES AND THE OTHER IMPURITY PHASE OF Mg_2Si . THE CORRESPONDING ELEMENTAL MAP IS ALSO PRESENTED. 101
- FIGURE 6–11 TYPICAL BACKSCATTERED (BS) SEM IMAGE OF AA7050 CDS CAST SAMPLE IN T4 HEAT TREATMENT CONDITION ALONG WITH THE COMPOSITION PROFILE OF THE ALLOYING ELEMENT (SUCH AS ZN, MG AND CU) OBTAINED BY THE EDS DETECTOR. 103
- FIGURE 6–12 SEI BY SEM FROM THE GRAIN BOUNDARY AND CENTRAL AREAS OF ANNEALED AND FURNACE COOLED SOLUTIONIZED CAST PARTS OF CDS 7050 WITH ELEMENTAL MAP BY EDS DETECTOR. (A) TO (D) SHOW IMAGES OF MICROSTRUCTURE WITH PROGRESSIVELY INCREASING MAGNIFICATION OF AREAS DEMARCATED IN THE RESPECTIVE IMAGES. 104
- FIGURE 6–13 TYPICAL TEM BRIGHT FIELD MICROGRAPH IN VARIOUS MAGNIFICATIONS OF THE RELATIVELY LARGE AND FULLY INCOHERENT H- $MgZn_2$ PHASES FORMING DURING THE ANNEALING (O) GRAINS IN AA7050 CDS CAST SAMPLE; SHOWING THE PSUEDO-WIDMANSTAATEN PATTERN OF H- $MgZn_2$ PHASES, PRECIPITATED WITHIN THE GRAIN AREA AND AWAY FROM PFZ FORMING AROUND THE GRAIN BOUNDARY AREAS; NOTE THAT THE PRECIPITATE OF A GROUP ARE ALIGNED IN A DIFFERENT ORIENTATION RELATIONSHIP WITH RESPECT TO THE NEIGHBOURING GROUP. 106
- FIGURE 6–14 COMPARISON OF THE PHASE FRACTIONS FOR THE VARIOUS PHASES FORMING DURING THE SOLIDIFICATION PROCESS OF AA7050 ALLOY: SIGMA, S/θ AND THE FE- AND SI-INTERMETALLIC PHASES, OBTAINED USING QUANTITATIVE METALLOGRAPHY ON SEM MICROGRAPHS AND SIMULATION USING NON-EQUILIBRIUM SCHEIL-GULLIVER SOLIDIFICATION AND EQUILIBRIUM SOLIDIFICATION (PANDAT SOFTWARE). 107
- FIGURE 6–15 TYPICAL PARTICLE SIZE AND PHASE FRACTION OF VARIOUS PHASES FORMING DURING THE SOLIDIFICATION PROCESS OF AA7050 ALLOY, IN THE AS-CAST F TEMPER: SIGMA, S/θ, AND FE- AND SI-INTERMETALLIC PHASES. 108
- FIGURE 6–16 TYPICAL SIZE AND FRACTION AREA DISTRIBUTION OF IMPURITY AND SECONDARY PHASES IN THE AA 7050-CDS CASTING IN T4 TEMPER. 108
- FIGURE 6–17 TYPICAL PARTICLE SIZE AND PHASE FRACTION OF VARIOUS PHASES FORMING DURING THE ANNEALING (O) PROCESS (SIGMA IN THE GRAIN INTERIORS AND S AT GRAIN BOUNDARIES) MEASURED BY THE IMAGE ANALYSIS ON THE SEM MICROGRAPHS OF THE CDS CASTINGS OF AA 7050 ALLOY IN O TEMPER. 109
- FIGURE 6–18 SEI ON SEM OF FE-BEARING INTERMETALLIC PHASES IN AA7050 CDS CASTINGS IN T4 TEMPER; THE $FeAl_7Cu_2$ PHASES ARE FOUND TO BE IN DIFFERENT MORPHOLOGIES; IN (A), (C), (E) AND (G) THE ROD OR PLATE-LIKE SHAPED FE-BEARING PHASES ARE PRESENTED ALONGSIDE WITH THEIR RESPECTIVE EDS ELEMENTAL MAPS IN (B), (D), (F) AND (H). 110
- FIGURE 6–19 SEI ON SEM OF FE-BEARING INTERMETALLIC PHASES IN AA7050 CDS CASTINGS IN T4 TEMPER; THE $FeAl_7Cu_2$ PHASES ARE FOUND TO BE IN DIFFERENT MORPHOLOGIES; IN (A), (C), (E) AND (G) THE BULKY OR CHUNKY-TYPE SHAPED FE-BEARING PHASES ARE PRESENTED ALONGSIDE WITH THEIR RESPECTIVE EDS ELEMENTAL MAPS IN (B), (D), (F) AND (H). 112

- FIGURE 6–20 SADP PATTERNS OF AL MATRIX BROUGHT TO [001]-ZONE AXES FOR SAMPLES IN T6 TEMPER FROM (A) AL-5.8ZN-2.2MG-2.5CU, (B) AL-3.8ZN-2.2MG-1.7CU AND (C) AL-3.5ZN-0.8MG-0CU ALLOYS. (D) SCHEMATIC ILLUSTRATION OF OBSERVATIONS IN (A) TO (C). 113
- FIGURE 6–21 SADP PATTERNS OF AL MATRIX BROUGHT TO <111>-ZONE AXES FOR SAMPLES IN T6 TEMPER FROM (A) AL-5.8ZN-2.2MG-2.5CU, (B) AL-3.8ZN-2.2MG-1.7CU AND (C) AL-3.5ZN-0.8MG-0CU ALLOYS. (D) SCHEMATIC ILLUSTRATION OF OBSERVATIONS IN (A) TO (C). 114
- FIGURE 6–22 TEM BRIGHT-FIELD IMAGES ALONG WITH DARK-FIELD MICROGRAPHS FOR T6-AGED SAMPLES OF: (A) AND (D) AL-5.8ZN-2.2MG-2.5CU; (B) AND (E) AL-3.8ZN-2MG-1.7CU; (C) AND (F) AL-3.5ZN-0.8MG-0CU; SHOWING POPULATION AND SIZE DISTRIBUTION OF H'-PHASE. 114
- FIGURE 6–23 TEM BRIGHT-FIELD IMAGES ALONG WITH DARK-FIELD MICROGRAPHS FOR T6-AGED SAMPLES OF: (A) AND (D) AL-5.8ZN-2.2MG-2.5CU; (B) AND (E) AL-3.8ZN-2MG-1.7CU; (C) AND (F) AL-3.5ZN-0.8MG-0CU; SHOWING POPULATION AND SIZE DISTRIBUTION OF H'-PHASE. 115
- FIGURE 6–24 HR-STEM IMAGES IN: (A) AND (C) DARK FIELD MODE; (B) AND (D) HAADF (Z-CONTRAST) MODE, SHOWING THE GP ZONES AND H'-/H-PHASES PRECIPITATING DURING THE AGE HARDENING (T6) PROCESS OF: (A) AND (B) AL-3.5ZN-0.8MG-0CU; AND (C) AND (D) AL-5.8ZN-2.2MG-2.5CU ALLOY. 116
- FIGURE 6–25 TYPICAL HAADF AND CORESPONDING ELEMENTAL MAPS FOR THE (A) AL-3.5ZN-0.8MG; (B) AL-3.8ZN-2MG-1.7CU; AND (C) 5.8ZN-2.2MG-2.5CU; SHOWING RELATIVE EFFECT OF COPPER ON THE PARTICLE SIZE AND DISTRIBUTION OF PRECIPITATES, INCLUDING GP ZONES, H' AND H PRECIPITATES. 117
- FIGURE 6–26 MEASUREMENTS FOR THE PARTICLE SIZE AND AREA FRACTION OF PRECIPITATES IN THE THREE ALLOYS SHOWN IN FIGURE 6–25. THE RESULTS HERE SHOW THE TOTAL FOR ALL OF GP ZONES, H' AND H PRECIPITATES IN THE RESPECTIVE ALLOYS. 117
- FIGURE 6–27 TYPICAL DISTRIBUTION OF PARTICLE SIZE FOR THE PRECIPITATE PHASES IN THE AL-3.5ZN-0.8MG; AL-3.8ZN-2MG-1.7CU; AND 5.8ZN-2.2MG-2.5CU ALLOYS. THE RESULTS HERE SHOW THE TOTAL FOR ALL OF GP ZONES, H' AND H PRECIPITATES IN THE RESPECTIVE ALLOYS. 118
- FIGURE 6–28 TYPICAL STEM MICROGRAPHS IN (A) DF MODE AND (B) HAADF MODE. IN THE CU-FREE AL-3.5ZN-0.8MG-0CU ALLOY. 118
- FIGURE 6–29 TYPICAL MICRO- AND MACRO-HARDNESS DATA AS A FUNCTION OF TIME MEASURED FROM IMMEDIATELY AFTER QUENCHING THE SAMPLES IN WATER AT ROOM TEMPERATURE AFTER T4 TREATMENT AT 477 °C FOR AA 7050 CDS ALLOY CASTINGS. THE ISOTHERMAL TEMPERATURE OF THE SAMPLES WERE (A) 200 °C, (B) 160 °C, (C) 120 °C AND (D) 70 °C. THE FOUR REGIONS OF SALIENT EVENTS DURING THE PRECIPITATION PROCESS ARE ALSO DEMARCATED. 121
- FIGURE 6–30 TYPICAL VARIATION OF THE PEAK MICRO-HARDNESS VALUES WITH AGEING TEMPERATURES FOR THE TWO DISTINCT PEAKS OBSERVED ON THE AGE-HARDENING CURVES OF AA 7050 CDS ALLOYS MEASURED DURING THE ARTIFICIAL AGE HARDENING (T6) PROCESSES AT 70, 120, 160 AND 200°C. 123
- FIGURE 6–31 PLOT OF DIFFERENCE BETWEEN THE MICRO-HARDNESS VALUES AT PEAK #1 AND LOCAL MINIMA FOR VARIOUS TEMPERATURES SHOWN IN FIGURE 6–29 (A) TO (D). 124
- FIGURE 6–32 MACRO-HARDNESS MEASUREMENT DATA FOR VARIOUS AL-7XXX CDS ALLOYS MEASURED DURING THE NATURAL AGEING (NA) PROCESS AT ROOM TEMPERATURE FOLLOWING QUENCHING IN WATER AT ROOM TEMPERATURE THE SOLUTIONIZING TEMPERATURE OF 477 °C. 124
- FIGURE 6–33 TYPICAL OPTICAL MICROGRAPHS IN RELATIVELY HIGH MAGNIFICATIONS FOR COPPER FREE AL-7XXX ALLOYS IN ANNEALED (T4+O) CONDITION THAT ARE CAST FOR THIS STUDY BY THE CDS PROCESS COUPLED WITH TILT POUR GRAVITY CAST (TPGC) MACHINE: (A) AND (E) AL-3.5ZN-0.8MG ALLOY; (B) AND (F) AL-3.5ZN-1.6MG ALLOY; (C) AND (G) AL-5.2ZN-1.7MG ALLOY; (D) AND (H) AL-6.6ZN-1.7MG ALLOY. 125
- FIGURE 6–34 TYPICAL COMPARATIVE BAR GRAPHS OF (A) SIZE DISTRIBUTION AND (B) FRACTION AREA (%) OF SIGMA (MG(ZN,AL,CU)₂) PHASES, PRECIPITATING DURING THE ANNEALED (O) HEAT TREATMENT OF THE AL-7XXX CDS ALLOYS SELECTED FOR THIS STUDY. NOTE, THE EFFECT OF TOTAL ALLOYING ELEMENT CONTENT ON THE AREA FRACTION (OR THE NUMBER DENSITY) AND THE SIZE DISTRIBUTION OF PRECIPITATES; AND PARTICULAR EFFECT OF CU CONTENT ON THE SIZE DISTRIBUTION OF THE PRECIPITATES. 126

- FIGURE 6–35 TYPICAL STRESS-STRAIN CURVES OF AA 7050 CDS CASTINGS IN VARIOUS HEAT TREATMENTS SUCH AS AS-CAST (F), SOLUTION (T4), ANNEALED (O) AND NEAR PEAK AGED (T6) CONDITIONS. 127
- FIGURE 6–36 TYPICAL STRESS-STRAIN CURVE FOR AA 7050 ALLOY CAST USING THE CDS TECHNOLOGY AND AA356.2 ALLOY; BOTH ALLOYS WERE CAST IN THE TPGC PROCESS. TWO HEAT TREATMENT TEMPERERS FOR EACH ALLOY IS SHOWN: T4 AND T6. 128
- FIGURE 6–37 COMPARATIVE BAR GRAPH OF THE TENSILE PROPERTIES OF THE AA7050 CDS CAST SAMPLES UNDER VARIOUS HEAT TREATMENT CONDITIONS FROM THE TABLE 6–9 SHOWING THE SOFTENING EFFECT OF ANNEALING TREATMENT AS AN INTERMEDIATE PROCESS. 129
- FIGURE 6–38 GRAPHICAL UNIAXIAL TENSILE TESTING RESULTS FOR TYPICAL SAMPLES OF THE AA7050 ALLOY CAST WITH THE CDS TECHNOLOGY, SHOWING THE T4, T4+O AND T6 TEMPERERS. 130
- FIGURE 6–39 TYPICAL LIGHT OPTICAL MICROGRAPHS OF AS-CAST SAMPLES FOR AA7050 ALLOY CAST USING THE TPGC PROCESS WITH CDS TECHNOLOGY IN HIGH- AND LOW-MAGNITUDE: (A) AND (C) FOR ANNEALING HEAT TREATMENT CONDITION (T4+O), AND (B) AND (D) FOR SOLUTIONIZING HEAT TREATMENT CONDITION (T4), RESPECTIVELY, SHOWING THE PRECIPITATION WITHIN THE PRIMARY AL MATRIX. 130
- FIGURE 6–40 TYPICAL COMPARATIVE BAR GRAPHS OF UNIAXIAL TENSILE PROPERTIES, INCLUDING YIELD (YS), ULTIMATE TENSILE (UTS) STRENGTHS AND ELONGATION (EL) OF AL-7XXX CDS ALLOYS SELECTED FOR THIS STUDY, IN SOLUTION HEAT TREATED (T4) CONDITION. 132
- FIGURE 6–41 TYPICAL COMPARATIVE BAR GRAPHS OF UNIAXIAL TENSILE PROPERTIES, INCLUDING YIELD (YS), ULTIMATE TENSILE (UTS) STRENGTHS AND ELONGATION (EL) OF AL-7XXX CDS ALLOYS SELECTED FOR THIS STUDY, IN THEIR OPTIMAL PEAK AGE HARDENING (T6) CONDITION. 132
- FIGURE 6–42 EFFECT OF CU ADDITION ON THE YS AND ELONGATION OF THE AL 7XXX ALLOYS IN THIS STUDY. (A) PLOT OF YS IN BOTH T4 AND T6 TEMPER CONDITIONS AND (B) PLOT OF ELONGATION IN THE T4 TEMPER CONDITIONS. 134
- FIGURE 6–43 THE COMPARATIVE BAR GRAPHS REPRESENTATION OF THE AVERAGE GRAIN SIZES OF THE AL-7XXX CDS ALLOYS, LISTED IN TABLE 6–12. 135
- FIGURE 6–44 TYPICAL COMPARATIVE BAR GRAPHS OF FRACTION AREA (%) OF EUTECTIC PHASES AT GRAIN BOUNDARIES, SIMULATED BY THERMODYNAMIC DATABASE (PANDAT) AND ALSO MEASURED BY IMAGE ANALYSIS ON THE OPTICAL MICROGRAPHS OF THE AS CAST (F) AND SOLUTION (T4) HEAT TREATMENTS FOR THE AL-7XXX CDS ALLOYS. 135
- FIGURE 6–45 THE POROSITY CONTENT OF THE AL-7XXX CDS ALLOYS SELECTED FOR THIS STUDY. 136
- FIGURE 6–46 TYPICAL COMPARATIVE BAR GRAPHS OF POROSITY CONTENT (%) FOR AA 7050 IN CDS AND WROUGHT PRODUCTS BOTH FROM EXPERIMENTAL MEASUREMENTS CARRIED OUT IN THIS STUDY ACCORDING TO STANDARD EXPLAINED IN EXPERIMENTAL CHAPTER 5; IT IS NOTABLE THAT THE WROUGHT SAMPLES WERE PROVIDED BY THE MANUFACTURE IN T7651 CONDITION. MOREOVER, THE EXPERIMENTAL POROSITY MEASUREMENTS ARE ALSO COMPARED WITH THAT OF 7050 FOUND IN THE BACKGROUND LITERATURE (CAST IN COPPER MOLD) [181]. 136
- FIGURE 6–47 COMPARATIVE BAR GRAPHS OF UNIAXIAL TENSILE PROPERTIES OF AA 7050 ALLOY PRODUCED BY TWO DIFFERENT METHODS: (1) USING THE CDS TECHNOLOGY AND (2) PROCESSING WITH THE WROUGHT (ROLLED) METHOD. NOTE THAT IN (A) THE UNIAXIAL PROPERTIES OF BOTH CDS AND WROUGHT RESULTS ARE REPORTED IN AN OVER AGED (T7) CONDITION; WHEREAS IN (B) THEY ARE IN SOLUTION (T4) HEAT TREATMENT CONDITION. 137
- FIGURE 6–48 OPTICAL STEREOGRAPH IMAGES SHOWING SHEAR LIPS AND FIBROUS AREAS ON THE FRACTION SURFACES (UNDER TENSION LOAD): (A) AL-3.6ZN-0.8MG-0CU (C) AL-3.8ZN-2.2MG-1.7CU (E) AL-5.8ZN-2.2MG-2.5CU. ALL THE ALLOYS WERE CAST WITH CDS TECHNOLOGY AND HEAT-TREATED TO T4 TEMPER. 138
- FIGURE 6–49 CROSS SECTIONAL IMAGE BY OPTICAL MICROSCOPY FOR AL-5.8ZN-2.2MG-2.5CU-CDS SAMPLES IN ANNEALED (T4+O) HEAT-TREATED CONDITION IN RELATIVELY LOW AND HIGH MAGNIFICATIONS; (A) AND (B) SHOW CREAK INITIATION REGION; (C) AND (D) SHOW EXISTENCE OF MICRO VOIDS AND THEIR

- COALESCENCE THAT INITIATE FRACTURE; (E) TO (H) PREFERRED NUCLEATION AND GROWTH OF THE CRACKS AS INTER-GRANULAR FRACTURE ON THE INTERFACE BETWEEN THE SECONDARY INTERMETALLIC PHASES AND PRIMARY AL GRAINS. 139
- FIGURE 6–50 SEI ON SEM SHOWING THE NATURE OF THE FRACTURE SURFACE AFTER UNIAXIAL TENSILE TEST ON AL-5.8ZN-2.2MG-2.5CU-CDS SAMPLES IN T4 TEMPER. (A) AND (B) SHOW THE FRACTURE SURFACE FEATURES; (C) TO (H) SHOW THE ROLE OF SHRINKAGE CAVITIES IN THE CASTINGS ON THE NATURE OF FRACTURE. 141
- FIGURE 6–51 RELATIVELY HIGH MAGNIFICATION SEM MICROGRAPHS SHOWING DEMARCATED POINTS FOR EDS CHEMICAL MEASUREMENTS TABULATED IN TABLE 6–13. 142
- FIGURE 7–1 TYPICAL MICRO-HARDNESS (VICKERS HARNDNESS) DATA AS A FUNCTION OF TIME MEASURED FROM IMMEDIATELY AFTER QUENCHING THE AA 7050 CDS ALLOY CASTINGS SAMPLES IN WATER AT ROOM TEMPERATURE AFTER T4 TREATMENT AT 477 °C. THE SUBSEQUENT ISOTHERMAL AGEING TEMPERTAURE OF THE SAMPLES WERE (A) 200 °C, (B) 160 °C, (C) 120 °C AND (D) 70 °C. THE DEMARCTED REGIONS IN EACH FIGURE REPRESNET THE SELECTION OF THESE RESPECTIVE FEATURES WITH THE ASSUMPTION THAT THE FEATURES COULD OCCUR IN ANY TIME LOCATION WITHIN THESE RESPETCIVE REGIONS OF INTEREST. 145
- FIGURE 7–2: THE TYPICAL GRAPHS OF ARRHENIUS PLOT OF $\ln(T_p/T)$ VS. $1/T$ BY WHICH A VALUE FOR THE Q_A (ACTIVATION ENERGY) IS CALCULATED FROM THE SLOPE OF THE ARRHENIUS PLOT. IT IS NOTEWORTHY THAT. THIS VALIDITY TEST HAS BEEN TRIED FOR VARIOUS DESIGNATED STAGES PRESENTED ON THE AGE HARDENING CURVES (FIGURE) SUCH AS (A) FOR 50% OF THE PEAK HARDNESS VALUE OF PEAK HARDNESS POINT #1 (PEAK#1), (B) FOR THE PEAK HARDNESS POINT #1 (PEAK#1), (C) FOR THE LOCAL MINIMA PEAK HARDNESS POINT BETWEEN THE TWO PEAK HARDNESS POINTS #1 AND #2, AND (D) FOR THE PEAK HARDNESS POINT #2 (PEAK#2). 146
- FIGURE 7–3 QUANTITATVE IMAGE ANALYSIS ON THE TEM MICORGRAPHS FOR THREE ALLOYS OF THE AL-7XXX FAMILY SELECTED FOR THIS STUDY (TABLE 6–7). 148
- FIGURE 7–4 UNIAXIAL TENSILE PROPERTIES IN T4 AND T6 CONDITON FOR THE THREE ALLOYS SHOWN IN TABLE 6–7. 149
- FIGURE 7–5 ENGINEERING STRESS-STRAIN CURVES FOR DIFFERENT COMPOSITIONS OF THE AL-7XXX ALLOYS IN T4 HEAT TREATMENT CONDITION, THAT WERE SELECTED FOR THIS STUDY AND CAST WITH THE CDS PROCESS COUPLED WITH THE TPGC MACHINE INCLUDING THE THREE ALLOYS USED FOR THE APPLICATION OF STRENGTHENING MODELS. IT IS SHOWN IN THE FIGURE THAT INCREASING THE TOTAL ALLOYING ELEMENTS IN THE COMPOSITION OF THE A-ZN-MG-CU ALLOY INCREASES THE YIELD STRESS OF THE MATERIAL. 152
- FIGURE 7–6 COMPARISON OF TOTAL YIELD STRENGTH, Σ_y , FOR THE THREE MODELS AND EXPERIMENT DATA. THE MODELS ARE DEFINED IN TABLE 7–12. 158
- FIGURE 7–7 COMPARISON OF TOTAL YIELD STRENGTH, Σ_y , FOR THE CONSOLIDATED MODELS AND EXPERIMENT DATA. 159
- FIGURE 9–1 STEM MICROGRAPHS IN (A) HIGH ANGLE ANNULAR DARK FIELD MODE OF THE PHASES FORMING AT THE GRAIN BOUNDARY (GB) IN THE CU-FREE ALLOY OF AL-3.5ZN-0.8MG-0CU IN THE T6 TEMPER; ALONG WITH ELEMENTAL EDS MAPS FOR (B) ZN+MG, (C) AL, (D) ZN, (E) MG, (F) CU, AND (G) SI; SHOWING THAT THESE GB FORMING AT GB ARE SIGMA $(MG(ZN,AL,CU))_2$ PHASES IN CU-FREE AL-7XXX ALLOYS AS COMPARED TO THE S (AL_2CUMG) PHASES FORMING IN THE CU-BEARING AL-7XXX PHASES THAT ARE SHOWN IN FIGURE 9–2. 165
- FIGURE 9–2 STEM MICROGRAPHS IN (A) HIGH ANGLE ANNULAR DARK FIELD MODE OF THE PHASES FORMING AT THE GRAIN BOUNDARY (GB) IN THE CU-BEARING ALLOY OF AL-5.8ZN-2.2MG-2.5CU (7050) IN THE T6 TEMPER; ALONG WITH THE ELEMENTAL EDS MAPS FOR (B) ZN+MG+CU, (C) ZN+MG, (D) AL, (E) ZN, (F) MG, (G) CU, AND (H) SI; INDICATING THAT THESE GB PHASES ARE THE S (AL_2CUMG) PHASES FORMING IN THE CU-BEARING AL-7XXX PHASES AS OPPOSED TO THE SIGMA $(MG(ZN,AL,CU))_2$ PHASE FORMING AT GB IN THE CU-FREE AL-3.5ZN-0.8MG-0CU ALLOYS, AS SHOWN IN FIGURE 9–1. 165

List of Tables

TABLE 1–1. TYPICAL ECONOMICAL AND ENVIRONMENTAL BENEFITS OF CURB WEIGHT REDUCTION OF A CHRYSLER TOWN AND COUNTRY MINIVAN [].	2
TABLE 1–2 SOME RECENT ADVANCES IN ALLOYS AND CASTING PROCESSES FOR AL CASTING ALLOYS FOR IMPROVED UNIAXIAL TENSILE PROPERTIES IN AUTOMOTIVE APPLICATION.	4
TABLE 4–1 PRIOR-ART IN DIFFUSIONAL SOLIDIFICATION.	19
TABLE 4–2: ALUMINUM CAST AND WROUGHT ALLOY FAMILIES [5]	23
TABLE 4–3 TYPICAL PHYSICAL PROPERTIES OF ALLOYING ELEMENTS IN THE AL-7XXX SERIES SYSTEM	24
TABLE 4–4: DIFFUSION COEFFICIENT OF COMMON ALLOYING ELEMENTS IN AL MATRIX [66].	27
TABLE 4–5 IDENTIFICATION OF THE THERMAL REACTIONS OCCURRING IN THE DSC TEST OF 9 ALLOYS FROM THE AL-ZN-MG-CU FAMILY THAT ARE AGED FOR 8 HOURS AT 172 °C. [72].	29
TABLE 4–6: NUMBER OF VACANCIES PER ATOM IN EQUILIBRIUM CONDITION IN PURE ALUMINUM, AS A FUNCTION OF TEMPERATURE [66].	30
TABLE 4–7 EXAMPLES FOR HARD AND SOFT OBSTACLES IN TERMS OF HOW THEY CAN RESIST THE DISLOCATION MOTION IN ALUMINUM ALLOYS [125].	54
TABLE 4–8 A SUMMARY OF THE STRENGTHENING MODELS APPLICABLE FOR THE AL-7XXX WROUGHT ALLOYS	64
TABLE 4–9 TYPICAL TENSILE MECHANICAL PROPERTIES OF AA 7050 WROUGHT ALLOYS BY VARIOUS PROCESSING ROUTES	65
TABLE 4–10 TERMINOLOGY OF FRACTURE PHENOMENON	66
TABLE 5–1 NOMINAL COMPOSITION (WT.%) OF THE AL-7XXX ALLOYS THAT ARE MEASURED BY GDOES TEST METHOD, WHICH WERE SELECTED FOR THIS STUDY.	71
TABLE 5–2: CDS PROCESS PARAMETERS FOR THE PRECURSOR ALLOYS (ALLOY1, ALLOY2 AND ALLOY3) FOR THE AL-7XXX ALLOYS SELECTED FOR THIS STUDY. THE COMPOSITIONS (WT.%) WERE MEASURED BY THE GDOES TEST METHOD.	74
TABLE 5–3 TYPICAL HEAT TREATMENT/TEMPER CONDITIONS USED FOR THE TENSILE TEST-BARS CAST SAMPLES FROM THE AL-7XXX ALLOYS THAT ARE SELECTED FOR THE CDS EXPERIMENT IN THIS STUDY.	84
TABLE 5–4 DETAIL DATA USED FOR THE CALCULATION OF THE THEORETICAL DENSITY OF EACH ELEMENT IN THE AL-7XXX (AL-ZN-MG-CU) ALLOY COMPOSITION THAT ARE FOUND IN THE BACKGROUND LITERATURE [31,68].	88
TABLE 5–5 THE EFFECT OF CHEMISTRY VARIATION MEASURED BY GDOES FOR EACH ALLOYING ELEMENT IN THE ALLOY COMPOSITION OF EACH OF THE NINE ALLOYS ON THE THEORETICAL AND EXPERIMENTAL DENSITY AND POROSITY MEASUREMENTS.	89
TABLE 6–1 EXPLANATIONS FOR TYPICAL PRECIPITATION AND DISSOLUTION REACTIONS DURING THE DCS EXPERIMENT SHOWN IN FIGURE 6–6.	95
TABLE 6–2 EDS ELEMENTAL ANALYSES OF SPECIFIED AREAS REFERENCED IN FIGURE 6–7	98
TABLE 6–3 EDS ELEMENTAL ANALYSIS OF THE SPOTS REFERENCED IN THE SEM IMAGES IN FIGURE 6–10.	101
TABLE 6–4 EDS ELEMENTAL ANALYSIS OF THE NUMBERED REGIONS SHOWN IN FIGURE 6–12.	104
TABLE 6–5 TYPICAL LIST OF PHASES FORMING IN THE AL-7050 ALLOY THAT ARE DETERMINED BY EQUILIBRIUM AND NON-EQUILIBRIUM SIMULATIONS, AND EXPERIMENTAL RESULTS FOR THE AL-5.8ZN-2.2MG-2.5CU ALLOY IN F AND T4 HEAT TREATMENT CONDITION.	107

TABLE 6–6 PARTICLE SIZE AND FRACTION AREA DISTRIBUTION FOR IMPURITY AND SECONDARY PHASES, MEASUREMENTS BY IMAGE ANALYSIS ON AA 7050-CDS IN T4 AND AS-CAST CONDITION.	109
TABLE 6–7 THE COMPOSITION OF THE THREE ALLOYS FROM THE AL-7XXX THAT ARE SELECTED FOR FURTHER TEM INVESTIGATION IN PEAK AGE (T6) HEAT TREATMENT CONDITION ACCORDING TO TABLE 5–3; THE COMPOSITIONS WERE MEASURED GDOES.	112
TABLE 6–8 EDS ELEMENTAL ANALYSES OF SPECIFIED AREA AND POINTS THAT ARE DEMARCATED IN FIGURE 6–28.	119
TABLE 6–9 UNIAXIAL TENSILE TEST RESULTS OF CDS SAMPLES OF AA7050 IN DIFFERENT HEAT TREATMENT COMBINATIONS BETWEEN AGEING, SOLUTIONIZING AND ANNEALING	129
TABLE 6–10 TYPICAL UNIAXIAL TENSILE PROPERTIES OF THE AL-7XXX ALLOYS SELECTED FOR THIS STUDY, CAST BY CDS PROCESS USING TILT POUR GRAVITY CASTING (TPGC) MACHINE AND HEAT TREATED IN THE SOLUTION TREATMENT (T4) CONDITION, (24 HOURS AT 477°C FOLLOWED BY WATER QUENCHING AND 96 HOUR INCUBATION AT THE AMBIENT TEMPERATURE).	131
TABLE 6–11 TYPICAL UNIAXIAL TENSILE PROPERTIES OF THE AL-7XXX CDS ALLOYS SELECTED FOR THIS STUDY, OBTAINED IN THEIR OPTIMAL PEAK AGED (PAC/T6) CONDITION (T4 + 24 HOURS AT 120°C).	132
TABLE 6–12 AVERAGE GRAIN SIZES OF THE AL-7XXX CDS ALLOYS IN VARIOUS HEAT TREATMENTS.	134
TABLE 6–13 EDS RESULTS FOR POINT INDICATED ON THE FRACTURE SURFACE OF IN FIGURE 6–51.	142
TABLE 7–1 RESULTS OF THE WEIGHTED LINEAR REGRESSION ANALYSIS FOR EACH OF THE CURVES SHOWN IN FIGURE 7–2 (A) TO (D), RESPECTIVELY.	146
TABLE 7–2 RESULTS OF P_p AND Q_d ALONG WITH THE RESPECTIVE 95% CONFIDENCE INTERVAL FOR EACH OF THE FOUR SALIENT FEATURES IN THE TRANSIENT HARDNESS CURVES SHOWN IN FIGURE 7–1 (A) TO (D), RESPECTIVELY.	147
TABLE 7–3 EXPERIMENTAL DATA USED IN THE PROCESS MODELS FOR STRENGTHENING MECHANISMS.	148
TABLE 7–4 DETAILS OF THE MATERIAL CONSTANTS USED FOR APPLICATION OF PROCESS MODELS EXPLAINED EARLIER FOR THIS STUDY.	149
TABLE 7–5 CONTRIBUTING FACTORS TO THE TOTAL YIELD STRENGTH OF AL 7XXX ALLOYS.	149
TABLE 7–6 VALUES OF INTRINSIC STRENGTH (Σ_A) IN VARIOUS MODELING APPROACHES.	150
TABLE 7–7 VALUES OF A_{SS} FOR THE VARIOUS APPROACHES TO STRENGTHENING MODELING.	151
TABLE 7–8 EVALUATION OF Σ_{SS} FOR THE THREE ALLOYS IN THIS STUDY	151
TABLE 7–9 EXPRESSIONS TO EVALUATE Σ_{ppt} IN THE VARIOUS APPROACHES TO STRENGTHENING MODELING.	153
TABLE 7–10 EVALUATION OF Σ_{ppt} IN THE VARIOUS APPROACHES TO STRENGTHENING MODELING.	154
TABLE 7–11 GRAIN BOUNDARY STRENGTHENING (Σ_{GB}) IN THE DMS APPROACH TO STRENGTHENING MODELING.	155
TABLE 7–12 THE MODELS THAT YIELDED VALUES OF Σ_y THAT WERE COMPARABLE TO THE EXPERIMENT DATA. THE TAYLOR FACTOR, $M = 2$.	157
TABLE 7–13 A CONSOLIDATED MODEL THAT YIELDED VALUES OF Σ_y THAT WERE COMPARABLE TO THE EXPERIMENT DATA. THE TAYLOR FACTOR, $M = 2$.	158
TABLE 9–1 THE DETAIL CALCULATIONS FOR ALL AND EACH POSSIBLE COMBINATIONS OF STRENGTHENING CONTRIBUTION TO THE TOTAL YIELD STRESS OF THE AL-3.5ZN-0.8MG-0CU ALLOYS AS EXPLAINED IN THE SECTION OF 7.3.	166
TABLE 9–2 THE DETAIL CALCULATIONS FOR ALL AND EACH POSSIBLE COMBINATIONS OF STRENGTHENING CONTRIBUTION TO THE TOTAL YIELD STRESS OF THE AL-3.8ZN-2.2MG-1.7CU ALLOYS AS EXPLAINED IN THE SECTION OF 7.3.	166

TABLE 9-3 THE DETAIL CALCULATIONS FOR ALL AND EACH POSSIBLE COMBINATIONS STRENGTHENING CONTRIBUTION TO THE TOTAL YIELD STRESS OF THE AL-5.8ZN-2.2MG-2.5CU ALLOYS AS EXPLAINED IN THE SECTION OF 7.3. 167

1 INTRODUCTION

The global requirement of significant reduction in the Green House Gas (GHG) emission and energy reduction has led to several widespread efforts in the automotive industry to reduce the curb weight of both light and heavy-duty automobiles around the world. In North America (USA and Canada), there is a sense of urgency amongst the automotive Original Equipment Manufacturer (OEM) to seek out several commercially viable strategies for significant automotive light weighting. This has been further emphasized and triggered by the strong recommendations from the Federal governments of both USA and Canada [1]. In 2009, the US Environmental Protection Agency (EPA) published a strong recommendation to improve the fuel efficiency of light duty automobiles in North America from the 28.8 miles per gallon (mpg) in 2009 to 34.1 mpg by the year 2016 to maintain the Green House Gas (GHG) Emission Standards and Corporate Average Fuel Economy (CAFE) standards [2]. Cheah, in her PhD dissertation [3] recently, has presented the trend in the historical average fuel economy of light duty vehicles in the USA since 1975 and shows the new requirements from the US EPA alongside, as shown in Figure 1–1; wherein, the fuel economy has remained nearly constant between the years 1985 and 2005 with a significant improvements required by the year 2016.

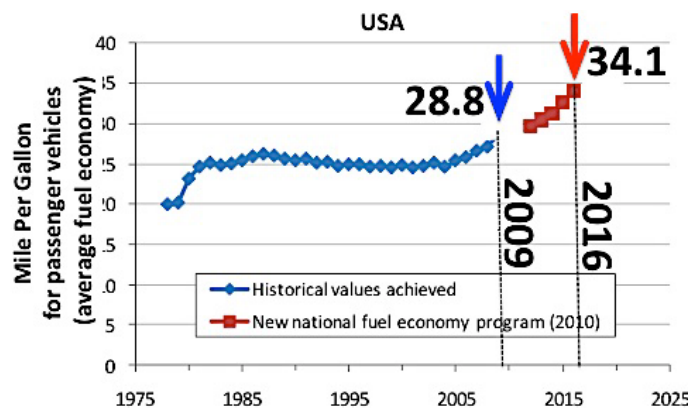


Figure 1–1 Sales-weighted average fuel economy of new U.S. light-duty passenger vehicles [2].

In the parlance of fuel consumption, an improvement from 28.8 mpg to 34.1 mpg translates to an improvement from 8.17 L/100km to 6.89 L/100km, respectively. There are three strategies that could individually and / or collectively lead to achieving this stringent target of fuel economy: reducing the curb weight of the vehicle by nearly 40 %, improving the fuel efficiency of the automotive powertrain components and introducing hybrid-electric powertrain systems. As an example, with the existing powertrain system in a Chrysler Town and Country minivan, there needs to be a nearly 50% reduction in the curb weight of the automobile (from 2041 kg to 1225 kg) to satisfy the requirement imposed by the US EPA to reduce fuel economy from 25 mpg to 35 mpg by the year 2016; the economic and environmental benefits from such a reduction in the curb weight is shown in Table 1–1.

Table 1–1. Typical economical and environmental benefits of curb weight reduction of a Chrysler Town and Country Minivan [4].

Baseline Minivan (Curb Weight 4,500 lb, EPA City/Hwy Unadjusted 25 mpg)					
% Wt Reduction	%FE Improvement	FE City/Hwy Combined (Unadjusted)	Fuel Savings per Vehicle at 15,000 miles/yr	Cost Savings per Vehicle at \$3.00/gallon	CO ₂ Reduction per vehicle
10%	8.0%	27.0 mpg	44 gallons	\$133 /yr	862 lbs/yr
20%	16.0%	29.0 mpg	83 gallons	\$248 /yr	1606 lbs/yr
30%	24.0%	31.0 mpg	116 gallons	\$348 /yr	2253 lbs/yr
40%	32.0%	33.0 mpg	145 gallons	\$436 /yr	2822 lbs/yr
50%	40.0%	35.0 mpg	171 gallons	\$514 /yr	3326 lbs/yr

There are two major technological routes for innovation within the realm of automotive lightweight: lightweight high strength steel intensive and Aluminum alloys intensive, respectively. Typically, both these technological routes aim at substituting the majority of the heavy (high density) iron and steel components in a vehicle by either high strength steel or aluminum alloys; Figure 1–2 presents the proposed material breakdown in a typical light duty automobile that is required to achieve gradual reduction in the curb weight of the vehicle by up to 40 % of the baseline weight in the year 2009. Also, shown in Figure 1–2 is the two separate technological routes of using high-strength steel intensive in Figure 1–2 (a) and Aluminum alloys intensive in Figure 1–2 (b).

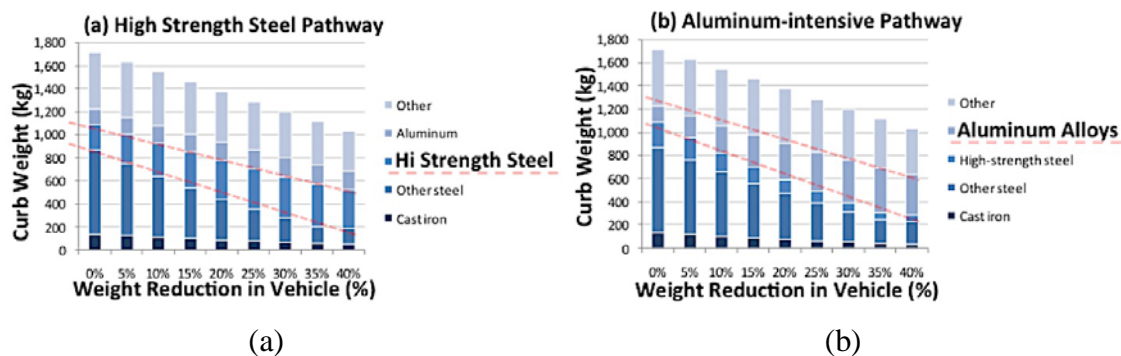


Figure 1–2 Material breakdowns for automotive light-weighting strategy using two separate technological routes: (a) high strength steel intensive and (b) aluminum alloy intensive [2]. The 0% shown in the above graphs represents the average material breakdown and curb weight for a light duty automobile in the year 2009.

The mission of the current research program at the Light Metal Casting Research Centre (LMCRC) in McMaster University, of which I am presently a part of, is to explore the possible technological innovations that would enable nearly 50 % reduction in the curb weight of a light duty automobile through the aluminum alloys intensive route wherein major heavy structural and non-structural components of ferrous material is replaced by advanced aluminum alloys. There are two families of aluminum alloys: cast and wrought alloys. The former family enables near net shaped manufacturing of components through solidification processes (liquid to solid) with minimum post processing such as machining and finishing, while the latter requires casting the alloys into stock products such as billets, rods and sheets to further transform them into near net shaped products using solid state transformation technologies such as a forging, extrusion, drawing, etcetera [5]. It is notable that the present day technologies do not allow near net shape manufacturing of Al wrought alloys solely through solidification processes such as casting [6].

Cheah et al [7, 8] explains that a typical light duty automobile with a curb weight of 1616 kg contains 7 % by weight of cast Al alloys and 1.8 % by weight of wrought Al alloys products and to achieve a 20% reduction in this total curb weight to a final weight of 1294 kg, it is mandatory to increase the amount of cast Al alloys to 15.4 % by weight and wrought Al alloys to 17.2 % by weight. This increase is proposed while considering both the low density of Al alloys compared to its ferrous counterparts and the relative mechanical properties of both the cast and wrought Al alloys [7]. It is nearly impossible to attain the significant increase in the use of Al wrought alloys in the vehicle unless novel technologies are developed to enable near net shaped manufacturing of the Al wrought alloys into final components through direct solidification processes (casting) akin to those used in manufacturing of Al cast alloy components at present. It is the aim of this PhD dissertation to explore one such viable manufacturing technology to enable near net shaped cast products of Al wrought alloys, specifically, the 7xxx family of alloys [9].

The low density of Al compared to Fe is not the only criteria that will enable the realization of light weighting of any specific automotive component from replacing the heavy ferrous alloy components with Al alloys. Unless the Al alloy counterpart could achieve a certain minimum baseline of mechanical and performance properties, the switch to the lighter alloys is not viable; specifically so in components of structural application in an automobile. The vast majority of the heavy ferrous alloy components in an automobile are used for critical structural support applications and to replace these components with Al alloys, the latter should have a minimum of 400 MPa for Ultimate Tensile Strength (UTS), 300 MPa for Yield Strength (YS) (0.2 % proof stress) and about 7 % or greater in elongation [4]. If the Al alloys do not meet these minimum criteria for mechanical properties, then the redesign of the component for lightweight alloys will not yield the anticipated (>35%) reduction in weight of the component. Recent global efforts in developing advanced Al casting alloys and affiliated processes have shown significant improvement in attaining higher mechanical properties of these alloy components, however, they still fall short of the required mechanical properties to enable structural application with these alloys while realizing significant weight reduction in the components. Table 1–2 presents some of the salient recent efforts around the world in the development of Al casting alloys and processes to suite the current requirements of high mechanical properties demanded by automotive lightweight measures. It is notable that only one candidate in the B206 alloy in Table 1–2 meet the requirement of the uniaxial tensile properties described earlier in this paragraph to enable structural automotive application and replace the heavier ferrous alloy components. However, it is notable that this B206 alloy (Al-4.5Cu) can only be cast successfully by the sand casting process which is not the most economical and is fraught with a high rate of scrap and reject generation from the casting process; further, the alloy is highly temperamental in its response to heat treatment and it is commercially tedious to enable a consistent high yield product with this alloy [10]. The B206 alloy is used in specialty application that could be cast by precision sand casting process. A viable automotive alloy that could be used for structural applications and one that is economically viable in a commercial process should have the capabilities of manufacturing through a variety of conventional casting process routes such as sand, permanent mould, tilt pour gravity, low pressure die casting and high pressure die casting processes. The quest for such a family of Al alloy and casting process is still underway globally.

Table 1–2 Some recent advances in alloys and casting processes for Al casting alloys for improved uniaxial tensile properties in automotive application.

Alloy	Process	UTS	YS	%El	Ref
		MPa (Ksi)	Mpa (Ksi)		
356 type (T6)	PM	280 (41)	235 (34)	6.5	Jeyakumar et al [11]
356 Type (T6)	Ablation	330 (48)	239 (35)	14	Grassi et al [12]
206 type (T6)	Sand Casting	430	336	11	Sigworth et al [13]
6063 type (T6)	Ablation	334	268	14	Grassi et al [12]
367 (T5) (Mercialloy)	HPDC	310 (45)	240 (35)	7	Kopper et al [14, 15]
Silafont 36 (T6)	HPDC	290 – 350 (42 – 50)	200 – 280 (29 – 40)	6 – 12	Rheinfeldten [16]

The above-cited reasons for the limitations of using Al casting alloys for replacing the structural ferrous alloy components in an automobile has necessitated a larger use of Al wrought alloys for automotive components to better realize the proposed light-weighting measures. Hence, Cheah et al [7,8] have evaluated that the use of Al cast alloys should increase from 7 % to 15.4 % by weight and that for wrought alloys should be significantly higher from 1.8 % to 17.2 % by weight to realize a 20 % reduction in the curb weight of a light duty automobile.

Among the several Al wrought alloys, the 7xxx family of alloys constituted by the Al-Zn-Mg-Cu element combination have displayed the highest uniaxial tensile properties with the best combination of YS and elongation. Developing enabling casting technologies for near net shaped manufacturing of these alloys will have a significant and positive impact in substituting several heavy ferrous alloys automotive components and realize the significant light-weighting requirements. Figure 1–3 shows a typical comparative graph of the uniaxial tensile properties of the AA7050 wrought alloy and A356.2 casting alloy of Al; wherein, the significant increase in the properties of the wrought counterpart is evident. Notably, in Figure 1–3, the wrought AA7050 alloy has been manufactured to near net shape by forging process; if a novel process were to be developed to manufacture the same through solidification (casting) process, the economic viability and advantage of a commercial production of this alloy for lightweight and structural automotive component could be realized. It is the aim of this PhD dissertation to present evidences and data to support the use of the Controlled Diffusion Solidification (CDS) technology [6] to enable near net shaped casting of Al wrought alloys of the 7xxx family series.

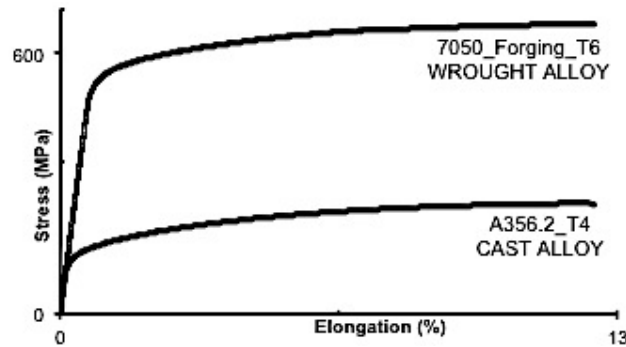


Figure 1–3 Typical strain-stress curves of A356.2 in T4 condition and AA 7050 forgings in T6 condition [5].

Traditionally, Al wrought alloys do not lend themselves to near net shaped manufacturing of components using a direct solidification (casting) process due to the inherent problems of hot tearing (hot cracking) [17, 18] in the component during solidification, that renders the cast component defective; the problem of hot tearing arises from the fundamental solute redistribution in the solidifying wrought alloy and seldom an issue from the casting process. The problem of hot tearing also exists in certain Al casting alloys which have solute element levels below the maximum solid solubility in Al at the eutectic temperature; B206 alloy (Al-4.5Cu) is a typical example wherein hot tearing is a prevalent casting defect in components [17]. One of the common methods to circumvent hot tearing in Al casting alloys is to develop casting processes that would yield a non-dendritic morphology of the primary Al phase during solidification to alleviate the root cause of the problem in feedability of the liquid alloy in the inter dendritic regions [19]. To circumvent the problems of hot tearing and additionally enhance the properties and performance of the cast component, several solidification-processing technologies under the umbrella of Semi Solid Metal (SSM) processing were developed in the past forty years [19,20]. In the SSM processes, the alloy is brought and held in the two-phase semi-solid regime to enable copious nucleation and nearly uniform distribution of the solid phase of the primary Al in the semi-solid slurry; subsequent to homogenization of the temperature field in the slurry, it is cast into a near net shaped component using a pressure assisted casting process such as high pressure die casting and squeeze casting. The primary phases in the microstructure of the products in SSM casting are typically non-dendritic due to the breakdown of the solidifying dendrites with the application of an external force [21]. In SSM processing of Al casting alloy, typically, when the solid fraction is less than about 25 % by volume, the alloy behaves like a viscous slurry that would flow under a positive pressure gradient; and when the solid fraction becomes more than 60 % by volume, the alloy ceases to flow [22,23]. A detailed presentation of the hot tearing defect in cast alloys is presented in Section Shrinkage and Hot Tearing of this dissertation (4.1.1).

SSM processes are broadly classified as thixo-forming/casting and rheocasting processes. Figure 1–4 (a) and (b) show schematics of temperature-time graphs for typical rheocasting and thixocasting processes, respectively. In the rheocasting process route (Figure 1–4 (a)), the liquid alloy of a desired composition is brought to the semi-solid region (fraction solid of about 0.15 to 0.25) by continuously applying an external force such as mechanical, magneto hydro dynamic or electromagnetic force on the cooling liquid to induce forced convection coupled with copious nucleation of the primary solidifying phase in the liquid. Subsequently, the semi-solid slurry is maintained in an isothermal environment inside an induction furnace for a few minutes to enable thermal homogenization and stable/homogenous growth of a non-dendritic primary phase [24,25]. The slurry is then cast into a near net shaped component via a pressure assisted casting process. In thixo-forming/casting (Figure 1–4 (b)), the alloy melt of a desired

composition is initially solidified as billets or rods with a highly grain refined primary phases, which were caused by means of rapid solidification, grain refinement and/or stirring. These billets are further sectioned into slugs to the required dimensions and weights as dictated by the final shaped component. The slugs are then re-heated and maintained in an isothermal environment with an induction furnace within a temperature range of the semi-solid region as dictated by a fraction solid of about 0.15 to 0.25 for the specific composition of the alloy; subsequently, the slurry is cast into near net shaped components by a pressure assisted casting/forging process, which is also known as thixo-forming/casting, respectively [26,27].

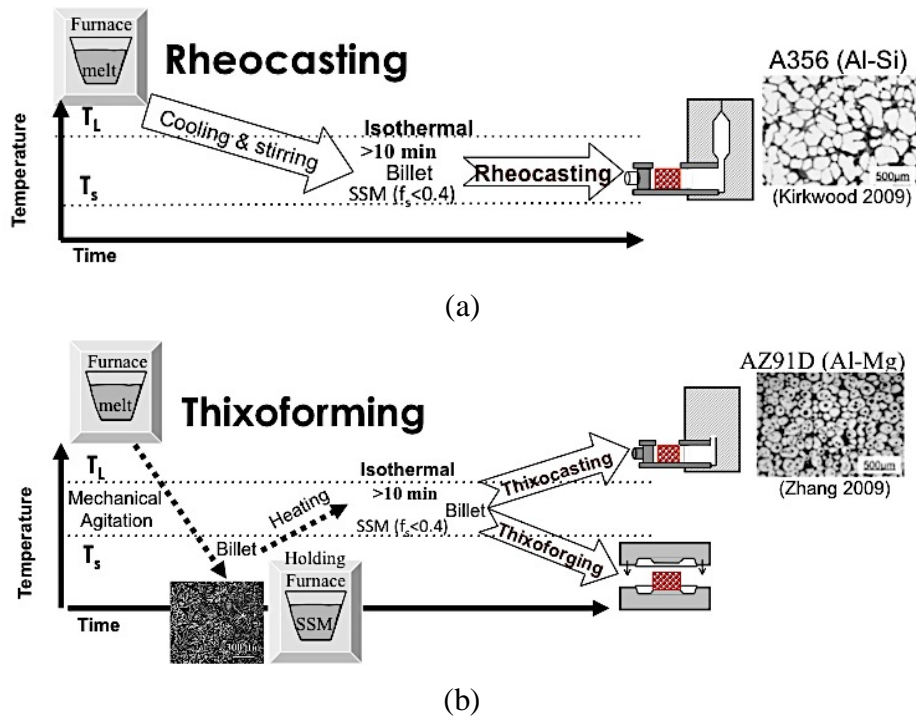


Figure 1–4 Schematic process plots of the temperature versus time for (a) rheocasting [25] and (b) thixocasting semi-solid metal processes [26].

The thixo-forming/casting processes have been cost prohibitive due to the additional stages of billet casting and re-heating; this technology is being phased out commercially around the world [28]. Most of the rheocasting processes have been under research and development for the past thirty years except the New Rheocasting Process (NRP) [20]; because of the high capital cost and the inability to overcome inclusions and casting defects in most processes. The NRP has had limited commercial success [29].

Presently, the notable rheocasting processing routes that attempt to achieve commercial production are the Semi Solid Rheocasting (SSR), Sub-Liquidus Casting (SLC), New Rheocasting Process (NRP) and Continuous Rheo-conversion Process (CRP) [30, 23]. Each of these rheocasting processing has respective proprietary technologies to achieve the two required conditions of copious nucleation of the primary solidifying phase and forced convection for uniform distribution of these nuclei to achieve the nearly non-dendritic morphology of the primary phase in the cast product. The main drawbacks of these technologies in enabling such solidification are the high capital cost of infrastructure, introduction of unwanted artifacts such as oxides from the rapid break down of the Al alloy melt surface and create high scrap and unpredictable flow of the semi-solid slurry into the mould cavity due to lack of fluid flow knowledge. The time required to bring a large volume

of alloy melt (usually in the tens of pounds weight) from a superheated liquid state to the favorable semi-solid state while inducing the desired nucleation and distribution phenomena is significantly high (in minutes) compared to the desired productivity of the cast component from such alloys (in seconds), resulting in the requirement of multiple casting stations being set up to append to the high capital investment in the casting process infrastructure. Hence, none of the rheocasting technologies have found prevalent acceptance and use in the commercial Al casting industry.

Rheocasting is a viable technological route to cast components of Al alloys with a non-dendritic morphology. However, the rheocasting processing would not be a viable method to cast Al wrought alloy into near net shaped components. Figure 1–5 (a) and (b) present the relationship between fraction solid and temperature range (or freezing zone) of the alloy during solidification of AA7050 Al wrought alloy and Al-7wt%Si casting alloy, respectively; the temperature regime for a fraction solid region between 0 and 0.3 is also shown in these respective graphs for the two alloys. In Figure 1–5 (a), it is evident that to process AA7050 by rheocasting technology, one would have to cool a large quantity of liquid down to a slurry which contains about anywhere between 20 to 30 % fraction solid by volume, which would require that the temperature gradient in the cooling liquid bulk to be less than 2 °C as dictated by the thermodynamics; this is commercially not viable in a production environment. Whereas, in Figure 1–5 (b), for a typical casting alloy the temperature gradients within the bulk semi-solid slurry could be around 10 °C to enable the rheocasting process and this is commercially feasible. Hence, it would be a commercially futile effort to adapt the rheocasting technologies for near net shaped casting of Al wrought alloys.

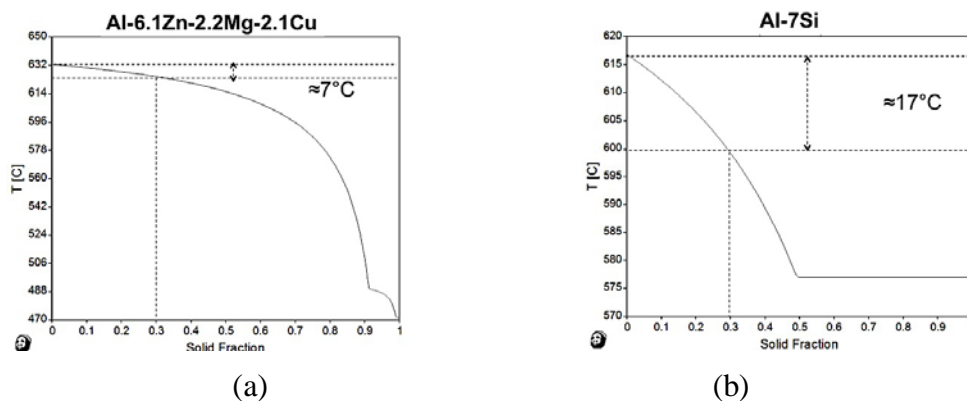


Figure 1–5: Trace of solid fraction (f_s) as a function of temperature for (a) AA7050 wrought alloy and (b) Al-7Si casting alloy to show the temperature drop to obtain semi-solid slurry of about 0.3 solid fractions [6].

Amongst the wrought and cast aluminum alloys, the 7xxx series alloys (Al-Zn-Mg-Cu) and 2xxx series alloys (Al-Cu-Mg) are the most applicable for structural automotive and aerospace castings; in part this is because of their high strength to weight ratio [5,31]. Typically, the 7xxx series Al wrought alloys in their as cast condition do not offer their best mechanical properties and performance due to inherent production deficiencies such as the coarse intermetallic constituent phases, coarse grains, micro-segregation, solid solubility limitations and, above all, macro-segregation and hot cracking (due to the inability of the solidifying liquid metal to accommodate the strain field imposed by contracting solid fraction) [32,33,34]. Among these inherent casting defects, the hot tearing or hot cracking is predominantly responsible for the inability to manufacture near net shaped cast components from the 7xxx alloys. In theory, the hot tearing defect could be overcome during solidification by two methods: significant refinement of the Secondary Dendrite Arm Spacing

(SDAS) of the primary Al phase and by altering the morphology of this phase to a non-dendritic one. The former objective is achieved by one or many of precise control over the process parameters such as pouring temperature (superheat), cooling rates (design of cast part) and grain refinement by alloying elements; all of which reduce the complication associated with the solidification network of dendrites of the primary phase, which in turn would allow the solidifying liquid phase to better accommodate the strain field applied by the shrinking solid fraction [18,35]. The morphological modification of the primary Al phase in the solidified casting could be achieved by employing one of the several Semi-Solid Metal (SSM) processes such as thixo-forming/casting and rheocasting; all of which are carried out by using external or natural forces to physically or thermally alter the morphology of the solidifying Al phase during the intermediate stages of solidification [19,36]. However, these SSM processes are not commercially favored by industry due to the complexity and cost of these processes coupled with the lack of repeatability and reproducibility of the commercial processes [20]. Further, recent research [37,38,39] on the flow characteristics of metallic alloys could be extrapolated to explain the difficulties associated with casting of these alloys due to the complexities in the flow behavior of the Al alloys which is reflected in their fluidity and viscosity. Thus, the Al shaped casting industry remains unable to fully benefit from the superior properties of Al 7xxx wrought alloys used in near net shaped casting processes. Figure 1–6 illustrates one of common casting defects of aluminum wrought alloys (2xxx series) known as “hot tearing” in its macro-scale appearance [40, 41]. All the alloy compositions in this publication will be in weight percentage of the respective elements except otherwise mentioned.

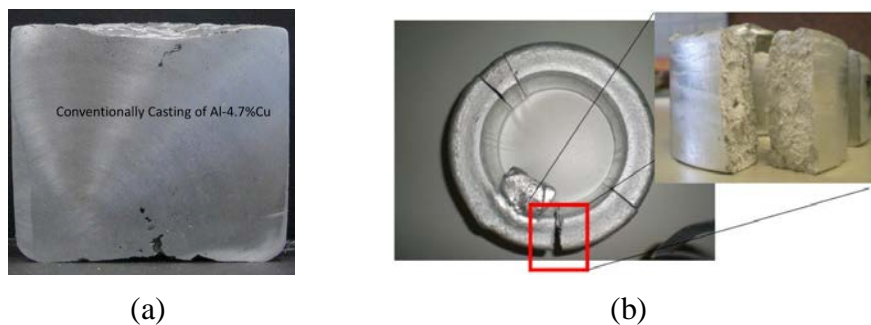


Figure 1–6 Photographs of typical shrinkage and hot tearing defects in castings of Al alloys (a) shrinkage in B206 (Al-4.7Cu) alloy, (b) hot tearing in ring casting of Al-Mg-Cu (AA2014) alloy [40], respectively.

CDS (Controlled Diffusion Solidification) is a casting technology that has been developed mainly to enable near net shaped manufacturing of Al wrought alloys through a conventional casting process such as sand, permanent mould, tilt pour gravity and high pressure die casting processes [42, 43]. The novelty of the CDS technology is to provide copious inoculants of the primary Al phase while uniformly distributing the nuclei in the entire bulk liquid above the liquidus temperature of the alloy being cast. A detailed explanation of this technology and the underlying mechanisms of the process are provided in Section 4.1.2 of this dissertation.

The use of CDS technology along with the tilt pour gravity casting process has been shown to be a viable method to enable the near net shape cast of the Al 7xxx wrought family alloys [42] and it is the aim of this dissertation to present a comprehensive understanding of the relationship among the uniaxial tensile properties, alloy composition of the 7xxx alloys and their respective heat treatments (solutionizing, annealing and ageing) to further the technology from a ‘*proof-of-concept*’ to ‘*commercial viability*’ status. This work aims to

establish that it is commercially viable to obtain and exceed the desired baseline tensile properties of 400 MPa for UTS, 300 MPa for YS and about 7% elongation that is mandatory to be able to substitute some of the heavy ferrous alloy structural components in a light duty automobile to enable a significant reduction in the curb weight of the same.

It is notable that when I was embarking on this PhD dissertation, the following was unknown:

- Difference in the nature of the microstructure between these components and those made from these alloys using conventional solid-state transformations typically used with Al wrought alloys.
- The heat treatment responses of the Al-7xxx castings such as solute redistribution, and alterations to secondary solidified phase nature and morphology during solution treatment, and mechanisms and sequences of precipitation reactions during natural and artificial ageing may be markedly different from those observed in components manufactured by traditional solid state transformations for Al wrought alloys.

Hence, the primary aim of this dissertation is to develop a qualitative and quantitative understanding of the phase evolution during solidification, heat treatment (solutionizing, annealing and ageing) of these Al-7xxx alloys and consequently their impact on their uniaxial tensile properties. The dissertation aims to establish and quantify the operational boundaries of using the CDS technology coupled with tilt pour gravity casting process for near net shaped manufacturing of the 7xxx series of Al wrought alloys with respect to alloy chemistry and heat treatment regimes. The results and discussion of this dissertation will directly lead to selection of specific alloy chemistry and heat treatment procedures to attain desired uniaxial tensile properties for the Al 7xxx wrought alloys using the CDS technology with tilt pour gravity casting process.

The above-mentioned scientific motivation in this project lead to a lucid definition of the objectives and subsequently, a methodology was strategized and implemented: as presented in 3 (Project objectives and Methodology) of this dissertation.

2 ABBREVIATIONS AND NOMENCLATURE

The abbreviation and nomenclature used in the dissertation to define the various alloys and parameters are given below:

Notation	Description
Alloy1	Precursor alloy with higher thermal mass (higher temperature and higher mass).
Alloy2	Precursor alloy with lower thermal mass.
Alloy3	Resultant desired alloy.
m_r	Mass ratio (m_1/m_2)
k	Equilibrium partition ratio
r^*	Critical radius calculated from nucleation theory
S/L	Solid –liquid interface
T	Temperature
ΔT	Undercooling below alloy liquidus temperatures.
T_{L1}, T_{L2}, T_{L3}	Liquidus temperatures of Alloy1, Alloy2 and Alloy3, respectively
W_a	Weight of the part in air
ρ_w	Density of water
$\rho_{\text{material}}^{\text{theoretical}}$	Theoretical density of material
W_w	Weight of the part in water
N_A	Avogadro's Number ($6.0221413e^{+23}$); molar number of atoms in a substance
ε	Strain field caused in solid solution due to foreign atom with different size
a	Crystallographic lattice parameter
r	Atomic radius
r_o	The Dislocation core (~0.6 nm)
c	Atomic concentration (at%)
λ	Inter particle spacing between dispersed barriers to dislocation motions
$\Delta\sigma$	Increasing increment in yield stress
G	Shear modulus
f	Phase fraction of dispersed secondary phases
τ	Shear stress needed for moving a dislocation
τ_y	Resolved shear stress in stage II strengthening model in FCC single crystal
b	Burgers' or slip Vector (displacement occurring during slip)
ρ_{dis}	Density of dislocations in the material created during the deformation
k/k'	Locking parameter in Hall-Petch equation
D_p	Average diameter of the precipitates

D_{gs}	Average grain size diameter
D_{gs}	Average grain size diameter
σ_y	(Total) Yield stress
$\sigma_\alpha / \tau_\alpha$	Friction stress
σ_{gb}	Grain boundary strengthening effect
σ_{dis}	Strengthening effect due to dislocation interaction with each other
σ_{ss}	Solid solution strengthening effect
$\sigma_{ppt.}$	Precipitation strengthening effect
α	A-rich primary phase in A-B binary system
β	B-rich primary phase in A-B binary system
α'	Supersaturated solid solution primary phase in A-B binary system
SSSS	Supersaturated solid solution

3 PROJECT OBJECTIVES AND METHODOLOGY

At the inception of this project the vision was to be able to establish with data that the CDS technology coupled with the tilt pour gravity casting (TPGC) process is a viable route to enable the near net shape cast of the Al 7xxx family of wrought alloys. To realize this vision, the following four overarching objectives were laid out for the project:

- Establish the feasibility of using the CDS technology to solidify the Al 7xxx series of alloys with a non-dendritic morphology of the primary Al phase.
- Develop a quantified database to describe the interaction boundaries of alloy chemistry of Al 7xxx alloys, heat treatment procedures (solutionizing, annealing and ageing) and uniaxial tensile properties of castings made with the CDS technology coupled with the tilt pour gravity casting (TPGC) process.
- Develop a mechanistic understanding of the precipitation reactions during ageing treatment for the AA 7050 alloy samples cast using the CDS technology.
- Develop an understanding of the predictive capabilities for the yield strength of Al 7xxx alloys cast using the CDS technology.

The following presents the strategy employed in this project to achieve the above-mentioned objectives:

Quantify the regime of parameters for the alloy chemistry and process to enable near net shaped casting of Al 7xxx alloys with the CDS technology coupled with the tilt pour gravity casting (TPGC) process. Specific laboratory scale solidification experiment for the CDS technology was carried out to establish the viable regimes of alloy chemistry and process:

- Demonstrate the feasibility of sound and structurally viable castings of Al 7xxx alloys using the CDS technology coupled with the tilt pour gravity casting process. The entire project used a standard tensile test bar mould outfitted in a Tilt Pour Gravity Casting (TPGC) machine for casting the Al 7xxx alloys with the CDS technology that is further elaborated in Section 5.3 (The CDS casting experiments using (TPGC) machine) of this dissertation.
- A study of the effect of conventional heat treatment tempers of the Al-7xxx CDS castings on the phase evolution and modification in the cast microstructure was carried out. Specifically, the nature and distribution of secondary solidifying phases that are formed during the solidification process changes during the subsequent heat treatments such as: solutionizing (T4), precipitation age hardening (T6) and annealing (O) heat treatments. Also the specific effect of Cu element on the nature, distribution and evolution of strengthening precipitates forming during the precipitation ageing hardening (T6) treatments was investigated. It is notable that the heat treatment procedures used in this study were not developed for shape castings of Al 7xxx alloys but were inherited from the prior-art of such practices for the Al 7xxx wrought alloy counterparts which were obtained from background literature. The aim of this exercise was to investigate the microstructural evolution and features occurring in the Al-7xxx castings during the four heat treatment conditions that formed the boundary of operational performance of the Al-7xxx CDS castings: as-cast (F temper), annealed (O temper), solutionized (T4 temper) and near peak aged (T6 temper). The aim of this segment of the strategy was not to develop an optimum heat treatment procedure for these near net shaped castings of Al 7xxx alloys but to present a quantified understanding of the phase evolution and modification due to the various conventional heat treatment techniques.

- A study of the effect of various alloy chemistries within the realm of Al 7xxx alloys processed by the Controlled Diffusion Solidification (CDS) technology coupled with Tilt Pour Gravity Casting (TPGC) machine were carried out on the uniaxial tensile properties of the cast test bars in two heat treatment tempers such as solution (T4) treatment and near peak aged (T6) heat treatment tempers. Again, it should be noted that this was not an exercise to optimize the mechanical properties against the alloy chemistry and heat treatment procedures but to present the various boundaries of observed mechanical properties in relation to the conventional heat treatments. The intended deliverable was to enable automotive cast component designers to better understand the extremities of tensile properties that could be obtained by the shape castings of the Al 7xxx alloys using the CDS technology coupled with the TPGC process.
- A study of structural-properties modeling for the various strengthening effects to the yield strengths of the Al-7xxx CDS alloys by means of the strengthening models recently proposed specifically for the Al-7xxx wrought counterparts.

The aim of the project is to establish a baseline of quantified relationship among alloy chemistry of 7xxx alloy, conventional heat treatments and uniaxial tensile properties to enable development of specific commercial application routes for this alloy and the CDS process in the automotive light weighting initiatives.

Figure 3–1 presents a schematic flow chart of the methodology employed in this project to compliment the above-mentioned strategy. In Figure 3–1, the project methodology was divided into three phases:

- Phase 1. Determination of appropriate alloy chemistry and process parameters to enable using the CDS technology in the 7xxx series of Al wrought alloys and obtain a favorable non-dendritic morphology of the primary Al phase in the solidified microstructure. This was carried out by using thermodynamic phase diagram simulation software coupled with small-scale laboratory experiments.
- Phase 2. Casting of standard tensile test bar specimen of various compositions within the 7xxx Al alloy regime using the CDS technology coupled with the tilt pour gravity casting (TPGC) process. Evaluation of uniaxial tensile properties of the cast test bars under various heat treatment conditions such as As-Cast (F temper), solutionizing (T4 temper), annealing (T4+O temper), and ageing at elevated temperatures (T6 temper). In addition to quantified understanding of the effect of heat treatment on uniaxial tensile properties, the effect of varying individual major alloying elements such as Zn, Cu and Mg within the regime of the 7xxx Al alloy designation on the heat treatment response and tensile properties were quantified.
- Phase 3. Characterization of the secondary phases, transformation of the secondary phases during heat treatment, precipitation phases during natural and artificial ageing was carried out using optical, scanning electron and transmission electron microscopes and differential scanning calorimetry. Fractography of the fracture surface was also carried out to further explain modes of fracture. Quantified explanations for the observed relationship among alloy chemistry, heat treatment and uniaxial tensile properties were formulated in this Phase of the project.

In the next Chapter, detailed analyses of the relevant prior-art in the global academic literature sources have been presented for topics related to this project.

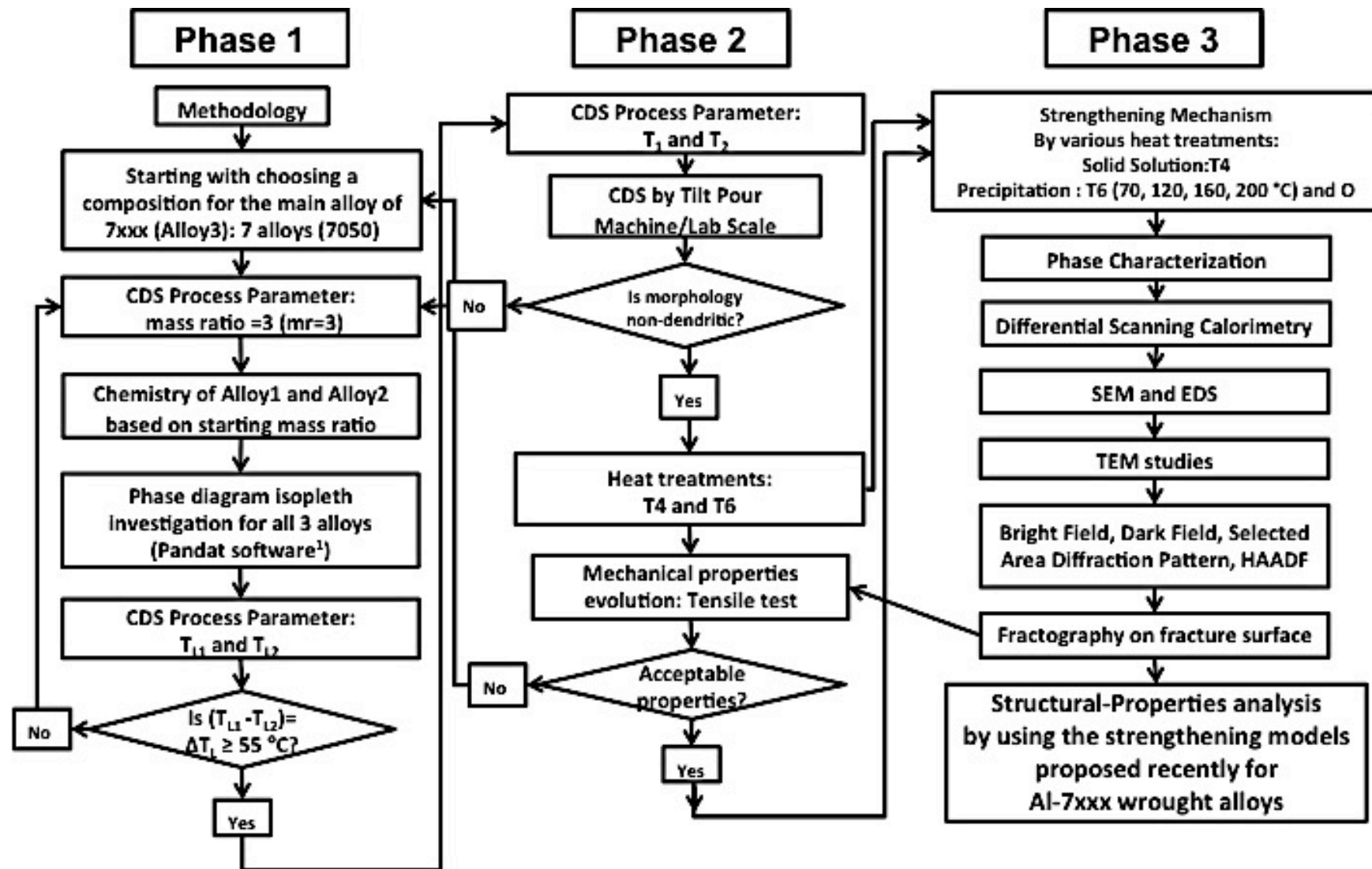


Figure 3–1. Flow Chart outlining the methodology used in this project.

4 PRIOR-ART

In the 2 of this dissertation, it was mentioned that one of the major impediments to near net shaped casting of Al 7xxx alloys was the pronounced occurrence of shrinkage which typically leads to hot tearing in the cast component while rendering it defective. A detailed understanding of the mechanisms that lead to hot tearing from prior-art was warranted in this chapter. An in-depth understanding of the CDS technology and the mechanisms of the process that enables circumventing the occurrence of hot tearing during solidification of Al 7xxx alloys will be presented to introduce the technology to the reader. Since, the project attempted to enable near net shaped casting of 7xxx Al alloy, the state-of-the-art in the various alloy compositions of this family of alloy coupled with the phase evolution during solidification, heat treatment and mechanical properties of the components manufactured from 7xxx Al alloys is critical information that forms a baseline to compare the results of this project. Hence, the subsequent sections of this chapter would present comprehensive information on the prior-art of:

- Solidification in Al-Zn-Mg-Cu System
- Heat-treatments of Al-Zn-Mg-Cu system
- Deformation in metals and Dislocation Interactions
- Mechanical properties of Al-7xxx Alloys
- Al 7xxx Series wrought Alloys

4.1 SOLIDIFICATION IN AL-ZN-MG-CU SYSTEM

In conventional casting such as sand casting, and gravity and pressure die-casting, the molten alloy at a high superheat temperature is poured into the mold cavity and solidified to obtain the near net shaped component [44]. Typically the primary Al phase morphology in the cast microstructure is that of a dendritic network due to the solute rejection occurring ahead of solid/liquid interface [45]. The size and complexity of the dendritic structure is more pronounced in the Al wrought alloys than its cast alloy counterparts. A simple schematic of such a dendritic network is shown in Figure 4–1. During solidification of these alloys, the liquid continuously feeds the dendritic network to compensate for the volumetric shrinkage associated with phase transformation. The coagulation of the microscopic shrinkage defects can cause “hot tearing or hot cracking”: hot tearing is a complicated phenomenon occurring because of complex interaction between heat flow, melt flow and mass flow, and the stress/strain which are developed within the coherent network of growing dendrites during solidification. The occurrence of hot tearing is a result of combined interactions between thermo-mechanical and metallurgical parameters [17].

4.1.1 Shrinkage and Hot Tearing

During solidification of an alloy melt, a pronounced two-phase region called the mushy zone exists at a specific range of temperature and composition wherein the liquid and solid phases co-exist. Within this mushy zone, in the direction of the heat extraction, the complexity of the network formed by the dendrites increases from the liquid to solid interface; this is coupled with a temperature gradient decreasing from the liquid to the solid interfaces as well. The liquid in the mushy zone transforms to solid leads to volumetric shrinkage; unless the liquid from the bulk flows through the mushy zone and feeds this volumetric shrinkage, voids

form and evolve. Typically in alloys with solute elements content less than the respective maximum solubility in the primary phase, such as the Al 7xxx alloys, the mushy zone is very large with a complex dendritic network. In solidification of such alloys, the complexity of the dendritic network may lead to closure of the feeding paths of the bulk liquid to compensate for the volumetric shrinkage during solidification at the high solid fraction regions of the mushy zone. This will result in formation of voids, which under the strains developed during phase transformation (solidification) in these regions will begin to fail through fracture leading to the defect commonly referred to as *Hot Tearing* [46, 47]. In certain alloys, the solidification strains in the final stages of the mushy zone solidification may not lead to complete fracture of the solid / liquid interface but rather result in extensive shrinkage porosity [48]. Typically, alloys that solidify with a large range of temperature in the mushy zone (large freezing temperature range) are more prone to extensive shrinkage porosity and hot tearing.

Figure 4–1 presents a schematic of the mushy zone in a hypothetical unidirectional solidification to highlight the complexity of the dendritic mushy zone, direction of the flow of bulk liquid into the mushy zone to compensate for the volumetric shrinkage caused by the liquid to solid transformation in the mushy zone and the strain field generated in the mushy zone due to the stresses arising from the volumetric shrinkage during solidification. Figure 4–1 also presents a schematic of the pressure gradient in the mushy zone during the unidirectional solidification [46]; wherein the pressure gradient ceases to exist when the dendritic network closes the feeding path of the bulk liquid to compensate for solidification shrinkage and leading to formation of shrinkage voids which could fracture and form hot tears if the solidification strain is sufficiently large.

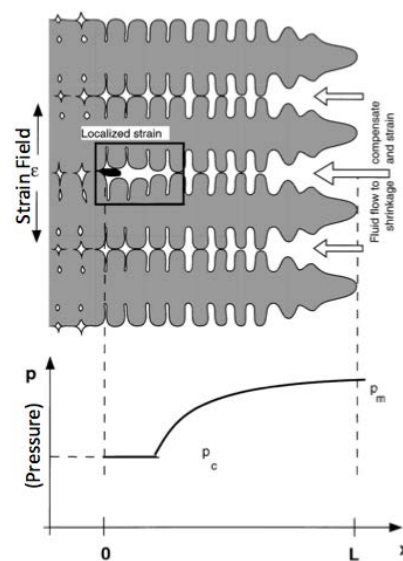


Figure 4–1 A schematic of the solidification of the mushy zone highlighting (a) dendritic network of the dendritic primary phase along with the initiation of a hot tear at the region demarcated as *localized strain* (b) the pressure graient [46].

Figure 4–2 presents a schematic of the phase diagram of a hypoeutectic alloy and the various thermal regimes of the two-phase (mushy zone) solidification coupled with the schematic representation of the distribution of the solid and liquid phases in these regimes. In Figure 4–2, the various thermal regimes are shown with their respective levels of hot tearing susceptibility of the two-phase (mushy) state of solidifying material. The region demarcated by less than 0.25 fraction solid represents the temperature range that exhibits negligible tendencies for hot tearing because, there is enough liquid to flow through the highly

permeable dendritic (solid) network to compensate for the solidification shrinkage. The region with about 0.30 to 0.55 fraction solid represents the temperature range with low risk of hot cracking, and the amount of residual liquid phase and the permeability of the dendritic network could accommodate the nominal stresses induced by solidification shrinkage. The susceptibility for hot cracking is significantly high when the fraction solid is greater than 0.60 in the mushy zone where in the complexity of the dendritic network and the low volume of liquid enables solidification shrinkage voids to coalesce and tear during solidification. Figure 4–2 shows that the mushy zone for cast alloys (with an average solute composition close to the eutectic) lies completely within the white colored thermal regime and hence has minimum hot cracking susceptibility due to extensive feedability of the inter dendritic liquid; whereas in the wrought alloys, the white and yellow thermal regimes are minimal and for the most part the mushy zone exists in the orange thermal regime which indicates a high hot cracking susceptibility. In other words, as shown in Figure 1–5, the percentage solid evolving during solidification does so in a rapid rate for wrought alloys as opposed to its cast counterpart, thus rendering the former to increased hot tearing susceptibility. A typical example for wrought alloys with high risk of hot cracking is the Al 7xxx alloys (Al-Zn-Mg-Cu) [17].

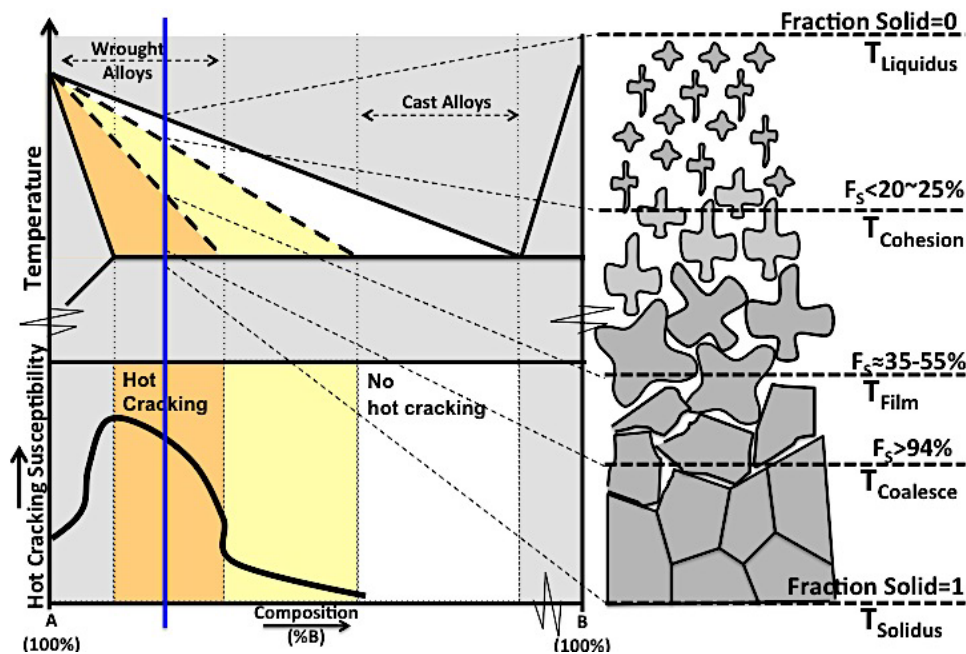


Figure 4–2 Schematic of a typical binary hypoeutectic alloy showing the various thermal regimes in the mushy zone along with the schematic of the anticipated distribution of the solid and liquid phases in these thermal regimes and the hot cracking susceptibility of these regimes as a function of solute composition Schematic diagram of temperature-hot tearing susceptibility in aluminum alloys along with illustrative grain growth coherency during solidification process, correlating the phase diagram and hot tearing susceptibility. The schematic composite shown here was composed from two different references in the prior-art [18, 48].

One viable method to alleviate the hot tearing susceptibility in Al 7xxx wrought alloys is to solidify the cast component with a nearly non-dendritic morphology of the primary phase which will enable to maintain the high feedability of the liquid in the mushy zone to compensate for solidification shrinkage even at high solid fraction regions due to the lack of a complex network that would stop the feeding. For reasons explained earlier in **Error! Reference source not found.**, none of the present semi-solid metal (SSM) processing technologies would enable near net shaped manufacturing of Al wrought alloys. However,

the Controlled Diffusion Solidification (CDS) technology could circumvent the problems associated with near net shaped casting of Al wrought alloys and enable a sound cast component of these alloys. As a benchmark comparison, Figure 4–3 (a) and (b) shows the cast component and microstructure highlighting severe hot tearing for an AA7050 Al wrought alloy cast conventionally with a tilt pour gravity casting (TPGC) machine from an initial temperature of about 720 °C*. Alternately, the same alloy (AA7050) when cast with the TPGC process coupled with the CDS technology does not show any signs of hot tearing as shown in Figure 4–3 (c) because of the non-dendritic morphology of the primary Al phase, as shown in Figure 4–3 (d).

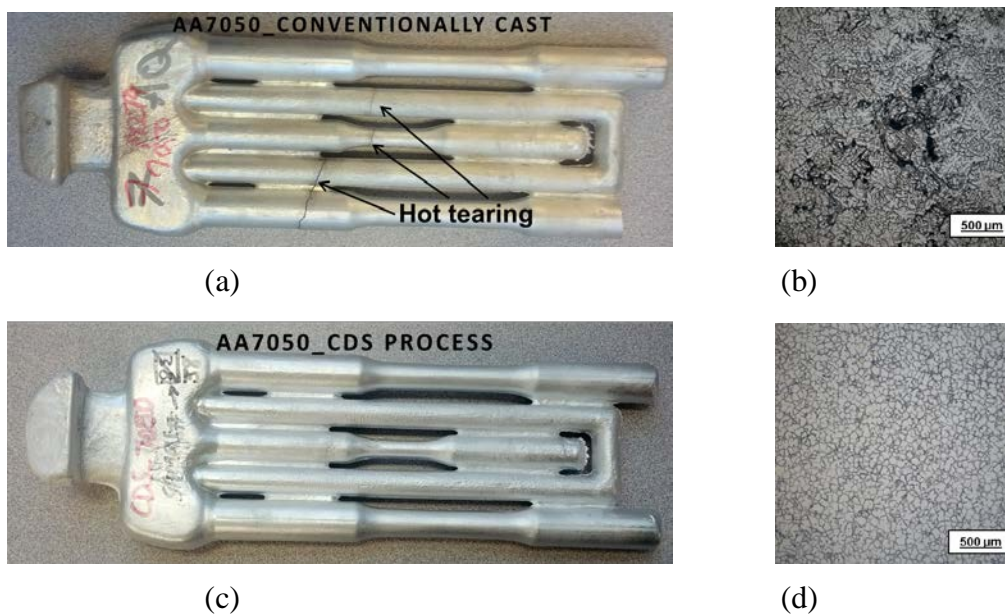


Figure 4–3 The uniaxial tensile and fatigue test bars of AA 7050 cast by Tilt Pour Gravity Casting (TPGC) machine along with their optical micrographs: (a) and (b) shows the hot tearing defects in conventionally cast parts in macro- and micro-scale images, respectively; (c) and (d) shows the sound and flawless CDS castings.

The underlying mechanisms that help the CDS technology circumvent the problems of extensive shrinkage cavities and hot tearing in a cast component of Al 7xxx alloys is explained in the next section of this chapter.

4.1.2 CDS Technology: History and Mechanism

Table 4–1 presents historical overview of prior research work on the technology of diffusion solidification leading to the development of the Controlled Diffusion Solidification (CDS) technology. The original notion of diffusion solidification dated back to 1952 when Goetzl and Ellis [49] proposed the concept for casting steel; further development of diffusion solidification was carried out by Langford and Cunningham [50], and Langford and Apelian [50]. Figure 4–4 shows a schematic of the typical thermo-solute fields occurring during diffusion solidification of a eutectic binary alloy, wherein, solid particles with solute composition C_1 are introduced into the liquid metal with solute composition of C_L and the

* It is noteworthy that the melt of the conventionally cast Al-7050 alloy contained no Ti; whereas in the melt of CDS cast of the Al-7050, the 0.13 wt.% Ti were added. Moreover, the mold temperature in the case of conventional cast Al-7050, the mold temperature of the tilt pour gravity casting machine were lower (~275 °C) than that of the CDS experiments (~375 °C).

mixture held at an isothermal condition at temperature T_1 in an insulated refractory vessel. The temperature of the mixture rises to temperature T_2 due to the heat added from the latent heat of fusion during solidification. The final product with a homogeneous solute composition of C_2 is obtained as a result of the process as shown in Figure 4–4 (d). Langford and Apelian first introduced this concept in 1980 for the development of a rapid-cycle casting process of steel [50].

Table 4–1 Prior-art in Diffusional Solidification.

Authors	Date	Description	Ref
Goetzl and Ellis	(1952)		[49]
Langford, Cunningham	(1978)	Patent on diffusion solidification developed for steel casting	[50]
Langford and Apelian	(1980)		[51]
Saha	(2005)	PhD Dissertation containing diffusion solidification to the aluminum-silicon alloy by solid machining chips	[52]
Saha, Shankar and Apelian	(2002)	Patent on the CDS process in liquid phase with aluminum alloys: fundamental thermodynamic frame work	[53]
Symeonidis	PhD (2009)	CDS process in liquid phase with aluminum alloys: mechanistic study (lab scale experiment)	[40]
Birsan	MSc. (2009)	CDS process in liquid phase with aluminum alloys: Tilt Pour Gravity Casting (TPGC) Machine	[54]
Khalaf	PhD (2011)	CDS process in liquid phase with aluminum alloys: mechanistic study (lab scale and TPGC experiment)	[40]
This study	PhD (2015)	CDS process: application on Al-7xxx alloys	

Saha and Apelian (1999-2002) [52] applied the idea of diffusion solidification to the aluminum-silicon alloy by introducing chips generated during machining of the solid alloy into shot sleeve prior to casting of liquid Al-Si alloys. Saha et al (2002-2005) developed the idea of diffusion solidification (mixing process of solid chips into liquid metal) into the Control Diffusion Solidification (CDS) process where both precursor components mixed in their liquid state but with different temperature and weight, i.e. at different thermal mass condition [52].

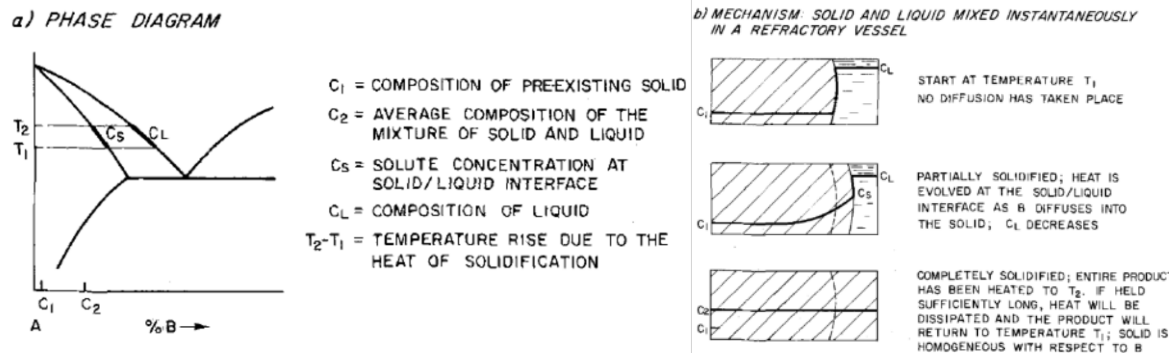


Figure 4-4 Mechanism of diffusion solidification (a) binary alloy phase diagram and (b) mechanism of diffusion solidification [50].

Apelian [55] in 2006 proposed a theoretical base frame for the CDS mechanism that consists of three prominent conditions for a successful CDS process with non-dendritic microstructure. Saha et al [42] further proved that CDS Casting for 2014, 4145, 5056 and 7050 Al wrought alloys, and 222 and 319 Al cast alloys could be carried out to successfully yield non-dendritic primary phase morphology with small-scale experiments. They observed that in all the experiments, the increasing the superheat of the Alloy1 increased the tendency of a dendritic morphology of the primary Al phase in the solidified part.

Recently, from 2007 to 2011, Kimon Symeonidis [56] and Abbas Khalaf [40] separately endeavored to set a mechanistic base ground for the CDS process. First, Kimon Symeonidis [56] investigated the CDS process with Al-4.5Cu and proposed a three-stage mechanism for the CDS process: mixing, nucleation, and growth. Symeonidis' three-stage mechanism was then revised by Khalaf [40,57,58,59] as shown in Figure 4-5: (I) mixing and nucleation stage, (IIa) homogenization of thermal field with further nucleation, (IIb) homogenization of solute fields followed by (III) growth of stable nuclei.

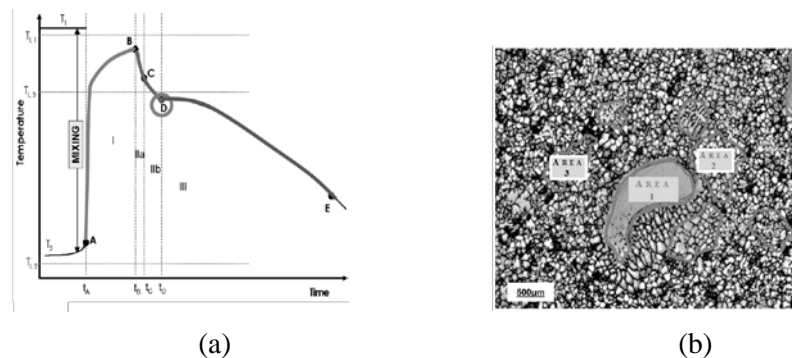


Figure 4-5 The three stages in the mechanism of the CDS technology. (a) Schematic of the typical thermal profile observed in the CDS process with three distinct stages starting with mixing of alloys at point A, and (b) the three morphologies of the primary Al phase which are associated with the three stages shown in (a) for the Al-4.5Cu alloy [40].

Figure 4-6 presents the schematic procedure for the CDS process, wherein two precursor alloys, i.e., Alloy1 and Alloy2, each of which with specific temperature and composition, are to mix with each other and immediately afterwards, the mixture is to cast as the shaped component in a process that may or may not be pressure assisted. In a successful CDS process, the mixing of the two precursor alloys is at the root of what makes the desirable non-dendritic structure; and that is in part because in the mixing step of the CDS mechanism, both the forced convection and copious nucleation operating together to enable the favorable condition for the non-dendritic morphology during solidification.

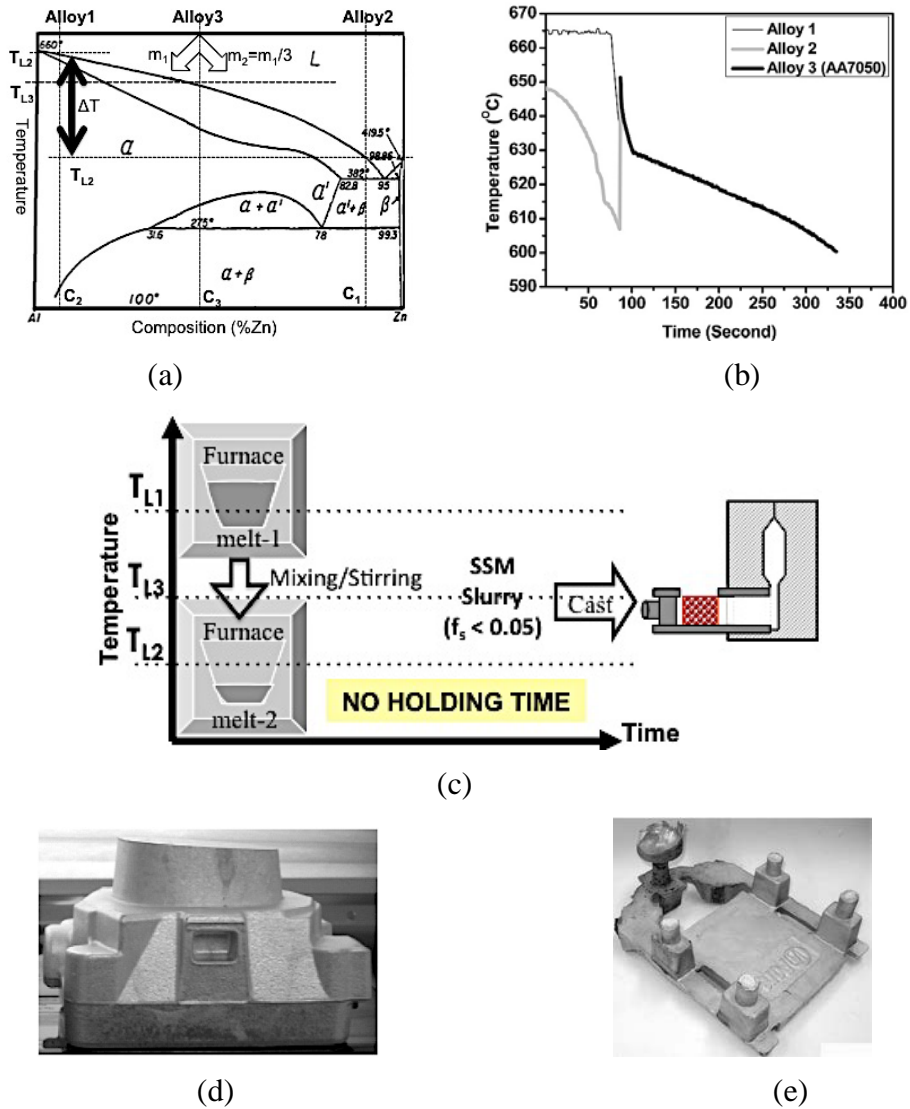


Figure 4–6: (a) a typical Al-Zn binary phase diagram schematically showing the alloy constituents of the CDS process technology; (b) actual thermal curves obtained while casting AA7050 alloy with the CDS technology; (c) Operational stages in a typical Controlled Diffusion Solidification (CDS) process; (d) and (e) Sample products manufactured via CDS technology coupled with TPGC and sand casting processes, respectively [60].

Khalaf et al [40] succeeded in obtaining a non-dendritic Al morphology of various aluminum wrought alloys series such as 2024, 6082, 7005 and 7075 using the CDS process in laboratory scale experiments. Further, Khalaf [61] proposed optimum CDS process conditions for a successful casting [40, 43, 54, 62]: (a) a temperature difference between the liquidus (and/or pouring) temperatures of the precursor alloys before mixing should be at least 50-80°C, (b) the maximum temperature attained during mixing of the two precursor alloys should preferably be more than the liquidus temperature of the resultant alloy (Alloy3) to facilitate complete filling of the casting mould, (c) the mass ratio between the two precursor alloys should be at least 3. The three-step mechanism proposed by Khalaf et al [40,] could be briefly described as below and in reference to Figure 4–5 (a).

Segment AB (Stage I): At this stage of “mechanical mixing”, the Alloy1 continuously entering the Alloy2 will break down into small masses (at temperature T_1) in the resultant mixture (at a temperature less than T_1) to form the resultant Alloy3. The exposure of hot liquid of Alloy1 to the low temperature liquid mixture in this stage of mixing results in the

nucleation of broken liquid pockets of Alloy1 typically shown by the morphology of the “AREA 1” in Figure 4–5 (b).

Segment BCD (Stage II: (a) and (b)): At this stage of “re-distribution of the thermal and solute fields in the resultant mixture”, convective cells (which are akin to Bernard cells [63]) form in the mixture where the nucleation of the grains shown as “AREA 2” in Figure 4–5 (b) takes place. These hexagonal cells resemble a plate-like colloidal phase of Alloy1 (impoverished in solute) enclosed by the liquid Alloy2 (enriched in solute). These AREA2 nucleation sites act similarly to those created in stage AB (AREA1), in that the solute back diffuses from Alloy2 in the walls of the cells toward the central part which is predominantly Alloy1; in a direction opposite to the heat extraction. Nucleation in these cells occurs when the actual temperature of the respective solute composition region is undercooled below the liquidus temperature [41,43]. The nuclei forming in the AB segment stage of Figure 4–5 have stable growing interface leading to a non-dendritic (planar) morphology; because, the solute back diffuses toward the solid liquid interface, which is quite opposite to what occurs in a conventional solidification process where the solute piles up in front of the growing solidification front; as shown comparatively in Figure 4–7 [6]. In Figure 4–7, the two thermal graphs shows the negligible constitutional supercooling for the CDS process when compared to the typically significant one in the conventional solidification process; caused by the reversal of the diffusion paths of the solute in the former and leading to a significantly different solute redistribution field in the two [41,43].

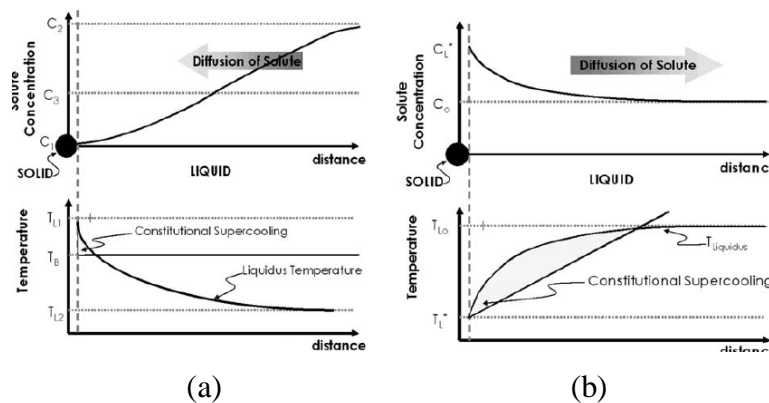


Figure 4–7 Comparative schematic solute and temperature redistribution regimes ahead of the solidifying solid-liquid interface are presented for (a) the CDS process and (b) conventional solidification [40].

Point D nucleation (stage III): At this stage, the final nucleation events in CDS process occur. At this stage, as the temperature field and solute concentration field of the residual liquid have reached a nearly homogenized state, where they can nucleate and grow as “AREA3”, which is similar to conventional solidification with constitutional undercooling resulting in growing interface instabilities, and the resultant morphology might be a dendritic structure albeit a small Secondary Dendrite Arm Spacing (SDAS) due to the spatial limitations offered by the interaction of several solidifying interfaces. However, the spatial constraints existing during solidification does not allow for the growth of large dendritic networks but rather a mildly perturbed set of primary phase grains similar to those observed in the central equiaxed region of a Direct Chill (DC) cast ingot [64].

Given the extensive prior-art developed in the CDS technology, the inception of this project was aimed at using this enabling technology to explore feasibility in near net shaped casting the strongest of Al alloys, the 7xxx alloys, and develop a quantified relationship among alloy chemistry, heat treatment and tensile properties.

4.1.3 Al 7xxx Series wrought Alloys

Table 4–2 [5] and Figure 4–8 [65] present the various designation and classification of Al casting and wrought alloy groups, respectively. Table 4–2 shows the cast alloys designation by means of alloying elements and also Figure 4–8 summarize the classification of the Al wrought alloys based on the alloying elements and type of solid-state processes and heat treatments that are commercially applied to each alloying system.

Table 4–2: Aluminum cast and wrought alloy families [5]

Cast Alloy	Alloy Element	Wrought Alloy	Alloy Element
1xx.x	Al (> 99.0 %)	1xxx	Al (> 99.0 %)
2xx.x	Cu	2xxx	Cu
3xx.x	Si-Mg-(Cu)	3xxx	Mn
4xx.x	Si	4xxx	Si
5xx.x	Mg	5xxx	Mg
		6xxx	Si-Mg
7xx.x	Zn	7xxx	Zn-Mg- (Cu)
8xx.x	Sn	8xxx	Sn
9xx.x	Other Elements	9xxx	Other Elements

Al alloys & treatment classification system

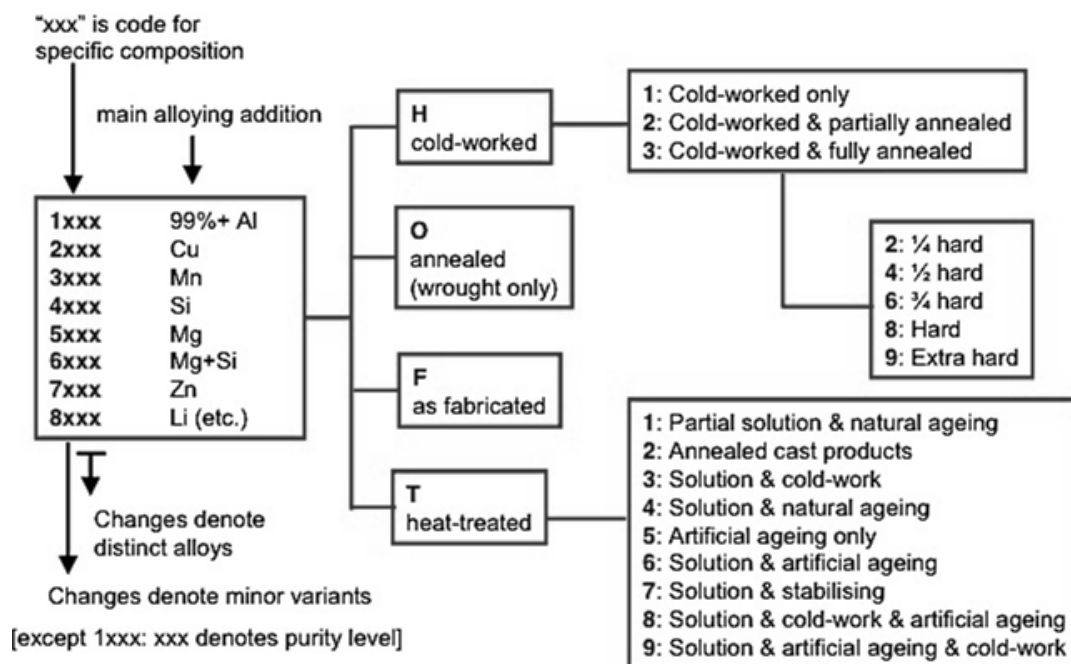


Figure 4–8 Basic Aluminum Wrought alloy family classification and heat treatments [5,31].

4.1.3.1 Al-Zn-Mg-(Cu) alloy system

The addition of Zn to Al as an alloying element is believed to date back to the time when Al was itself used in commercial production [66]. Very first studies on the Al-Zn-Mg system could be traced back to the turn of the nineteen-century (1913) however, the introduction of

Al-Zn-Mg systems as commercial alloys started in 1926 by *Sander* and *Meissner* [66], when they presented Al-Zn-Mg alloys with high mechanical properties that lead to a series of investigation exploring various commercial applications for these alloys that is still presently on-going.

The mechanical properties of the Al-Zn-Mg alloys are highly sensitive to the nature and extent of the precipitation reaction products during heat treatment [66, 67]; further, the nature and extent of the precipitation reactions are highly sensitive to the alloy chemistry coupled with the history of the heat treatment [66]. Hence, conclusive relationships between mechanical properties and alloy composition for these alloys must always be accompanied by a detailed history of heat treatment and incubation of the alloy [66,67].

In the Al-Zn-Mg-Cu alloy system, the maximum solubility of Zn, Mg and Cu in Al at near equilibrium conditions is 82.8 wt.%, 17.4 wt.% and 5.65 wt.% by weight, respectively. Table 4–3 presents the typical physical properties of Al, Zn, Mg and Cu such as diffusion coefficient, atomic radius and their imposing misfit strain arising from their respective solubility in Al matrix [31,66,67].

Table 4–3 Typical physical properties of alloying elements in the Al-7xxx series system

Atom	Radius (Å)	Density (gr/cm ³)	Self-Dif. Coef. (μm ² /sec) (~@T _m)	Inter-dif. Coef. Ax10 ⁻² (μm ² /sec) (~@750K)	Misfit in Al (%)	Misfit zone shape	Reference
Al	1.432	2.71	1.9	7.0	-	Sphere	
Zn	1.33	7.13	0.98~1.6	10.7	-3.5	Sphere	
Mg	1.60	1.74	2.3~2.9	5.9	+12	Plate-like (disc)	
Cu	1.28	8.94	0.6	3.2	-10.5	Plate-like (disc) {Al-Cu→η} Lath-like (needle) {Al-Cu-Mg→S}	[31,68,69,70]

The Al-Zn-Mg-Cu system is a very complex alloying system. This complexity can be graphically seen in Figure 4–9, wherein several vertical-projections of the Al-Zn-Mg-Cu quaternary system are illustrated. Equilibrium phases of the Al-Zn-Mg-Cu system can briefly be represented by its quaternary eutectic reaction:



The only Cu-containing phase in the Al-Zn-Mg-Cu alloys is the Zn free CuMgAl₂.

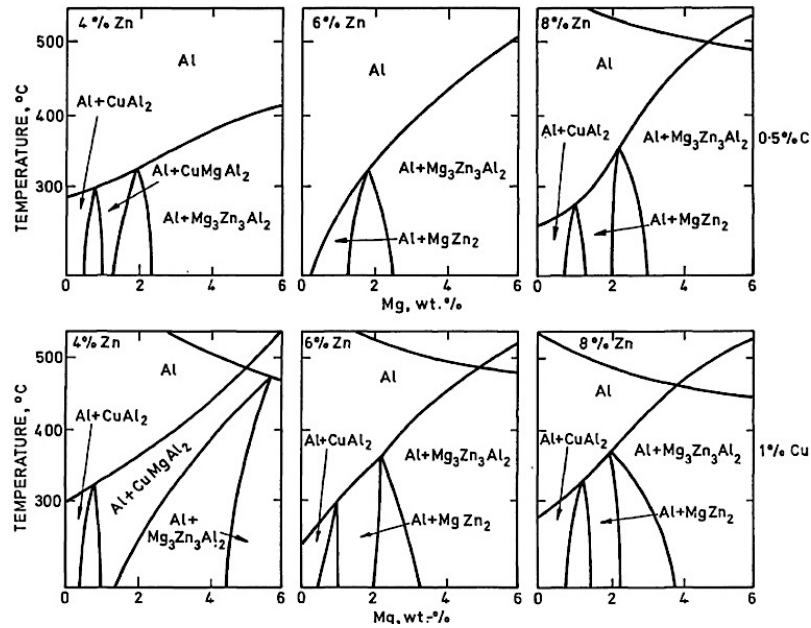


Figure 4-9: Sections at different zinc and copper content in the Al-Zn-Mg-Cu system [66].

In Al-Mg-Zn-Cu alloys, during non-equilibrium freezing (solidification), typical of commercial shaped casting processes, the solute rejection caused by the growth of the primary solid solution would typically result in two main effects: (1) uneven distribution of solute elements in the primary phase (micro segregation) and (2) evolution of non-equilibrium solidifying phases: both these effects have significant effect on the properties and performance of the cast component. In the Al-Zn-Mg-Cu system, in alloys with low amount of alloying element ($Mg+Zn+Cu < 6\%$), because each alloying elements are well within their respective maximum solid solubility limits, micro-segregation is minimal. On the other hand, in alloys with high amount of alloying elements ($Mg+Zn+Cu > 6\%$), other non-equilibrium phases with low melting points evolve on the grain boundaries regions during solidification [66].

The intermetallic phases evolving during non-equilibrium solidification of the Al-Zn-Mg-Cu alloys are categorized into two groups: one group comprises of compounds that are insoluble in primary Al matrix such as Al_6 (Fe, Mn), $Al_{13}Fe_4$, α -Al (Fe, Mn, Si) and Al_7Cu_2Fe , while the second group consists of the soluble phases such as $MgZn_2$, Al_2Cu , Al_2CuMg , and Mg_2Si , both of which form a network surrounding the grain boundaries in the as-cast microstructure [65]. Both these groups of phases play a critical role during the solution heat treatment process of the casting because some of them may cause non-equilibrium melting prior to the heat treatment temperature, also known as incipient melting, leading to poor mechanical properties. One way to alleviate the problem of incipient melting is to carry out very slow heating on the sample from room temperature to the solutionizing temperature [5].

4.2 HEAT-TREATMENTS OF AL-ZN-MG-CU SYSTEM

High strength 7xxx Aluminum alloys (Al-Zn-Mg-Cu) in the wrought condition undergoes several combinations of heat treatments among annealing, solutionizing, quenching after solutionizing, precipitation hardening at room temperature and high temperature ageing and work hardening. In the near net shaped cast condition, most of these heat treatment procedures would be feasible except work hardening. Broadly, the homogenization of the solute elements in the primary Al matrix, dissolution of low melting secondary intermetallic

phases, morphological and compositional modification of secondary intermetallic phases, and precipitation reactions for strengthening are typical microstructural modifications occurring during the various procedures of heat treatment in these alloys. In order to design an optimal and pragmatic process, it is vital to understand the origins of microstructural evolution appearing in the final product [5].

Typically, heat treatment (or thermal processing) of these alloys has several steps, which could be carried out in any preferred order to suite the end product requirement. Figure 4–10 presents a schematic of the temperature ranges for the various typical heat treatment processes in an alloy from Al-Zn-Mg-Cu family; the figure also presents an illustration of the operative temperature range for these thermal processes. A brief description of these processes are also presented below:

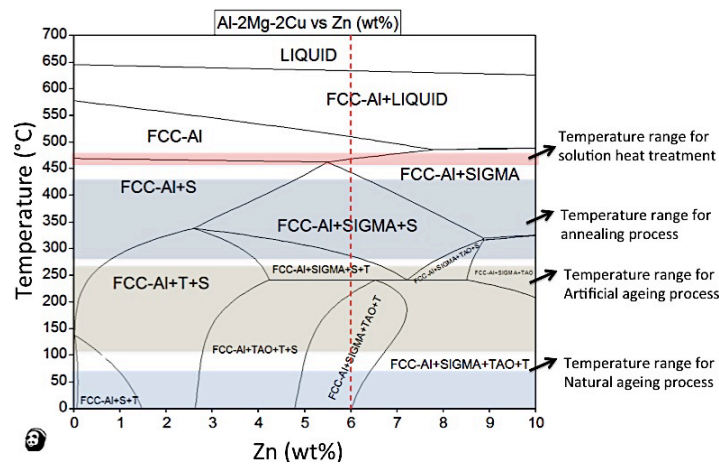


Figure 4–10 Isoleth of simulated equilibrium phase diagram of the Al-Zn-Mg-Cu system showing Al-2Mg-2Cu alloy with varying composition of Zn in the alloy. The typical temperature regimes used for the various heat treatment procedures are shaded in the phase diagram.

- As-cast (as Fabricated) → F temper
- Annealing → O temper

The part is isothermally soaked at a suitable temperature which is marginally above the dissolution temperature of all the possible precipitation phases from the solute elements dissolved in the primary Al matrix and subsequently cooled to room temperature at a very slow rate to significantly soften the Al matrix in the microstructure.

- Solutionizing → T4 temper

The part is isothermally held at a temperature of 5 to 10 °C below the melting point of the alloy to enable complete homogenization of the solute element in the primary Al matrix forming a Super Saturated Solid Solution (SSSS) of the Al matrix while additionally, causing morphological modifications to the inter-granular secondary phases that formed during solidification. In some alloy compositions, the low volume fraction of non-equilibrium secondary phases may melt and spheroidize or dissolve into the Al matrix as dictated by the isothermal holding temperature and the heating rate to the same.

- Quenching

The quenching of the samples immediately after the solutionizing treatment is critical to the subsequent precipitation ageing process in the alloy. High quenching rates retain the SSSS state to a large extent while maximizing the retention of the atomic

vacancies formed in the Al matrix during solutionizing. Low quenching rates results in disappearance of the matrix vacancies and initiates the formation of certain favorable solute atom clustering during quenching. The thermodynamics and kinetics of the precipitation reactions after quenching of the samples significantly depend on the rate of quenching [71]

➤ Ageing → T5^{*}, T6[†] or T7[‡] temper

The process of precipitation of certain intermetallic phases in the Al matrix arising from the saturated solid solution (SSSS) at the end of quenching is termed as ageing process. Ageing could be classified as two: natural ageing (incubation), which is typically carried out at ambient temperatures or low temperatures (< 80 °C) and artificial ageing, which is typically carried out at higher temperatures (>100 °C). The thermodynamics and kinetics of the precipitation reactions in Al-Zn-Mg-Cu alloys is fairly complex and explained in greater detail in Section 4.2.3 of this dissertation.

4.2.1 Solutionizing of the Al-Zn-Mg-Cu alloys

The solutionizing heat treatment of the Al 7xxx alloys at nominal temperatures are basically designed to dissolve the elemental micro-segregation in the primary Al phase of the as-cast microstructure. Several solute elements such as Zn, Mg, Cu, Si, and Ag completely dissolve and homogenize in the Al matrix due to their high diffusivity, whereas, there are certain heavier transition elements such as Fe and Cr which are quite sluggish in dissolving and could remain segregated in the matrix even after prolonged times of solutionizing processes at higher temperatures [66]. Table 4–4 presents diffusivity values of all elements participating in the Al-7xxx alloying system.

Table 4–4: Diffusion coefficient of common alloying elements in Al matrix [66].

$D = D_0 \exp(-Q/RT) \text{ cm}^2/\text{s}$		
Element	$D_0, \text{ cm}^2/\text{s}$	$Q, \text{ kcal/g atom}$
Ag	0.21–43	25–39
Cr	3×10^{-7}	15
Cu	0.084–0.29	30–35
Fe	4.1×10^{-9}	14–38
Mg	0.12–1.05	28–38
Mn	0.22	29
Si	0.9	30–38
Zn	10^{-2} –1.1	20–46

The solutionizing treatment must be carried out at a safe temperature below the maximum solute solubility temperature of the alloying elements in Al so as to avoid undesirable consequences such as over-heating causing incipient melting [5]; alloys such as AA7050 and AA7075 exhibit significant incipient melting at temperatures much lower than their equilibrium solidus temperature because of evolution of non-equilibrium phases during solidification. Both the AA7050 and AA7075 alloys have two soluble phases that are referred to as Sigma (or M) {Mg (Zn,Al,Cu)₂ (with aluminum and copper substituting for some zinc)}, and S (Al₂CuMg). The latter is very slow to dissolve and local concentrations of Al₂CuMg can produce a non-equilibrium melting point between 485 and 490 °C (905 to 910 °F) especially under a rapid rate of heating to the solutionizing temperature. Figure 4–11

* T5: The alloy is rapidly cooled down following a process an elevated temperature (such as solutionizing) directly (without any intermediate quenching stage) into an ageing temperature above room temperature.

† T6: The alloy is artificially aged at an elevated temperature immediately after an intermediate quenching process following the solution heat treatment; the artificial ageing process (T6) is adjusted to reach the near peak hardness that is caused by the precipitation hardening.

‡ T7: The alloy in artificially aged (T6) condition is longer aged to reach the over age condition.

presents this incipient melting appearing on the thermal signature from a Differential Thermal Analysis (DTA) experiment on AA7075 alloy [5]; wherein, for a homogenized (solutionized) alloy sample began to melt somewhere in excess of 540 °C (1000 °F) and for a non-homogenized sample: an endothermic spike in data indicating incipient melting occurs at around 490 °C (910 °C): the melting temperature of the S phase is around 490° C.

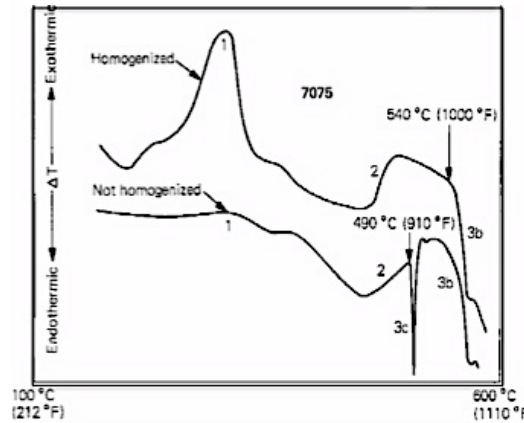


Figure 4–11 Typical thermal data from a DTA experiment of AA7075 alloy carried out at a heating rate of 20° C/min (36° F/min). Homogenized in the figure refers to solutionizing. The arrows indicate the start of a melting process. Significant inflections on the curves are marked as (1) precipitation from saturated solid solution, (2) re-solution of precipitated phase(s), and (3) melting area; equilibrium solidus melting for the alloy is shown by (3b) and nonequilibrium incipient melting by (3c), which is the melting point of S-phase [5].

In order to better understand the precipitation reactions that are more likely to occur on the subsequent heat treatment processes carried out after the solutionizing (T4), it is useful to first know how the equilibrium fraction of precipitation phases changes as a function of temperature, as shown in Figure 4–12. Robson [72] in his studies based on the thermodynamically calculated volume fractions of phases suggested that the homogenization temperature (~480°C) lies very close to the S-phase solvus so that it is likely that some S-phase constituents will remain undissolved specially in the solute enriched regions.

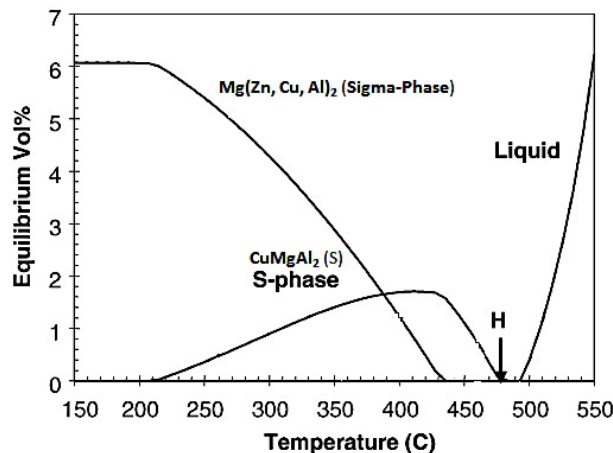


Figure 4–12 Calculated equilibrium phase fraction for Direct Chilled cast 7050 ingots; H corresponds to the solutionizing (homogenization) temperature (753K). However, the calculation is limited to equilibrium therefore it does not allow the effect of metastable precipitation to be explored [72].

Figure 4–12 presents the changes in the volume fraction (%) of the equilibrium phases during the thermal process of AA7050, as simulated thermodynamically by Robson [72]. Figure 4–12 shows that the solvus temperature of the S-phase (Al_2CuMg) is almost the same as the preferred solutionizing (homogenization) temperature (H) for the alloy. This strongly suggests that the complete removal of the S-phase is seldom possible during solutionizing treatment. It is noteworthy that the simulated calculations plotted in Figure 4–12 are restricted to the solid state transformations under equilibrium conditions in the AA7050 alloy and it predicts the relative volume fractions of the S-phase (Al_2CuMg) and Sigma-phase ($\text{Mg}(\text{Zn},\text{Al},\text{Cu})_2$) in these conditions; further, it implies that neither the metastable precipitations are included in the prediction nor the phases formed from impurity solute elements such as Fe and Si. However, it still provides a viable guide in terms of the precipitation sequences expected to form in an equilibrium condition with a very slow cooling or heating rate. This would be helpful in interpreting the experimental results during the heat treatment.

Figure 4–13 and Table 4–5 show the thermal data from three successive runs of Differential Scanning Calorimetry (DSC) experiments (with a heating rate at $10^\circ\text{C}/\text{min}$ for each run and a cooling rate of $2^\circ\text{C}/\text{min}$ between each run) of AA7050 wrought alloy in the original T7* condition [73]: the point A was attributed to the dissolution of η' -phase, point B to the onset of the η -phase formation, point C to the dissolution of η -phase, points D and E to the formation and the dissolution points of the S phase (Al_2CuMg), respectively, which is consistent with its solvus temperature, as in Figure 4–12, point F to the incipient melting of the T phase ($\text{Mg}_3\text{Zn}_3\text{Al}_2$) which is only observed in the third DSC run and point G to the incipient melting of the undissolved S phase. This indicates that after very slow cooling ($2^\circ\text{C}/\text{min}$) in between the DSC test runs, there was not sufficient time for the coarse T phase to be completely dissolved, and hence a melting of T phase occurred at 480°C . The difference among the three DSC runs is caused by the heating cycles of DSC, for instance, in the second run there is a GP zone dissolution effect prior to the first exothermic peak corresponding to the η' -precipitation [73].

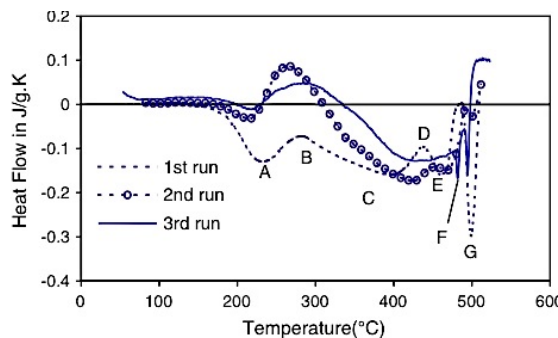


Figure 4–13 DSC curves in three consecutive runs with heating rate of $10^\circ\text{C}/\text{min}$ for Al-6.1Zn-2.3 Mg-2.6Cu (wt.%) alloy in artificially over-aged condition (T7=16 hr @ 172°C); A= dissolution of η' -phase; B= formation of η -phase; C= dissolution of η -phase; D and E= dissolution and formation of S-phase; F and G= melting of T and S phases; the identification of these phases are listed in Table 4–5 [73].

Table 4–5 Identification of the thermal reactions occurring in the DSC test of 9 alloys from the Al-Zn-Mg-Cu family that are aged for 8 hours at 172°C . [72].

* Aged at 172°C for 16 hr

Effects	A	B	C	D	E	F	G
Alloy							
1	η' dissolution	η formation	η dissolution	T melting	S melting
2	η' dissolution	η formation	η dissolution	T melting	S melting
3	η' dissolution	η formation	η dissolution	T melting	...
4	η' dissolution	η formation	η dissolution
5	η' dissolution	η formation	η dissolution	S formation	S dissolution	T melting	S melting
6	η' dissolution	η formation	η dissolution	T melting	S melting
7	η' dissolution	η formation	η dissolution	S formation	S dissolution	T melting	S melting
8	η' dissolution	η formation	η dissolution
9	η' dissolution	η formation	η dissolution	S formation	S dissolution	T melting	S melting

Higher temperatures of solutionizing treatment before quenching gives rise to higher number of quenched-in vacancies. Table 4–6 presents number of vacancies per atom in a pure Al sample at various temperatures. The higher number of vacancies accelerates the kinetics of the precipitation reaction during natural and artificial ageing processes. Besides, the higher solutionizing temperature can provide a better super saturated solid solution (SSSS), which in turn can improve mechanical properties of the alloy part [66]. Additionally, the amount of quench-in vacancies can directly influence the volume and width size of precipitation-free zones (PFZ), which plays an important role on the corrosive response of the Al-Zn-Mg-Cu material.

Table 4–6: Number of vacancies per atom in equilibrium condition in pure aluminum, as a function of temperature [66].

°C	Temp., K	Number of vacancies
661	934	1.6×10^{-3}
600	873	4.6×10^{-4}
400	673	2.2×10^{-5}
200	473	8.3×10^{-9}
20	293	10^{-12}

4.2.2 Precipitate free zone (PFZ)

PFZ are precipitation-free areas around the grain boundaries and sub grains; and they can even form around the precipitates and undissolved phases [68]. PFZ are very important because of their strong effect on the stressed corrosion susceptibility of the Al-Zn-Mg-Cu alloys. However, they have little effect on mechanical properties of the materials (very slight decrease in ductility and no effect on strength) [66]. The PFZ was originally contributed to the solute depletion occurring around the grain boundaries due to the formation of precipitation at grain boundaries [67,74]. Embury et al [75] found out that the precipitation free areas around the grain boundaries are supersaturated with solute atom; therefore, he concluded that what makes PFZ's to be free of precipitation is not the depletion of solute but the shortage of enough vacancies required for the nucleation of precipitates. Therefore, quench rate and solutionizing temperature are the most important parameters controlling the size/width of PFZ areas because they have strong effect on the amount of quenched-in vacancies. This is shown in Figure 4–14, by means of TEM micrographs of PFZ areas in the Al-5.9Zn-2.9Mg (wt.%) wherein the effect of different quenching rates on the width of PFZ areas are presented. As it can be seen in Figure 4–14 (b), in the samples quenched in oil, not only the PFZ areas are wider but also the precipitates forming within the grain interiors are larger in size; whereas in the water-quenched samples, as in Figure 4–14 (a), the PFZ areas become narrower and the grain precipitates are far smaller. This is mainly because in the

water-quenching condition, the number of entrapped vacancies is larger than that in oil-quenched samples. This in turn enhances the precipitation process from the super saturated solid solution (SSSS) aluminum matrix during the subsequently artificial ageing process (T6). Further, in Figure 4–15 the vacancy concentration profiles at grain boundary areas are schematically presented for various quenching conditions. This includes a few combinations of various parameters such as solutionizing (T4) temperatures and quenching rates, followed by different ageing (T6) processes. As it can be seen in Figure 4–15, the width of PFZ areas decreases with increasing solutionizing temperature as well as with increasing the quenching rate. The samples solutionized at 510°C followed by the same water-quenching condition has a narrower PFZ area than the samples solutionized at 465°C; it is shown in Figure 4–15 that the samples quenched in water from the same solution treatment temperature (510°C) has a narrower PFZ area than those in oil [75].

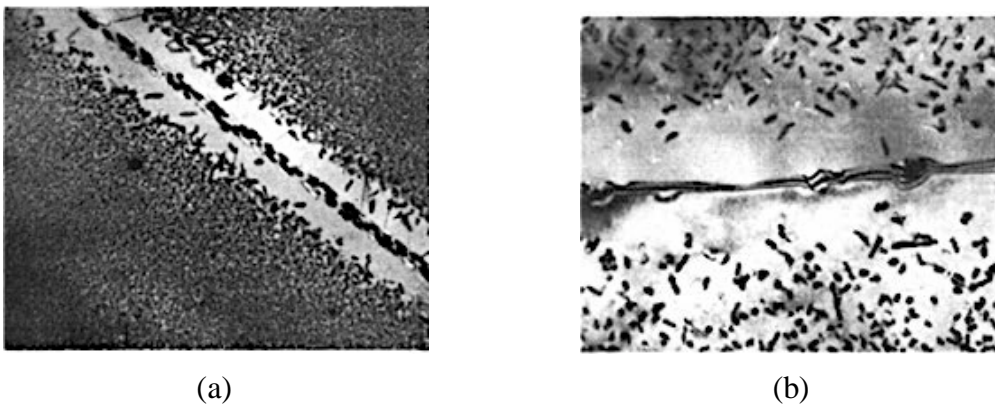


Figure 4–14: Typical precipitate free zones (PFZ) near grain boundaries in Al-5.9Zn-2.9Mg (wt.%) alloy: (a) water quenched from 465°C and then aged for 12 hours at 180°C, and (b) oil quenched from 465°C and then aged for 3 hours at 180°C. Note the effect of quenching rate on the width of the zone and the dispersion of precipitates within the grains. Magnification of both (a) and (b) is X27,000 [75].

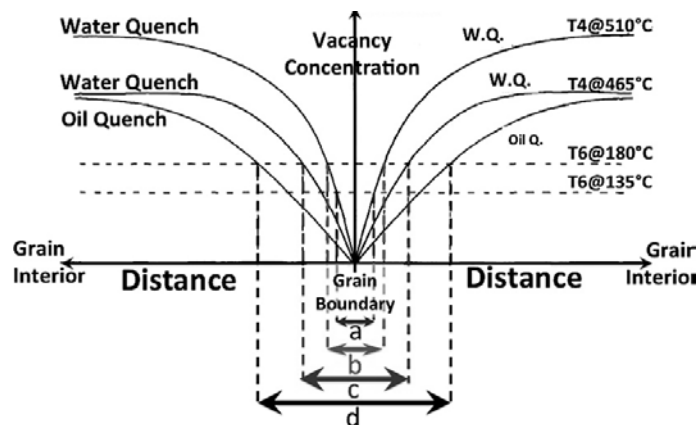


Figure 4–15: A comparison of the vacancy concentration profiles for various solution treatments temperature, quenching conditions of Al-5.9Zn-2.9Mg (wt.%) alloy. The precipitate free zone widths depicted are (a) solution at 510°C, water quench, age at 135°C, (b) solution at 510°C, water quench, aged at 180°C, (c) solution at 465°C, water quench, age at 180°C and (d) solution at 465°C, oil quench, age at 180° [75].

4.2.3 Precipitation age-hardening process of Al-Zn-Mg-Cu alloys

Precipitation hardening, or as it was first called “age hardening” by Martin [76], is a production of solution treating (T4) and quenching of an alloy. Precipitation hardening of 7xxx aluminum wrought alloys usually occurs during the non-isothermal condition wherein the precipitates are formed in the high strength Al-7xxx alloys during the cooling process from the solution treatment temperature. These non-isothermal precipitates that are industrially important have been carefully studied [77,78]. The reason being these precipitates can remove solute elements from the supersaturated solid solution matrix to form coarse precipitates which in turn have a detrimental effect on the subsequent age-hardening response of the material. These precipitates can heterogeneously nucleate on high-energy structural defects such as grain and sub-grain boundaries, dispersoids and dislocations [79].

In the complex system of the Al-Zn-Mg-Cu alloys, several precipitation phases could evolve during the subsequent heat treatment processes, namely, the η phase (MgZn_2), M/Sigma phase $\text{Mg}(\text{Zn,Cu,Al})_2$, T phase $\{(\text{Al}_2\text{Mg}_3\text{Zn}_3) \text{ or } \text{Al}_{32}(\text{Mg,Zn})_{49}\}$, S phase (Al_2CuMg), θ phase (Al_2Cu), irregularly shaped iron containing intermetallic of $\text{Al}_7\text{Cu}_2\text{Fe}$ (bulky-shape), plate shaped iron containing intermetallic of $\text{Al}_{13}\text{Fe}_4$ and Mg_2Si ; some of which could evolve below the solidus temperature [80]. The impurity intermetallic phases in the Al-7xxx alloys such as Cu_2FeAl_7 , FeAl_3 and Mg_2Si are not more than 1% [81].

The hexagonal phases of η or M are mostly observed in the as-cast microstructures whereas the orthorhombic phases of S and T are more common in solid solution states with the extended composition ranges containing all four elements, i.e., Al, Zn, Mg, and Cu [72]. During natural ageing (NA) process of the Al-Zn-Mg-Cu alloys occurring immediately after quenching from solution heat treatment temperature, precipitation process starts with the formation of solute clusters from the supersaturated solid solution (SSSS). These unstable vacancy-rich solute clusters (VRC) are also known as Guinier-Preston (GP) zones. These early stage GP clusters are named after Guinier [82] and Preston [83], French and American researchers, who observed these coherent phases by x-ray diffraction in aluminum-zinc alloys at nearly the same time in history, in the year of 1943. A widely accepted sequence for the precipitation sequence of Al-Zn-Mg-Cu alloys is given in the below sequence which is also schematically presented in Figure 4–16:

Supper saturated solid solution \rightarrow VRC or GP zones (type I & II) \rightarrow Intermediate phases (η') \rightarrow Stable phases (η or T)

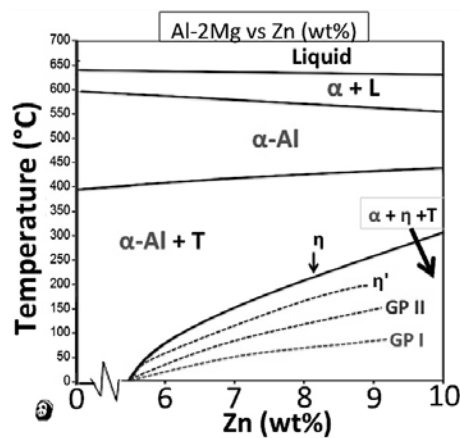


Figure 4–16 The Al-2Mg- (0~10) Zn isopleth phase diagram showing the schematic equilibrium solvus temperature lines for the metastable GP zones (GP-I and GP-II), η' and equilibrium η - MgZn_2 ; note that just for the purpose of simplicity, the composition range in the isopleth phase diagram is chosen to represent the ternary Al-Mg-Zn system within the compositional range that is selected for this study.

Despite all the extensive investigations [80,84], there still exists some uncertainty about the transient stage from GP zones to the intermediate phases: Evidently, there are two types of GP zones: type I is proposed to be spherical and the type II is observed to be with its internal ordered structure. . Figure 4–17 presents schematically the transitional reaction occurring during the ageing process of the Al-7xxx alloys.

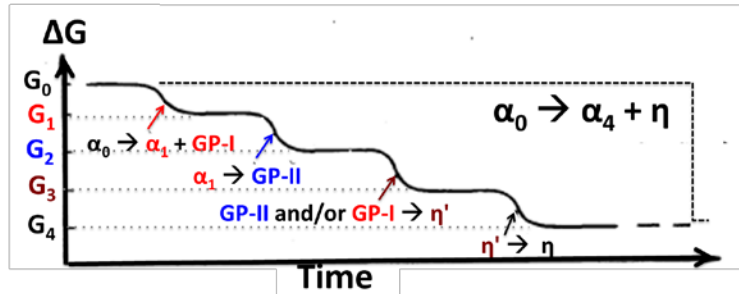


Figure 4–17 Schematic presentation of total free energy as a function of time; note the distinct reactions for formation of η' -precipitates from GP zones type I and II [68].

At a temperature slightly higher than the formation temperature range for GP zones (as schematically shown in Figure 4–18), other metastable precipitate (or intermediate η' -phase) is formed either indirectly by nucleating on the GP zones (type I) as the preferred locations for the formation of these η' -phase or directly from larger GP zones (type II) as an ordering and transformation phenomena. Finally, at a relatively higher temperature range, the equilibrium η ($MgZn_2$) phases become stable as a solid state phase transformation or ordering phenomena from the intermediate η' (transient) phases. The precipitation sequence (as $GP \rightarrow \eta' \rightarrow \eta$ -phases) occurs because direct formation of stable η -phases from supersaturated solid solution matrix requires a large driving force to overcome the energy barrier for the nucleation of the equilibrium η ($MgZn_2$) phases therefore the system tries to minimize the required energy for the nucleation of the precipitates by formation of a few intermediate phase such as GP zones and transient (η') phase. This is schematically shown in Figure 4–19. The structure and composition of the intermediate and stable final precipitates is strongly dependent on both the alloy composition and ageing temperature. In practice, the GP zones (type I & II), η' (transient) phase, η and T (stable) phases consist the precipitation phases forming during the artificial ageing processes. The metastable and stable precipitation phases do not form independently. The formation of the metastable phases influences strongly the nucleation of the stable precipitates [80].

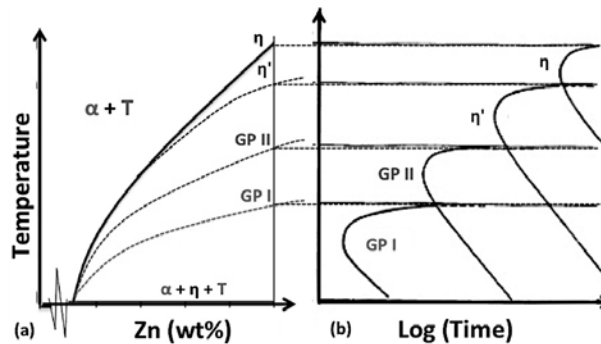


Figure 4–18 The schematic presentation of precipitation sequences in Al-2Mg-XZn alloys: (a) the metastable solvus lines in the Al-2Mg vs. Zn phase diagram; and (b) relative time for the start of formation of each precipitation stage at different temperature for alloy with X composition in (a) [68].

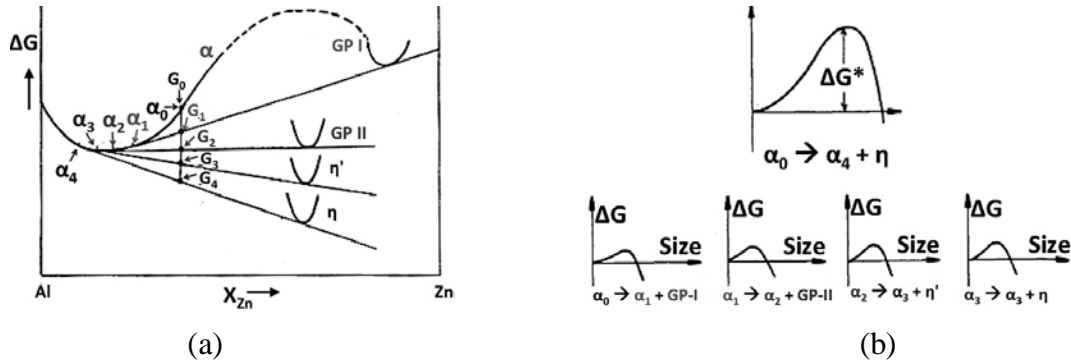


Figure 4–19 Schematic presentation of molar free energy for Al-Zn-Mg-(Cu) alloy showing the activation energy barrier to nucleation/formation of the transient phases are smaller than that of direct transformation from supersaturated solid solution (α_0) Al matrix to the equilibrium η -MgZn₂ precipitates; the schematic diagrams were revised from the original schematics presented for Al-Cu system [68].

Naudon et al [85] reported that the size of very early-stage fine-scale GP zones are in the range of 5-10 Å in diameter, which is smaller than the detection capability of the electron microscope dictated by the wavelength of the electron beam. Upon subsequent ageing, the GP zones grow and could reach diameters of about 50 Å and even in some cases of prolonged ageing processes, they might grow to about 100Å diameter in size [66]. Regardless of the mechanism, these spherically coherent GP zones are replaced by platelet or discs shaped phase, which are semi-coherent with the Al-matrix. These intermediate phases are elongated either on {111} or {100} planes [66], which contain the soft directions in cubic metals [68]. The thickness of the platelet/disc shaped η' -phases can reach a size of about 50Å, which remains relatively unchanged over the course of ageing process. However, the diameter of precipitates increases by time and temperature, and they could reach a maximum value of 200 Å (after 800 hour at 135°C) to 500Å (after 700 hour at 175°C). At this stage reversion (re-dissolution of the precipitates) is no longer possible because the η' -phases are very close to becoming the stable η -phase (MgZn₂) [66].

Schmalzries and Gerold [86], by means of oscillating single-crystal method and SAXS* in the samples of Al-2.6 Zn-3.9 Mg (wt.%), found that the weak and diffuse X-ray (100) reflections already appear during a room temperature ageing process; and the intensity of (100) reflection remains somewhat unchanged even after 4 months. They concluded that the unchanging (100)-diffraction pattern might be because of the constant lattice parameter of matrix in <100> direction during GP formation. Whereas, at higher temperature such as at around 100°C, the (220) weak reflection of the hexagonal η' -phase start to appear after 8 hours. They concluded that GP zones are fine scale solute-vacancy clusters or parallel atom layers to {111} planes of aluminum matrix, which are alternatively enriched and impoverished in zinc and magnesium atoms; and because of the opposite effect of the size difference between zinc and magnesium atoms on the lattice parameter of the Al matrix, the lattice parameter of the GP zones remain constant [67].

Li et al. [87] and Berg et al [88], by means of HRTEM[†] and SAED[‡] analyses, re-affirmed the existence of two types of GP-Zones, with distinct structures: GP (I) and GP (II), forming during the artificial ageing processes of AA-7108-alloy[§] at 100°C and 150°C temperatures.

* Small-Angle X-Ray Scattering

† High-Resolution Transmission Electron Microscopy

‡ Selected Area Electron Diffraction

§ Al-5.36Zn-1.21Mg-0.16Zr (wt.%)

They found that the GP type (I) zones (solute-rich clusters) are coherent with the Al matrix; with an internal ordering of Zn and Al/Mg on the $\{001\}_{Al}$ planes. Also, they reported that the GP type (I) zones form over a temperature range, room temperature (RT) to 140–150 °C and their formation is independent from quenching temperature. On the other hand, they found that the GP type (II) zones are zinc-rich layers forming on $\{111\}_{Al}$ planes and they reported that the formation of the GP (II) depends on the quenching rate and ageing temperatures as they were only discernable in the samples quenched from a temperature above 450 °C and aged at a temperatures above 60~70 °C [67,88], which is in consistence with prior work found in the background literature [66,67,80]. Generally, either or both types of GP zones are believed to be forming as precursors prior to formation of the metastable η' -phase [66,88]. Figure 4–20 presents the SAED patterns of the various zone axes of $\langle 001 \rangle$, $\langle 111 \rangle$ and $\langle 112 \rangle$ of aluminum matrix, illustrating the precipitation evolution in the under aged* samples (Figure 4–20 1(a) to 1(c)), peak aged (T6)[†] (Figure 4–20 2(a) to 2(c)) and over aged (T7)[‡] samples (Figure 4–20 3(a) to 3(c)). SAED patterns of under aged samples, as in Figure 4–20 1(a) to 1(c), present the characteristic diffuse spots associated with GP zones: type II and I. In the T6 sample, as in Figure 4–20 2(a) to 2(c), reflections from the metastable hardening η' -phase are shown; and in Figure 4–20 3(a) to 3(c), the super-lattice reflections of η -MgZn₂ in the T7 samples are presented. Super-lattice reflections of GP (I) and η' -phase are observed on the $[001]_{Al}$ SAED projections as they appear in the form of rows of diffuse spots on the $hkl = 1, (2n + 1)/4, 0$ positions on the aluminum reciprocal lattice, corresponding to a tetragonal or orthorhombic anti-phase structure, with a four-doubling along one cubic axis. The strongest diffuse spots from GP (I) and η' -phase appeared at positions $1, 1/4, 0_{Al}$ and $1, 7/4, 0_{Al}$. The characteristic spots of GP (II) and η -phase are detectable at $1/2\{3\ 1\ 1\}_{Al}$ in $[112]_{Al}$ projections of SAED pattern. Further, the GP (II) and η -phase can be identified by strong spots of irregular shaped super lattices just outside the $1/3\{422\}_{Al}$ positions in $[111]_{Al}$ projections of SAED pattern [88].

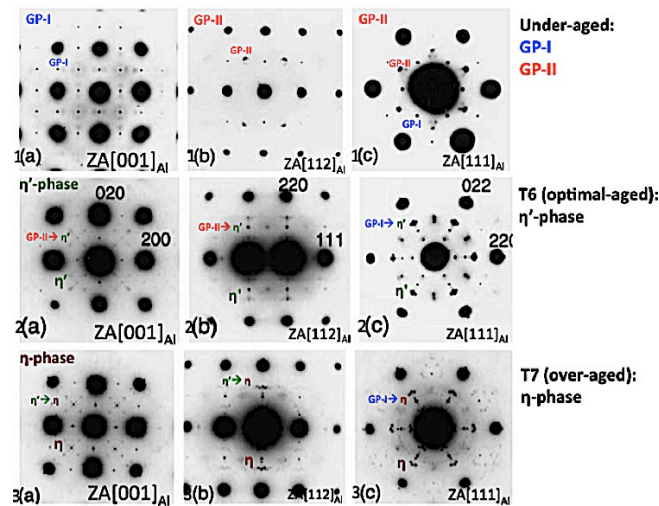


Figure 4–20 Selected area diffraction patterns (SAED) from samples aged to an (1) under-aged, (2) optimal age (T6) and (3) over-age (T7) conditions of Al7050 alloys are shown in (a) the $[001]_{Al}$ -projection, (b) $[112]_{Al}$ -projection, and (c) $[111]_{Al}$ -projection. Precipitate spots are from GP zones, η' and η -phases. Sharp extra spots at simple cubic positions 100_{Al} , are from the Al_3Zr dispersoids [88].

* Under aged condition: at 100°C for 1.5–5 h

† Peak aged (T6) condition: at 100°C for 5 hr + at 150°C 6 hr

‡ Over aged (T7) condition: at 150°C for 24 hr

Su et al [89], by means of TEM and SAED, studied the precipitation evolution for various heat-affected regions of friction stirred weld (FSW) process of AA 7050*-T651. Figure 4–21 and Figure 4–22 present the corresponding SAED patterns along [111] and [001] zone axes of the aluminum matrix, respectively. Some diffraction positions overlap with two or three diffraction spots from different precipitates or the aluminum matrix due to the orientation relationships mentioned above. This situation necessitates extra care for interpreting the diffraction patterns [89].

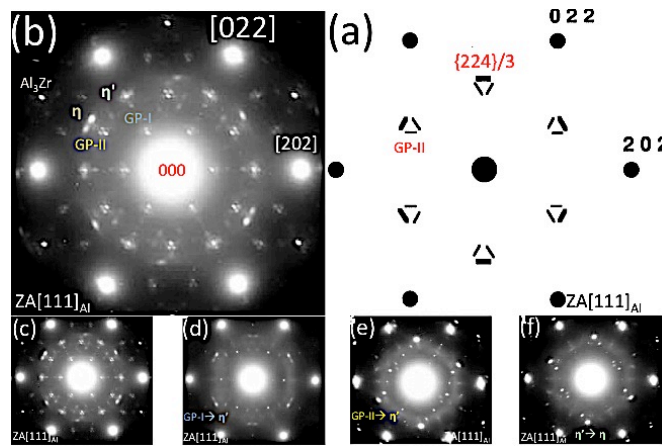


Figure 4–21 (a) Schematic diagram of the SAED pattern from GP (II) zones; (b) to (f) SAED pattern along the [001]_{Al} zone axis from various heat affected areas in FSW of AA 7050-T651; showing the precipitation evolution (GP (I)/η'-phases and GP (II)/η-phases) by means of the reflection spots [89].

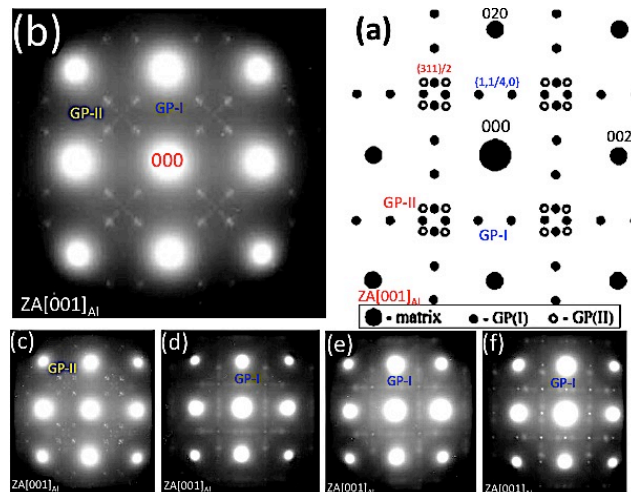


Figure 4–22 (a) Schematic diagram of the diffraction pattern from GP (I)/η'-phases and GP (II)/η-phases in the [111]_{Al} zone axis; and (b)-(f) the SAED patterns along the [111]_{Al} zone axis from various heat affected areas close to the friction stir weld (FSW) area of AA 7050-T651, showing the precipitation formation procedure by evolution within their SAED patterns [89].

The chemical composition of the GP zones in the Al-Zn-Mg-(Cu) alloys with $0.5 \leq \text{Zn/Mg} \leq 2$ measured by integrated intensity of small-angle x-ray scattering (SAXS) or neutron SAXS exhibit a range of composition such as 40 to 80 at% Zn, and 20 to 60 at% Mg [67]. Recently, Sha et al [90], by means of 3-dimensional atom probe (3DAP) succeeded to determine the

* Al- (5.7~6.7) Zn- (1.9~2.6) Mg- (2.0~2.6) Cu- (0.08~0.115) Zr

composition of GP zones in the Al-7xxx alloys. They showed that in the AA 7050^{*}, GP zone type (I) nucleated homogeneously in aluminum matrix during a very short ageing time (< 30 min) at 121 °C. Their 3DAP observations showed that the small GP (I) (forming with less than 30 solute atoms) could appear as Mg-clusters with an approximate Zn/Mg ratio of 0.9. However, they reported that the larger GP (II) could form as Zn-clusters with Zn/Mg ratio close to 1 and 1.1, in the shape of elongated clusters. They also reported a composition of Zn/Mg ratio of 1.2 for η' -phase. Also, Stiller et al [91], by means of transmission electron microscopy (TEM) and three dimensional atom-probe (3DAP) field ion microscopy, investigated the fine-scale precipitation of the metastable Zn- and Mg-rich η' -phase in an Al-Zn-Mg alloy[†] during and after the two-step ageing treatments at 100°C and 150°C; their TEM observations confirmed the presence of two distinct GP clusters (GP type (I) and (II)) in the under aged samples, which play an important role to identify the two different precipitation paths: (1) formation and dissolution of GP (I) prior to formation of η' -phase and (2) formation of GP (II) with a completely different atomic arrangement with Al-matrix atoms, which will further transform to the η' -phases. However, his 3DAP investigations did not show any distinction between the GP clusters (in the under aged samples); further he reported that in general the Zn:Mg ratio in all observed types of precipitates (including the early stage GP cluster in the under aged samples) was close to 1:1 and the total solute atomic content of the precipitates increased with ageing time. Therefore, he concluded that neither the precipitation sequence nor the structure and composition of the intermediate precipitate phases are completely clear.

Sha et al [90] also observed that the small GP (I) may contain higher amount of copper than that of the larger GP (II). Thus, they concluded that copper might play more important role in affecting the kinetics of the initial clustering process during ageing of the Al-7xxx series alloys. This is in consistence with other researchers' work about the effect of copper on the early stage clustering and precipitation of Al-Zn-Mg-(Cu) alloys. Engdahl et al [92], by means of transmission electron microscopy and atom probe field ion microscopy, studied three alloys of Al-Zn-Mg-(Cu)[‡] family aged at 150 °C. They found GP (I) zones in the copper sample; whereas in copper free samples, only GP (II) zones were detectable. Also they reported that Cu addition to the alloying system decreases the average particle size of GP clusters while it increases the number density of GP clusters, as shown in Figure 4–23. Chihn et al [93], by means of compression and indentation tests, DSC, TEM and 3DAPFIM[§], studied the Al-2.4Zn-2.1Mg-0.5Cu (at.%) aged at various aging temperature from room temperature to 130°C. They found that even a small addition of Cu (0.5 at.%) could increase the number density of GP zones. Furthermore, they reported that Cu influenced the morphology and composition of the GP clusters because they appeared to be more elliptical in copper samples as compared to that of copper free samples wherein the GP zones appear to be more in the spherical shape. Also, Marlaud et al [94], by means of atom probe tomography and systematic anomalous SAXS^{**} studies AA7150^{††} and AA7449^{‡‡} under various ageing conditions between 120°C to 160°C. They found that the copper content of early stage GP clusters decreases with the time of ageing at 120°C. Further he concluded that the gradual

^{*} Al-6.29Zn, -2.22Mg-2.28Cu-0.11-Zr (wt.%)

[†] The nominal composition of the material was (at%): 96.08 Al, 2.30 Zn, 1.38 Mg, and 0.09 Si, with Cu, Fe, and Mn in the remainder.

[‡] Al- (2.3~2.6) Zn- (1.4~1.1) Mg- (0.13Cu) (wt.%)

[§] Three Dimensional Atom Probe Field Ion Microscopy

^{**} Small-Angle X-ray Scattering

^{††} Al-6.4Zn-2.2Mg- 2.3Cu (wt.%)

^{‡‡} Al-8.5Zn-1.9Mg-2.2Cu (wt.%)

incorporation of Cu in the precipitates during the heat treatment is essentially related to the slower diffusivity of Cu in Al.

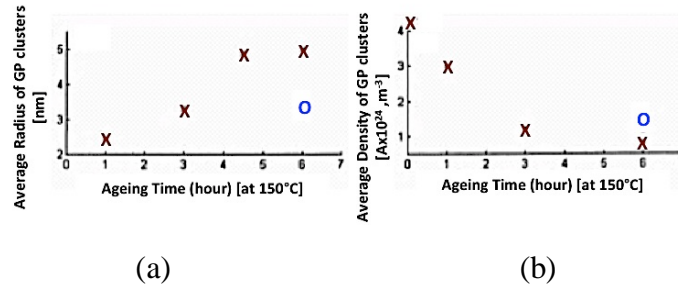


Figure 4–23 Graphs summarizes the 1DAP results showing the changes of (a) average particle size and (b) number of density for the precipitates in two of Al-Zn-Mg-(Cu)-alloy samples; the data points shown by cross sign (X) belong to the copper free sample (Al-2.3Zn-1.38Mg (wt.%)); and the stand-alone, one data point shown by empty circle is representing the copper sample (Al-2.3Zn-1.38Mg-0.13Cu (wt.%)) [92].

4.2.4 Rate of hardening during ageing process:

The parameters controlling the precipitation hardening or growth rate in the ageing process of Al-Zn-Mg-(Cu) alloys are: (1) ageing time, (2) ageing temperature, and (3) solute element concentration / solubility. Ageing time has a direct effect on the size and the number density of the early stage clusters (GP zones), most of which subsequently transform to semi-coherent strengthening (η' -) precipitates. This is presented in Figure 4–24 (a) and (b), wherein the experimental data points, measured by 3-dimensional atom probe (3DAP) method, of the average size and the number of GP zones of AA7050 alloy, respectively, are plotted against isothermal incubation time during the artificial ageing process at 121 °C [90]. Similarly, ageing temperature can affect the GP zone formations during the early stage clustering of the ageing process in the Al-Zn-Mg-Cu alloys. Effect of aging temperature is more sensible on the growth rate of the ageing process. In other words, irrespective of mechanism, at higher ageing temperature, the early stage (GP) clusters transform to the strengthening (η' -) precipitates in a shorter incubation isothermal time. However, ageing temperature can have counter effect on the maximum obtainable hardness value, meaning a higher ageing temperature may lead to a lower maximum attainable hardness value [66].

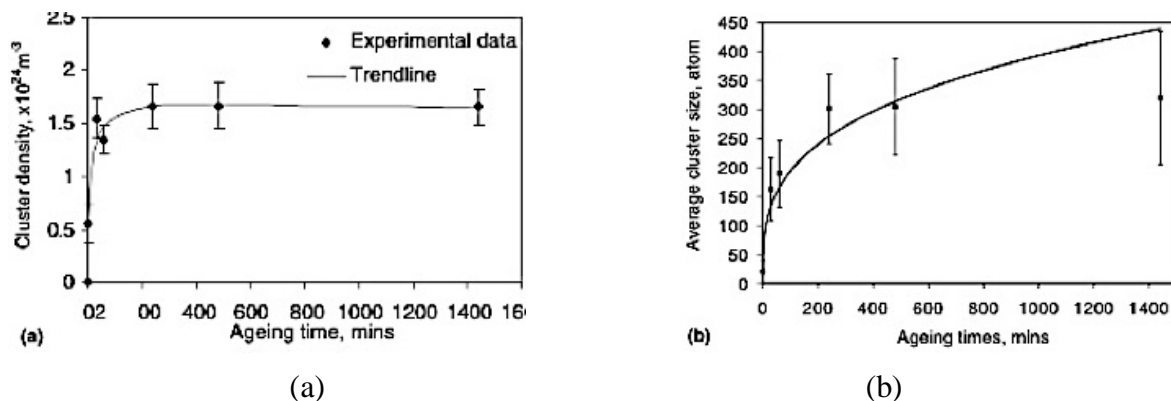


Figure 4–24 (a) Typical experimental data of the number density and the size of the early stage clustering (GP zones), evolving during ageing process at 121 °C of AA 7050 alloy, which were measured by 3DAP for a duration of 1440 minutes time period [90].

4.2.5 Effect of alloying elements on the ageing process:

The amount of total solute elements in the Al-Zn-Mg-Cu alloys has a direct effect on the age hardening process of the alloy. This is mainly attributed to the effect of alloying elements on the degree of the supersaturated solid solution (SSSS) within the Al-matrix, which subsequently affects the amount of coherent Vacancy-Rich solute Clusters (VRC or GP zones) and strengthening (η') precipitates. The maximum attainable hardness value for these alloys by ageing process at an elevated temperature is attributed to the correct stoichiometric ratio of solute elements for $MgZn_2$ (η) and $Mg_3Zn_3Al_2$ (T) phases. For instance, the maximum possible hardness achievable with η -phase is possible in an alloy with the correct Mg/Zn ratio of 1:5 (for η -phase) and similarly the maximum hardness expected from T-phase is expected in the alloys with the Mg/Zn ratios within the range of 1:1 to 1:2 [66]. Figure 4–25 (a), (b) and (c) present the experimental hardness-test results for various ageing processes of three different compositions of Al-Zn-Mg alloys. In Figure 4–25 (a) and (b), the effect of excessive Mg is presented, that is an acceleration of the hardening rate in the alloy; this is because Mg has directly affecting the amount of GP clusters and strengthening (η') precipitates. On the other hand, Zn excess amount can lead to a higher maximum attainable hardness values is shorter ageing incubation at the similar ageing conditions, which is mostly because of its strong effect on the supersaturation degree of solid solution (SSSS) forming within the Al-matrix [66].

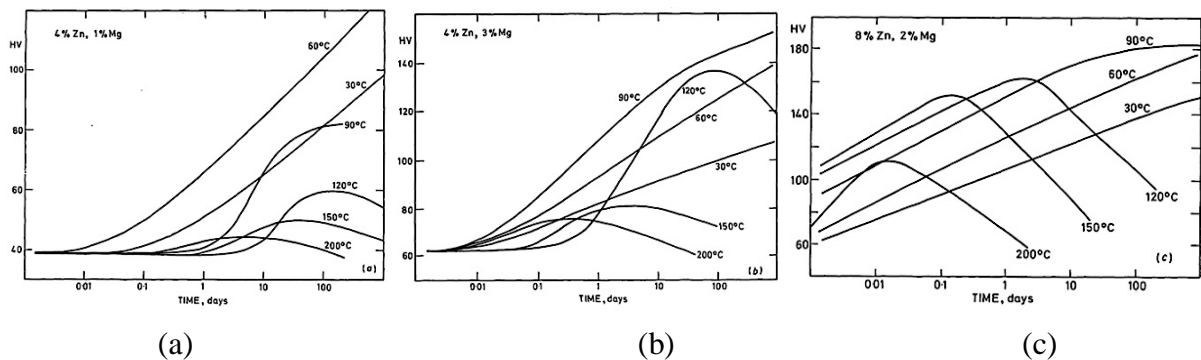


Figure 4–25: The effect of excess alloying elements such as Mg and Zn on various ageing processes of Al-Zn-Mg alloys: (a) Al-4Zn-1Mg, (b) Al-4Zn-3Mg, and (c) Al-8Zn-2Mg (wt.%) [66].

4.2.5.1 Effect of Copper (Cu)

General effects of copper addition to Al-Zn-Mg system are on mechanical properties and quench rate sensitivity; both of which are attributed to the corresponding increase in total alloying element [5]. Moreover, copper in some cases is added mainly to enhance the resistance to stress corrosion, although it tends to reduce the general corrosion-resistance, as well [66]. Nonetheless, as mentioned earlier in the previous sections, copper has a strong effect on the early stage clustering and precipitation of the Al-Zn-Mg-(Cu) alloys as it accelerates the rate of age hardening in the alloy; this is of importance considering the fact that copper does not belong to the compound stoichiometric chemistry of the strengthening (η) precipitates ($MgZn_2$) [66,67,90,92,93,94]. Recently, Sobrino [95], by means of micro and macro hardness tests, investigated the effect of copper on the age hardening process of Al-Zn-Mg-(Cu) alloys during a various combination of natural and artificial ageing processes. In his investigation, he used three of the Al-Zn-Mg-Cu alloys; Figure 4–26 presents the macro hardness test results of the age hardening processes for three different compositions of the Al-Zn-Mg-(Cu) alloy samples cast using the CDS technology, at ambient temperature (Natural Ageing). As it can be seen in Figure 4–26 (b), as copper increases in the

composition of the alloy, the initial slope of hardness curves of the respective alloy is noticeably increasing, which shows the acceleration effect of copper element on the hardening rate of the Al-Zn-Mg(-Cu) alloys [95]. However, this acceleration of the early ageing stages is accompanied by an increase in susceptibility to stress and inter-granular corrosion [66].

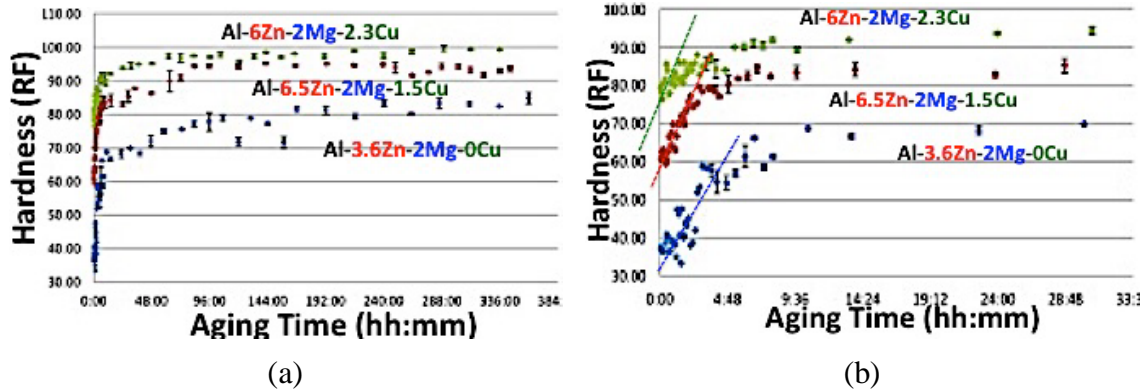


Figure 4-26 Macro-hardness curves of three distinct alloys from Al-7xxx family cast by CDS processes using tilt pour gravity casting machine, showing the effect of alloying element effect on the hardness value and hardening rate [95].

4.3 DEFORMATION IN METALS AND DISLOCATION INTERACTIONS

The partial movement of a crystal part over another part of it defines plastic deformation in metallic materials. The process of the plastic deformation occurs along certain crystallographic directions and planes that are also termed as slip systems. The existence of a large difference between theory and practice in measuring the shear stress required for activation of a slip system during the plastic deformation process leads to conceptual introduction of dislocations theory as a mandatory part of plastic deformation by slipping [96]. Cottrell proposed one of the most instructive way of studying the deformation in metals by slip and dislocation motions, in which the deformation is defined as a transition from an un-slipped state of metallic material to a slipped condition, as shown in Figure 4-27 (a). This transition process has an energy barrier, which is needed to minimize to facilitate the slip to occur. The slipped part of material will grow by means of movement of an interfacial region between un-slipped and slipped blocks, which is the dislocation, as shown in Figure 4-27 (b).

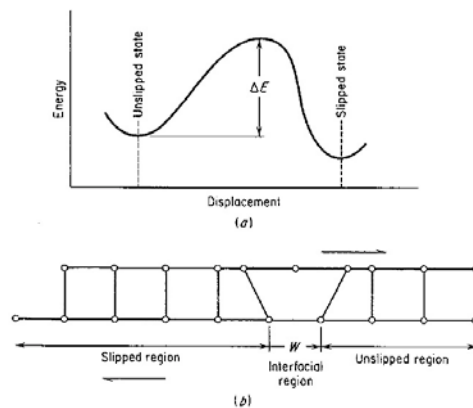


Figure 4-27 Schematics showing the transition from an unslipped to slipped state. (a) variation of energy from an unslipped state to slipped state and (b) interfacial region between the slipped and unslipped state which is a dislocation core [96].

Plastic deformation of a single (or perfect) crystal occurs by slip mechanism and dislocation movements during which a dislocation can move through the lattice once the shear stress that is applied to the crystal exceeds a critical value. The dislocation movement through the lattice during the plastic deformation by the slip mechanism is graphically illustrated in the slip model proposed for dislocation movement in Figure 4–28. The existence of the *critical resolved shear stress* required for activation of slip system by the dislocation movement mechanism was first observed experimentally by Schmid [97], therefore, it is also known as Schmid's law.

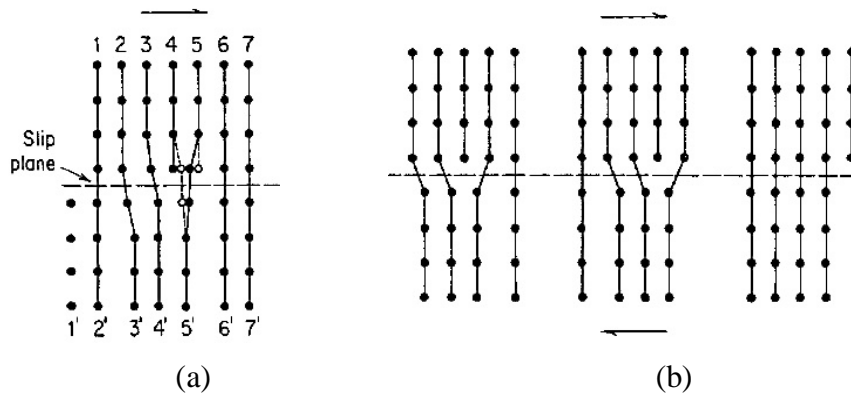


Figure 4–28 Schematic presentation dislocation movement as a step during the plastic deformation by means of the slip mechanism: (a) atom movement near dislocation in slip; and (b) movement of an edge dislocation [96].

4.3.1 Solid Solution Strengthening

Addition of a very small alloying element to a metallic material even as impurity in the solid solution of the solvent microstructure can significantly increase the critical resolved shear stress required during the plastic deformation of metals for activation of slip system by dislocation movements through the matrix lattice. The strengthening effect of alloying elements as solid solution in metallic crystal attributed to the elastic interaction between dislocations and isolated solute atoms that are acting as point defects within the matrix lattice. This strengthening effect is proportional to the lattice distortion (da/a) caused due to the solute atom presence in the matrix lattice. This can be approximately explained as though the strain field caused around a point defect which is elastically distorting the matrix lattice; wherein an elastic sphere with a radius of a' is forced in place of a smaller spherical hole with a radius of a ($a < a'$), as per the following Equation 4–1:

$$\varepsilon = \frac{a' - a}{a} = \frac{da}{a} \quad \text{Equation 4-1}$$

The lattice distortion that is caused by the solute atoms as solid solution in the lattice of the matrix crystal can create an elastic strain field around each isolated solute atom, resulting in raising the elastic interaction energy between the dislocation and solute atoms as point defects, which is required for movement of dislocations through the matrix lattice, i.e., increasing the critical resolved shear stress and strengthening of the material. The strengthening effect of alloying elements is a function of various factors such as the size difference and type of solid solution [98]. Interstitial solute atoms are more effective in strengthening the matrix lattice than substitutional ones because the former create non-spherical distortion areas in the matrix while the latter creates more spherical ones. The strengthening effect in alloys increases with increasing the total alloying elements in the primary solid solution, as shown in Figure 4–29. The addition of solute elements increases

the yield stress, tensile strength and toughness of the material, which led to conclude that solute atoms have more effect on the frictional resistance to dislocation motion (σ_a) than on the static locking of dislocations [96].

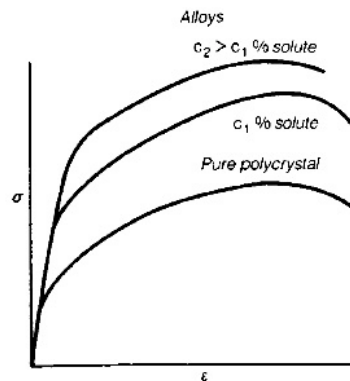


Figure 4–29 The schematic presentation of the strengthening effect of addition of alloying elements as solid solution on the stress strain curve [96].

FCC metals typically exhibit larger strain hardening than HCP metals and that is because FCC metals have a greater number of slip systems as compared to a HCP crystal, as shown in Figure 4–30. This results the deformation of FCC crystals by means of *multiple slip* systems or *duplex slip* mechanism during the plastic deformation process. Deformation by *duplex slip* mechanism can cause a higher degree of strain hardening because of more efficient interaction process between dislocations among themselves as they can interact with one another on two intersecting slip systems. Figure 4–30 presents schematics of the strain hardening responses of the FCC and HCP single crystals: Mg and Zn with HCP structure that are deformed on a single slip system show a very low strain hardening rate (slope of the stress-strain curve) whereas the Al and Cu with a FCC structure show a high rate of strain hardening because they can be oriented for duplex slip mechanism [96].

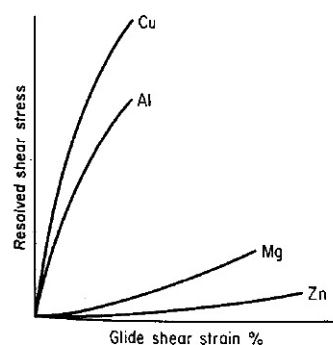


Figure 4–30 Typical single-crystal stress-strain curve for Al and Cu with FCC structure and Mg and Zn with HCP structure; note the FCC structure with higher number slip systems (12) show higher strain hardening due to possibility of duplex or multiple slipping systems; whereas in HCP structures (Mg and Zn) with mere one slip system are not capable of creating high degree of deformation by dislocation mechanisms [96].

There are two main approaches to explain the solid solution strengthening [99,100,101], (1) Friedel and Fleischers's [102,103,104] and (2) Mott & Nabarro [105] and Labusch [106].

The strong-pinning theory (Friedel-Fleischer) considers the solute atoms in the slip plane of the dislocation and they are assumed to be independent obstacle point in order to pin down the dislocations. Therefore, the dislocations may bow in the regions between the solutes

while passing through them. Equation 4–2 present the zero temperature yield stress for the Friedel mechanism that corresponds to the stress required to bow the dislocation line in between the pinning solutes.

$$\tau_y^F = A_1(C_i)^{(1/2)}$$

or

Equation 4–2

$$\sigma_y^F = A_1(C_i)^{(1/2)}$$

Where the A_1 is the constant depending on the solute's maximum resistive force; and C_i is the concentration of the solute atoms within the matrix.

The weak-pinning model (i.e., Mott and Labusch theory) considers the collective interaction of many solute atoms around the dislocation. In this theory each individual solute atom alone would not be strong enough to pin the dislocation at the same stress level. Labusch derived a zero-temperature flow stress in which he introduced an extra parameter to those in the Friedel model; mainly in order to capture the idea of three-dimensional concept of interaction between the dislocations and the solutes. Equation 4–5 explains the zero-temperature Labusch strength that is given in the standard model.

$$\tau_y^L = A_2(C_i)^{(2/3)}$$

or

Equation 4–3

$$\sigma_y^L = A_2(C_i)^{(2/3)}$$

Where the A_2 is the constant, which includes the parameter capturing the spatial range of interaction of the solutes with the dislocation.

4.3.2 Grain Boundary Strengthening

Single crystals, under uniaxial tensile load, start their deformation on a single slip system and change the orientation of the slip system by lattice rotation, when necessary. However, in polycrystalline specimen, individual grains are not subjected to a pure uniaxial stress system in uniaxial tension deformation.

Figure 4–31 shows how a single crystal deforms under a uniaxial tensile load, wherein the *resolved shear stress* in a single crystal under uniaxial tension is given by the Equation 4–4.

$$\tau_R = \frac{(P)(\cos \lambda)}{\left(\frac{A}{(\cos \phi)}\right)} = \left(\frac{P}{A}\right)(\cos \phi)(\cos \lambda) = (\sigma)(\cos \phi)(\cos \lambda) = \frac{\sigma}{M}$$

Equation 4–4

Where M is an orientation factor, which is the reciprocal of the Schmid factor. The orientation factor (M) for each grain in a polycrystalline material is uniquely different and an average orientation factor \tilde{M} represents the resultant orientation of all the grains, which in them have a wide variety of orientation relationship to the loading axis. The best estimate \tilde{M} for an FCC polycrystalline lattice is 3.1 [96]. This value was first obtained by Taylor* [107] and later treated more rigorously by Kocks [108,109]. The orientation factor of M or \tilde{M} is also known as Taylor factor.

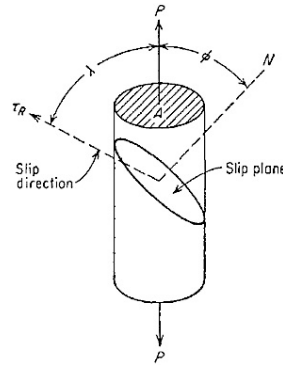


Figure 4-31 Schematic presentation of calculation of the Critically Resolved Shear Stress (CRSS) in a presumably cylindrical single crystal under uniaxial tension. The CRSS value is the equivalent of the yield stress of an ordinary stress-strain curve and it depends mainly on the composition and temperature. It is noteworthy, that, it is very difficult to determine the CSRR value, which is basically the stress at which the first slip bands are formed; in practice, for the most cases, the CRSS values are obtained by the extrapolation technique of elastic and plastic regions of the stress-strain curve [96].

In the deformation of the polycrystalline materials, in order to maintain the continuity of material, the grain boundaries are kept intact during the deformation process. This causes excessive strain near a grain boundary as compared to the strain at the center of the grain [110, 111]. This results in higher number of operative slip systems near the grain boundaries which in turn leads to higher hardness in the vicinity of grain boundary areas than the interior central grain areas. Therefore, for materials with smaller grain size, the strain field is high and the deformation becomes more homogeneous across the material. This is because the continuous strain gradient across the grain areas including the boundaries becomes more homogeneous so that the effects of grain boundaries will be felt at the grain center. Therefore, the strain hardening of a fine grain size metal will be greater than that of a coarse-grain one [96]. Deformation modes in polycrystals are more complex than single crystals. This is because the grain boundaries impose additional constraints to maintain the continuity of material during the deformation process.

A general relationship between the yield stress (and other mechanical properties) and grain size was first proposed by Hall [112], which was later extended by Petch [113], as presented in Equation 4-5.

$$\sigma_y = \sigma_\alpha + k \cdot (D_{gs})^{(-1/2)} \quad \text{Equation 4-5}$$

Where σ_y = the yield stress; σ_α = the "friction stress," representing the overall resistance of the crystal lattice to dislocation movement; k = the "locking parameter," which measures the relative hardening contribution of the grain boundaries; D_{gs} = grain diameter [96].

* Based on the use of the von Mises compatibility condition and assuming that all grains undergo the same deformation as the overall deformation.

Although the Hall-Petch equation is a general structural-property relationship, the importance of grain boundaries as an effective dislocation sources questions the validity of the dislocation pile-up model in the Hall-Petch equation. Li [114] proposed another model to avoid the description of the stresses at grain boundaries and instead concentrate on the influence of grain size on the dislocation density and the consequent effect on the yield or flow stress. The flow stress model proposed by Li, shown in Equation 4–6, is in terms of dislocation density.

$$\sigma_y = \sigma_\alpha + \alpha Gb(\rho_{dis})^{(1/2)} \quad \text{Equation 4-6}$$

Where σ_y is the yield stress; α is a numerical constant assumed to be between 0.3 and 0.6; ρ_{dis} is the dislocation density. The experimental observation validated the inter-relationship between the grain size (D_{gs}) and dislocation density (ρ_{dis}), $\rho_{dis} = 1/D_{gs}$ [96]; therefore, the Hall-Petch equation can be rewritten in the form of Equation 4–7.

$$\sigma_y = \sigma_\alpha + \alpha Gb(D_{gs})^{(-1/2)} = \sigma_\alpha + k \cdot (D_{gs})^{(-1/2)} = \sigma_\alpha + \alpha Gb(\rho_{dis})^{(1/2)} \quad \text{Equation 4-7}$$

Where the factor k has the same meaning as the k factor in Hall-Petch equation (Equation 4–5) and it is the slope of the straight line that is obtained when σ_y is plotted against $D_{gs}^{-(1/2)}$. There are many physical interpretations for the k term, which is roughly independent of temperature. The term σ_α is the intercept obtained from the plot of σ_y vs $D_{gs}^{-(1/2)}$ and σ_α is interpreted as the friction stress which is needed to move unlocked dislocations along the slip plane in the closest pack slip directions. This term (σ_α) is strongly depending on temperature, strain, and alloy composition, especially the impurity concentrations [96].

4.3.3 Strain Hardening Mechanisms

Strain hardening or *work hardening* is attributed to the increase in the shear stress required to activate slip mechanisms due to the partial deformation caused previously in the material during the deformation process. During a deformation process, strain hardening rises from the interaction of dislocations with one another and with other barriers to their motion that existing in the matrix of the crystal. One of the earliest dislocation concepts to explain strain hardening was the idea of *dislocations pile-up* around the barriers on the slip planes in the crystal. The dislocation pile-ups at the barriers can produce a *back stress*, which in turn can impose a resisting force on the slip plane in a direction opposite to the applied stress. Examples for effective barriers for dislocation movement are the solute atoms that are present in both the solid solution and strengthening precipitates that are formed during the ageing process from the supersaturated solid solution matrix with coherent or semi coherent interfaces with the matrix. The back stress caused by the dislocation pile-ups at the fine-scale strengthening precipitates is the main strengthening mechanism leading to the strain hardening during plastic deformation in metals. In addition to dislocation pile-ups due to fine-scale strengthening precipitates, the interaction of dislocations with one another can also create effective barriers to their motion. A typical example is the reaction between the two dislocations that are gliding on separate slip plane and collided with each other on the intersection of these slip planes; the resultant dislocation from such an interaction are termed *glissile* or *sessile dislocations* [115].

The *sessile dislocations* have a lower mobility than other parent dislocations and shown schematically Figure 4–32. It is noteworthy that the reason why the sessile dislocations have lower mobility is that they are required to find a new slip plane to continue gliding and this required a higher level of applied shear stress. Therefore, the sessile dislocations are also considered as effective barriers for dislocation motion. One of the most important examples

of these dislocation interactions leading to the formation of effective barriers for dislocation motion is the *Lomer-Cottrell barrier* that are formed in FCC metals on two intersecting $\{111\}$ slip planes. Figure 4–32 shows the schematic presentation of the *sessile dislocations* by means of a small step or jog that are formed on the dislocation line which in turn restricts the dislocation movement during the deformation process. The dislocations interactions through the active slip plane are often called a *dislocations threading* or *dislocation forest*, and the consequent strain-hardening effect is therefore referred to as the *intersection of a forest of dislocations* [96].

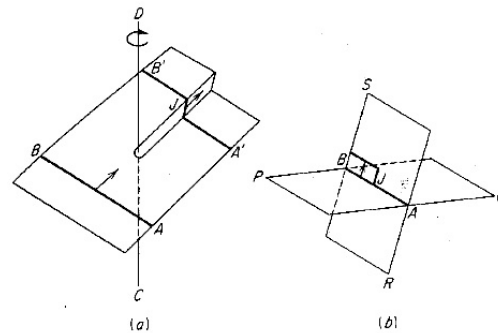


Figure 4–32 Formation of glissile or sessile dislocations: (a) a jog (J) by a dislocation that is cutting through a screw dislocation as it glides from AB to A'B'; (b) by part of a screw dislocation line AB cross slipping from the primary slip plane PQ into the plane RS [115].

Following the notation proposed by Seeger [116], Figure 4–33 presents a schematic of a typical stress-strain curve for a pure FCC metal; wherein it is shown that the flow stress curve is divided into three distinct stages: **Stage I** (laminar flow), **Stage II** (linear part of the flow curve) and **Stage III** (dynamical recovery).

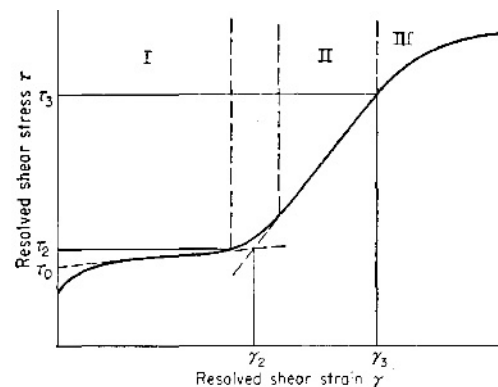


Figure 4–33 Typical flow curve for FCC single crystal, indicating different stages of dislocation interactions: I) easy glide of dislocations; II) piled-up mechanism of dislocation groups; and III) cross slipping and intersection of forests of dislocations [96].

Stage I (laminar flow or easy glide of dislocations): At this stage, dislocations can easily glide over relatively large distances without encountering any barriers. There is hardly a discernable strain hardening effect in this stage; which subsequently implies that the dislocations might escape from the crystal at the surface. Also, there is always only one active slip system in this stage of easy glide [96].

Stage II (linear part of the flow curve): Here at stage II, the strain-hardening rate is significantly high. This implies that unlike the easy glide stage; there is more than one set of operating slip planes. This can result in a greater number of Lomer-Cottrell barriers, which

in turn leads to a set of much shorter active slip lines. The strain-hardening coefficient (the slope of the curve) at this stage is nearly independent of stress, temperature, crystal orientation and purity, thus implying that the main cause of strain hardening is the *pile-up* of dislocations. Because of *multiple slip systems* operating at the same time or *duplex slip mechanism* at this stage, the lattice irregularities can be formed, which in turn may result in the formation of the *dislocation tangles* and *dislocation cell structure* leading to regions within these dislocation clusters (in the matrix) that are almost free of dislocations; which are surrounded by regions with high dislocation density (about five times larger than the average dislocation density in the matrix). Figure 4–34 presents a schematic presentation of the dislocation tangles and cell structures. Although at this stage, due to the high dislocation interactions that are distributed very heterogeneously, it is hardly possible to have a relatively precise measurement of the dislocation densities. This is shown that over a wide range of deformed systems, the average dislocation density in stage II are correlated with resolved shear stress according to Equation 4–8:

$$\tau_y = \tau_\alpha + \alpha Gb(\rho_{dis})^{1/2} \quad \text{Equation 4-8}$$

Where τ_α is the shear stress required for the motion of a dislocation through the lattice in the absence of other dislocations; and α is a numerical constant, which varies from 0.3 to 0.6 for various FCC and BCC metals [96].

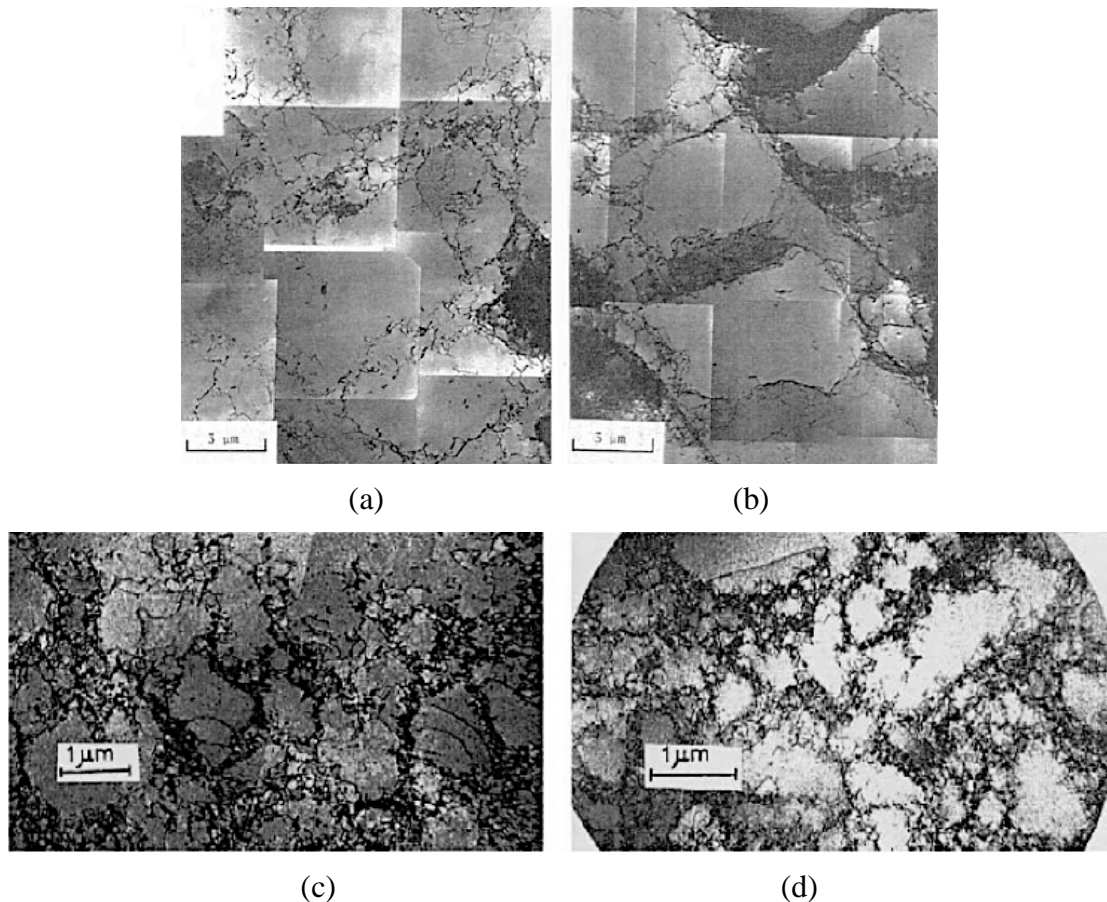


Figure 4–34 Typical electron transmission micrographs of the dislocation tangles forming during the deformation process (in the late stage I and II, shown Figure 4–33) in the FCC single crystals: (a) and (b) $\langle 111 \rangle$ aluminum specimen after compression to 59 MPa with recovery at 453K; and (c) and (d) TEM foils of copper polycrystals deformed at room temperature with the flow stress levels of (c) 28 MPa; and (d) 69 MPa [117].

Stage III (dynamical recovery): The rate of strain hardening at the final stage of deformation in an FCC single crystal is lower than that in stage II because of the higher level of stresses at the final stage of the deformation process. The interaction of dislocations with one another had been suppressed at lower level of stresses in the previous stages. One example for such dislocation interactions is *cross slip*, by which the piled up dislocations that are tangled around obstacles during stage II of deformation can escape and relieve. This can result in reduction of the internal strain field in the matrix. The flow stress at this stage is temperature dependent, suggesting that the *intersection of forests of dislocations* or *dislocation threading* occurring due to dislocation interactions and subsequent creation of sessile dislocation is the primary cause of strain-hardening [96].

4.3.4 Strengthening from Fine-Scale Precipitates

Small second-phase particles distributed in a ductile matrix are effective source of strengthening. Most of alloy systems with a decreasing solubility with temperature can be strengthened by precipitation reactions in the solid state. Precipitation hardening or age hardening [118] is a process of formation of the fine-scale strengthening precipitates from the super saturated solid solution (SSSS) matrix, which is formed immediately after the quenching of an alloy from a solid solution condition (at a temperature above the solubility limit of solute atoms in the solvent matrix) (Figure 4–35).

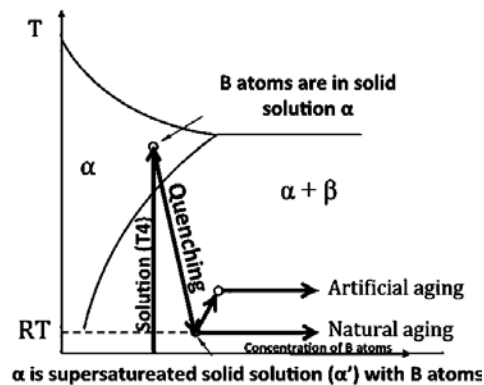


Figure 4–35 Schematic presentation of age hardening process after solution treatment between ambient and an elevated temperatures described as natural and artificial ageing, respectively.

The requirement for minimization of nucleation (or formation) energy of these fine-scale strengthening precipitates necessitates the precipitates to find the atomic match or coherency by means of adjusting themselves to find an appropriate orientation relationship with the crystallographic structure of the solvent matrix. This is especially important at the beginning of the precipitation process, leading to a decrease in the energy barrier caused by the strain field at the atomic interface between the precipitate and matrix. In the case of the Al-7xxx alloys, in which the equilibrium stable strengthening precipitates ($MgZn_2$) are of hexagonal structure, Al matrix is of FCC structure, this crystallographic orientation relationship between the precursor metastable clusters for the precipitates (i.e., GP Zones which are rich in Zn and Mg atoms with HCP structure) occurs on the closed-packed planes between the HCP and FCC structures, which are $\{0001\}$ and $\{111\}$, respectively [68].

As the ageing process progresses and the metastable precipitates such as the GP clusters grow, the coherency between the precipitates and matrix gradually decreases due to developing the strain field energy at the interface caused by the increasing mismatch between the lattice crystallography of the precipitate and matrix.

The degree of strengthening of fine-scale precipitates depends on the dispersion of strengthening precipitates within the ductile matrix. This can be expressed by their volume fraction. In addition to dispersion, the shape of strengthening precipitates is also a very important factor on their strengthening contribution to the total yield strength of the material. It has been shown that the non-spherical particles have a larger strengthening effect than the spherical precipitates [96].

There are several ways that fine scale precipitates can act as barriers to dislocations. One is where they can act as strong impenetrable, non-shearable and incoherent precipitates through which the dislocations can only “bypass” by making a sharp bend or curvature in their line, as shown in Figure 4–36 (b). This mechanism is also known as *Orowan bowing mechanism*. The other is where they can act as soft shearable and coherent precipitates through which dislocations may cut through to pass; but only at applied stress levels higher than that required for the dislocations to move through the matrix phase, as shown in Figure 4–36 (a). This mechanism is also known as *Friedel shearing mechanism*.

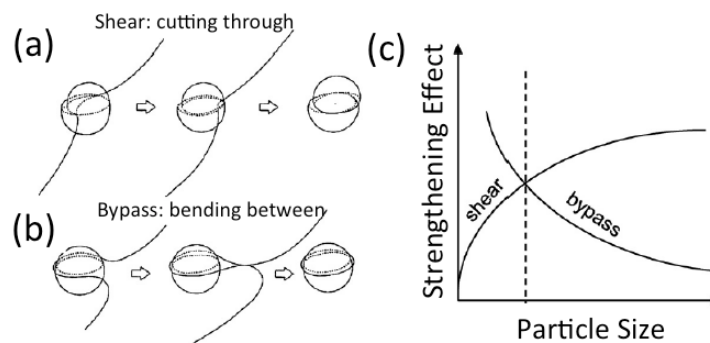


Figure 4–36 Dislocation passing precipitates by (a) shearing or cutting through the strengthening particles; or (b) bowing between them; and (c) schematic comparative presentations of strengthening effect of these two mechanisms: shearing and bypassing the strengthening particles [31].

Orowan [119] proposed a mechanism for the bending of the dislocation line around the dispersed strengthening precipitates while passing and moving through them during the deformation process. The original mechanism was proposed based on the assumption that the strengthening precipitates to be overaged, i.e., none-shearable and incoherent precipitates with matrix as shown in the illustration in Figure 4–37; wherein it is shown that a component contributing to the total yield stress is determined by the shear stress required to bow a dislocation line between two precipitates with an average radius of R that are separated by an linear inter-particle distance of λ_L , ($\lambda_L > R$, R is the dislocation curvature while passing through the particles). The Orowan shear stress is explained in Equation 4–9.

$$\tau_y = \frac{Gb}{\lambda} \quad \text{Equation 4–9}$$

Where G is the Shear modulus of the matrix and b is the Berger’s vector of the matrix.

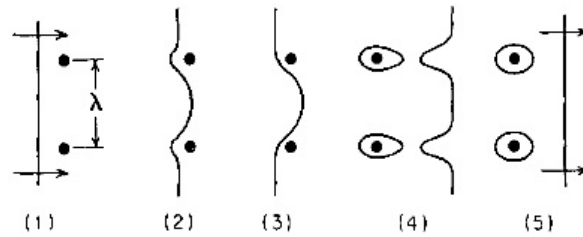


Figure 4–37 Schematic presentation of different stages of a dislocation movement between widely separated obstacles in a matrix; based on Orowan’s mechanism of dispersion hardening for non-shearable and incoherent precipitates [96].

In order to modify the basic Orowan’s theory, other researchers introduced additional estimations and assumptions to the Orowan’s basic theory of dispersion hardening. Ashby [120] applied an extra correction factor for the opposite interaction between the dislocations on the either side of the non-deformable particles and further Kocks [121] treated Orowan’s theory statistically by introducing planar and spatial spacing (λ_p and λ_v). This leads to a number of versions of Orowan-based theoretical models such as the Equation 4–10 that was developed by Ashby and Orowan [96].

$$\sigma_y = \frac{0.13Gb}{\lambda} \ln\left(\frac{r}{b}\right) \quad \text{Equation 4–10}$$

The Orowan’s bowing mechanism of dislocation movement will lead to a complex network of dislocation cells, i.e., a cellular structure of dislocation tangles (Figure 4–34). Accordingly, the dislocation cells and subsequent back-stresses lead to an increase in the total yield stress of the material. This is attributed to the necessity for retaining the continuity of material between the matrix, and relatively hard and non-deforming precipitates occurring during the deformation process.

4.3.5 A process model strengthening mechanism in the Aluminum alloys

Shercliff and Ashby [122,123] were the first researchers attempted to develop an overall “*process model*” for the age hardening process of aluminum wrought alloys. Their *process model* was a mathematical description or relationship between the process variables (such as alloy composition, and heat treatment temperature and time) and total yield strength and/or hardness of the alloy.

4.3.5.1 Shercliff and Ashby’s basic Model for Al-base wrought alloys

Shercliff and Ashby originally developed and proposed their process model for the Al-alloys. For their model, they used a *Kinetic validation test* by which the applicability of their model for a specific alloy composition in order to correlate the structural and strength properties of the material. Their *validation test* was defined based on a single kinetic equation as explained in Equation 4–11.

$$P = \frac{t}{T} \exp\left(\frac{-Q_A}{RT}\right) \quad \text{Equation 4–11}$$

Where, Q_A is the activation energy required for the volume diffusion of atoms between the coarsening precipitates; T is the isothermal ageing temperature; t is the ageing time and the *kinetic P-parameter* is a kinetic measure of the number of kinetic jumps taking place during the elapsed time (t) during the ageing process. The parameter P is essentially the same as the “*kinetic strength*” defined by Ion-Easterling-Ashby [124] for the welds samples. The value of

this kinetic parameter (P) that corresponds to the peak age condition is P_p and is a constant-value; P_p is also known as the *temperature-corrected peak-time parameter*. At the peak aged condition Equation 4–12 becomes Equation 4–12 where t_p is the time for peak age condition at any temperature, T . In Equation 4–12, the value of Q_A and P_p are obtained as constants.

$$P_p = \frac{t_p}{T} \exp\left(\frac{-Q_A}{RT}\right) \quad \text{Equation 4-12}$$

They reported that their model could successfully be presented as a first stage to assemble a process model for the ageing process of a couple of Al-alloys with simpler age hardening processes such as the binary Al-Cu (2000) series alloys and Al-Mg-Si (6000) series alloys.

The basic foundation of Shercliff and Ashby's *process model* was laid on the simple physical principles such as phase equilibrium, precipitate coarsening, and dislocation-precipitate interactions. All the components were combined to form an over all *process model*. The Shercliff and Ashby simple *process model* includes the three main contributions to the total yield strength: (1) intrinsic strength, (2) solid solution strengthening and (3) strengthening contribution due to the fine scale precipitations. Their comprehensive strengthening model can be outlined briefly by the following equation:

$$\sigma_y = \sigma_\alpha + \sigma_{ss} + \sigma_{ppt} \quad \text{Equation 4-13}$$

Where the σ_α^* is the intrinsic friction stress of the pure aluminum; and σ_{ss} and σ_{ppt} are the contributions to the yield stress due to solid solution and precipitates, respectively.

The solid solution contribution of their process model to the total yield stress is calculated based on the *Mott and Labusch theory* [104,105], which was discussed in earlier in this chapter in Section 4.3.1; wherein, the solute elements are considered to be as the weak pinning obstacles and the collective strengthening effect of solute atoms in the plane of dislocations can be calculated according Equation 4–3.

In their model, Shercliff and Ashby [122,123] considered the contribution of the precipitates to the yield stress (σ_{ppt}) to be harmonic mean[†] of individual contribution of shearing and bypassing mechanisms of dislocations while they cut through or bend around the strengthening particles. Figure 4–38 presents a schematic presentation of the Shercliff and Ashby strengthening model, wherein the superimposition of the various strengthening contributions to the intrinsic yield stress of the pure aluminum for the Al-base wrought (age-harden able) alloys is presented. In Figure 4–38, the net effect of precipitation of intermetallic phases on the matrix on the total yield strength is a combination of both strengthening mechanisms from dislocation movement: (1) the *shearing mechanism* of the small, coherent and closely spaced particles by the passing dislocations ("*Friedel effect*") and (2) the *bypassing mechanism* of the larger, fully or semi coherent particles that are more widely spaced ("*Orowan bowing mechanism*"). In Figure 4–38, apart from the *precipitation hardening* effect, there exist two other contributors to the total yield stress of the material:

* In the calibration procedure, Shercliff and Ashby used a value for the intrinsic strength σ_α of aluminum (~53 MPa as the measured yield strength of pure aluminum) from background literature. They argued that this value of the intrinsic strength of the pure aluminum can also be obtained by the extrapolation of the as-quenched hardness for binary Al-Cu alloys containing 2, 3, 3.5, 4 and 4.5 wt.% copper to zero concentration that are given by the same result.

† $\sigma_{ppt} = \left\{ \frac{1}{\sigma_{Shear}} + \frac{1}{\sigma_{Bypass}} \right\}^{-1}$

one is the strengthening effect due to the alloying elements presence the Al-matrix as solid solution (which has a decaying effect as the precipitates are formed and grow), and the other is the intrinsic strength of the Al-matrix (in addition to any structural defects such as dislocations that are created by the pre-deformation processes such as the cold work applied after the solution treatment and before the age hardening process [122]).

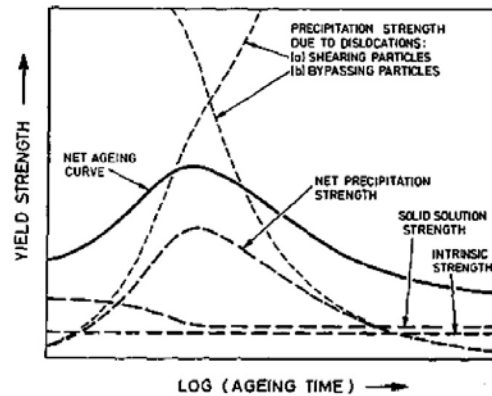


Figure 4-38 The schematic presentation of the relative contributions of various factors to the intrinsic yield stress of the material. The factors are such as solid solution strengthening, precipitation hardening due to shearable and non-shearable particles [122].

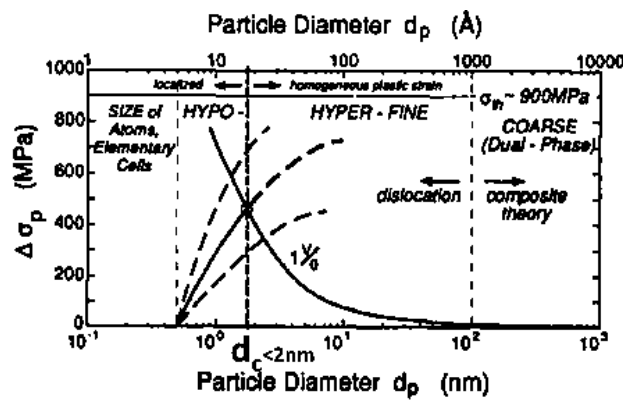
Shercliffe and Ashby [122] state, “This was carried out using straightforward principles while the application and the calibration of the model to the give alloys were not. The model gives a good description of some 2000 and 6000 series alloys, but it was not yet comprehensive enough to describe the more complicated 7000 series alloys in which the precipitation sequence involves many stages; and the metastable precipitate forms at slower coarsening rate at such low temperatures, for which further work is necessary”. The classical Shercliff and Ashby process-model for strengthening mechanism of the Al-base wrought alloys could give a good description of some Al-2xxx and Al-6xxx series alloys, but their model was not able to describe the more complicated Al-7xxx series alloys. This is mainly because, as Shercliff and Ashby along with other researchers argued, the precipitation sequence in the Al-Zn-Mg-(Cu) alloys is a much more complicated that that of other Al-based alloys with several stages wherein the precipitation kinetic requires a much more comprehensive process model [122]. However, the important point about Shercliff and Ashby strengthening overall approach is its ability in capturing all the contributions to the total yield strength of an aged alloy sample. Their proposed process model could also be adapted to any age-hardening alloy system and more importantly, could be elaborated to include new or more sophisticated treatments of its components [122].

4.3.5.2 Hornbogen and Starke process Model for Al-base wrought alloys

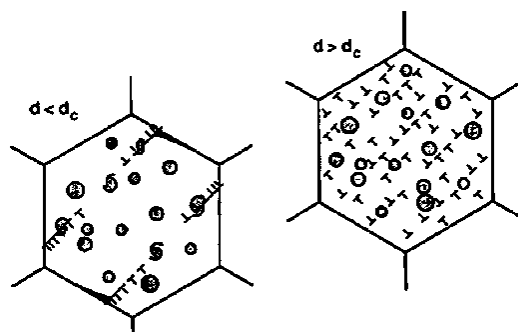
Hornbogen and Starke Jr [125] later proposed a theatrically assisted model for the design of the high strength Al-alloys by modifying the classical Shercliff and Ashby model [122]. Their model includes the two additional strengthening effects: (1) the strengthening contribution due to the grain boundaries and (2) the strengthening contribution due to the interaction between one and two-dimensional structural defects such as dislocations (including the size and volume fraction of the fine scale strengthening particles). The comprehensive strengthening model proposed by Hornbogen and Starke is shown in the Equation 4-14:

$$\sigma_y = \sigma_\alpha + \sigma_{ss} + \sqrt{\left\{ (\sigma_{ppt})^2 + (\sigma_{dis})^2 \right\}} + \left(\frac{k}{\sqrt{D_{gs}}} \right) \tag{Equation 4-14}$$

Where σ_α is the yield stress of pure (99.99) Al (that can have a value from 16 MPa at ambient temperature to 60 MPa at (-200)°C [126]); σ_{ss} is the solid solution effect due to the solid solution atom and the coherent or soft particles; σ_{dis} is the strengthening contribution due to the dislocations; σ_{ppt} is the strengthening contribution due to the hard particles; and the final term in the above equation accounts for the strengthening effect due to the grain boundary and the sub-boundaries to the total yield stress of the alloy in which the k is the *locking parameter* similar to that of the Hall-Petch equation (Equation 4-5 and Equation 4-7) and D_{gs} is the average grain size of the alloy microstructure. The importance of Hornbogen and Starke model [125] is in the clear definition of hard and soft particles in order to distinguish between the shearing and bypassing mechanisms for strengthening as shown in the Figure 4-39. Moreover, The critical particle size is an important microstructural parameter of high strength Al-alloys that they are dealt with in their model (Table 4-7).



(a)



(b)

Figure 4-39 (a) Definition of the critical particle size (d_c) for the transition from shearing to bypassing in aluminum alloys with 1% volume fraction of particles as per below table; (b) schematic presentation of consequent effect of particle size on the strain localization [125].

Table 4-7 Examples for hard and soft obstacles in terms of how they can resist the dislocation motion in aluminum alloys [125].

Hard Obstacles (H)	Soft Obstacles (S)
Particles $d > d_c$ (Hyper-fine particles)	Particles $d < d_c$ (Hypo-fine particles)
Particles, Pores, Sessile dislocations	Solid solution atoms, vacancies, short range order, clusters antiphase domain boundaries (APB)

4.3.5.3 Attempts to develop a process model to 7xxx series alloys

The fact that the majority of the existing models cannot predict the total yield strengths of ternary and higher order alloying systems with various compositions is mainly attributed to the complication of the precipitation sequence and composition of the strengthening precipitates in such multiple alloying systems such as Al-Zn-Mg-Cu alloys (7xxx family class). That is mainly because in such multiple systems (the Al-7xxx alloys), the composition of the strengthening precipitates varies significantly with the actual composition of the alloy [127].

The concept of modeling yield strength in the heat treatable Al-Zn-Mg-Cu aluminum wrought alloys is important because the total yield strength is a critical parameter in several commercial applications of these high strength alloys. Further, the precipitation strengthening in the Al-Zn-Mg-Cu alloy family has by far the strongest contribution to their yield strength. The main strengthening precipitates that has been proved to dominate the age-hardening process of most commercial 7xxx alloys is a combination of the η' and η -phases, forming during a sequential transition from supersaturated solid solution (SSSS) \rightarrow Vacancy-Rich Clusters (VRC) (GP zones) \rightarrow metastable η' -phase \rightarrow stable η -phase [66,67,128]. The η' - and/or η -phases are quaternary phases containing Al, Zn, Mg and Cu elements. They are considered to have a structure that is based on a substitutional solid solution of $MgZn_2$ with Al, Cu and Mg elements by substituting the Zn atoms ($Mg(Zn,Al,Mg)_2$ or $Mg(Zn_2,AlMg)$) [129]. The compositions of the η' and η phases is highly dependent on the nature of heat treatment and alloy composition [127].

4.3.5.4 Deschamps-Brechet integrated strengthening model for Al-7xxx alloys

Over the past recent 15 years, the published literature in the modeling field of the yield strength for the Al based alloys provide a variety of modeling approaches, e.g. thermo-physical process models with complex and adaptive numeric analysis to derive complex relations among thermo-mechanical treatment, ageing treatment, microstructural changes and mechanical properties.

Recently, in an attempt to improve the Shercliff and Ashby model with a more descriptive approach for the Al-Zn-Mg-Cu (Al-7xxx) alloys, Deschamps et al [130,131], initially developed a kinetic model to incorporate the competition between the homogeneous nucleation of precipitates and heterogeneous nucleation on dislocations. Subsequently, a comprehensive model, for the Al-Zn-Mg-(Cu) alloy family, was developed to predict the total yield strength consisting of four main strengthening components: (1) intrinsic or friction stress, (2) precipitation hardening, (3) dislocation hardening and (4) solute hardening. Equation 4-15 present the comprehensive strengthening model analytically developed and proposed by Deschamps and Brechet [130,131].

$$\sigma_{gb} = \sigma_{\alpha} + \sigma_{ss} + \sqrt{\{(\sigma_{ppt})^2 + (\sigma_{dis})^2\}} \quad \text{Equation 4-15}$$

Where σ_{α} is the friction stress* in aluminum (that they found it to be $\sigma_{\alpha} \sim 10$ MPa as an adjustable parameter); and σ_{ss} is the solid solution strengthening contribution, σ_{dis} is the dislocation strengthening contributions and σ_{ppt} is the precipitation strain hardening effect to the yield strength of the material, respectively. The solid solution contribution to the yield stress (σ_{ss}) in Equation 4-15 is calculated according to the Mott and Labusch [105,106] equation as shown in Equation 4-3; where the A_2 in the equation is an adjustable constant to the yield stress of the material in solid solution ($A_2=840$ MPa for Al-Mg-Zn alloys) and C_i is the residual amount of solid solution elements remaining in the primary Al-matrix material after the precipitation in atomic percent (at.%).

The dislocation contribution to the yield stress (σ_{dis}) in Equation 4-15 is shown in Equation 4-16.

$$\sigma_{dis} = M \alpha G b \sqrt{\rho_{dis}} \quad \text{Equation 4-16}$$

Where M is the Taylor factor (that is also known as the orientation/texture factor); G and b are the shear modulus (~ 26 GPa for aluminum [125,148]) and the Berger's Vector ($\sim 2.84 \text{ \AA}$ [125,148]) of the Al-matrix material; and α is a constant (~ 0.27) that is adjusted for the material; and ρ_{dis} is the dislocation density in the Al-matrix. The dislocation strengthening contribution (σ_{dis}) to the yield stress of the Al-Zn-Mg-(Cu) alloy is mainly to incorporate the strain hardening component of the strengthening mechanism in the Al-7xxx wrought products; this may arise from the pre-deformation prior to ageing process in the Al-Zn-Mg-(Cu) alloys.

Finally, for the calculation of the precipitation strengthening contribution (σ_{ppt}) to the yield strength in Equation 4-15, Deschamps and Bre chet [130,131] considered the Gaussian distribution for the precipitate size in the matrix. This is important because, by using the particle size distribution, they eliminated the effect of particle morphology from their model. Thus, they used various expressions for the precipitation contribution (σ_{ppt}) to the yield strength that are analytically derived, separately, based on two different statistical approaches: (1) the *Friedel* and (2) *Kocks* statistics. They also used both of statistical bases with the two distinct strengthening mechanisms: (a) the *shearing* and (b) *bypassing* of dislocations moving through the precipitates in the matrix during [121]. However, it is widely accepted that in the Al-Zn-Mg-(Cu) (7xxx) alloy system, almost all the dislocation movement through the precipitates in the Al matrix is by the *bypassing* mode [132,133]. The precipitation contribution (σ_{ppt}) to the yield stress of the Al-7xxx alloys that are developed in the Deschamps and Bre chet model [130,131] for the *bypassing Orowan mechanism* are

* The friction stress of aluminum (σ_{α}) and other adjustable constant and parameters such as K (the coefficient of the solid solution strengthening effect to the yield stress) and M (Taylor factor or orientation factor) in the Deschamps-Bre chet model are adjustable parameters that is obtained based on the results of a series of experiments on the Al-Zn-Mg-(Cu) alloys which have been carried out and published by themselves separately prior to development of their integrated model.

described by Equation 4–17 and Equation 4–18 using the Friedel and Kocks statistics, respectively [130, 131, 134].

$$\sigma_{ppt} = 0.7Mgb \left\{ \frac{2\sqrt{f_v}}{\left(D_p \left[\frac{\pi}{4} \right] \right)} \right\} \quad \text{Equation 4–17}$$

$$\sigma_{ppt} = 0.6Mgb \left\{ \frac{2\sqrt{f_v}}{\left(D_p \left[\frac{\pi}{4} \right] \right)} \right\} \quad \text{Equation 4–18}$$

It is noteworthy that both expressions give the same dependency in f_v (precipitates volume fraction) and D_p (average precipitate diameter or average equivalent circular diameter of particles). The Kocks statistics in Equation 4–18 gives the usual calculation of the Orowan stress [131] and the Friedel statistics in Equation 4–17 gives good results for the completely shearing mode, and a close prediction for the Orowan stress by the completely bypassing mode. The origin of the difference between the two expressions is the constant multiplier, which arises from the extra 15% length factor introduced by Kocks for the average particle spacing. In the strengthening model, Deschamps and Bre chet [130,131] use the Kocks' statistics for their calculation of particle spacing along the dislocation line. This is carried out based on a number of assumptions such as the Gaussian distribution of circular particle size [121]. For the bypassing mechanism, the inter-particle spacing is described by Equation 4–19; wherein it is assumed by Kock [121,135] that the average interparticle spacing (λ_K) along the dislocation line is approximately 15% larger than the average precipitate spacing in the gliding plane:

$$\lambda_K = 1.15 \left(\sqrt{\frac{2\pi}{3f_v}} \right) \cdot \left(\frac{2D_p}{\pi} \right) \quad \text{Equation 4–19}$$

Where f_v is the volume fraction of the precipitates and D_p is the average particle diameter or the circular particle size.

It is noteworthy that in the Deschamps and Breâchet physical strengthening model, they validated their model and found the best fitted prediction for the structure-property relationships of the Al-Zn-Mg-(Cu) wrought alloys. This was carried out based on their own extensive experimental studies on the Al-Zn-Mg-(Cu) alloys [130]; by which they adjusted the constant values in the analytical models (such as $\alpha \sim 0.27$, $A_2 \sim 840$ MPa, $\sigma_\alpha \sim 10$ MPa and $M \sim 2$). Some of these values are not consistent with the literature; for instance, they used the relatively low Taylor value ($M \sim 2$) instead of the theoretical value of 3.1 proposed for a FCC crystal structure [96] (which was explained earlier in the Section 4.3.2 of this Chapter). For the low M value of 2 instead of theoretical value of 3.1, they argued that during the deformation process at low strain (that occurs at around the proof strain of 0.02%), the grains are not fully constrained so that the homogeneous stress hypothesis is not applicable [131]. Accordingly, the random alignment of grains that is signified by the Taylor factor in the polycrystalline material is lower ($M=2$) than the theoretical value of 3 (for a FCC system with at least 5 active slip system). Furthermore, Guyot and Cottignies [136] also used a Taylor factor of $M=2$.

4.3.5.5 Starink-Wang strengthening model for the Al-Zn-Mg-Cu alloys

Later, Starink and Wang [137] proposed another strengthening model based on physical principles for prediction of the total yield strength of the multi-component Al-Zn-Mg-Cu alloys. The Starink and Wang model [137] has more in-line with the fundamental *thermo-physical model* by Shercliff and Ashby [122,123] than that of *integrated model* developed with Deschamps and Breâchet [130,131]. Starink and Wang [137] used the basic framework proposed in the Shercliff and Ashby model and incorporated the compositional change of the precipitates due to alloy composition variations into their model for the over-aged condition of the precipitates. Starink and Wang [137] offered a *strengthening model* which included, all the precipitation kinetic parameters (such as alloy composition, and the heat treatment temperature and time) as well as the alloy yield strength or hardness (such as dislocation mechanics); whereas Deschamps and Breâchet [130,131] *integrated model* consisted of two independently separate models: one for precipitation kinetic and the other for the structural hardening of yield strength. Some of the salient features in the Starink and Wang model are the influence of *super-saturation* on precipitation rates and influence of *volume fraction* of precipitates on the coarsening rates and the average size and morphology of the precipitates (which can deviate from idealized situation of spherical shape). The Starink and Wang model was also developed mainly for the over aged condition of the 7xxx alloys, wherein the precipitation hardening is the main strengthening component; thereby, the *by-passing mechanism* was assumed as the sole method of dislocation movement in the matrix.

Dissimilar to the models proposed by Shercliff-Ashby and Deschamps-Brechet (wherein the main strengthening components were principal stresses), the Starink-Wang model allows for four contributions to the *critical resolved shear stress (CRSS)*: (1) the intrinsic CRSS (τ_α), (2) the solid solution contribution (τ_{ss}), (3) the contribution due to the grain boundaries (σ_{gb}) and (4) the contribution due to precipitation strengthening (τ_{ppt}). Prior to explaining the model's components, it is noteworthy that Starink and Wang assumed that the strain hardening effect includes both the strengthening contributions due to dislocation (τ_{dis}) and precipitation (τ_{ppt}). They argued that based on the fact that the magnitude of the resistance to the dislocation movement offered individually by the dislocations and precipitates in the matrix are similar and hence, reasonable to apply a superposition rule by considering the geometric mean of the

two*. Further, based on the phenomenological superposition approximation for obstacles of similar strengths, they assumed that the strengthening contributions due to precipitation include the dislocation strengthening effect as well. Therefore, they did not consider a separate expression for the strengthening effect due to dislocation force in their process-strengthening model.

Another important feature of the Starink and Wang model is the crystallographic texture and recrystallization† parameter. This is an important feature and factor in the design of the 7xxx alloys and is included in their model by means of M factors. Dissimilar to Shercliff-Ashby and Deschamps-Brechet models, instead of principal stresses, Starink and Wang considered the yield strength to be generally related to the $CRSS$ as shown in Equation 4–20:

$$\sigma_y = \sigma_{gb} + M \cdot (\tau_\alpha + \tau_{ss} + \tau_{ppt}) \quad \text{Equation 4–20}$$

Where σ_{gb} is the strengthening effect due to the presence of (sub-) grain boundaries. M is the Taylor factor or orientation factor which depends on texture and the orientation of the uniaxial tensile axis with respect to the main axes of the worked specimen; τ_α is the intrinsic strengthening contributions to the *critical resolved shear stress* of the pure aluminum (~7 MPa for the 1060 aluminum in the fully annealed condition [137]); and τ_{ss} and τ_{ppt} are the strengthening contributions to the *critical resolved shear stress (CRSS)* of the Al-Zn-Mg-(Cu) alloy that are introduced due to the solid solution and precipitation hardening effects, respectively.

In the Starink and Wang model that is mainly designed for the Al-Zn-Mg-Cu wrought alloys, the effect of recrystallization is an important variable parameter because it has a marked contribution on the entire model.

In the Starink and Wang model that is specifically designed and developed for the Al-Zn-Mg-Cu alloys, the grain boundary strengthening contribution (σ_{gb}) is considered to be small as compared to that of the strain hardening effect (i.e., the precipitation strengthening or $M\tau_{ppt}$) and this is expressed as shown in Equation 4–21 [138,139].

$$\sigma_{gb} = \alpha_2 G b \left[\left(1 - f_{ReX}\right) \left(\frac{1}{\delta}\right) + f_{ReX} \left(\frac{1}{D_{gs}}\right) \right] \quad \text{Equation 4–21}$$

Where G is the shear modulus (~26GPa for aluminum [125,148]); b is the Burgers vector (~2.84Å [125,148]), f_{ReX} is the volume or area fraction of the recrystallized portion of the microstructure; δ and D_{gs} are the sub-grain (or cell) and the grain size in the respective unrecrystallised and recrystallized portions of the microstructure of the material; α_2 is a

* $\tau_{ppt\&d} = \{(\tau_{dis})^2 + (\tau_{ppt})^2\}^{1/2}$

† Most commercial 7xxx alloys can be categorized in two groups depending on the type of element that is controlling the grain structure: Zr- or Cr-containing alloys. The former (Zr-bearing) alloys can form the β phase (Al_3Zr ; L_{12} structure) particles, whilst the latter (Cr-containing) alloys generally contain Al_7Cr particles. These particles (that control the grain structure) are generally called dispersoids in aluminum metallurgy. Typically, these dispersoids influence the recrystallization and quench sensitivity of the 7xxx alloys. Also, these dispersoids can influence the texture and the related anisotropy because of their effect on recrystallization temperatures.

constant value of 2 [140]. Based on the TEM work on hot rolled 7xxx alloys with Zr additions [141], they use a value of about $\delta \sim 1.5 \mu\text{m}$ for the unrecrystallized portion of microstructure in their strengthening model.

In their model, Starink and Wang considered the Taylor factor (M) as a highly dependent parameter on the texture and orientation of the tensile axis with respect to the texture direction such as rolling direction. Several models are available to determine the texture dependency of the M . The lower boundary solution for orientation dependency of the microstructure (M) is obtained using the Sachs model [142], wherein it is assumed that there is only one active slip system operating during the deformation process in the polycrystalline material. On the upper boundary, the solution is obtained using the Taylor model [143], which assumes at least five active slip systems operating during the deformation process in the polycrystalline material. These theoretical boundary conditions for the texture-free FCC metals predict a value of $M_T = 3.07$ with the Taylor theoretical model; whereas with the Sachs theory, the classical model predicts a value of $M_S = 2.24$ for a texture-free FCC metal. However, in an attempt to find a realistic model for polycrystals, Hutchinson [144] indicated that on average there are about 3.5 slip systems actively operating during the deformation process of polycrystalline material. Further, Hutchinson's self-consistent model predicts a value of $M_H \approx 2.6$ for a texture-free FCC metal with equiaxed grains [145].

In their strengthening model, Starink and Wang [137] developed an analytical expression in order to estimate a value for the orientation factor ($M(\varphi, \phi)$) as a function of orientation angles (Figure 4–40) and the recrystallization fraction (f_{ReX}) of the microstructure without measuring the textures. This is important because, it allows the incorporation of recrystallization into the strengthening model.

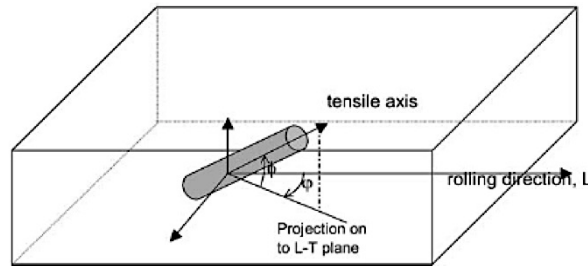


Figure 4–40 Definition of the orientational angles that are determined with respect to the rolling direction (L) and the uniaxial tensile axis. The angle ϕ is defined as the angle between the uniaxial tensile axis and its projection on the longitudinal-transverse (L-T) plane; and the angle φ is defined mainly on the L-T plane between the projection of the uniaxial tensile axis and the texture direction that are the working or rolling direction [137].

In the Equation 4–22, the relationship between the M -factor and the recrystallization is expressed that is used in the Starink and Wang strengthening model.

$$M(\varphi, \phi) = (1 - f_{ReX})M_{roll}(\varphi, \phi) + f_{ReX}M_{ReX}(\varphi, \phi) \quad \text{Equation 4–22}$$

Where M_{roll} is the M factor measured in the rolling direction or that account for the unrecrystallized portion of the microstructure, which is rolled (i.e., the rolling texture); and M_{ReX} represents the M factor that account for the recrystallization portion of the microstructure (i.e., recrystallized texture). Based on the EBSD work on eight Zr-containing and four Cr-containing alloys (Figure 4–41) coupled with their yield strength database, Starink and Wang calibrated the main part of the strengthening model. This results in determination of the $M(\varphi = 0^\circ, \phi = 0^\circ)$ and recrystallization fractions which accordingly lead to determining the $M_{roll}(\varphi = 0^\circ, \phi = 0^\circ) \approx 2.8$ and $M_{ReX}(\varphi = 0^\circ, \phi = 0^\circ) \approx 2.55$.

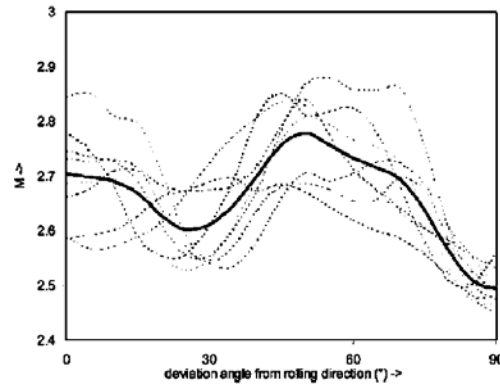


Figure 4–41 Direction dependency of orientational factor (M) for the eight (8) Zr-containing alloys. The solid black line is a presentation of average M value for all the eight alloys; whereas the dotted lines presents the average M value for the cases with three and four active slip systems [137].

For the solid solution contribution (τ_{ss}) of the strengthening model, Starink and Wang used Equation 4–3 based on the Mott and Labusch [104,105] solid solution strengthening theory [106]; where, similar to the Deschamps and Beachet model, the C_i is the linear summation of the concentration of the residual solid solution alloying element in at% that are remaining in the Al-matrix after the peak ageing process completes; and A_2 is a constant that is determined using the data by Dorward [146] for the Al–6.5Zn–2.1Mg–2.2Cu–0.1Zr alloy in an overly aged condition for a very long aging time. This allows the coefficient for solution strengthening contribution (A_2) to be fixed by considering infinite limit of time; at which extent the yield strength of this alloy reach an asymptotic value of 130 MPa. This result in a value of $A_2=924$ MPa.

In Equation 4–20, Starnik and Wang assumed a plate-like morphology of the precipitates oriented parallel to the $\{111\}_{Al}$ plane of the matrix. This assumption results in a certain quantified value of τ_{ppt} in their model, which was evaluated based on the extensive study on various precipitate morphology and crystallographic relationship with the Al matrix on the strength of the alloy by Zhu and Starke Jr [147].

Zhu and Starke Jr [147] presented a variety of equation to evaluate τ_{ppt} in Equation 4–20; they considered two morphologies of the strengthening precipitates, namely, circular cross-section (spherical and cylindrical rods) and plate like (disc shaped). Equation 4–23 presents the general expression to evaluate τ_{ppt} for a circular cross-section morphology of the precipitates; and Equation 4–24 and Equation 4–25 are modifications of the Equation 4–23 for Spherical and rod morphologies of the precipitates, respectively by converting the λ_{cc} to volume fraction (f_v).

$$\tau_{ppt} = \frac{0.82Gb}{2\pi\lambda_{cc}} \left\{ 1 + 0.83 \left(\frac{D_p}{\lambda_{cc}} \right) + 1.91 \left(\frac{D_p}{\lambda_{cc}} \right)^2 \right\} \cdot \ln \left(\frac{D_p}{r_0} \right) \quad \text{Equation 4–23}$$

$$\tau_{ppt} = \left[\frac{(0.18)Gb}{D_p} \right] \left\{ (f_v)^{(1/2)} + (0.9)f_v + (2.25)(f_v)^{(3/2)} \right\} \cdot \ln \left[\frac{(0.79)D_p}{r_0} \right] \quad \text{(Sphere) Equation 4–24}$$

$$\tau_{ppt} = \left[\frac{(0.15)Gb}{D_p} \right] \left\{ (f_v)^{1/2} + (1.84)f_v + (1.84)(f_v)^{3/2} \right\} \cdot \ln \left[\frac{(1.316)D_p}{r_0} \right] \quad (\text{Rod}) \quad \text{Equation 4-25}$$

Equation 4–26 and Equation 4–27 presents the expressions to evaluate τ_{ppt} for disc or plate-like precipitates that are parallel to the {111}Al and {100}Al planes of the Al matrix, respectively.

$$\tau_{Sphere} = \left[\frac{(0.21)Gb}{D_p} \right] \left[(f_v)^{1/2} + (1.21)f_v + (0.36)(f_v)^{3/2} \right] \cdot \ln \left[\frac{(0.1)\lambda_{cc}}{r_0} \right] \quad \{111\}_{Al} \quad \text{Equation 4-26}$$

$$\tau_{Sphere} = \left[\frac{(0.225)Gb}{D_p} \right] \left[(f_v)^{1/2} + (1.29)f_v + (0.42)(f_v)^{3/2} \right] \cdot \ln \left[\frac{(0.1)\lambda_{cc}}{r_0} \right] \quad \{100\}_{Al} \quad \text{Equation 4-27}$$

In Equation 4–23 to Equation 4–27, G is the shear modulus (~ 26 GPa for aluminum [125,148]), and b is the Berger's Vector ($\sim 2.84\text{\AA}$ [125,148]) of the aluminum matrix; D_p is the average precipitate diameter; λ_{cc} is the average inter particle spacing (center to center distance) between the strengthening precipitates; f_v is the average volume fraction of the precipitates; and r_0 is the inner cut-off radius or the dislocation core width used for the calculation of the dislocation line tension that is also known as the dislocation core radius and is considered to be in an approximate range of two times the size of the Berger's vector ($\sim 6\text{\AA}$) [148].

4.3.5.6 Dixit-Mishra-Sankaran Model

In an approach, similar to Starink and Wang [137], Dixit, Mishra and Sankaran [149] assembled a new *strengthening model* for the yield strengths of the Al-Zn-Mg-Cu alloys; wherein instead of principal stresses, the strengthening components of their *assembled model* are the *critical resolved shear stress* (CRSS) of the grains in the Al-7xxx alloys. Dixit et al. calibrated or examined their *assembled model* specifically for the two alloys of the 7xxx series, namely, Al-7050 and Al-7055 in an overaged T7 condition.

The main components of the Dixit et al model are outlined in the Equation 4–28.

$$\sigma_y = \sigma_{gb} + M \left\{ \sqrt{(\tau_{ss})^2 + (\tau_{dis})^2 + (\tau_{ppt})^2 + (\tau_{sf})^2 + (\tau_{Mod})^2} \right\} \quad \text{Equation 4-28}$$

Where σ_{gb} is the strengthening due to the presence of grain boundaries. M is the Taylor or orientation factor that is considered to be around $M \sim 3$ in Equation 4–28. τ_{ss} is the strengthening contributions due to solid solution effect and τ_{dis} is that due to the dislocation strain hardening effects. Also, τ_{ppt} is the precipitation strain hardening contribution to the CRSS of the alloy due to the precipitation particles that are considered to have a rod-shape morphology. In Equation 4–28, two new contributions were introduced; τ_{sf} and τ_{mod} for the excessive strengthening contributions that are caused due to the structural defects such as stacking faults and modulus difference (between the precipitates and the Al-matrix), respectively, which are formed during the deformation process.

The strengthening effect of grain boundaries (σ_{gb}) in Equation 4–28 is described by a Hall-Petch relationship and expressed in Equation 4–5; where σ_a is the yield strength of the pure aluminum at infinite grain size (~16 MPa) [125]; k_i is the Hall-Petch constant, which is about $0.065\text{MPa}\cdot\text{m}^{-1/2}$ for pure aluminum [150]; D_{gs} is the average grain size, which Dixit, Mishra and Sankaran considered it to be of $1.5\ \mu\text{m}$ from Starink and Wang work [137, 149]. In Equation 4–28, τ_{ss} is expressed by the Mott and Labusch [104,105] theory according to Equation 4–3; where C_i is the linear summation of the initial alloying elements concentration in the alloy in weight percent (wt.%) and A_2 is a constant that is calibrated for each individual alloying element in the Dixit, Mishra and Sankaran model. The calibration for the A_2 values for each alloying element was carried out by means of the data extracted from the plot containing the increase in the yield strength as a function of each solute element concentration, respectively [151,152]. The values of A_2 for each alloying element in Dixit, Mishra and Sankaran Model are as following: $A_{Mg}=20.481$, $A_{Cu}=12.431$, $A_{Zn}=3.085$; by which the total solid solution contribution of the alloying elements are calculated according to a linear summation equation expressed in Equation 4–29.

$$\tau_{ss} = \tau_{Zn} + \tau_{Mg} + \tau_{Cu} = A_{Zn}(C_{Zn})^{2/3} + A_{Mg}(C_{Mg})^{2/3} + A_{Cu}(C_{Cu})^{2/3} \quad \text{Equation 4-29}$$

For the precipitation strain hardening component of their assembled model, Dixit et al selected the effect of the rod shape strengthening particles based on the elaborated work of Kelly [153]. In the following, the theoretical equations that are derived by Kelly for the dispersion hardening due to different particle morphologies such as spherical shape, rod-like, and disc-like particles are, respectively, presented in the Equation 4–30, Equation 4–31 and Equation 4–32.

$$\tau_{Sphere} = \left[\frac{\frac{0.85Gb}{2\pi(1-\nu)^{1/2}}}{\left(\frac{D_p}{\pi/4}\right)\left(\sqrt{\left(\frac{\pi}{6f_v}\right)} - \sqrt{\left(\frac{2}{3}\right)}\right)} \right] \cdot \ln \left[\frac{\left(\sqrt{\left(\frac{2}{3}\right)}\right)\left(\frac{D_p}{\pi/4}\right)}{r_0} \right] \quad \text{(Sphere) Equation 4-30}$$

$$\tau_{Rod} = \left[\frac{\frac{0.85Gb}{2\pi\sqrt{1-\nu}}}{\sqrt{3}\left\{\sqrt[3]{\left(\frac{2C}{3}\right)}\right\}\left(\frac{D_p}{\pi/4}\right)\left\{\left(\sqrt{\left(\frac{\pi}{6f_v}\right)} - \sqrt{\left(\frac{2}{3}\right)}\right)\right\}} \right] \cdot \ln \left[\frac{\sqrt{2}\left\{\sqrt[3]{\left(\frac{2C}{3}\right)}\right\}\left(\frac{D_p}{\pi/4}\right)}{r_0} \right] \quad \text{(Rod) Equation 4-31}$$

$$\tau_{Plate} = \left[\frac{\left(\frac{0.85Gb}{2\pi(1-\nu)^{1/2}}\right)\left(\sqrt{(Cf_v)} + \left(\frac{2}{\pi} - \frac{\pi}{2C}\right)f_v C\right)}{\left(\frac{D_p}{\pi/4}\right)\left(1 - \left[\frac{\pi}{(2C)}\right]\left(\sqrt{(Cf_v)} + \left(\frac{2}{\pi} - \frac{\pi}{2C}\right)f_v C\right)\right)} \right] \cdot \ln \left[\frac{2\left(\frac{D_p}{\pi/4}\right)}{\pi r_0} \right] \quad \text{(Disc) Equation 4-32}$$

Where D_p is the planar diameter of the strengthening particles; and r_o is the dislocation core distance which is approximately about $\sim 6\text{\AA}$ [148]. The parameter C is the diameter to length ratio in rods precipitates (Equation 4–31) and the diameter to thickness ratio in discs or plate precipitates calculations (Equation 4–32) [153,154]; where G and b are the shear modulus, and the Berger's Vector, respectively, of the aluminum matrix; and ν is the Poisson's ratio; the above equations for the sphere, and rod are simplified in the following Equation 4–33, and Equation 4–34, respectively.

$$\tau_{Sphere} = \left[\frac{(0.206)Gb}{D_p \left(\frac{0.72}{\sqrt{f_v}} - 0.816 \right)} \right] \cdot \ln \left[\frac{(1.04) \cdot D_p}{r_o} \right] \quad \text{(Sphere) Equation 4-33}$$

$$\tau_{Rod} = \left[\frac{(0.12)Gb}{D_p \left(\frac{0.72}{\sqrt{f_v}} - 0.816 \right)} \right] \cdot \ln \left[\frac{(1.09) \cdot D_p}{r_o} \right] \quad \text{(Rod) Equation 4-34}$$

The other important strengthening component in the Dixit et al model is the *CRSS* strengthening contribution to the yield stress of the alloys due to dislocation interactions which is described by the Equation 4–35:

$$\tau_{dis} = \left(\frac{BGb}{\lambda} \right) \quad \text{Equation 4-35}$$

Where, B is the constant value of 0.2 for FCC material; G is shear modulus (26 GPa) for aluminum; b is the Berger's vector (2.84 Å) of the aluminum. L is the average inter-particle spacing. Here, in the Dixit et al, the average inter-particle spacing is calculated from the following Equation 4–36 that is derived by the Martin [155]:

$$\lambda = \left(\frac{D_p}{2} \right) \left\{ \sqrt{\left(\frac{2\pi}{3f_v} \right)} + \sqrt{\left(\frac{8}{3} \right)} \right\} \quad \text{Equation 4-36}$$

Where D_p and f_{Vol} are the diameter size and the volume fraction of the strengthening particle.

A summary of the three main strengthening models applicable for the Al 7xxx wrought alloys is summarized in Table 4–8.

Table 4–8 A summary of the strengthening models applicable for the Al-7xxx wrought alloys

Model		σ_{gb}	$\sigma_{\alpha}/\tau_{\alpha}$	M	σ_{ss} / τ_{ss}		σ_d/τ_d	σ_{ppt}/τ_{ppt}	
					Solid Solution			Dislocation G=26 GPa	Precipitation
Author	Designation	Grain Boundary	MPa	Taylor	$A_2 \cdot (C_i)^{(2/3)}$		G=26 GPa		Shape
					Const. (MPa)	σ_{ss} / τ_{ss}			
Deschamps et al [130,131]	$\sigma_y = \sigma_{\alpha} + \sigma_{ss} + (\sigma_{ppt}^2 + \sigma_{dis}^2)^{(0.5)}$	None	$\sigma_{\alpha}=10$	2	$A_2=840$	$A_2 \sum_i (C_i^{(2/3)})$ Residual: (at%)	$\sigma_{dis} = M\alpha Gb(\rho^{0.5})$ $\alpha=0.2$	Sphere Equation 4–18	Kocks [130]
Starnik and Wang [137]	$\sigma_y = \sigma_{gb} + M(\tau_{\alpha} + \tau_{ss} + \tau_{ppt})$	$\sigma_{gb} = \alpha_2 Gb \left\{ \frac{f_{Rex}}{D} + \frac{(1 - f_{Rex})}{\delta} \right\}$ G=26 GPa & $\alpha_2=2$	$\tau_{\alpha}=7$	2.55~2.8	$A_2=924$	$A_2 \sum_i C_i^{(2/3)}$ Residual: (at%)	None	Plate Equation 4–26	Starke [147]
Dixit et al [149]	$\sigma_y = \sigma_{gb} + M(\tau_{ss}^2 + \tau_{ppt}^2 + \tau_{dis}^2)^{(0.5)}$	$\sigma_{gb} = \sigma_{\alpha} + k_i d^{(-0.5)}$ L=P.Space $k_i=0.065 \text{ MPam}^{(0.5)}$	$\sigma_{\alpha}=16$	3	$A_{Zn}=3.085$ $A_{Mg}=20.481$ $A_{Cu}=12.431$	$A_i \sum_i C_i^{(2/3)}$ Initial: (wt%)	$\tau_{dis} = \frac{BGb}{L}$ L=P.Space B=0.2	Rod Equation 4–31	Kelly [153]

4.4 MECHANICAL PROPERTIES OF AL-7XXX ALLOYS

Al-Zn-Mg-Cu alloys are one of the typical age-hardening Al-alloys that are strengthened by precipitation reactions. The ageing treatment is a critical process to achieve the desired microstructures and properties in these alloys. The peak hardness and tensile strength could be obtained with an artificial ageing process or T6 type temper. However, in T6 condition, the Al-7xxx component is susceptible to Stress Corrosion Cracking (SCC). The over-aged temper condition (T7) can improve the corrosion resistance of the material by modifying the microstructures. The T7 temper condition results in a loss of about 10-15% of strength as compared to the peak-aged condition (T6 temper) [159]. The AA 7075 alloy is one of the most popular alloys in the Al-7xxx wrought series alloys which has been the subject of many studies during recent years because of (a) its quench sensitivity (i.e., the reduction in age hardening capacity due to the low quenching rate), (b) its high susceptibility to Stress Corrosion Cracking (SCC) in T6 temper, and (c) its strength deterioration through the wall thickness of the plate. The superior mechanical properties of Al-Zn-Mg-Cu alloys make them a good choice for load bearing components in structural applications. Typical uniaxial tensile properties of the popular Al 7xxx alloys available in the background literature source is presented in Table 4–9; wherein, the mechanical properties of various products of the Al-Zn-Mg-(Cu) that are processed with various methods such as wrought condition and semi-solid metal (SSM) thixoforming are compared. It is noticeable that the mechanical properties of SSM products, especially in performance (ductility), are weaker as compared with their wrought counterparts. This difference between SSM and conventional forging wrought products of 7xxx series of Al alloys could be attributed to their inherent difference in elemental content and phase composition [160].

Table 4–9 Typical tensile mechanical properties of AA 7050 wrought alloys by various processing routes

Alloy / Heat Treat	Process/Product	UTS MPa	YS MPa	Elongation (%)	References
7050 / T7651	12.7 mm (0.5 in) thick plate	524	455	8	[156]
7050 / T7451	150mm hot-rolled thick plate	496	437	12.4	[157]
7050 / T6	Forging	570	469	11	[158]
7075* / T6 (120°C-22hr)	Pre-stretch hot-rolled thick plate [†]	595	---	---	[159]
7075/ T6 (135°C-6hr)		575	---	---	
7050 / T6 [‡]	Semi-Solid Thixoforming	405	---	6.6	[160,161]

In the subsequent sections a study of the prior-art on the mechanical properties of Al-Zn-Mg-Cu alloying system is presented.

* Al-6.23Zn-2.88Mg-1.58Cu-0.16Cr-0.31Mn-0.15Fe-0.048Si-0.025Ti (wt.%)

† Traditionally ingot cast slabs were, homogenized, scalped, hot-rolled to plates of 40 mm in thickness, and then solid solution treated at 743K, water quenched (a roller-type spray quenching equipment was used) to room temperature, and pre-stretched (residual stress relieving).

‡ T6: 2hr at 744+quenched+aged for 12hr at 398K +aged for 15hr at 439K

4.4.1 Fractography of the Al-7xxx alloys under tension load

Fractures are generally defined and characterized in terms of several features such as strain to fracture, crystallographic mode of fracture, and the appearance of the fracture surface. Table 4–10 summarizes the commonly used terms to describe the fracture phenomenon.

Table 4–10 Terminology of fracture phenomenon

Behavioural description	Technical term	
Crystallographic mode	Shear	Cleavage
Appearance of fracture	Fibrous	Granular
Strain to fracture	Ductile	Brittle

A *shear* fracture is a direct result of extensive slip on the active slip plane, which is promoted by shear stresses. The *cleavage* mode of fracture is controlled by tensile stresses acting normal to a crystallographic *cleavage* plane. At low magnification optical micrographs of fracture surface, the *shears* appear to be gray and fibrous, while a *cleavage* fracture appears bright or granular. Fracture surfaces are often a mixture of fibrous and granular or coarse fracture. Based on metallographic examination, fractures in *polycrystalline* samples are classified as either *trans-granular* (the crack propagates through the grains) or *inter-granular* (the crack propagates along the grain boundaries) [96].

The *ductile* fracture under *uniaxial tension load* is typically associated with a localized reduction in diameter called “necking” before failure. Formation of necking introduces micro-cavities (micro-voids) at the center region of necking area. During necking, the micro voids start to grow and coalesce leading to formation of a central crack, which grows in a perpendicular direction to the uniaxial load-axis because of high stress concentration at its tip. This is shown in Figure 4–42 (a). Further, the high stress concentration at the crack tip leads to formation of narrow bands of shear strain ahead of the crack tip at an angle of 50~60° with respect to the tensile axis [162], as shown in Figure 4–42 (d). These shear bands are nucleation source for micro voids, as shown in Figure 4–42 (e).

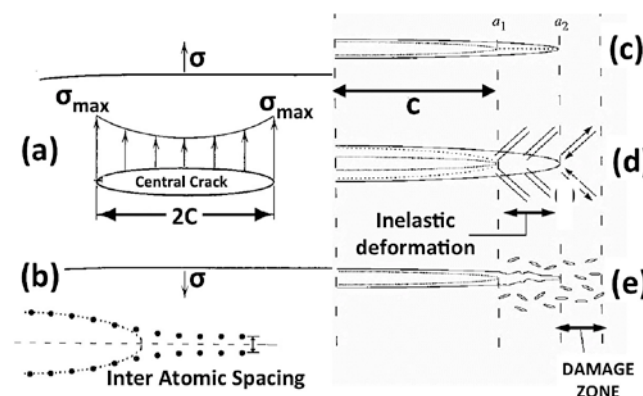


Figure 4–42 Schematic representation of: (a) the stress field in an elliptical central crack [96]; (b) the crack growth mechanism by influence of external forces and inter-atomic forces at its tip; (c) breaking of inter atomic bonds without plastic deformation or micro-cracking ahead of crack; (d) plastic flow at the crack tip by the formation of the shear strain bands; and (e) the formation of micro-cracks in the shear strain bands ahead of crack tip (void sheets) [162].

The localized fracture of these *void sheets* is the point where the growth rate of the central crack accelerates and propagates at an angle of $\sim 45^\circ$ with respect to the tensile axis; wherein the localized shearing planes are theoretically more active and leads to producing the “cone”

part of a “cup-and-cone” fracture surface, wherein the “shear lips” are aligned at the angle of $\sim 45^\circ$ to the tensile axis. This results in the formation of elongated and fine size “*dimples*” on the fracture surface; wherein numerous holes are separated with thin walls. *Voids* are the main source for the ductile fracture and they can heterogeneously nucleate and initiate on the sites where the plastic deformation cannot be accommodated easily. Examples for the preferred initiation sites for micro crack are the inclusions and secondary phases or fine oxide particles. However, in high purity metals, cracks can start from the triple-point joint at the grain boundaries. Figure 4–43 (a) to (c) present a schematic distribution of these particles along with an optical micrograph of the polished cross section of polycrystalline copper alloy that are fractured in the early stage of a creep test, where the elongated voids are clearly discernable at grain boundaries. In Figure 4–43 (e), it can be seen that microrholes (micro voids) are nucleated at the grain boundary areas where they can grow along the grain boundaries by sliding mechanism. The maximum sliding occurs on the grain boundaries that are aligned roughly at 45° angle to the tensile axis. Figure 4–44 presents the effect of purity of base metal in the aluminum alloys on the volume fraction of secondary phases and its direct impact on the fracture strain of the material [5].

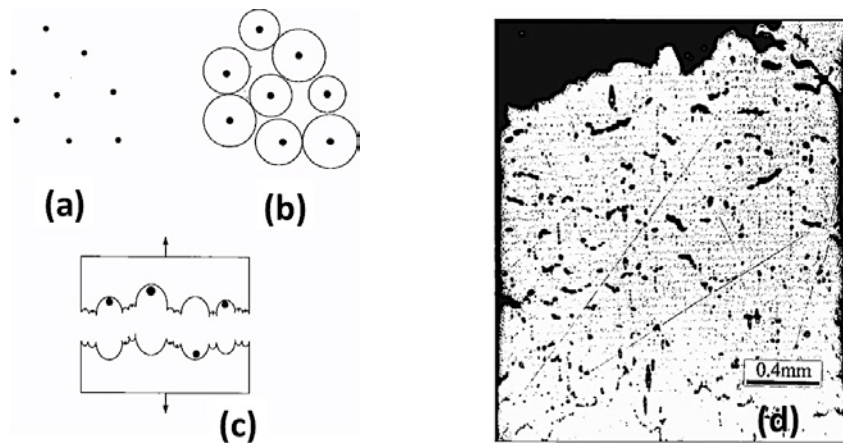


Figure 4–43 Schematic representing typical ductile fracture under the uniaxial tension load test, where the void coalescence is the dominate mechanism leading to formation of the equiaxed dimples on the fracture surface: (a) random planar array of particles as initiation sited for microcracks; (b) growth of the microvoids in the form of webs and columns, (c) cross-sectional appearance of “dimples” as a hole-joining mechanism for ductile fracture; (d) polished optical micrographs of the polished cross-section in low magnification of a polycrystalline copper alloy fractured under the uniaxial tension test at an elevated temperature [162].

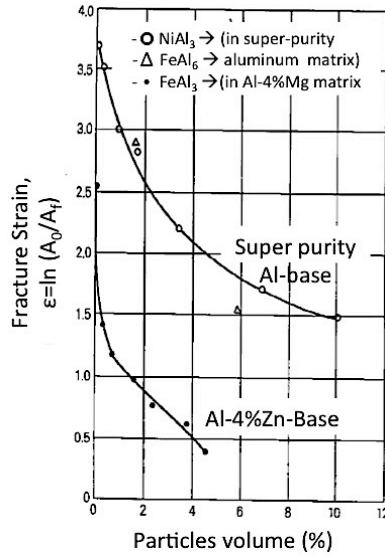


Figure 4-44 Effect of volume fraction of intermetallic particles and composition of Al-matrix on the fraction strain of 6mm (2in.) tensile specimen of Al-Zn alloys [5]

Under the uniaxial tensile tests, while most of aluminum alloys usually show a *ductile* fracture with micro voids coalescence mechanism, there are some examples from the Al-7xxx alloys with high amount of alloying elements that exhibit the characteristic features of the *brittle* fracture on the fracture surface. The secondary phases, narrow precipitation free zones (PFZ) and coarse intermetallic phases at grain boundary areas are the characteristic features of Al-7xxx alloys; they enhance *inter-granular* fracture. Cracks initiated at the brittle secondary phases in the grain boundaries would be able to propagate along the high angle grain boundaries [163] with ease. Figure 4-45 and Figure 4-46 present typical SEM micrographs of fracture surface of Al-12Zn-3Mg-2.5Cu-(0.1Ti) alloys, wherein typical examples of crack initiation sites such as micro void and shrinkage porosity are presented, respectively.

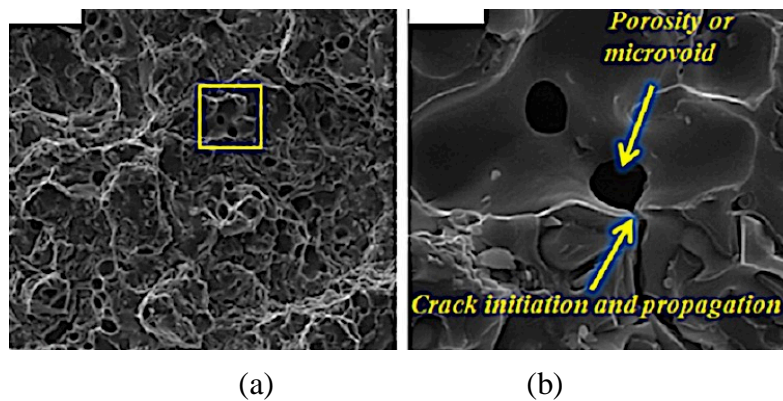


Figure 4-45 Typical SEM micrographs of fracture surfaces of refined Al-12Zn-3Mg-2.5Cu-0.1Ti in peak age (T6) condition: (a) low and (b) high magnification micrographs of the micro voids nucleated heterogeneously on secondary phase particles at grain boundary forming micro crack at grain boundary with its propagation paths along the grain boundary areas [163].

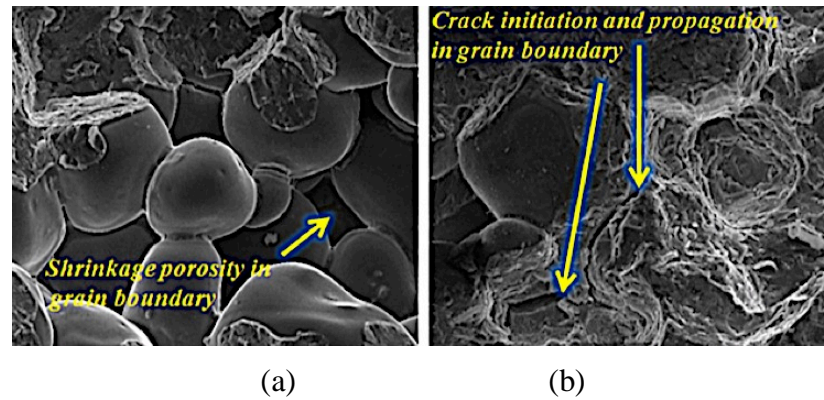


Figure 4-46 Typical high magnification SEM micrographs of fracture surface of refined Al-12Zn-3Mg-2.5Cu-0.1Ti in solution heat treatment (T4) condition, showing (a) shrinkage porosities with free surface as the heterogeneous initiation sites for the nucleation of micro voids; and (b) the preferred initiation paths at the grain boundary areas [163].

5 EXPERIMENT PROCEDURES

In this chapter the laboratory experiments carried out in this study along with the methodology of the data analyses and the materials used for the experiments are presented in the following sub-section:

- Materials and Experimental equipment
- Laboratory scale CDS experiments
- The CDS casting experiments using (TPGC) machine
- Microstructural Analysis
- Transmission Electron Microscopy (TEM)
- Image Analysis
- Heat treatments procedures and equipment
- Differential Scanning Calorimetry (DSC) Tests
- Uniaxial Tensile Tests
- Density measurement test

5.1 MATERIALS AND EXPERIMENTAL EQUIPMENT

The precursor alloys of the CDS experiments were freshly prepared using aluminum master alloy ingots and several raw materials such as Al-50Mg, Al-28Cu, Al-33Cu, Al-36Si, Al-25Mn, Al-50Fe, TiBor, and pure zinc ingots. The Ti element was added to the Alloy1 because of its grain refinement effect on the primary Al phase to further improve the mechanical properties of the resultant castings. It is notable that the range of elemental composition presented in the Table 5–1 denotes the composition range obtained during several experiments. It was ensured that the composition of the resultant (mixture) alloy from application of the CDS technology of the Al7xxx alloys in the cast components did not deviate from the nominal composition of commercial alloys. Further, Table 5–1 presents the experimental composition matrix, which was chosen for this study, wherein all the alloys selected as the resultant alloy (Alloy3) for the CDS experiments of the Al-7xxx alloys are tabulated. It is noteworthy that Si and Fe are the impurity elements and the Cr, Zr and Mn elements are not intentionally added to the alloys because the castings would not undergo any additional mechanical deformation process prior to evaluation of the tensile properties. In part this is because the Al-7xxx alloys selected for the present study are mainly chosen to study the Controlled Diffusion Solidification (CDS) casting process and they were not meant for any further thermo-mechanical processes such as the wrought processes. In wrought products of the Al-7xxx alloys, the Cr, Zr and Mn elements are critically important for their consequent pinning effects on the grain boundaries during the recrystallization stage of the subsequent heat treatments [31,149]; further the Cr, Zr and Mn elements can form the impurity dispersoids* [164,165], which can have an important role as the heterogeneous

* These dispersoids (which are most likely of impurity elements with an equilibrium partition coefficient $k > 1$ therefore they tend to concentrate at the center of grains or dendrites, such as chromium, titanium, vanadium, and zirconium [66]).

nucleation sites on the nucleation and growth of the precipitates forming during the age hardening process of the Al-7xxx wrought alloys [72,79]. Therefore, through out this dissertation, just for the purpose of easier way of recalling some of the Al-7xxx CDS alloys will be referred or recalled by their ASTM standard designations based on their main alloying element contents (Zn, Mg and Cu). The most frequently used example in this dissertation is the AA 7050 alloy.

Table 5–1 Nominal composition (wt.%)^{*} of the Al-7xxx alloys that are measured by GDOES[†] test method, which were selected for this study.

#	Alloy Designation	Zn	Mg	Cu	Fe	Si	Ti	Zn+Mg+Cu	Mg/Zn
1	Al-3.5Zn-0.8Mg-0Cu	3.48 ±0.30	0.79 ±0.39	0.027 ±0.004	0.09 ±0.03	0.025 ±0.004	0.05 ±0.02	4.3	0.23
2	Al-3.5Zn-1.62Mg-0Cu	3.53 ±0.44	1.62 ±0.42	0.077 ±0.231	0.04	0.000 ±0.000	0.06 ±0.01	5.22	0.46
3	Al-5.2Zn-1.7Mg-0Cu	5.18 ±0.48	1.73 ±0.08	0.022 ±0.001	0.04	0.002 ±0.004	0.06 ±0.00	6.94	0.33
4	Al-6.6Zn-1.7Mg-0Cu	6.56 ±0.45	1.72 ±0.12	0.022 ±0.001	0.05	0.001 ±0.003	0.06 ±0.01	8.30	0.26
5	Al-3.8Zn-2.18Mg-1.7Cu	3.81 ±0.18	2.18 ±0.05	1.75 ±0.07	0.07 ±0.01	0.019 ±0.002	0.04 ±0.05	7.75	0.57
6	Al-5Zn-2Mg-1.3Cu	5.05 ±0.23	2.04 ±0.07	1.29 ±0.09	0.11 ±0.01	0.604 ±0.043	0.05 ±0.00	8.38	0.40
7	Al-6.5Zn-1.5Mg-2Cu	6.47 ±0.16	1.47 ±0.07	2.01 ±0.05	0.09 ±0.01	0.031 ±0.003	0.09 ±0.03	9.96	0.23
8	Al-5.8Zn-2.2Mg-2.5Cu (Al-7050)	5.82 ±0.30	2.22 ±0.05	2.53 ±0.19	0.02 ±0.01	0.025 ±0.004	0.03 ±0.00	10.57	0.38
9	Al-9.97Zn-2.4Mg-0.9Cu	9.97 ±0.47	2.40 ±0.09	0.92 ±0.02	0.28 ±0.03	0.928 ±0.064	0.02 ±0.00	13.28	0.24

5.2 LABORATORY SCALE CDS EXPERIMENTS

The first step of the CDS experiments is to simulate the phase diagram isopleth of multi-component Al-Zn-Mg-(Cu) alloy using Pandat[‡] thermodynamic database. This is important for the purpose of critical investigation and selection of the appropriate compositions and initial temperatures for the precursor alloys in the CDS process, such as Alloy1 and Alloy2. The temperature difference between liquidus temperatures of the precursor alloys (T_{L1} for Alloy1 and T_{L2} for Alloy2) must be at least greater than ~50 °C [40] in order to ensure the non-dendritic microstructure. Further, the composition of the precursor alloys (Alloy1 and Alloy2) should be selected such that the mixing of Alloy1 into Alloy2 results in the desired

^{*} Measured by GDOES (Glow Discharge Optical Emission Spectroscopy) testing method. Average numbers are calculated over the total number of 10 data points for each condition.

[†] Glow Discharge Optical Emission Spectroscopy (GDOES)

[‡] Pan Aluminum Database; Computherm LLC, Madison, WI, USA; <http://www.computherm.com/>

composition of Alloy3 at a temperature T_3 , which is approximately around the value of its liquidus temperature (T_{L3}). The initial pouring temperatures of Alloy1 and Alloy2 (T_1 and T_2) are typically about $10\text{ }^\circ\text{C}$ above the respective liquidus temperatures of T_{L1} and T_{L2} . Figure 5–1 presents the typical phase diagram isopleth of AA7050 alloy, which were calculated by Pandat thermodynamic database. Figure 5–2 presents the actual thermal curves of the precursor alloys (Alloy1 and Alloy2) and the resultant (Alloy3) alloy that were specifically designed for the AA7050 as the resultant (Alloy3) alloy. The thermal curves in the Figure 5–2 were obtained with a slow cooling rate ($0.1\text{ }^\circ\text{C}\cdot\text{s}^{-1}$) within the melting furnace. The laboratory scale experiments were designed for the conceptual proof of the CDS process for the selected alloys from the Al-7xxx family to ensure a non-dendritic microstructure prior to running the CDS process in a larger scale using tilt pour gravity casting (TPGC) machine. Figure 5–3 presents the experimental set-ups for laboratory scale CDS experiments; wherein the precursor alloys (Alloy1 and Alloy2) are kept in separate crucibles in order to be mixed later at a pouring temperature about $10\text{ }^\circ\text{C}$ above their liquidus points. Table 5–2 presents the process parameters of the CDS process including the experimental and theoretical liquidus and pouring temperatures for the precursor alloys (Alloy1 and Alloy2) and the resultant alloy (Alloy3). It is noteworthy that the CDS process parameters were first obtained by the lab scale experiments and then were utilized in the larger scale CDS experiment using the Tilt Pour Gravity Casting (TPGC) machine. Figure 5–4 presents the typical phase diagram isopleth for the precursor alloys (Alloy1 and Alloy2) and the resultant alloy (Alloy3) that are selected for the desired Alloy3 from the Al-7xxx alloys. Figure 5–5 presents the simulated solid fraction of the resultant alloy (Alloy3) from the Al-7xxx alloy family selected for the CDS experiments in this study.

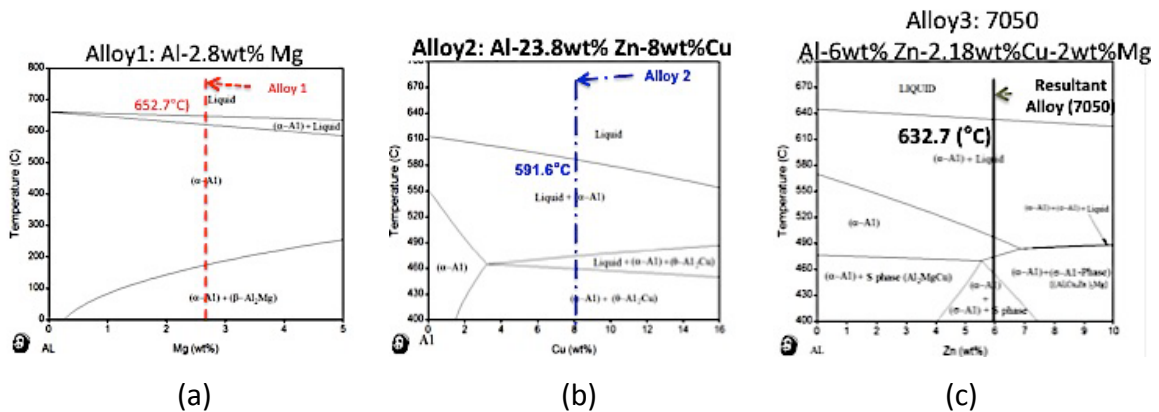


Figure 5–1 Phase diagram isopleth of (a) binary Al-Mg phase diagram (Alloy1); and (b) Al-Zn-Cu ternary phase diagram (Alloy2); both of which are designed for the CDS process of the Al-7050 alloy as the resultant alloy (Alloy3) of which the quaternary Al-Zn-Mg-Cu phase diagram isopleth is shown in (c).

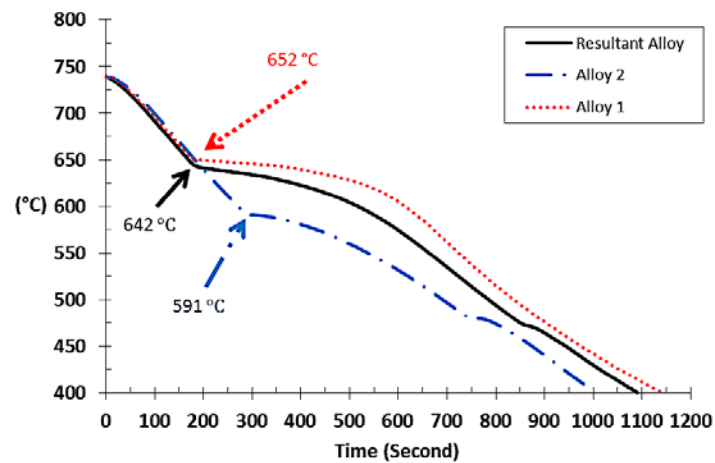


Figure 5–2 Actual thermal curves for the precursor alloys (Alloy1, Alloy2 and Alloy3) designed for the lab scale CDS experiments of the AA-7050 that are obtained experimentally by a slow cooling rate of about $0.1 \text{ }^\circ\text{C}\cdot\text{s}^{-1}$ inside the melting furnaces.

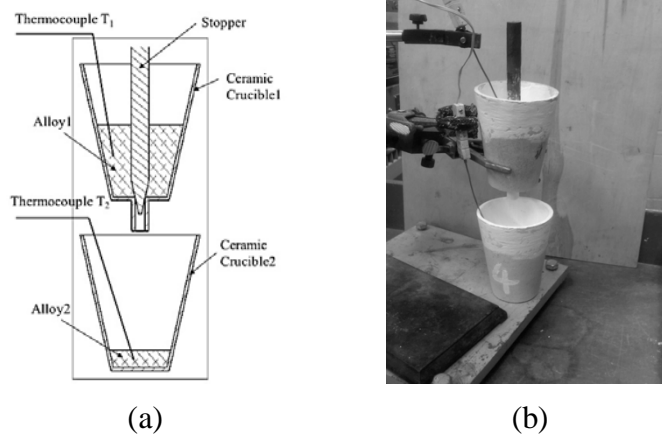


Figure 5–3 Laboratory scale experimental set-ups for CDS experiments: (a) the schematic and (b) the actual lab scale experimental set-ups: crucibles for precursor alloys (Alloy1 and Alloy2) and thermocouples used for monitoring the temperatures during the CDS experiments [54].

Table 5-2: CDS process parameters for the precursor alloys (Alloy1, Alloy2 and Alloy3) for the Al-7xxx alloys selected for this study. The compositions (wt.%) were measured by the GDOES test method.

#	Alloy#	Composition	Measured Liquidus Temperature (°C)	Measured Alloy Melt Temperature (°C)	Equilibrium Liquidus Temperature (°C)
1	Alloy1	Al-1.33Mg-0Cu	652~5	660~5	
	Alloy2	Al-18Zn-0Cu	630~4	635~40	
	Alloy3	Al-3.6Zn-1Mg-0Cu	647		648
2	Alloy1	Al-2.87Mg-0Cu	641~47	650~60	
	Alloy2	Al-18Zn-0Cu	625	630~5	
	Alloy3	Al-3.6Zn-1.8Mg-0Cu	639~642		644
3	Alloy1	Al-2.87Mg-0Cu	641~47	650~60	
	Alloy2	Al-24Zn-0Cu	618	625~30	
	Alloy3	Al-4.8Zn-1.8Mg-0Cu	640~643		642
4	Alloy1	Al-2.87Mg-0Cu	641~47	650~60	
	Alloy2	Al-30Zn-0Cu	608	612~7	
	Alloy3	Al-6.8Zn-1.7Mg-0Cu	635~638		638
5	Alloy1	Al-2.67Mg-0Cu	641~47	650~60	
	Alloy2	Al-18Zn-6Cu	612	620~25	
	Alloy3	Al-3.8Zn-2Mg-1.6Cu	642~643		640
6	Alloy1	Al-2.67Mg-0Cu	645~650	650~60	
	Alloy2	Al-22Zn-4Cu	607~8	615~20	
	Alloy3	Al-5Zn-2Mg-1.3Cu	637~638		637
7	Alloy1	Al-2.8Mg-0Cu	641~647	650~60	
	Alloy2	Al-23.6Zn-4.9 Cu	608~10	615~20	
	Alloy3	Al-6.5Zn-2Mg-1.5Cu	633~635		634
8	Alloy1	Al-2.8Mg-0Cu	645~52	655~60	
	Alloy2	Al-23.8Zn-8.68Cu	580~92	610~20	
	Alloy3	Al-6Zn-2.2Mg-2.3Cu	632~642		633
9	Alloy1	Al-3.47Mg-0Cu	641~45	650~60	
	Alloy2	Al-31.2Zn-8Cu	570~80	600~10	
	Alloy3	Al-7.9Zn-2.6Mg-2Cu	624.6~630.6		626

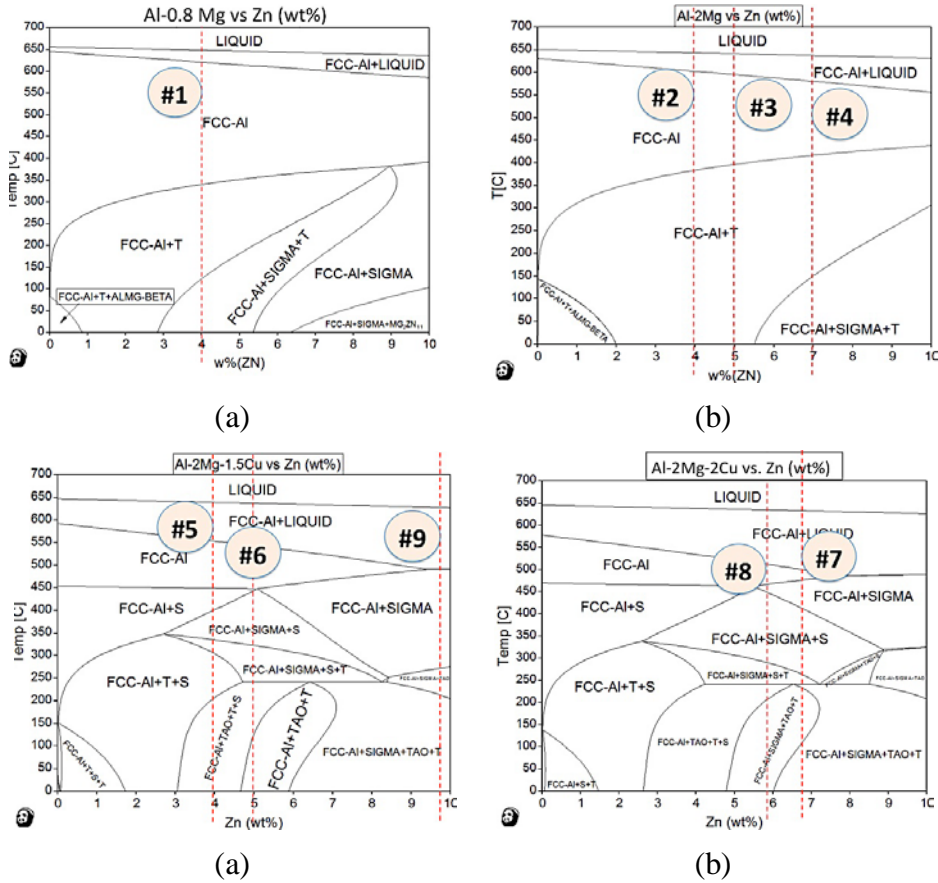
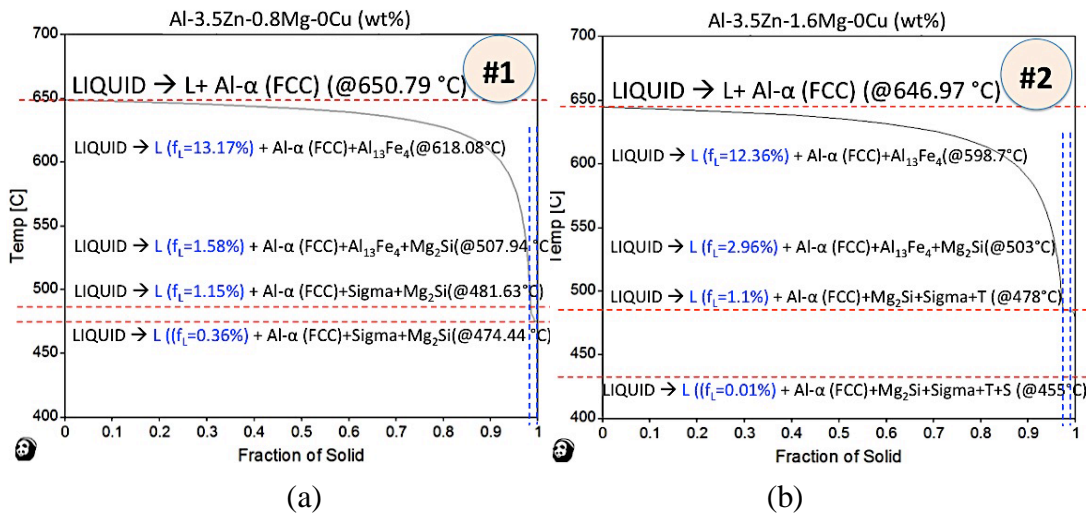
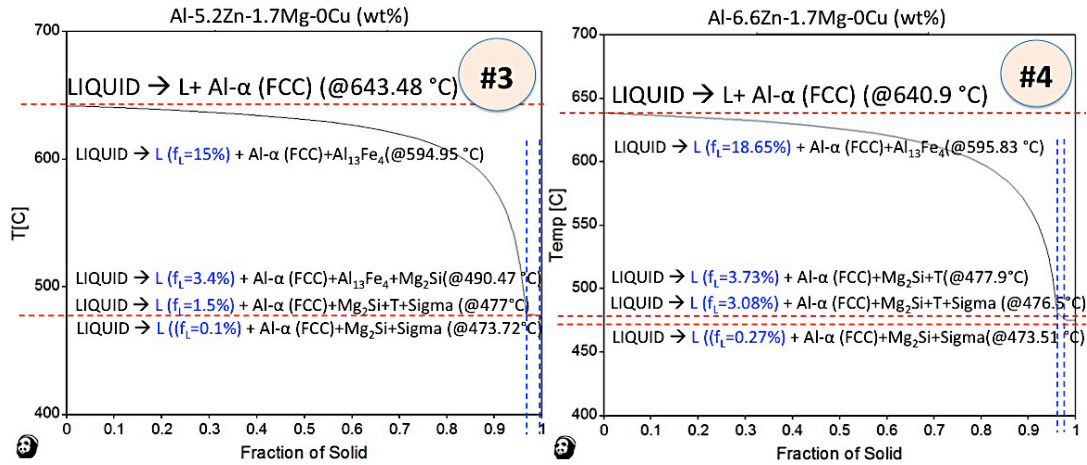


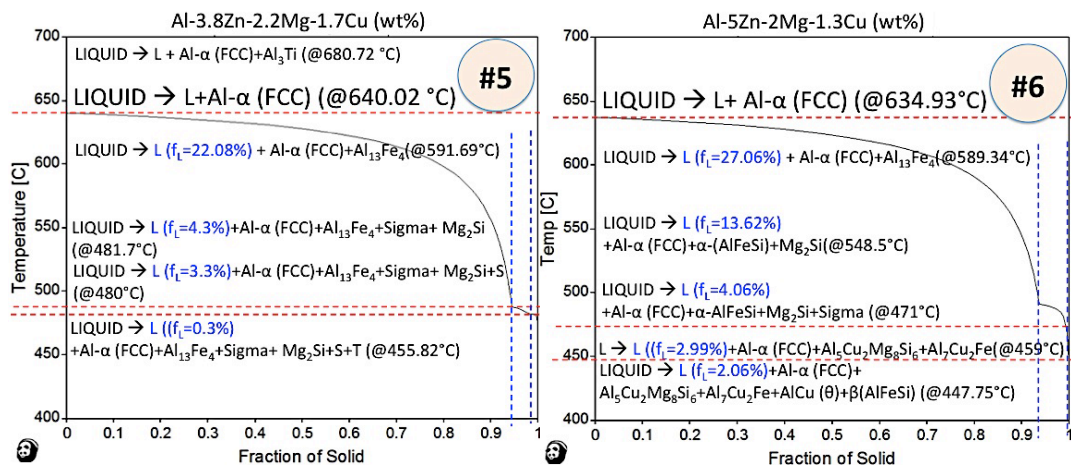
Figure 5-4 The phase diagram isopleth of the Al-7xxx alloys selected for the CDS experiments in this study.





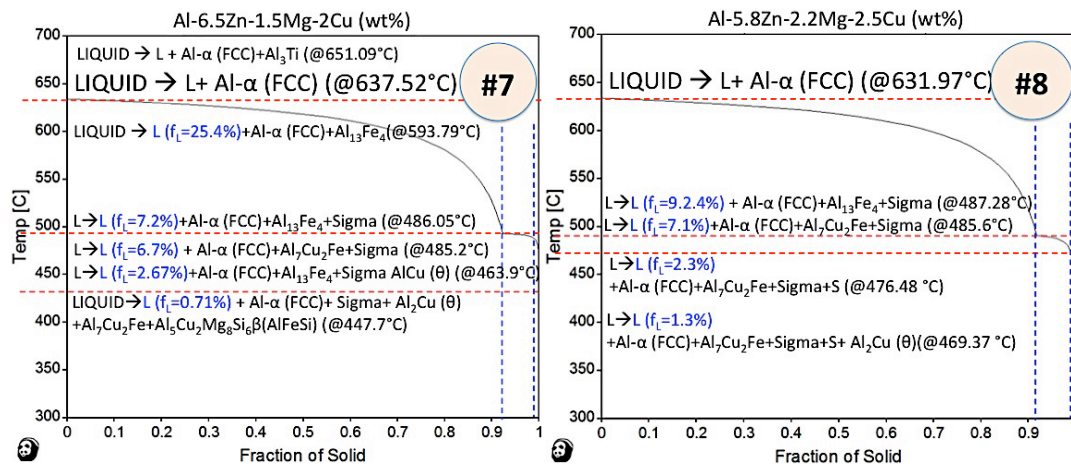
(c)

(d)



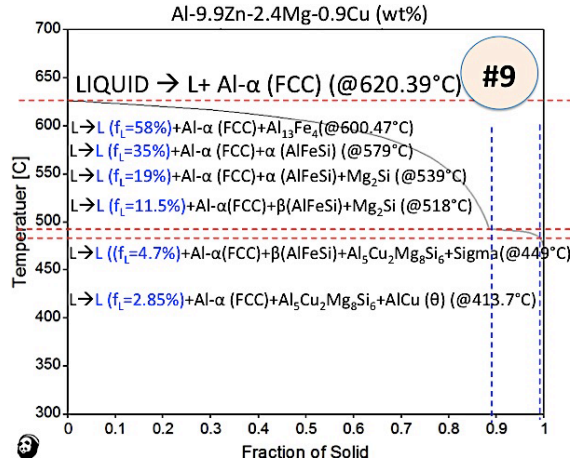
(e)

(f)



(g)

(h)

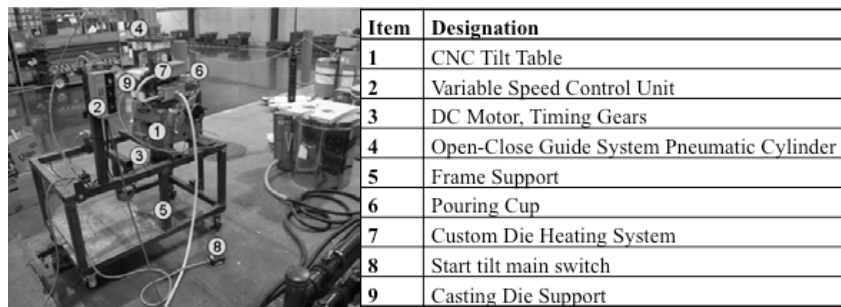


(i)

Figure 5–5 Typical solid fraction of the desired resultant alloys from the Al-7xxx alloys that are selected for the CDS experiments in this study; it is noteworthy that these solid fraction phase diagram isopleth were simulated using Panda thermodynamic database.

5.3 THE CDS CASTING EXPERIMENTS USING (TPGC) MACHINE

The CDS experiments in large scale using the Tilt Pour Gravity Casting (TPGC) machine. This is carried out utilizing the process parameters for the CDS experiments that were previously obtained in the laboratory scale experiments. The Tilt Pour Gravity Casting (TPGC) machine used for larger scale CDS experiments consists of a cavity mould with two tensile-bar and one fatigue-bar specimens that were designed in accordance with the ASTM standard. Figure 5–6 presents the TPGC machine used in this study for the CDS experiment in larger scale. It is noteworthy that the TPGC machine were specifically designed and built for the CDS experiments [54]. Figure 5–7 presents the permanent mould cavity of the TPGC machine equipped with an electrical heater.



(a)

(b)

Figure 5–6 Casting equipment for the study of the CDS process that is utilized for this study: (a) Tilt Pour Gravity Casting (TPGC) Equipment and (b) component parts list of the TPGC machine [54].

In the CDS experiment with TPGC machine, the precursor alloys (Alloy1 and Alloy2) were freshly prepared in two electric furnaces, each in about 50lb weight, and degassed separately with ultrahigh purity Argon gas purged into the molten alloys at a flow rate between 6 and 8 L.min⁻¹ using a rotary degasser at 120 RPM for 30 min. The alloy melts were then held isothermally at about 10 °C above their respective liquidus temperatures prior to mixing. The initial precursor alloys were mixed at their specific pouring temperatures into the preheated metal mould that is maintained at 375°C. The mixing is carried out using two fixed-volume ladles to ensure the desired mass ratio of the mixing between the two precursor alloys

according to the CDS process mechanism [41]. The gross weight of final casting shot cast into the mould of the TPGC machine is about 900 g.

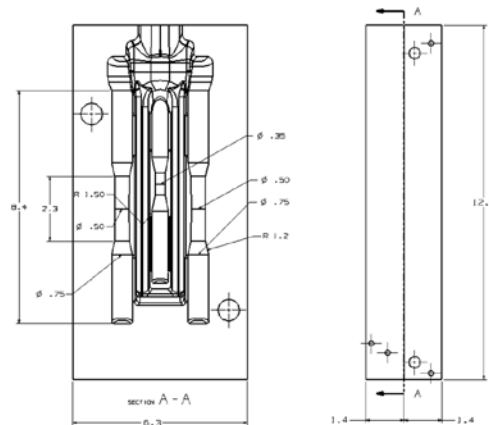


Figure 5–7 Cavity mould of tilt pour gravity casting (TPGC) machine which consists of two tensile test and one fatigue test bars, according to ASTM standard numbers ASTM B557 and ASTM E466-96, respectively [54].

As a benchmark, the AA7050 alloy was cast directly using the TPGC equipment without using the CDS process and will be referred to as conventional casting throughout this dissertation. The alloy melt of AA7050 was maintained at $\sim 75^\circ\text{C}$ superheat above the liquidus temperature (at $\sim 710^\circ\text{C}$) in an electric resistance furnace and the melt was degassed with Ar gas through a rotary degasser prior to casting. It is noteworthy that the mould temperature for the conventional cast experiment of the Al-7050 alloy were at about 275°C which is lower than that of the CDS experiments ($\sim 375^\circ\text{C}$); and also in the conventional cast experiment of the Al-7050 alloy, Ti-element was not added to the melt of the 7050 alloy. Figure 4–3 shows the photographs of the AA 7050 alloy castings obtained from the CDS and conventional casting processes using the same TPGC machine, respectively. It is noticeable in Figure 4–3 (a) that the castings from the CDS process were sound with no discernible casting defect such as hot tears; whereas, the casting from the conventional process is consistently defective, specifically, due to the presence of several hot cracks in the casting (Figure 4–3 (b)).

5.4 MICROSTRUCTURAL ANALYSIS

Microstructural analyses were carried out on the samples prepared from the gauge section area of the uniaxial tensile test specimens, shown in Figure 5–8. The samples were mounted (using Bakelite powder), ground and polished (in an automatic polishing machine) and etched (using freshly made Keller’s reagent: 1ml HF, 1.5ml HCL, 2.5ml HNO₃ and remainder H₂O) for the purpose of optical light microscopy. In case of the electron microscopy (SEM), the mounted samples were used as polished with no further etching process. The optical microstructural images were obtained using the Stereograph Microscope (Nikon AZ 100M* equipped with an image processing software: NIS BR 3.10 image acquisition system) and Light Optical Microscopy (Nikon Eclipse LV100 equipped with the NIS BR 3.0 image acquisition system). The SEM analysis was obtained using a JEOL JSM-7000F† Electron microscope, equipped with energy dispersive X-ray (EDX) analyzing system. Figure 5–8

*Eberbach Corporation, ANN Michigan.

†JEOL, INC Oxford

presents various locations on the uniaxial tensile specimens for sampling such as the microscopy specimens (optical and SEM), the hardness test specimens and the chemistry test specimens (used for the GDOES* test method).

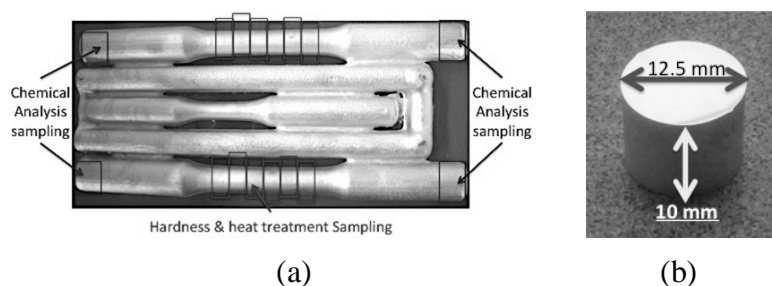


Figure 5–8 Sampling locations from the uniaxial tensile bars (a) for various tests such as microscopy and hardness-test (within the gauge length area); and chemistry-test specimens (from both ends of the tensile bars); (b) dimensional presentation of the microscopy and hardness-test specimen in as-polished condition.

5.5 TRANSMISSION ELECTRON MICROSCOPY (TEM)

Thin-foil specimens for TEM were prepared by means of a combined process of ion milling and electro-polishing. The electro-polishing was carried out in a solution of 10% Perchloric acid in 20% glycerol and 70% methanol at -20°C using standard twin-jet polishing. For the ion milling, the GATAN PIPS ion mill was used. TEM investigations were carried out under the electron beam of a transmission electron microscope JEOL 200CX and TEM FEI's Tecnai Osiris, operating at 200 kV and equipped with a Zeiss 912 camera lens and an omega energy filter; also a high angle annular dark field (HAADF) STEM detector and Chemi-STEM X-ray detection technology was employed to characterize the samples. In order to study the chemistry of different phases, Energy Dispersive Spectroscopy (EDS) technique was used in STEM-HAADF mode to perform quantitative analysis and elemental mapping. Conventional bright field and dark field imaging and diffraction techniques (selected area electron diffraction (SAED) and convergent beam electron diffraction (CBED) were used to study the microstructure and precipitation. Further, for the volume fraction calculation, TEM foil thickness was assumed to be 100 nm (or 1000\AA) [96,137] at which thickness the specimen is transparent to the impingement of the electrons of the microscope's electron beam.

5.6 IMAGE ANALYSIS

Quantitative metallography by image analyses on all the microstructural images including the electron (SEM or TEM) and Optical micrographs was carried out using the ImageJ[†] software. The grain size was measured by the linear intercept method as in the ASTM test method E112 [166] with a minimum number of 20 lines for each optical micrograph. For each alloy/heat treatment condition, at least 5 micrographs were used in low magnification of 200X. Four different orientations of lines were tried in each microstructure image analyses for grain size measurements; such as 0° , 45° , 90° and 135° angles from the horizontal line.

The particle size measurement in the, Optical, SEM and TEM micrographs were carried out in accordance with the ASTM standard E1245-03.

* Glow Discharge Optical Emission Spectroscopy Test Machine by Jobin Yvon Horiba

† ImageJ, Image processing and Analysis in Java, 1.42q Java 1.6.0 (32 bit)

In case of the micro-scale particle size measurement from the Optical and SEM micrographs, such as the relatively large precipitates formed after anneal (O) process, the linear or planar mean free paths between these precipitates can be calculated by the Equation 5–1 [167].

$$\lambda_{Linear} = \tilde{L}_3 * \left(\frac{1}{f_{Linear}} - 1 \right)$$

or

$$\lambda_{Planar} = E\tilde{C}R * \left(\frac{1}{f_{Area}} - 1 \right)$$

Equation 5–1

Where $L3$ represents a lineal measure of the average intercept length (edge to edge) by a random test line drawn on the 2-dimensional image analysis, which for the specific case of spherical particles ($L3=4/3*r$), gives the linear mean free path between the homogeneously distributed particles as per Equation 5–2.

$$\lambda_{Linear} = \left(\frac{4}{3} \right) (E\tilde{C}R) \left(\frac{1}{f_{Linear}} - 1 \right)$$

Equation 5–2

The volume fraction of the micron sized particles observed in the Optical and SEM micrographs were approximately assumed to be equal to the area fraction obtained from the planar measurements by the image analysis; which is suggested by the ASTM E1245-03 standard, which can be calculated by using the Equation 5–3.

$$f_{Volume} = f_{Area} = \left(\frac{\sum_{i=1}^N A_i}{A_{Total}} \right)$$

Equation 5–3

Where the A_i is the individual area measured by the image analysis and N is the number of particles that are counted per measured area of the specific image; and A_{Total} is the total area of the image that has been analyzed. Figure 5–9 shows schematic presentation of image analysis procedure that were carried out on the relatively high magnification optical micrographs for the area measurements of the relatively large precipitates during the annealing process in the Al-7xxx alloys; that were obtained by the thresholding technique using the ImageJ software. Similarly, this technique was used for the measurement of the area fraction or volume fraction of the secondary phases as the eutectic phases forming at the grain boundary areas, which is shown schematically in Figure 5–10.

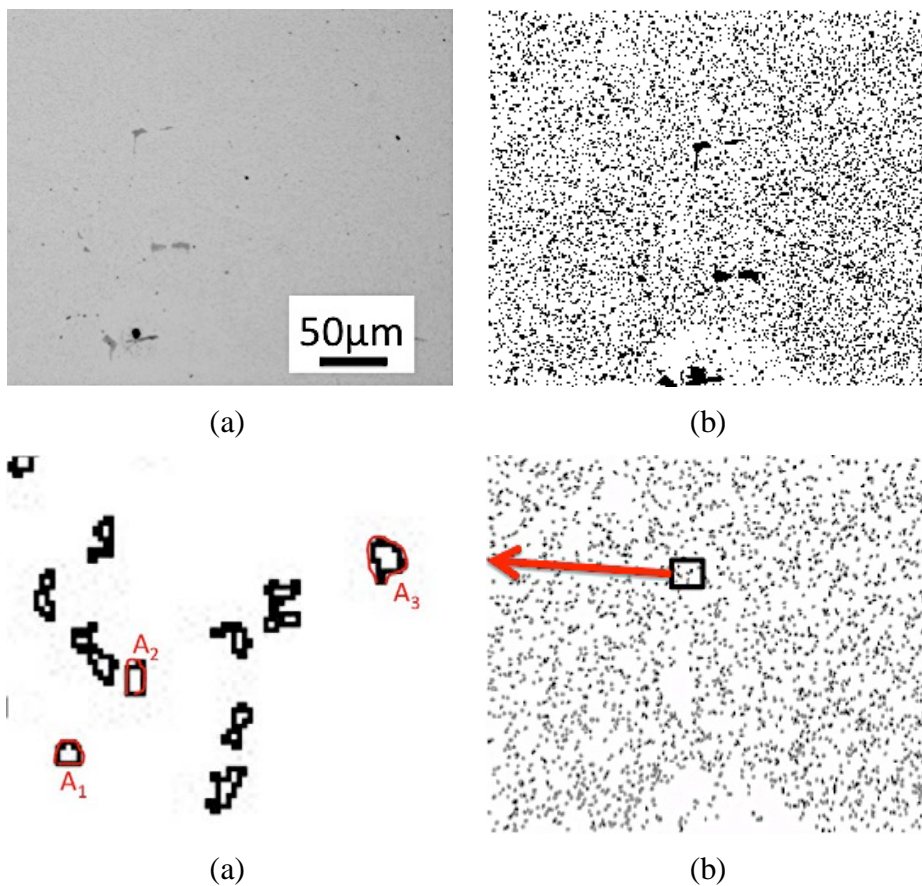
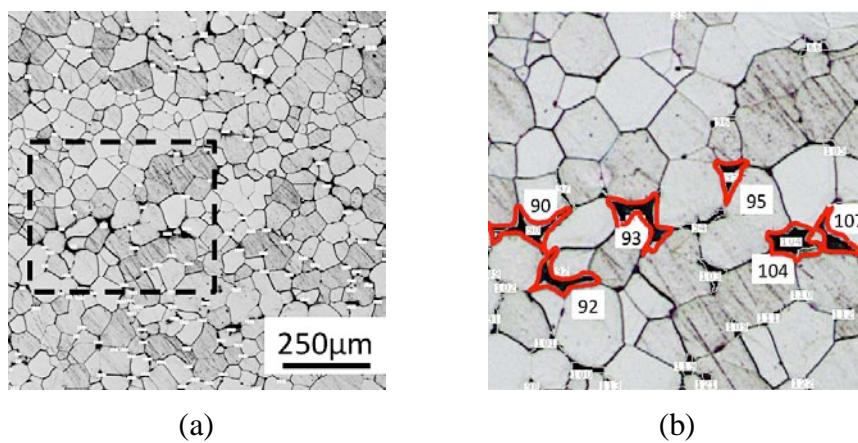


Figure 5-9 Schematic presentation of image analysis procedure on the relatively high magnification bright field optical micrographs for the area measurements of the relatively large precipitates during the annealing (O) process in Al-7xxx alloys.



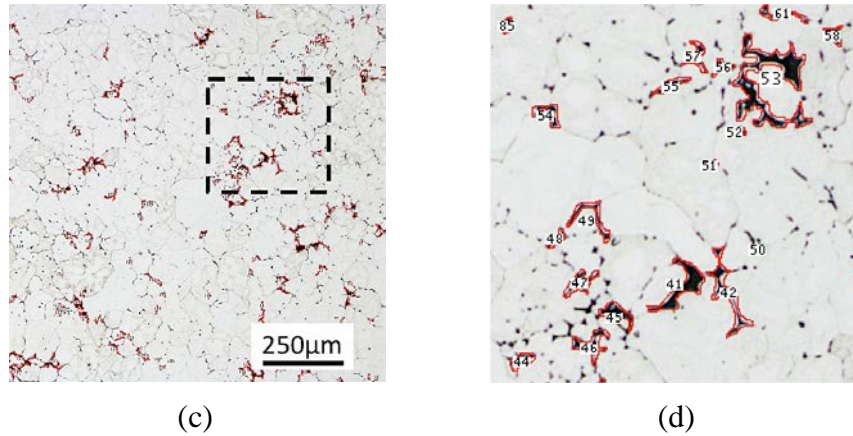


Figure 5–10 Schematic presentation of image analysis procedure using optical micrographs for the area fraction measurements of the relatively large secondary eutectic phases forming during the solidification process at grain boundary areas in (a) and (b) for the Al-5.8Zn-2.2Mg-2.5Cu alloy in T4 heat treatment condition; and in (c) and (d) for the Al-3.6Zn-1.8Mn-0Cu alloy in as-cast (F) temper.

However, the size measurements for the fine-scale precipitates in the TEM micrographs were carried out in accordance with the ASTM standard E1245-03: the particle size or Equivalent Circular Radius (ECR), the area measurement method was used by means of the Image J software with various threshold techniques. In the case of Nano-scale fine precipitates such as the precipitates forming during the T6 age hardening process that are mostly observable in the TEM micrographs, the volume fraction was calculated by considering the thickness of TEM thin foil due to stereology theorem [168], as schematically shown in Figure 5–11. The thickness of the thin foil TEM for the volume fraction calculation is assumed to be 100 nm (or 1000 Å). The volume fraction of the Nano-scale precipitate forming during the T6 process from the TEM micrographs were calculated using below Equation 5–4 that is derived for the presumably spherical particles.

$$f_{Volume} = \frac{\left(t^* \left(\sum_{i=1}^N A_i \right) \right)}{\left(t^* A_{Total} \right)} = \frac{\left(\left(\sum_{i=1}^N \left(\frac{4}{3} * \pi * \left(\tilde{ECR}_i \right)^3 \right) \right) \right)}{\left(t^* A_{Total} \right)} = \frac{\left(N * \left(\frac{4}{3} * \pi * \left(\tilde{ECR}_i \right)^3 \right) \right)}{\left(t^* A_{Total} \right)} \quad \text{Equation 5-4}$$

Where the ECR is the Equivalent Circular Radius, which is calculated by the following Equation 5–5, which is shown schematically in Figure 5–12.

$$\tilde{ECR}_i = \sqrt{\left(\frac{A_i}{\pi} \right)} \quad \text{Equation 5-5}$$

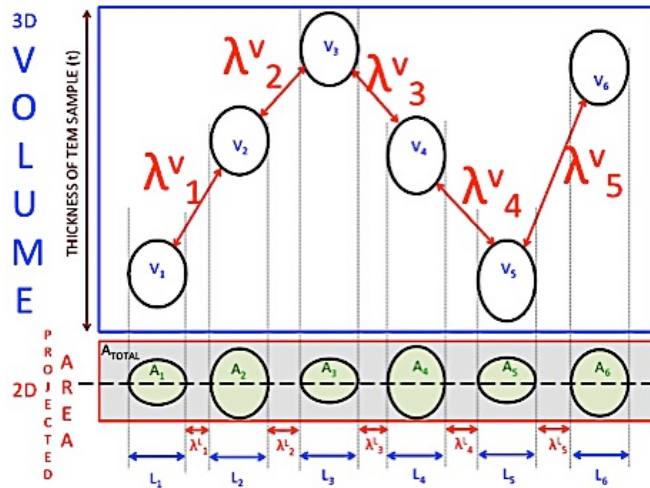


Figure 5–11 Schematic presentation of spatial distribution of Nano-scale particles within the volume of the TEM foil sample and the respective projection on a 2-dimensional image. This may affect the measurements of the actual inter-particle spacing with a spatial distribution within the volume of the TEM samples as compared to the 1D (linear) and 2D (area) measurements on the TEM projected micrographs.

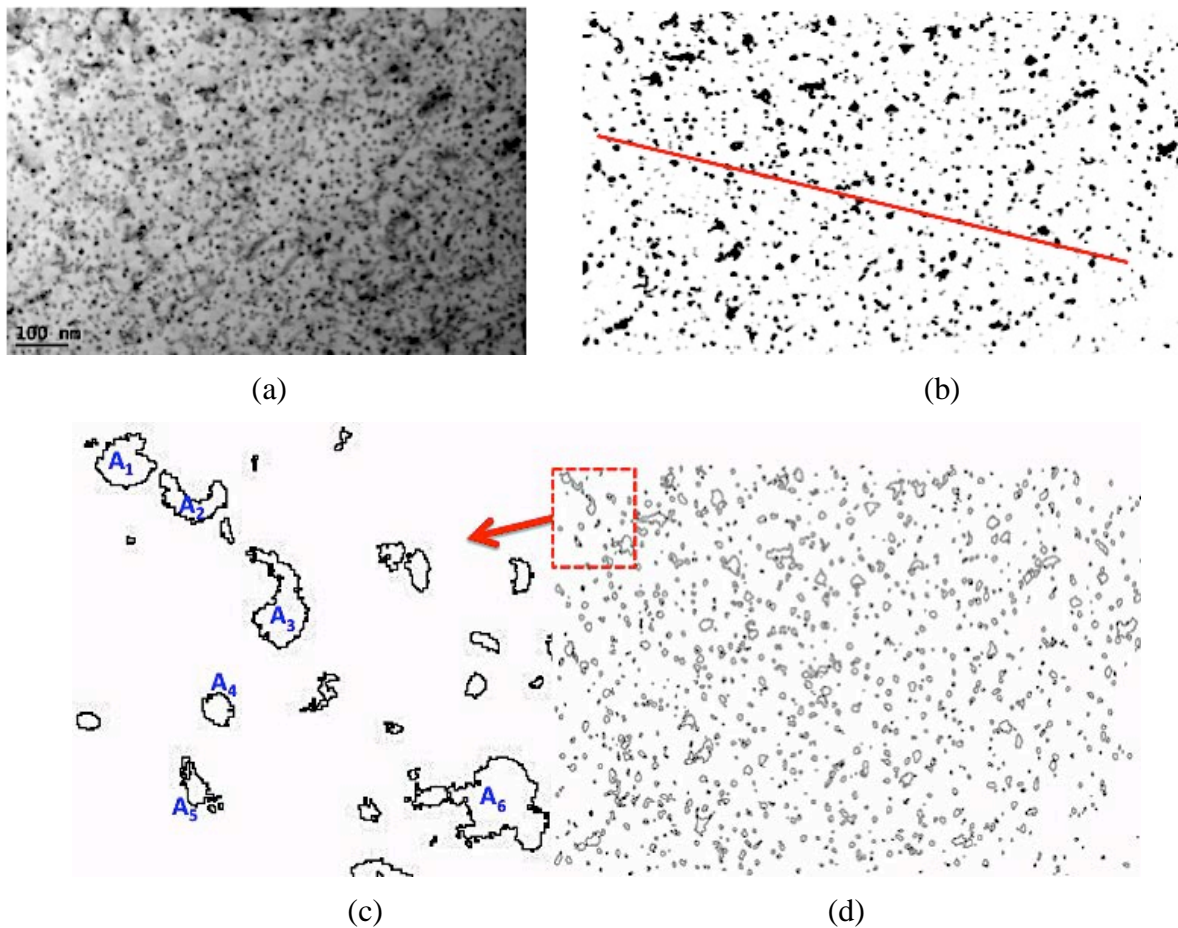


Figure 5–12 Schematic presentation of image analysis procedure on the relatively low magnification bright field TEM micrographs for the area measurements of the Nano-sized particles.

Example for these Nano-scale is the strengthening precipitates forming during the age hardening process that are only observed in the TEM micrographs; here in this study the mean free path between these strengthening precipitates is measured by the following

Equation 5–6, which is analytically obtained based on the assumption of Gaussian distribution of presumably spherical precipitates using the Kocks statistical theory and computer simulations for the bypassing or Orowan mechanism [121].

$$\tilde{\lambda}_{Volume} = 1.15 * \left(\sqrt{\frac{2 * \pi}{3 * f_v}} \right) * (ECR) \quad \text{Equation 5-6}$$

5.7 HEAT TREATMENTS PROCEDURES AND EQUIPMENT

Table 5–3 presents the various heat treatment procedures used in this study for the Al-7xxx CDS alloys. The various heat treatment procedures such as solutionizing (T4), annealing (T4+O), and peak-aged hardening (T6) heat treatments were carried out on the uniaxial tensile test specimens based on the prior art that are found from the existing background literature for the Al-wrought alloys. The heat treatment procedures were carried out in the electric furnaces, equipped with an internal fan in order to maintain the isothermal condition inside the furnace within 2°C of the set temperatures. For solutionizing (T4) heat treatment, the temperature was set at 477 °C that is about ~6°C below the mean solidus temperature (incipient melting point) and was measured separately by the thermal analysis during solidification process. The samples for thermal analysis of each casting part were sectioned from the in-gate and riser areas for re-melting and cooled down inside the furnace with a very slow rate of about 0.1 °C.s⁻¹, in order to obtain thermal curves during solidification.

Table 5–3 Typical heat treatment/temper conditions used for the tensile test-bars cast samples from the Al-7xxx alloys that are selected for the CDS experiment in this study.

Temp	Alloys	Solution treatment		Natural Ageing		Artificial Ageing (T6)				Ref.	
		T4		NA		Step 1		Step 2			
		Temp (°C)	Time (hr)	Temp (°C)	Time (hr)	Temp (°C)	Time (hr)	Temp (°C)	Time (hr)		
F (as-cast)	All	None		RT	>96	None		None			
O*	All	None		None		413	2	Slow Cooled to RT at 20°C/hour			
T4	All	477	24	RT	>96	100	6	140	15	[169, 170, 171]	
	Al-3.5Zn-0.8Mg-0Cu										
	Al-3.5Zn-1.62Mg-0Cu										
	Al-5.2Zn-1.7Mg-0Cu										
	Al-6.6Zn-1.7Mg-0Cu										
PAC†	Al-3.8Zn-2.2Mg-1.7Cu										
(T6)	Al-5Zn-2Mg-1.3Cu					120	24	None			[5,172, 173,174, 175]
	Al-6.5Zn-1.5Mg-2Cu										
	Al-5.8Zn-2.2Mg-2.5Cu										
	Al-9.97Zn-2.4Mg-0.9Cu										

*O → Annealed

†PAC → Peak-Aged Condition

Figure 5–13 presents the typical thermal regime of the electric-resistance furnaces used for this study and for the heat treatment processes used for the Al-7xxx CDS castings. Two types of furnaces were used: (1) the large size furnace equipped with internal fan with a forced air convection system and (2) the small size furnace with no internal or external convection assistance (fan), i.e., working only with the natural air convection. The temperature recordings were started immediately after the thermocouples inserted into the furnace. The thermocouples were embedded within the gauge section of uniaxial tensile bars during temperature recording, until the end of the isothermal heat treatments (24 hours at 477°C for solutionizing heat treatment). This is shown in Figure 5–13 (a). The incubation time before reaching the isothermal condition of 477°C in the large sized furnace (with forced air convection or internal fan) is about 3.3 minutes, which is roughly about 5 times faster than that of the small sized furnace (with natural air convection) with about ~16.6 minute heating up time. This is shown in Figure 5–13 (b).

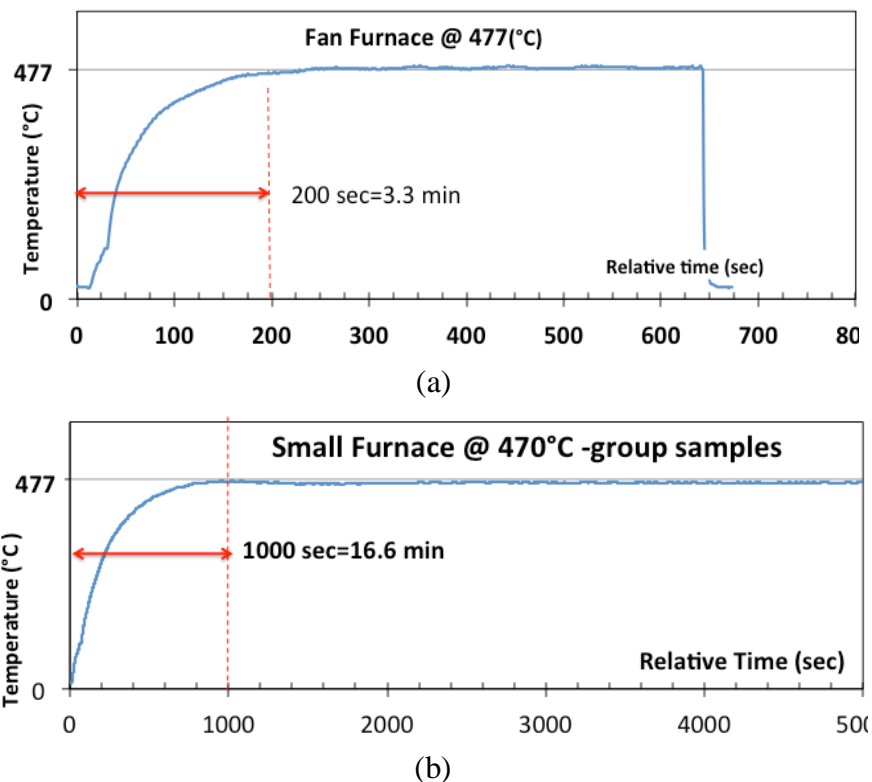


Figure 5–13 Typical heat-up curves obtained by the embedded thermocouples inside tensile bar samples inserted into the electric resistance furnaces for the isothermal solutionizing temperature at 477°C for 24 hours: (a) the thermal curve for the large sized furnace with forced air convection that is equipped with internal fan; and (b) thermal curve for the small sized furnace with natural air convection.

5.8 DIFFERENTIAL SCANNING CALORIMETRY (DSC) TESTS

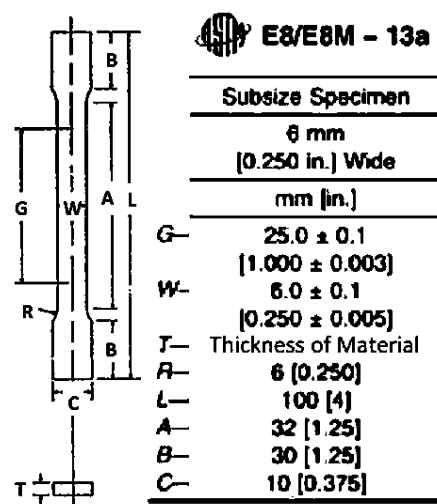
Further, the Differential Scanning Calorimetry (DSC) experiments were conducted according to the ASTM standard no. E793 – 06 (Reapproved 2012) at a heating rate of 10 °C/min using an average mass of between 25 to 30 mg of a few representative samples from the AA 7050 CDS castings in various tempers for the purpose of validating the solidus temperatures (or incipient melting points) that is likely to occur prior to solutionizing (T4) heat treatment. The result was further validated with data from the background literature [176]. A heat flux type

DSC test was employed in which the samples used were cut off from the gauge length section of the uniaxial tensile specimen of the Al-7xxx alloys that were cast using the CDS process coupled with tilt pour gravity casting (TPGC) machine. The DSC samples were in the various heat treatment conditions such as solutionizing (T4), artificial age hardening (T6) or/and annealed (O) (Table 5–3).

5.9 UNIAXIAL TENSILE TESTS

The Al-7xxx CDS cast samples were subjected to the uniaxial tensile test under various heat treatment conditions such as, as-cast (F), solutionizing (T4), annealing (O), peak aged (T6) heat treatment conditions. Prior to the heat treatments and uniaxial tension test, the CDS cast samples have undergone the mandatory inspection stages, including a visual inspection for macro-scale hot tearing on the cast sample surface and microstructural observations to ensure the non-dendritic morphology of the primary Al phase. It is noteworthy, all the CDS castings in this study were deemed successful without any hot tearing phenomena and a non-dendritic primary Al phase in the microstructure. The uniaxial tensile test specimens of the Al-7xxx alloys were cast by means of the CDS technology using Tilt Pour Gravity Casting (TPGC) machine, as shown in Figure 5–6. The uniaxial tensile-test specimens were designed according to the ASTM B557 (Figure 5–7). Prior to the uniaxial tensile test, the specimens were heat treated with various heat treatments listed in Table 5–3. The uniaxial tensile test were conducted by means of an Instron 8800 Machine (Model 312 MTS) with the MTS Frame equipped with a 250 kN Load cell coupled with an on-line Extensometer of 50 mm gauge length, which is connected to an on-line data acquisition system; the uniaxial tensile tests were executed with a load speed of 1mm/min.

For benchmark, the sub-sized tensile specimens according to ASTM standard number E8/E8M–(13a) were machined from the 0.25”X6.0” plates of the AA 7050 wrought (rolled) products* (provided by the manufacturer†) in an over aged heat treatment condition of T7651‡.



* In the form of 0.25”X6.0” plates in the over aged (T7) condition according to the ASM 4201B T7561 heat treatment standard.

† Alabama Specialty Products, Inc., Munford, AL, USA, www.alspi.com.

‡ It is noteworthy according to the ASM 4201B T7561 heat treatment standard, the plate was aged to an over aged condition, T7, solution heat treatment, quenching, and an artificial aging treatment beyond peak strength, aiming to enhance the corrosion resistance (exfoliation corrosion resistance: T76); further, the plate was subsequently stress relieved by stretching 1/2 to 3% (T7651) [178].

Figure 5–14 Sub-sized tensile specimen, according to ASTM standard number E8/E8M–(13a), used for the AA 7050 wrought (rolled) products.

5.10 HARDNESS TEST

The hardness tests on the Al-7xxx CDS samples were carried out using both macro-hardness and micro-hardness test methods. The hardness evolutions occurring during the natural ageing and artificial ageing processes were measured both for the bulk hardness and localized hardness evolution in the Al-matrix by the macro-hardness and micro-hardness test methods, respectively. The macro hardness measurements were measured by a Hardness Rockwell F and B (HRF or HRB) method using a steel ball indenter of 1/16-inch diameter with a 60 and 100-kg force, respectively. For the micro hardness measurements, the Hardness Vickers (HV) test method with pyramid shaped indenter was used with a 25-gram force. A minimum distance of at least 5 times the indenter diameters was kept constant between each of the indentations in both macro- and micro- hardness test measurements. Each hardness point on the age hardening curves is an arithmetic average of at least 15 hardness data point.

5.11 DENSITY MEASUREMENT TEST

The density measurement is a well-known quantitative method to measure the porosity content of a sample material, especially in an industrial field. There are two common ways to measure the density of the material: Helium pycnometry and Archimedes test methods. In Helium pycnometry, the surface area of the connected porosity inside the tested component is measured; whereas, Archimedes method is simply measure the aggregate porosity content of the test component [177].

The Archimedes test method is the one most commonly used method in the casting industries. Among various standard procedures explaining the Archimedes test method, ASTM D792-91 and ASTM B328-96 are specifically designed for plastics parts and structural metallic material, respectively [177]. Figure 5–15 shows a schematic presentation of the Archimedes experimental set-up, used for this study to measure the porosity content of the Al-7xxx CDS castings.

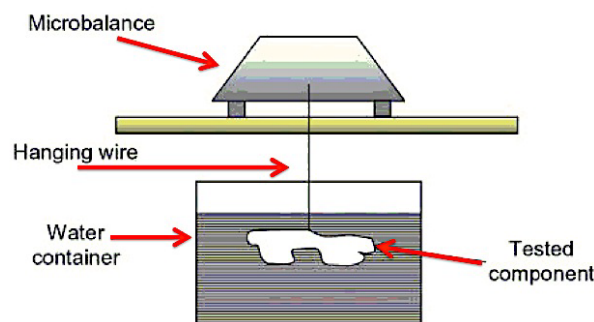


Figure 5–15 The schematic presentation of experimental set-up for porosity measurements based on Archimedes test method [177], which was used for density measurements of the Al-7xxx CDS alloys in this study.

The test samples for density measurements for the Archimedes test method were weighed both in the air (i.e., the dry weight) and in the water (i.e., the wet weight). The Archimedes buoyancy principle suggests that the weight of a solid objects with fixed shape immersed in a fluid decreases from that measured in ambient dry air due to the buoyancy force imposed

from the fluid to the body of solid object in a direction opposite to the gravity force. This weight loss is equal to the weight of displaced fluid. When the fluid used is water with a density of nearly 1000 kg.m^{-3} , the weight of water displaced by the sample is equivalent to the volume of the sample immersed. The porosity in the sample is obtained by evaluating the difference between the theoretical and measured densities of the samples. The theoretical density is calculated by Equation 5–7.

$$\rho_{\text{Theoretical}}^{\text{Material}} = (\text{Total mass of atoms in unit cell}) / (\text{Total volume of unit cell}).$$

or

$$\rho_{\text{Theoretical}}^{\text{Material}} = \frac{(n * A)}{(V_c * N_A)}$$

Equation 5–7

Where n is number of atoms per unit cell for each element in the alloy; and A is the atomic weight (g/mol) and V_c is volume of unit cell for each element in the alloy (a^3 for a cubic microstructure); and N_A is the Avogadro's number ($=6.023 \times 10^{23}$ atom/mol). Table 5–4 presents the theoretical density values calculated from the Equation 5–7 for each alloying elements in the Al-7xxx alloys, such as Al, Cu, Mg and Zn; further in Table 5–4 the detail data used for the density calculation are also tabulated from literature background [31,68].

Table 5–4 Detail data used for the calculation of the theoretical density of each element in the Al-7xxx (Al-Zn-Mg-Cu) alloy composition that are found in the background literature [31,68].

Element	Atomic Radius (Å)	Crystal Unit				Density (gr/cm ³)	Reference		
		Structure	Lattice Parameter		Volume Atoms#				
			(Å)					(Å) ³	
Al	1.43	FCC	$a = \frac{4R}{\sqrt{2}}$	4.04	4	$V = 16\sqrt{2}R^3$	66.17	2.71	[31,68]
Cu	1.28		$\frac{4.04}{\sqrt{2}}$	3.62					
Mg	1.60	HCP		3.20		46.3	1.74		
Zn	1.33	$\frac{c}{a} = \sqrt{\frac{8}{3}}$	$a = 2R$	2.76	2	$V = 8\sqrt{2}R^3$	29.7	7.13	

The theoretical densities of each of the nine alloys in this study (refer to Table 5–1) could be evaluated by the weighted average of the theoretical densities of all the elements in the alloy as shown in Equation 5–8 [178]:

$$\rho_{\text{Theoretical}}^{\text{Alloy}} = \frac{\sum_{i=\text{Al,Zn,Mg,Cu}} (wt\%)_i}{\sum_{i=\text{Al,Zn,Mg,Cu}} \left\{ \frac{(wt\%)_i}{\left(\rho_{\text{Theoretical}}^i \right)} \right\}} = \frac{100}{\sum_{i=\text{Al,Zn,Mg,Cu}} \left\{ \frac{(wt\%)_i}{\left(\rho_{\text{Theoretical}}^i \right)} \right\}}$$

Equation 5–8

Where the (wt%) is the weight percentage of respective element in the alloy as measured by GDOES* chemistry test method and $\rho_{theoretical}^i$ is the theoretical density of element i in the alloy. The difference between the two densities of the alloy sample, i.e., *theoretical* and *experimental* densities is a viable approximate measure of all the possible microscopic voids or porosity content existing inside the sample. The porosity in an alloy sample can be evaluated by Archimedes method [177] represented by Equation 5–9; wherein, the weight of the sample in dry air (W_{air}) and water (W_{wet}) is measured by controlled experiments.

$$Porosity(Vol.\%) = (100\%) \cdot (\rho_{Theoretical} - \rho_{Experimental}) = (100\%) \cdot \left(\rho_{Theoretical} - \left[\frac{W_{air}}{W_{air} - W_{wet}} \cdot \rho_{water} \right] \right) \quad \text{Equation 5-9}$$

It is notable that the spread *theoretical density* of the alloy is evaluated from the respective standard deviation of each solute element as measured by the GDOES; the solvent element, Al in the alloy is evaluated as a balance so as to maintain the conservation of elemental mass in the alloy. Hence, the maximum theoretical density of an alloy would be when the standard deviations of the solute elements whose theoretical density is higher than the solvent element, Al is considered as maximum and those of the solute elements whose theoretical density is less than Al is considered as minimum, and vice-versa. The effect of chemistry variation in the GDOES measurement on the *theoretical* and *experimental* density values are tabulated in the Table 5–5 and Table 5–5, respectively; further, Figure 5–16 and Figure 5–17 presents the comparative bar graphs for density and porosity measurements of all the nine alloys, respectively.

Table 5–5 The effect of chemistry variation measured by GDOES for each alloying element in the alloy composition of each of the nine alloys on the theoretical and experimental density and porosity measurements.

No.	Alloy Designation	Elemental Alloy Composition (wt%)						Density				Porosity (%)	
		Zn		Mg		Cu		Theoretical		Experimental			
1	Al-3.5Zn-0.8Mg-0Cu	3.48	±0.30	0.79	±0.39	0.027	±0.004	2.76	±0.0236	2.74	±0.0023	1.89	±1.18
2	Al-3.5Zn-1.62Mg-0Cu	3.53	±0.44	1.62	±0.42	0.020	±0.008	2.75	±0.0291	2.73	±0.0017	1.97	±1.46
3	Al-5.2Zn-1.7Mg-0Cu	5.18	±0.48	1.73	±0.08	0.022	±0.001	2.77	±0.0198	2.75	±0.0015	1.83	±0.99
4	Al-6.6Zn-1.7Mg-0Cu	6.56	±0.45	1.72	±0.12	0.022	±0.001	2.80	±0.0204	2.78	±0.0036	2.01	±1.02
5	Al-3.8Zn-2.18Mg-1.7Cu	3.81	±0.18	2.18	±0.05	1.75	±0.07	2.78	±0.0107	2.75	±0.0023	2.78	±0.54
6	Al-6.5Zn-1.5Mg-2Cu	6.47	±0.16	1.47	±0.07	2.01	±0.05	2.84	±0.0107	2.82	±0.0019	2.43	±0.53
7	Al-5.8Zn-2.2Mg-2.5Cu	5.82	±0.30	2.22	±0.05	2.53	±0.19	2.83	±0.0207	2.80	±0.0067	2.65	±1.03

* Glow Discharge Optical Emission Spectroscopy (GDOES)

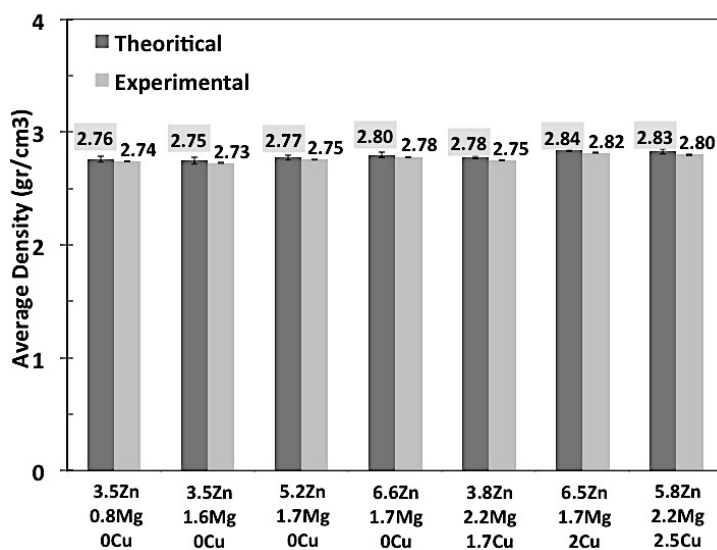


Figure 5–16 The effect of chemistry variation measured by GDOES for each alloying element in the alloy composition of each of the nine alloys on the theoretical and experimental density.

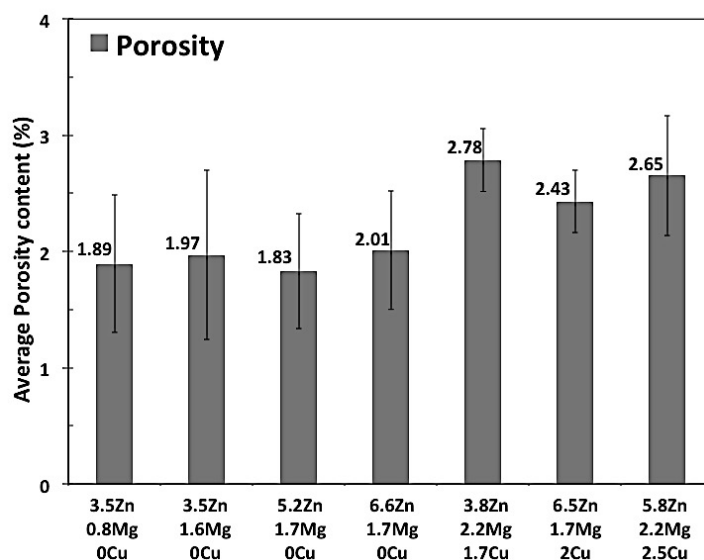


Figure 5–17 The effect of chemistry variation measured by GDOES for each alloying element in the alloy composition of each of the nine alloys on porosity measurements.

6 RESULTS AND DISCUSSION

In this chapter, the experiment results of this study with the Al 7xxx alloy will be presented and discussed using the following subtitles:

- The CDS Experiments using Tilt Pour Gravity Casting (TPGC)
- Microstructure Characterization
- Precipitation Hardening
- Uniaxial Tensile Properties
- Fractography after Tensile Test

6.1 THE CDS EXPERIMENTS USING TILT POUR GRAVITY CASTING (TPGC)

Figure 6–1 and Figure 6–2 presents the typical microstructure of the AA7050 CDS cast samples obtained from the center of the gauge section in a uniaxial tensile test bar in as-cast and T4 heat treatment conditions, respectively; wherein the predominantly non-dendritic morphology of the primary Al phase is observed; the light grey area is the non-dendritic primary Al matrix and the dark grey coupled with the nearly black phases are the eutectic phases.

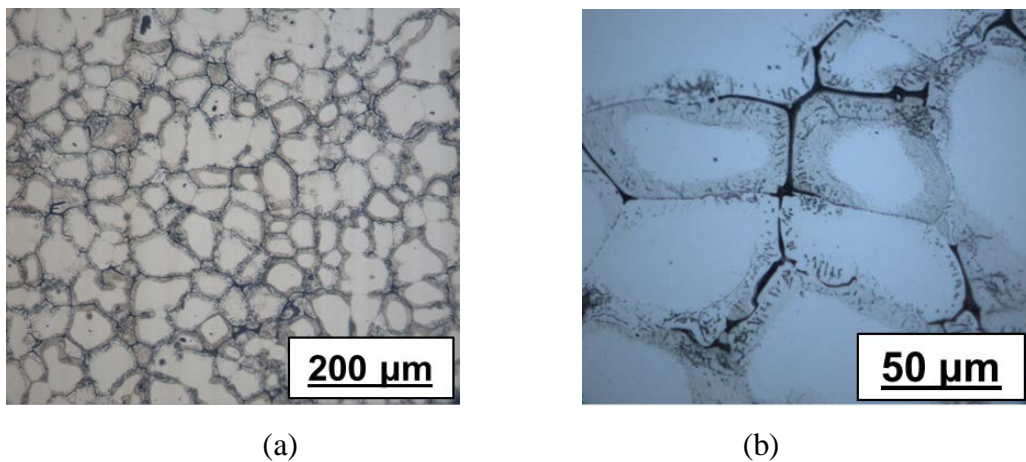


Figure 6–1 Typical light optical micrographs of as-cast samples for AA7050 alloy cast using the TPGC process with CDS technology. (a) and (b) show two different image magnifications.

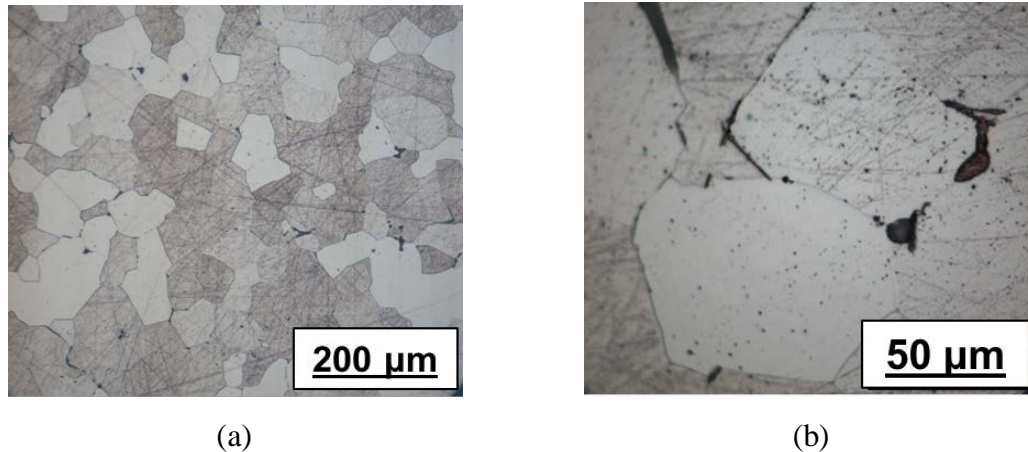


Figure 6–2 Typical light optical micrographs of solution heat treated (T4 temper) of the AA7050 castings shown in Figure 6–1. (a) and (b) show two different image magnifications.

In Figure 6–2, the morphology of the primary Al phase is non-dendritic after heat treatment to the T4 temper; the heat treatment resulted in significant solute redistribution resulting coupled with dissolution and transformation of the secondary solidifying phases in both nature and morphology; the details of such changes will be presented and discussed in the subsequent sections of this dissertation. In Figure 6–1, precipitates evolved from solute element micro-segregation during solidification, also known as coring effect could be observed at the boundary regions of the grains and secondary solidifying phases; these precipitates were dissolved and solute elements homogenized after the solutionizing treatment, as shown in the Figure 6–2.

6.2 MICROSTRUCTURE CHARACTERIZATION

In this section, the results of rigorous qualitative and quantitative characterization of the microstructural features in the casting of Al 7xxx alloys under various heat treatment temper conditions occurring in the Al-7xxx CDS alloys during various heat treatment conditions are presented and discussed. The primary tools used for such characterization are Differential Scanning Calorimetry (DSC), light optical microscope, Scanning Electron Microscope (SEM) and Transmission Electron Microscope (TEM).

6.2.1 Differential Scanning Calorimetry (DSC)

Figure 6–3 (a) and (b) present typical thermal data by the Differential Scanning Calorimetry (DSC) experiment obtained during heating process at $0.17\text{ }^{\circ}\text{C}\cdot\text{s}^{-1}$ for the two different as-cast (F) samples of AA7050 CDS alloy obtained from different cast shots; wherein the incipient (or none-equilibrium) melting temperature for the two different as-cast (F) samples are shown to be occurring at nearly the same temperature range of 482.12°C and 482.63°C , respectively. Further, Figure 6–4 presents the results of the DSC experiments for various heat treated samples of the AA 7050 alloy: F, T4, F+O and T4+O tempers; wherein the incipient melting temperatures of different heat treated samples of the AA 7050 CDS alloys are shown to be occurring at roughly the same temperature range of $\sim 482^{\circ}\text{C}$. The samples for the DSC experiments shown in the Figure 6–3 and Figure 6–4 were randomly selected from various sections of various castings to validate the constancy of the alloy composition in the CDS castings. Among all the alloys in this study, the composition of Al-5.8Zn-2.2Mg-2.5Cu (AA7050) with its highest copper content would exhibit the lowest temperature for the first incipient melting event during the heating process to the T4 treatment temperature because all

the low melting secondary phases evolved during solidification are those with Cu in them; Figure 6–5 presents the DSC experiment data of various alloy compositions from the Al-7xxx CDS samples selected for this study showing that the incipient melting in alloys with higher Cu content is the least. This coupled with the consistency in the incipient melting temperatures (Figure 6–3 and Figure 6–4) of samples in both the F and T4 temper conditions for the AA7050 alloy was used to select a constant temperature of 477 °C for the T4 treatment temperature of the alloys in this study in order to prevent any incipient melting during the T4 heat treatment.

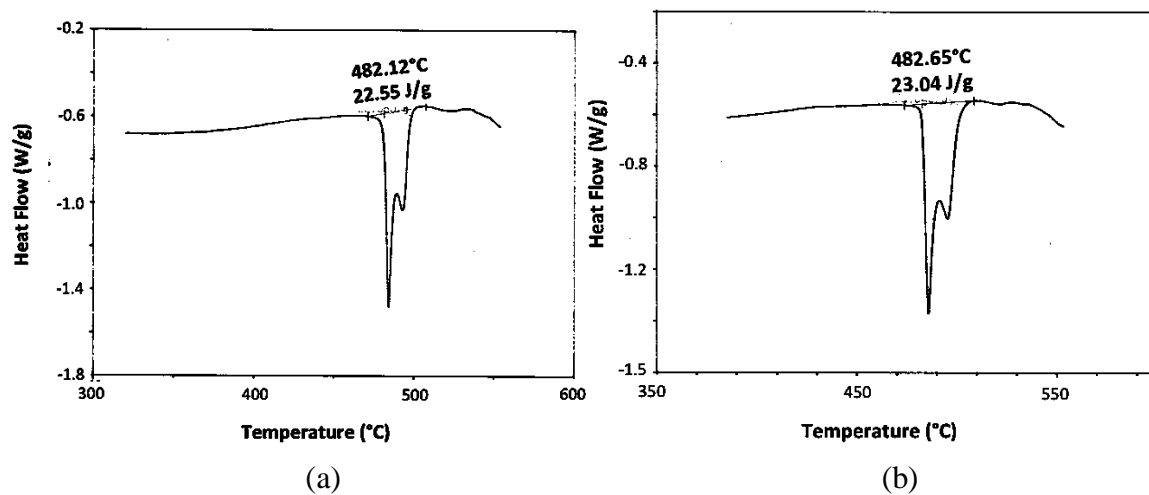


Figure 6–3 DSC thermal data, obtained during a heat-up experiment at $0.17\text{ }^{\circ}\text{C}\cdot\text{s}^{-1}$, for two different as-cast (F) samples of AA 7050 alloys cast by the CDS technology using tilt pour gravity casting (TPGC) machine; note that the DSC samples were selected from different CDS experiment cast-batches.

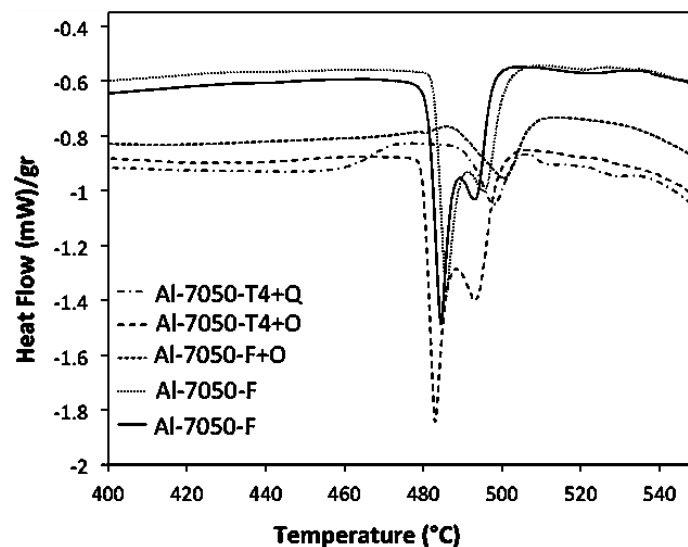


Figure 6–4 DSC thermal data, obtained during a heat-up experiment at $0.17\text{ }^{\circ}\text{C}\cdot\text{s}^{-1}$, for various heat treatment conditions of AA 7050 CDS alloys such as, as-cast (F), solutionized (T4) and annealed (F+O and T4+O) heat treatment samples; note that the DSC samples were selected from different CDS experiment cast-batches.

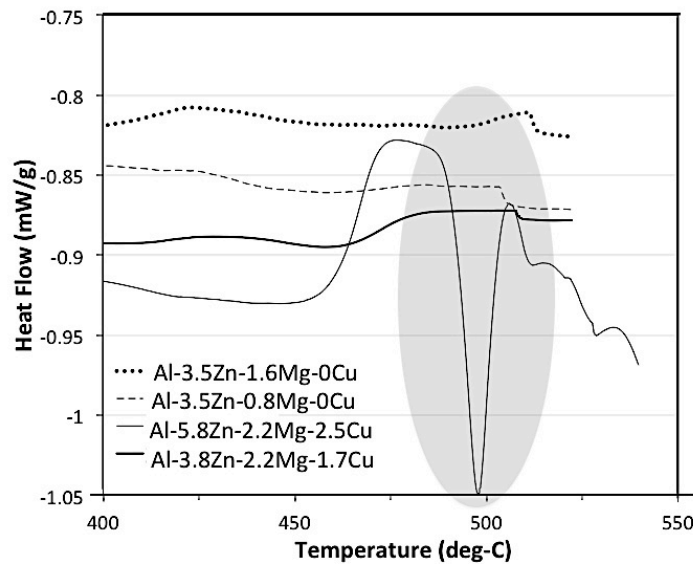


Figure 6–5 Typical thermal data for DSC experiments, obtained during heating at $0.17\text{ }^{\circ}\text{C}\cdot\text{s}^{-1}$, of various compositions of Al-7xxx CDS alloys selected for this study. The demarcated region shows the incipient melting of secondary phases in the alloy Al-5.8Zn-2.2Mg-2.5Cu.

Based on the nature of precipitation reactions occurring during the heating process of the DSC experiment, the DSC thermal curves show different features: *endothermic* reactions (i.e., absorbing heat during the reaction) and *exothermic* reactions (i.e., releasing/evolving heat during the reaction). The endothermic reactions appear as a drop from the starting base line of the DSC curve such as dissolution reactions of precipitates and melting phenomenon. Examples for typical endothermic reactions are shown in Figure 6–6:

- Dissolution of precipitates shown by $O \rightarrow A$ (dissolution of GP Zones) and $E \rightarrow F \rightarrow G$ (dissolution of η' - η - T -precipitates, and
- Start of melting of phases (incipient melting) shown by H.

In Figure 6 6, typical exothermic reactions are shown by segment $A \rightarrow B \rightarrow C$ denoting the evolution of precipitates of η' / η -phases. Table 6–1 presents the summary of the events that occur during the heating of a sample in the DSC experiments shown in Figure 6–6 wherein, the three main areas of interests marked Area #1, Area #2 and Area #3 denote the evolution and transformation of strengthening precipitates, dissolution of these precipitates and incipient melting of secondary phases, respectively. The results shown in Figure 6–6 and Table 6–1 were obtained from comparing the features of the DSC experiments in this study with those presented in Robson [72] shown in Figure 4–12 and Starink et al [72] shown in Figure 4–13 and Table 4–5

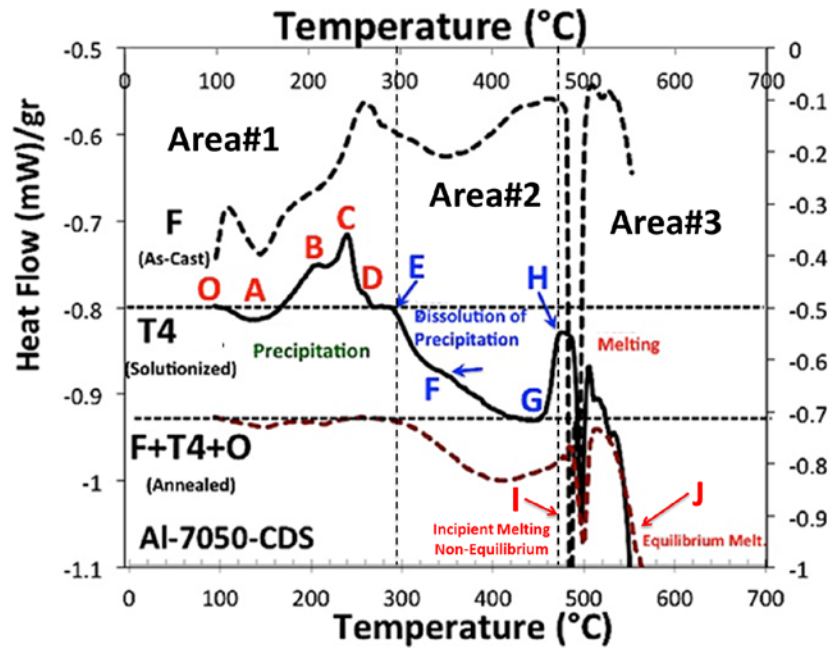


Figure 6–6. DSC thermal data, obtained during a heat-up experiment at $0.17\text{ }^{\circ}\text{C}\cdot\text{s}^{-1}$ for various heat treatment conditions of AA 7050 CDS alloys such as, as-cast (F), solutionized (T4) and annealed (T4+O) heat treatment samples; samples were selected from random CDS experiment castings.

Table 6–1 Explanations for typical precipitation and dissolution reactions during the DSC experiment shown in Figure 6–6.

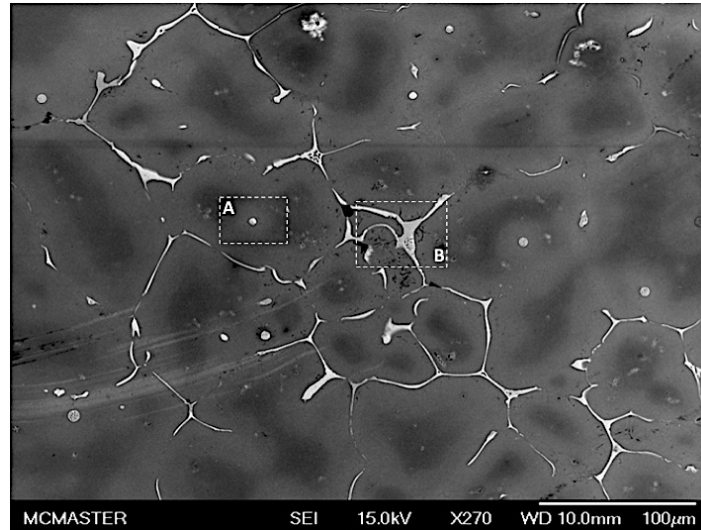
Segment	Temperature Range ($^{\circ}\text{C}$)	Possible phase transformation
Area #1		Evolution and transformation of precipitates
Area #2		Dissolution of Precipitates
Area #3		Incipient Melting
O	Below 110	The base line of the thermal (DSC) curve
O \rightarrow A	110~140	Dissolution of GP Clusters
A \rightarrow B	140~200	Formation of η' - (and/or η -) phases
B \rightarrow C	200~240	Formation of η - (and/or T-) phases
C \rightarrow D	250~280	Returning to base line
E \rightarrow F	280~340	Dissolution of η' -/ η - (and/or T-) phases
F \rightarrow G	340~420	Dissolution of η' -/ η (and/or T-) minimizes
G \rightarrow H	420~460	Returning to base line
I	485~500	S-phase melting (None-equilibrium/Incipient Melting)
J	~520	Equilibrium Melting (Equilibrium Solidus Temperature)

In the annealed (T4+O) heat treated samples shown in Figure 6–6, the microstructure of the sample at the start of the DSC test consisted of the relatively large, equilibrium and incoherent η - (MgZn_2) or Sigma ($\text{Mg}(\text{Zn,Cu,Al})_2$) phases in the Al-matrix. After the O

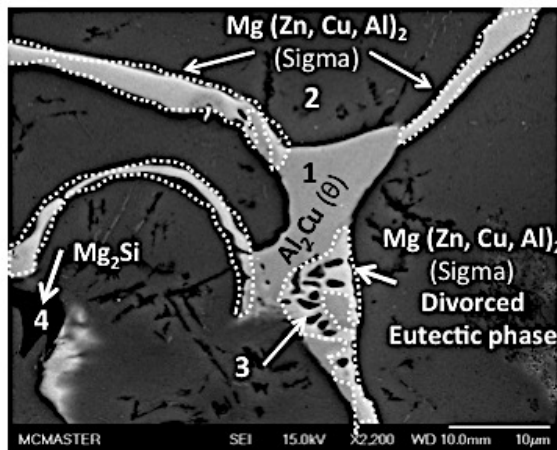
treatment, there is negligible amount of alloying elements in solid solution and available vacancies in the nearly pure Al matrix to present favorable energetics for the evolution and transformation of any strengthening precipitates. Hence, in Figure 6 6, there is no appreciable deviation from the thermal base line of the DSC experiment for the annealed (T4+O) samples; shown by segments O→A→B→C→D→E. In Figure 6 6, the dissolution phase in all the samples initiated at around 300 °C and the incipient melting of the S phase at around 485 °C.

6.2.2 Scanning Electron Microscopy (SEM)

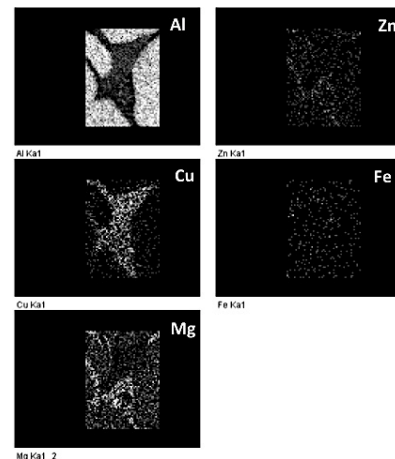
The possible non-equilibrium phases in the as-cast condition of CDS 7050 samples obtained using TPGC process are presented along with the elemental map of specified areas in Figure 6–7. The respective EDS chemical analyses of specified areas are tabulated in Table 6–2. The region demarcated as *B* in Figure 6–7 denotes the secondary phases solidified from the last remaining liquid during solidification. In Figure 6–7 (b), in Region A, the brightest areas are either the ternary eutectic structure of Al (α) + MgZn₂ (η -phase)/Mg(Zn,Cu,Al)₂ (Sigma-phase) or quaternary structure with CuMgAl₂ (S-phase). The second brightest area within the grain boundary (eutectic area) is the binary Al₂Cu (θ -phase). In Figure 6–7 (b), it shows a system of eutectic phases in Al + Al₂Cu (θ) + Mg (Zn,Cu,Al)₂ (Sigma) along with the Mg₂Si phase evolved due to the Si impurity in the alloy; the respective quantitative elemental compositions of these phases are shown in Table 6–2 along with the respective phase identification numbers. Figure 6–7 (c) and Figure 6–8 (a) and (b) show the typical examples for the system of the eutectic phases solidified from the last solidifying pockets of liquid wherein the Al + CuMgAl₂ (S) + Mg (Zn,Cu,Al)₂ (Sigma) forms during the eutectic reaction; in Figure 6–7 (c), it is shown that the Cu₂FeAl₇ phases have evolved along with the formation of the eutectic phases due to the Fe impurity in the alloy; the respective quantitative elemental compositions of these phases are shown in Table 6–2 along with the respective phase identification numbers [179]. Further, Figure 6–9 presents the typical SI SEM micro segregation observed in the as-cast (F) samples of Al-7050 alloy cast by the CDS process coupled with TPGC machine; where the micro segregation in the samples are presented by the compositional profile obtained by the EDS detector of the SEM.



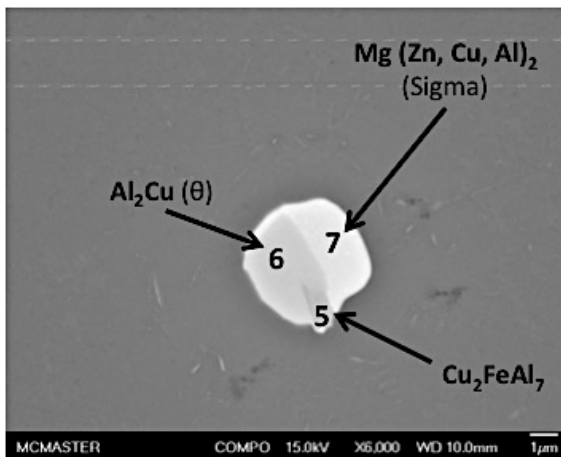
(a)



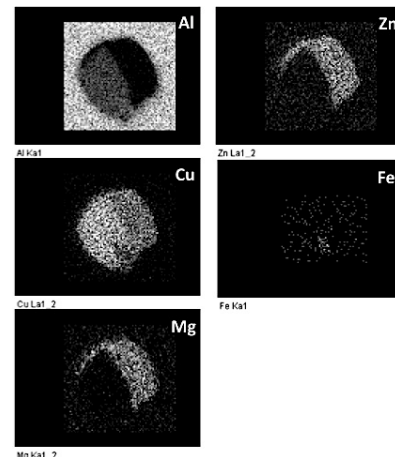
(b)



(c)



(d)



(e)

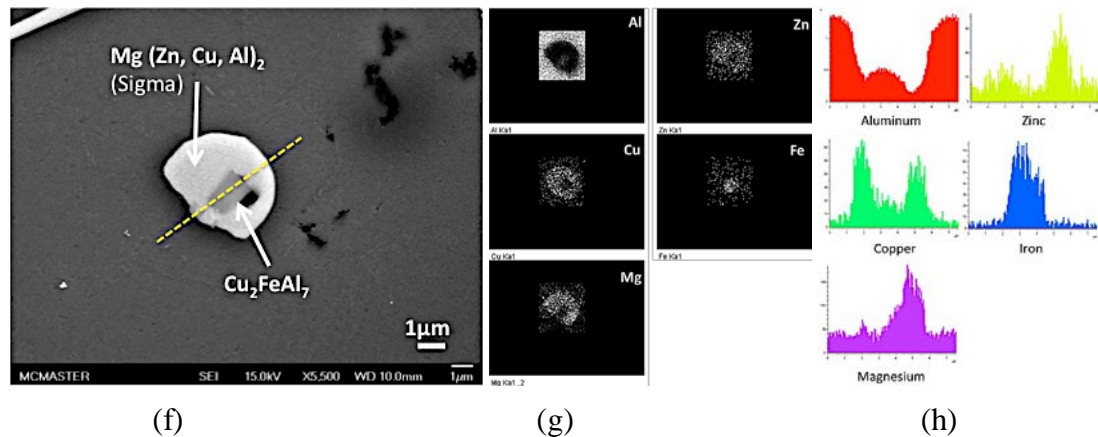


Figure 6–7 Secondary Electron (SE) SEM Image of AA7050 alloy in F temper. (a) Low magnification showing two regions of secondary phases evolved during solidification: A and B; (b) image along with the (c) elemental map of magnified section of phases in Region A of (b) image and elemental map of magnified section of phases in Region B which is solidified from the last remaining liquid during solidification; further in (d) and (f) the high magnified images for the Fe-bearing intermetallic phases are shown in the regions solidifying from the last part of remaining liquid, along with the elemental map of magnified section of phases.

Table 6–2 EDS elemental analyses of specified areas referenced in Figure 6–7

Phase ID	Al		Zn		Mg		Cu		Fe or Si		Possible Phase
	wt.%	at%	wt.%	at%	wt.%	at%	wt.%	at%	wt.%	at%	
1	45.45 (±0.39)	65.96 (±0.25)	1.63 (±1.15)	0.98 (±0.69)	0.45 (±0.12)	0.73 (±0.21)	52.46 (±0.67)	32.33 (±0.27)	-	-	Al ₂ Cu (θ)
2	17.58 (±0.69)	27.06 (±1.07)	29.60 (±1.65)	18.81 (±1.09)	18.59 (±0.85)	31.75 (±1.30)	34.23 (±1.71)	22.38 (±1.16)	-	-	Mg(Zn,Cu,Al) ₂ (Sigma)
3	36.21 (±4.26)	50.05 (±5.03)	24.99 (±1.65)	14.30 (±1.21)	13.44 (±1.68)	20.71 (±2.99)	25.36 (±1.33)	14.94 (±1.05)	-	-	Mg(Zn,Cu,Al) ₂ (Sigma)
4	14.75 (±9.78)	13.76 (±9.46)	-	-	49.43 (±6.43)	55.51 (±4.87)	0.31	0.134	Si:31.28 (±6.71)	Si:30.59 (±6.40)	Mg ₂ Si
5	46.86 (±0.75)	64.95 (±2.05)	6.11 (±1.50)	3.50 (±0.88)	2.59 (±1.41)	3.95 (±2.09)	29.04 (±7.03)	17.15 (±4.36)	Fe:13.44 (±4.70)	Fe:8.96 (±2.99)	Cu ₂ FeAl ₇
6	43.21 (±1.63)	63.47 (±1.87)	4.33 (±2.76)	2.63 (±1.70)	1.14 (±0.77)	1.86 (±1.26)	51.24 (±2.85)	31.98 (±1.90)	-	-	CuMgAl ₂ (S)
7	19.14 (±4.75)	29.33 (±6.15)	34.00 (±5.52)	21.83 (±4.29)	17.05 (±1.03)	29.28 (±2.31)	29.82 (±2.59)	19.56 (±1.62)	-	-	Mg(Zn,Cu,Al) ₂ (Sigma)

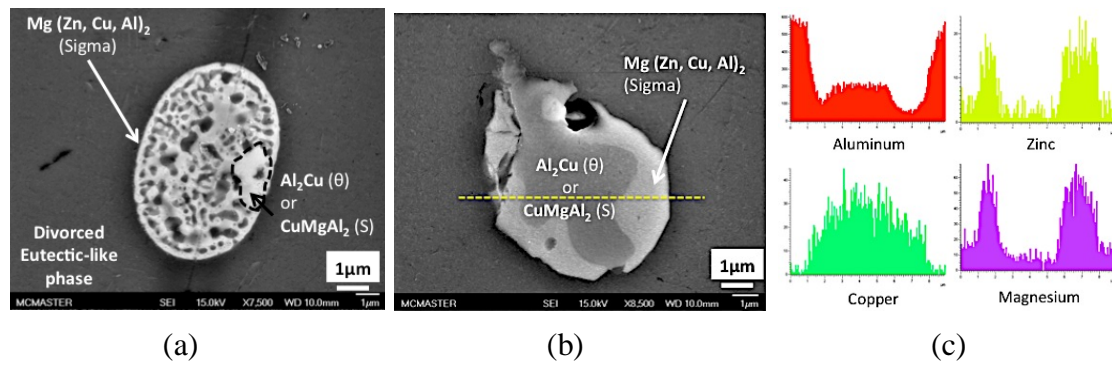


Figure 6–8 SEI from SEM of eutectic phases in the last drop of solidified liquid in AA 7050 CDS in the F condition showing (a) and (b) the divorced eutectic-like structure of S- θ - and Sigma phases; along with (c) the elemental line scan obtained by the EDS detector from (b).

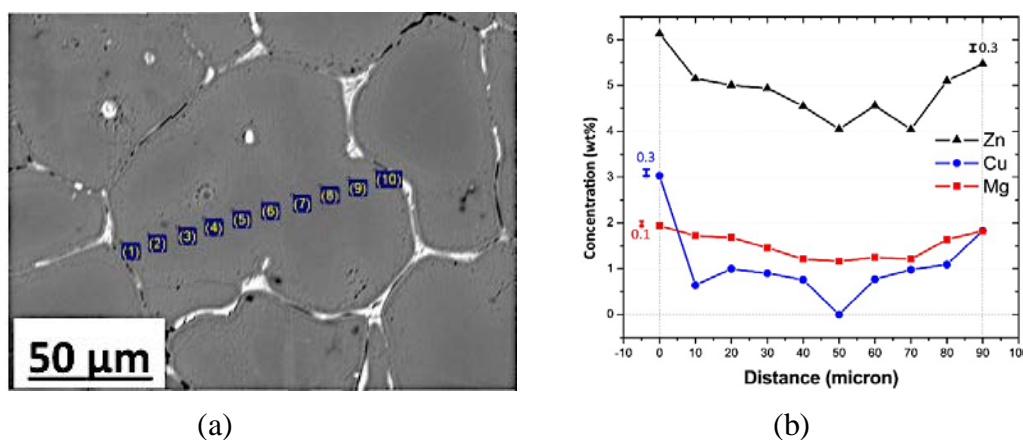
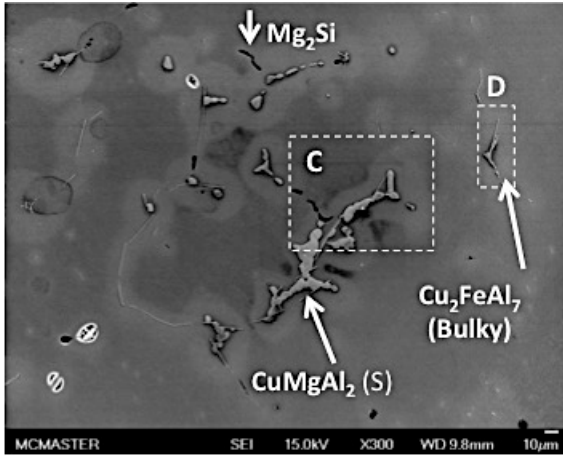


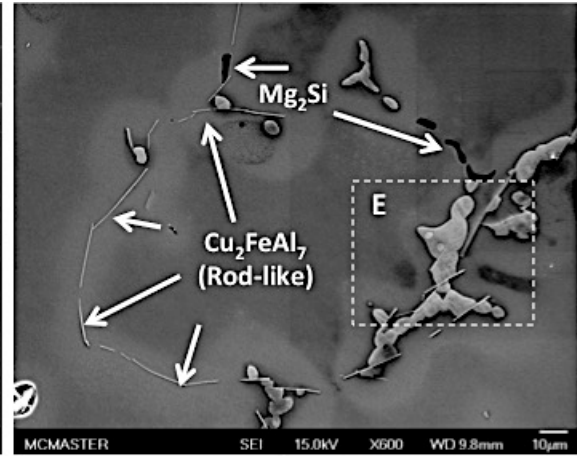
Figure 6–9 Backscattered Electron micrographs of a typical as-cast microstructure of AA7050 CDS castings (a); and (b) the concentration profiles of the alloying elements (Zn, Mg and Cu) plotted for a primary Al-grain demarcated on the BSE image (a) by means of EDS line scan results.

6.2.2.1 Solution treatment (T4) of AA 7050 CDS alloy

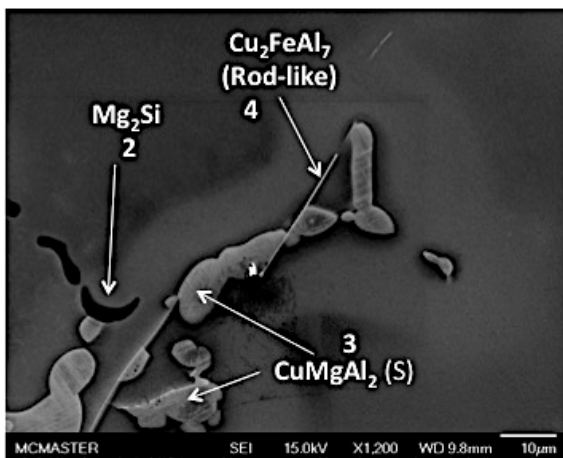
SEM images of the solutionizing condition (T4) of AA7050 castings using TPGC process and the elemental map obtained by EDS are presented in Figure 6–10. The corresponding EDS analyses of specified areas are tabulated in Table 6–3. In addition to the dominant S-phase shown in Figure 6–10 (c), a small volume fraction of entrapped spherical areas of Sigma phase within the S-phase areas are also observed. As expected, other impurity phases are also observed in the homogenized microstructure, namely, Cu_2FeAl_7 , FeAl_3 and Mg_2Si . This is consistent with the observation of iron containing intermetallic particles in the bulk-shape and plate-like morphologies, as illustrate in Figure 6–10. It is noteworthy that the SEM observation showed that Fe-bearing intermetallic phases ($\text{Cu}_2\text{FeAl}_7/\text{FeAl}_3$) that are evolved during the solution (T4) treatment can appear in two distinct morphologies: (1) the plate- or needle-like morphologies (Figure 6–18); and/or (2) the bulky or irregular shapes (Figure 6–19).



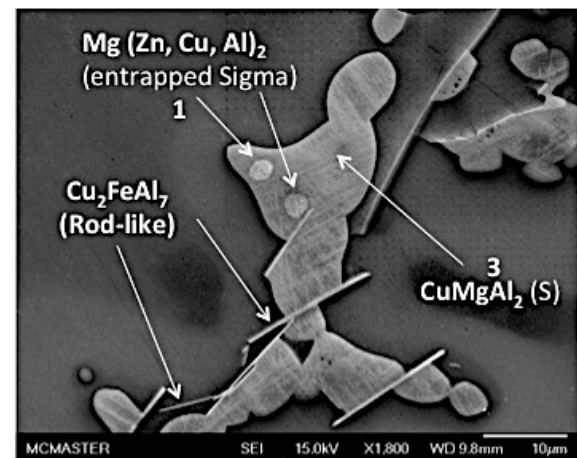
(a)



(b)



(c)



(d)

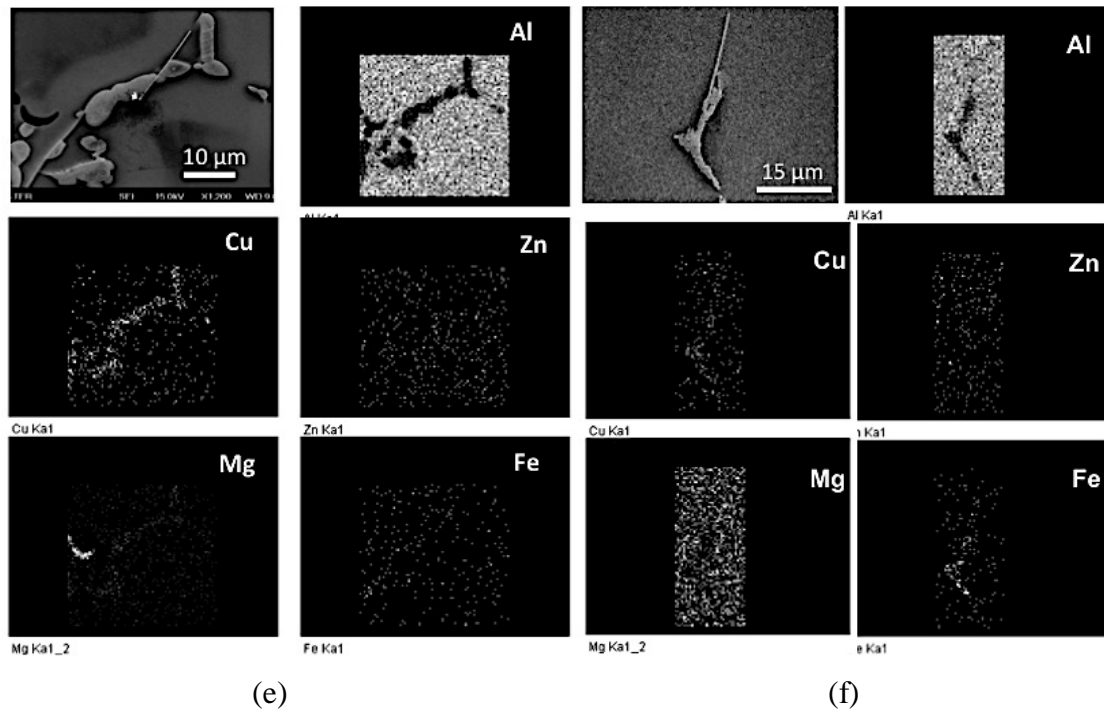


Figure 6–10 SEI from SEM of phases in the grain boundary areas of AA 7050 CDS in the T4 condition showing the dominant S-phase, plate like Iron-containing intermetallic phases and the other impurity phase of Mg_2Si . The corresponding elemental map is also presented.

Table 6–3 EDS elemental analysis of the spots referenced in the SEM images in Figure 6–10.

Elem.	Zn		Mg		Cu		Fe/Si		Al		Possible Phase
Area	wt.%	at%	wt.%	at%	wt.%	at%	wt.%	at%	wt.%	at%	
1	32.10	20.37	18.59	31.70	31.5	20.56	-	-	17.82	27.37	$Mg(Zn, Cu, Al)_2$ (Entrapped Sigma)
	± 1.66	± 1.19	± 0.3	± 0.8	± 0.86	± 0.42			± 1.195	± 1.66	
2	-	-	48.50	51.452	0.32	0.132	Si:32.58	31.84	13.55	13.50	$MgSi_2$
			± 7.73	± 6.37			± 5.41	± 5.10	± 10.48	± 10.1	
3	3.81	2.14	14.93	22.56	45.11	26.11	-	-	36.14	49.19	$CuMgAl_2(S)$
	± 0.6	± 0.33	± 0.68	± 0.78	± 2.20	± 1.73			± 1.40	± 1.23	
4	2.11	1.18	0.32	0.48	34.73	20.65	Fe:12.61	8.52	50.21	69.19	Cu_2FeAl_7 (Rod-like)
	± 1.58	± 0.85	± 0.5	± 0.87	± 6.36	± 4.63	± 2.15	± 1.76	± 6.61	± 5.18	

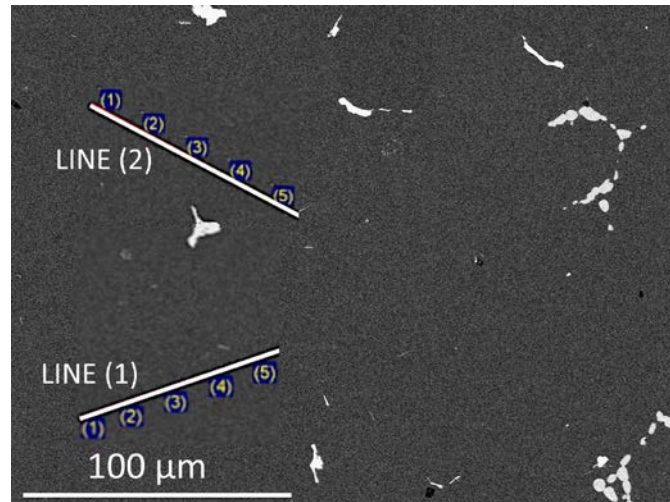
The typical SEM results represented the T4 microstructure of the AA7050 CDS alloy (Figure 6–10) present the following salient observations and analyses of the transformation in the microstructure during solution (T4) heat treatment:

- The Al_2Cu (θ) phase that were previously existed at grain boundary areas as typical eutectic region in the as-cast (F) microstructure (Figure 6–7) does not feature in the T4 heat-treated microstructure (Figure 6–10). The Fe, Mg and Cu atoms have redistributed by homogenization during the solutionizing (T4) treatment and further reacted with the Al_2Cu (θ) phase to form the $CuMgAl_2$ (S) (bulky) and Cu_2FeAl_7 (rod-like or bulky-shape) phases. It is noteworthy that the morphology of Fe-intermetallic phases during the

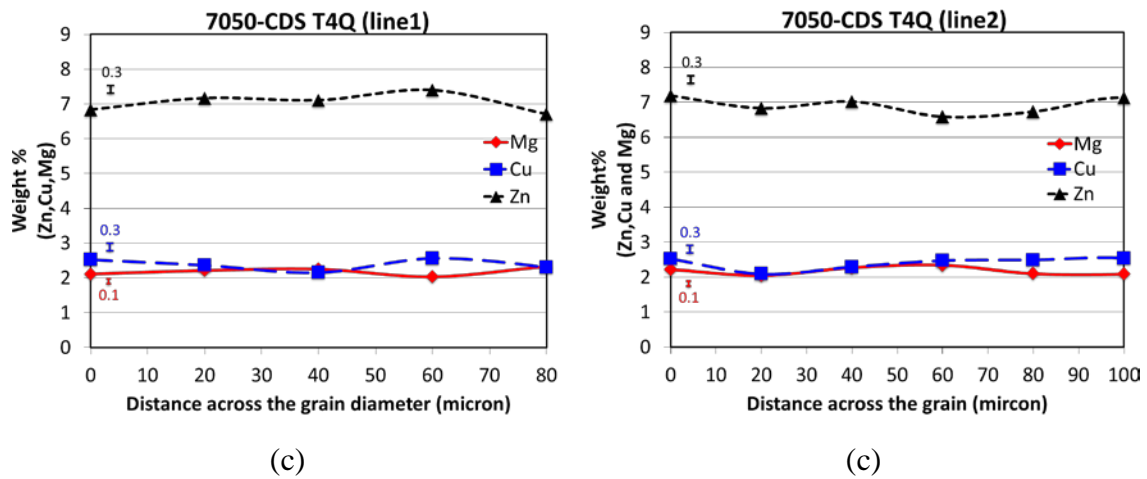
solution (T4) treatment has changed to a more plate-like shape as compared to merely bulky shaped observed in as-cast (F) condition (Figure 6–7 (d)).

- The divorced morphology of eutectic phases ($\text{Mg}(\text{Zn,Cu,Al})_2$ (Sigma)), that were previously observed in the as-cast (F) microstructure of the AA 7050 CDS alloy (Figure 6–7) seem to be almost entirely dissolved back into the primary Al-matrix grains during the solutionizing (T4) heat treatment except for a very small fraction that is remained as entrapped areas inside the CuMgAl_2 (S) (bulky) phases during the quenching stage of the T4 treatment (Figure 6–10). This is in agreement with Robson's work [72], wherein the simulated fraction volume of the equilibrium precipitation phases during the solid-state transformation is reported as a function of the sample temperature during the solutionizing treatment (Figure 4–12), wherein the S- CuMgAl_2 phase is predominant at temperatures higher than 400°C while the Sigma- $\text{Mg}(\text{Zn,Cu,Al})_2$ phase is predominant at temperatures below 200°C in the T4 microstructure of AA 7050 alloy. This was further confirmed by the quantitative (image analysis) measurements on the SEM micrographs of solutionized (T4) AA7050 alloy that large portion ($\sim 3.8\%$) of phases that were previously formed at the grain boundary areas evolves during solutionizing (T4) heat treatment as S- CuMgAl_2 phase with relatively large bulky morphology ($\sim 10\ \mu\text{m}$) while other alloying elements segregation that were previously observed in the GB area in F microstructure are dissolved back into primary Al-grains as supersaturated solid solution.
- The fraction volume of the impurity intermetallic phases of Cu_2FeAl_7 , FeAl_3 and Mg_2Si are reported in the literature to be less than 1% [81]. This is in agreement with our quantitative image analysis measurements ($\sim 1.5\%$) on the SEM micrographs of solutionized (T4) AA7050 CDS samples. Since these phases, especially the Fe-bearing ones evolve morphologically during the solutionizing heat treatment (T4) from a bulky shape in the non-equilibrium as-cast structure into needle or plate-like morphology in the T4 microstructure; they do play an important role in the mechanical properties of the materials.

Further, Figure 6–16 presents the micro segregation of the alloying elements in the Al-7050 alloy cast samples in T4 heat treatment by means of compositional profile obtained by EDS detector in SEM; wherein the homogeneously distributed alloying element after T4 heat treatment is shown for a line scan length of the typical average grain size in T4 samples.



(a)



(c)

(c)

Figure 6–11 Typical Backscattered (BS) SEM Image of AA7050 CDS cast sample in T4 heat treatment condition along with the composition profile of the alloying element (such as Zn, Mg and Cu) obtained by the EDS detector.

6.2.2.2 Annealing treatment (O)

The annealing treatment (O) was carried out to throw more light on the sequence of precipitation reactions after the solutionizing treatment (T4). The microstructure obtained after the annealing process (T4+O) of the AA7050 castings using TPGC process are shown in Figure 6–12 along with the EDS elemental analyses on numbered areas demarcated in Figure 6–12 are presented in the Table 6–4.

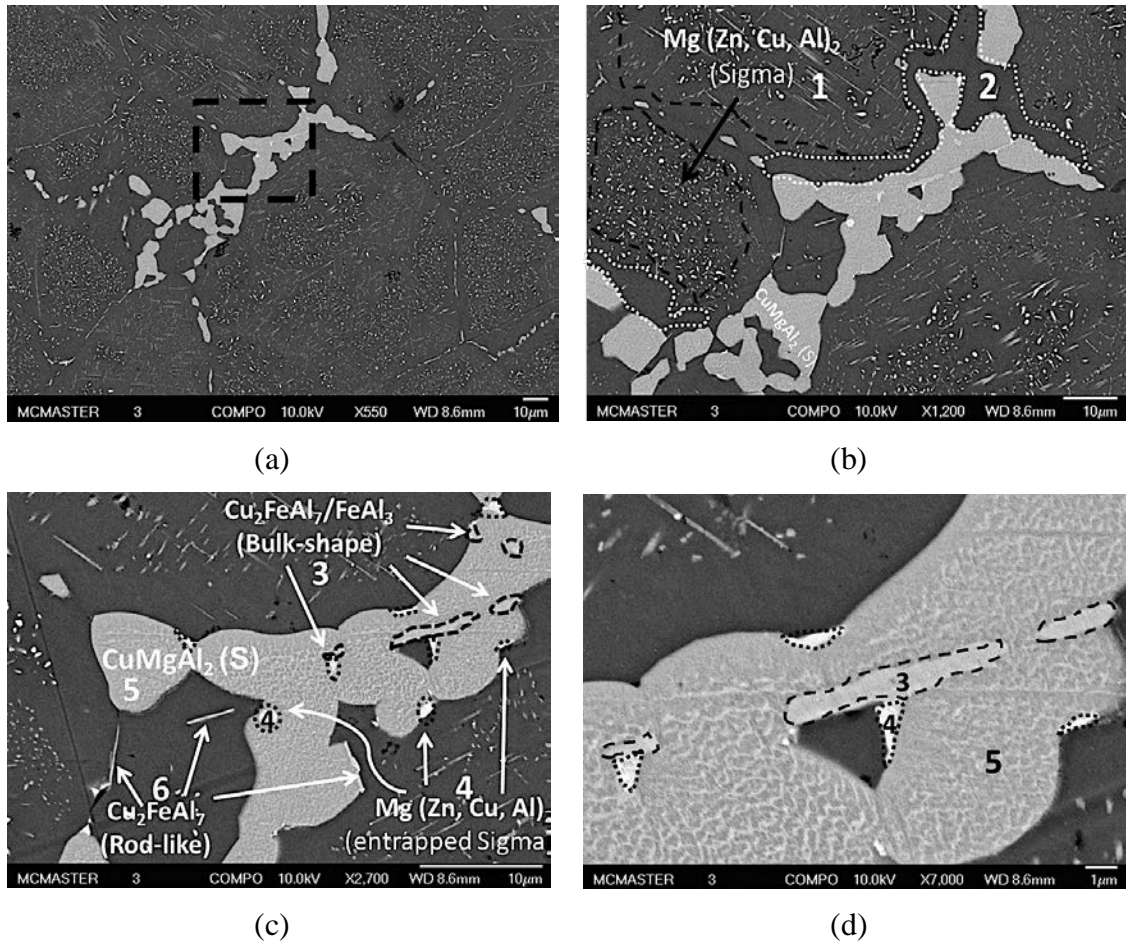


Figure 6–12 SEI by SEM from the grain boundary and central areas of annealed and furnace cooled solutionized cast parts of CDS 7050 with elemental map by EDS detector. (a) to (d) show images of microstructure with progressively increasing magnification of areas demarcated in the respective images.

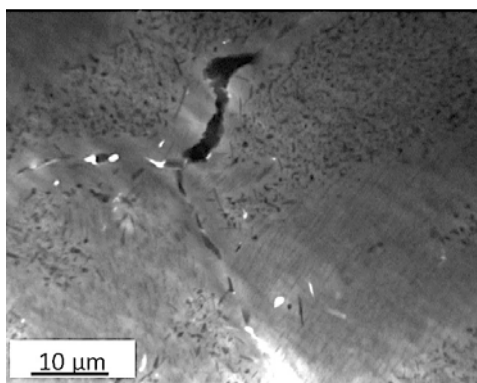
Table 6–4 EDS elemental analysis of the numbered regions shown in Figure 6–12.

Eleme.	Zn		Mg		Cu		Fe		Al		Possible Phase
	wt%	at%	wt.%	at%	wt.%	at%	wt.%	at%	wt.%	at%	
1	28.84	15.19	7.57	10.72	7.4	3.97	-	-	56.2	70.11	$Mg (Zn, Cu, Al)_2$ (Sigma phase)
	± 7.17	± 4.69	± 2	± 3.45	± 0.82	± 0.58			± 9.58	± 8.57	
2	5.47	2.33	1.04	1.19	-	-	-	-	93.5	96.48	Depleted Solid Solution PFZ around GB
	± 0.64	± 0.28	± 0.19	± 0.22					± 0.73	± 0.42	
3	3.5	1.73	2.57	3.95	32.91	19.06	9.78	7.01	55.2	71.78	Cu_2FeAl_7 (Bulk-shape)
	± 0.20	± 0.10	± 0.97	± 1.5	± 10.06	± 7.09	± 3.97	± 2.36	± 13.45	± 10.71	
4	48.2	30.49	16.05	27.35	13.81	9.19	-	-	21.94	32.98	$Mg (Zn, Cu, Al)_2$ (Sigma-phase on S phase at GB)
	± 4.09	± 3.39	± 1.64	± 3.52	± 6.91	± 5.11			± 7.41	± 9.39	
5	-	-	15.65	23.48	48.22	27.69	-	-	36.14	48.84	$CuMgAl_2$ (S-phase at GB)
			± 0.45	± 0.60	± 1.22	± 0.98			± 1.12	± 1.10	
6	3.5	1.7	2.8	4.1	24.8	13.3	8.6	5.2	64.1	79.1	Cu_2FeAl_7 (Rod-like)
	± 0.2	± 0.1	± 0.4	± 0.4	± 7.1	± 4.5	± 2.1	± 1.6	± 8.9	± 7.2	

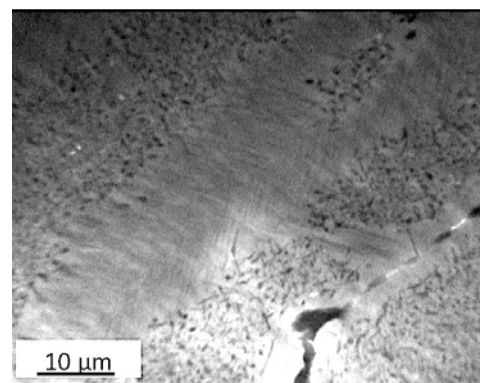
The low magnification image presented in Figure 6–12 (a) illustrates a significant fraction of coarse intermetallic phases decorating the grain boundaries after the annealing process; and these phases have been retained from after the T4 solution treatment process prior to the O treatment. The phases defining the grain boundaries have been identified as either insoluble iron-containing phases (Cu_2FeAl_7) and/or undissolved S phases (CuMgAl_2). Table 6–4 presents the EDS results of numbered areas designated in Figure 6–12. The Fe-bearing intermetallic phase appears in two distinct morphologies as can be seen in Figure 6–12 (c) and (d): irregular bulky and acicular (needle) or plate like shapes.

In addition to the large intermetallic phases at the grain boundary, Figure 6–12 (a) and (b) shows significant volume fraction of intermetallic phases precipitated within the primary Al grains during the annealing treatment (O); the morphological pattern of these precipitates resemble the “widmanstatten pattern” [68] and have been termed as pseudo-widmanstatten precipitates in this dissertation. These precipitates form during the slow cooling process in the annealing treatment wherein adequate thermodynamic and kinetic environments are presented for the complete precipitation of intermetallic phases with incoherent interfaces in the primary Al matrix. An observable feature of these pseudo-widmanstatten precipitates is that they evolve in groups of preferred orientation with the grain as typically demarcated in Figure 6–12 (b) by thick broken black line boundaries. The EDS elemental analyses (detailed in the Table 6–4) of these pseudo-widmanstatten precipitates coupled with the information gathered from the background literature [72] suggest that they are all the Sigma phase ($\text{Mg}(\text{Zn},\text{Al},\text{Cu})_2$), which are rich in Zn.

Apart from the homogeneously distributed fine-scale hardening particles (*pseudo-widmanstatten* precipitates), as shown in Figure 6–13, precipitates can be seen in the form of *high aspect ratio needles* distributed in the central areas of the grains away from the grain boundaries. The EDS elemental analyses of these needles detailed in the Table 6–4 reveal that they are rich in zinc content and their size, morphology and distribution suggest that they are most probably Sigma-phase precipitates. Following the slow furnace cooled annealing process; iron-containing intermetallic phases were observed to have been unaffected in size and morphology.



(a)



(b)

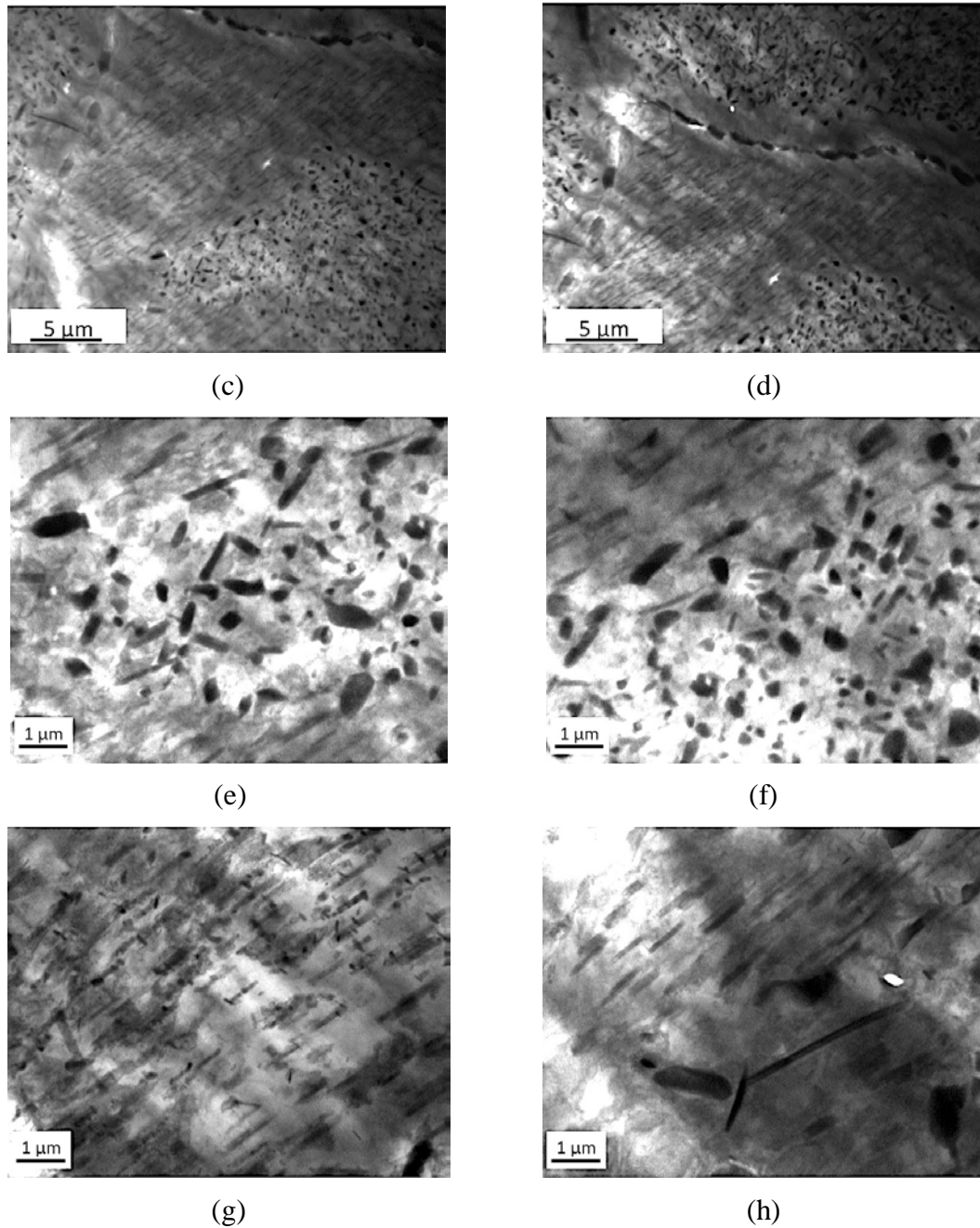


Figure 6–13 Typical TEM bright field micrograph in various magnifications of the relatively large and fully incoherent η - MgZn_2 phases forming during the annealing (O) grains in AA7050 CDS cast sample; showing the pseudo-widmanstaaten pattern of η - MgZn_2 phases, precipitated within the grain area and away from PFZ forming around the grain boundary areas; note that the precipitate of a group are aligned in a different orientation relationship with respect to the neighbouring group.

6.2.2.3 Intermetallic phases of Al 7050 alloy

Table 6–5 presents the list of phases forming in the Al-5.8Zn-2.2Mg-2.5Cu alloy that are determined by the various methods such as the equilibrium and non-equilibrium (Scheil-Guliver) simulations, and quantitative image analysis using experimental results (SEM micrographs) obtained for the F and T4 tempers. Figure 6–14 presents the comparative phase fractions bar graphs for the various phases forming in the Al-5.8Zn-2.2Mg-2.5Cu alloy (listed in Table 6–5) obtained from simulations and quantitative image analysis for the F and T4 heat treatment condition. The specific effect of copper on the microstructure of the Al-7xxx

alloys can be attributed to two factors: (1) the effect of copper on formation of new phases θ (Al_2Cu) and S (Al_2CuMg); and (2) the effect of copper on the morphological evolution of the secondary phases such as S-phases and impurity Fe-bearing phases during solidification and subsequent T4 heat treatment processes.

Table 6–5 Typical list of phases forming in the Al-7050 alloy that are determined by equilibrium and non-equilibrium simulations, and experimental results for the Al-5.8Zn-2.2Mg-2.5Cu alloy in F and T4 heat treatment condition.

Scheil-Gulliver (Simulation*)	Equilibrium (Simulation*)	As-Cast (Experiment)	T4 (Experiment)
α -Al	α -Al	α -Al	α -Al
Sigma (Mg (Zn,Cu,Al) ₂)	-	Sigma (Mg(Zn,Cu,Al) ₂)	Sigma (Mg (Zn,Cu,Al) ₂)
Mg ₂ Si	Mg ₂ Si	Mg ₂ Si	Mg ₂ Si
Al ₇ Cu ₂ Fe	Al ₇ Cu ₂ Fe	Al ₇ Cu ₂ Fe	Al ₇ Cu ₂ Fe
S (Al ₂ CuMg)	-	S (Al ₂ CuMg)	S (Al ₂ CuMg)
θ (Al ₂ Cu)	-	θ (Al ₂ Cu)	-

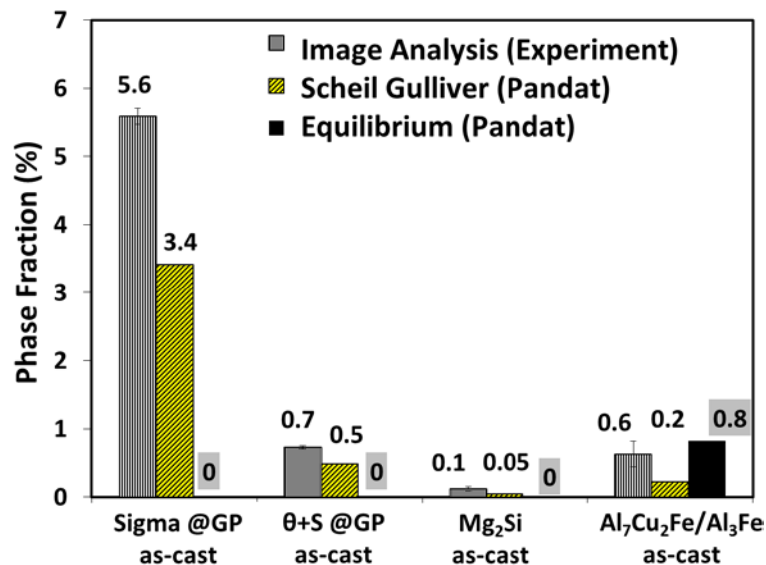


Figure 6–14 Comparison of the phase fractions for the various phases forming during the solidification process of AA7050 alloy: Sigma, S/ θ and the Fe- and Si-intermetallic phases, obtained using quantitative metallography on SEM micrographs and simulation using non-equilibrium Scheil-Gulliver solidification and equilibrium solidification (Pandata software).

Figure 6–15, Figure 6–16 and Figure 6–17 present the typical bar graphs of the particle size and fraction area of intermetallic phases (such as Al₇Cu₂Fe and Mg₂Si phases), eutectic phase (S-Al₂CuMg, θ -Al₂Cu and Sigma-Mg(Zn,Al,Cu)₂) in various heat treatment conditions such

* Pandat

as as-cast (F), solution heat treatment (T4) and annealed (O) heat treatment conditions, respectively. Table 6–6 presents the compositions of each type of the intermetallic phases, as measured by the EDS in SEM. In Figure 6–17, the Fe-containing intermetallic phases in the solution treatment (T4) condition of the AA 7050 CDS alloys that were found to be in the size range of 7 ~ 15 μm . It is noteworthy that the Fe-bearing intermetallic phases were observed in two distinct morphological shapes: (1) acicular shapes such as rod, needle or plate-like shapes (Figure 6–18); and (2) irregular bulky shapes (Figure 6–19).

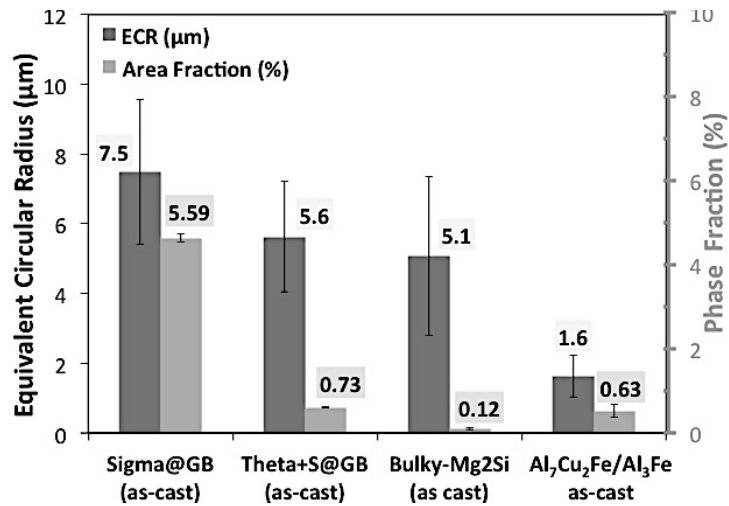


Figure 6–15 Typical particle size and phase fraction of various phases forming during the solidification process of AA7050 alloy, in the as-cast F temper: Sigma, S/ θ , and Fe- and Si-intermetallic phases.

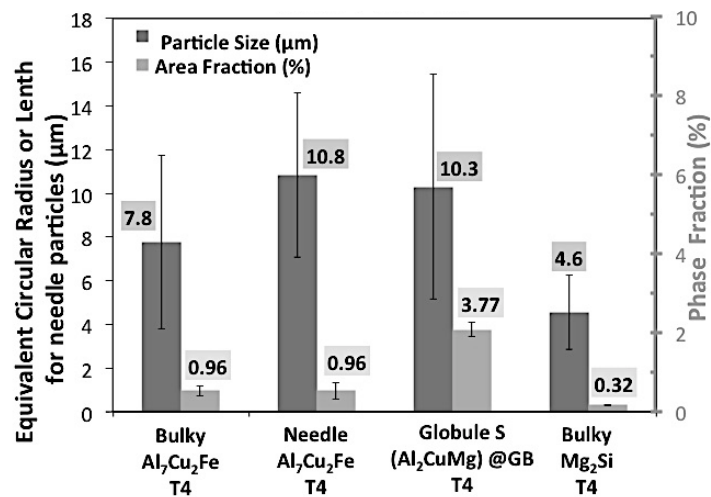


Figure 6–16 Typical size and fraction area distribution of impurity and secondary phases in the AA 7050-CDS casting in T4 temper.

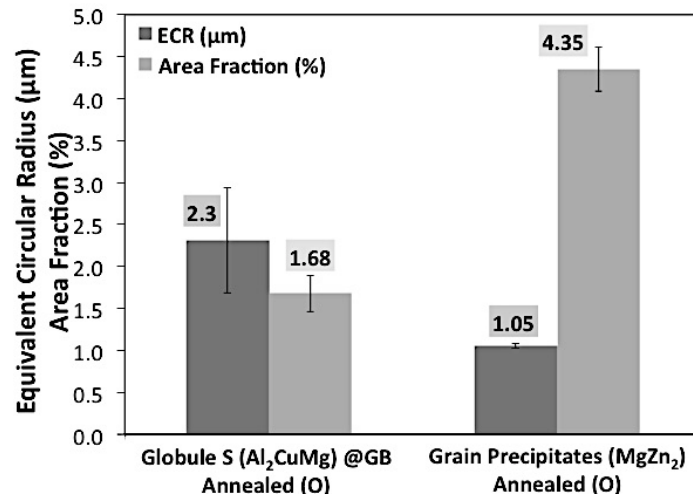
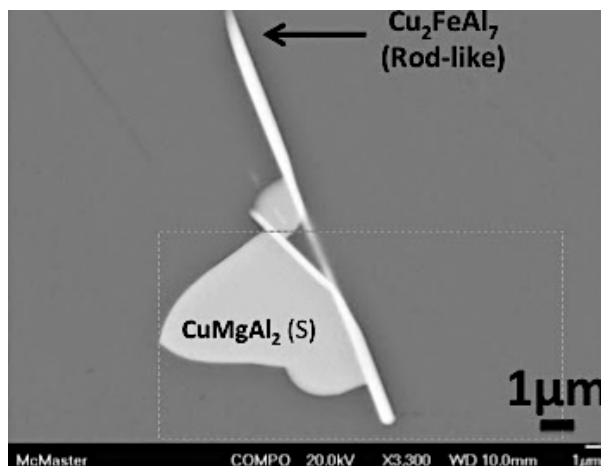


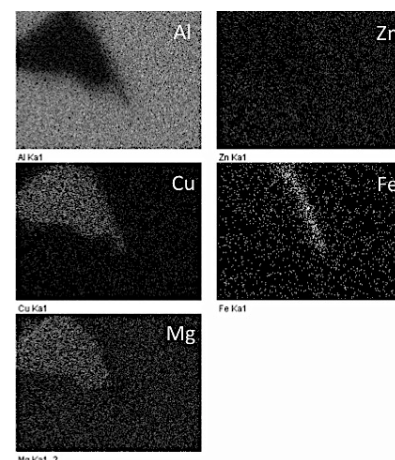
Figure 6-17 Typical particle size and phase fraction of various phases forming during the annealing (O) process (Sigma in the grain interiors and S at grain boundaries) measured by the image analysis on the SEM micrographs of the CDS castings of AA 7050 alloy in O temper.

Table 6-6 Particle size and fraction area distribution for impurity and secondary phases, measurements by image analysis on AA 7050-CDS in T4 and as-cast condition.

Phase ID (Temper)	Chemistry (wt.%)					Fraction Area (%)	Particle Size (μm)
	Al	Zn	Mg	Cu	Fe/Si		
Bulky-Al ₇ Cu ₂ Fe (as-cast)	50.21 (±6.61)	6.60 (±2.3)	3.33 (±1.7)	26.38 (±10.3)	Fe:14.13 (±7.9)	0.63 (±0.19)	1.63 (±0.60)
Bulky-Al ₇ Cu ₂ Fe (T4)	55.2 (±13.45)	4.20 (±2.9)	0.93	28.78 (±10.9)	Fe:11.91 (±4.9)	0.96 (±0.24)	7.75 (±3.97)
Needle-Al ₇ Cu ₂ Fe (T4)	64.1 (±8.9)	2.93 (±1.6)	-	36.75 (±9.6)	Fe:13.04 (±3.1)		10.83 (±3.75)
Bulky-Mg ₂ Si (T4)	13.55 (±10.48)	-	49.43 (±6.4)	0.31	Si:31.28 (±6.7)	0.32 (±0.03)	4.57 (±1.71)



(a)



(b)

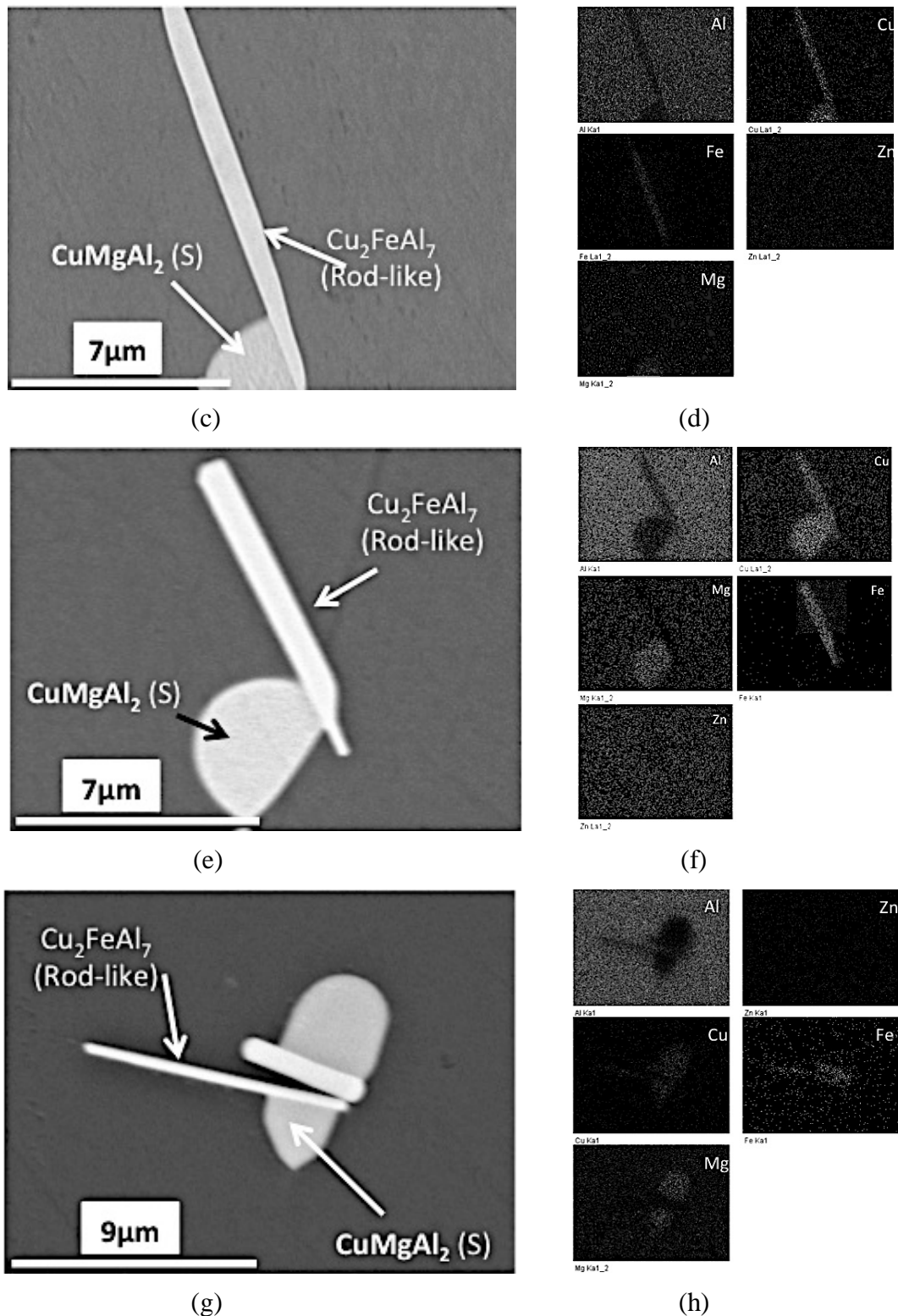
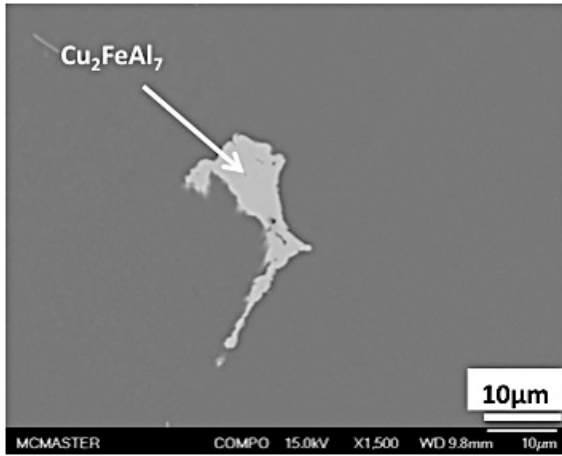
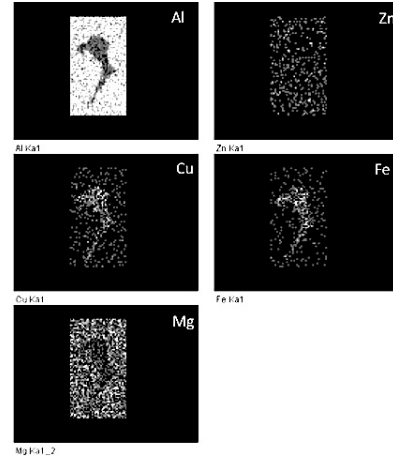


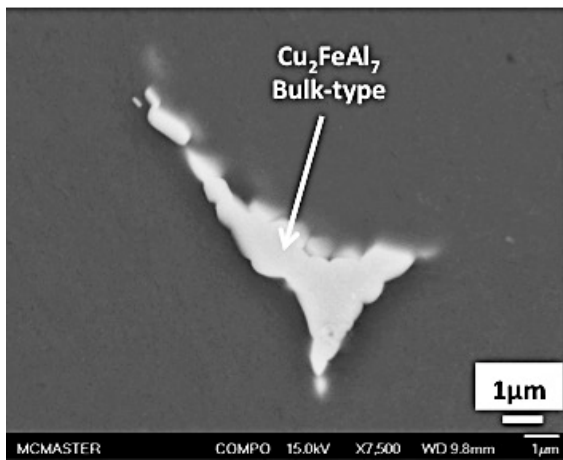
Figure 6–18 SEI on SEM of Fe-bearing intermetallic phases in AA7050 CDS castings in T4 temper; the FeAl_7Cu_2 phases are found to be in different morphologies; in (a), (c), (e) and (g) the rod or plate-like shaped Fe-bearing phases are presented alongside with their respective EDS elemental maps in (b), (d), (f) and (h).



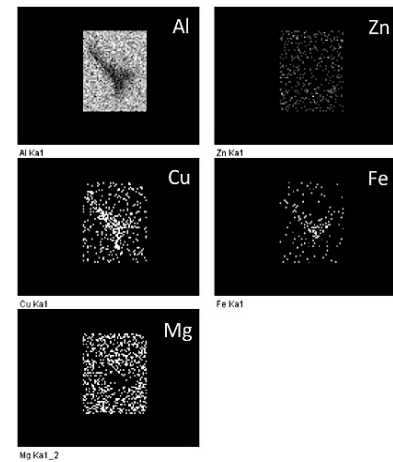
(a)



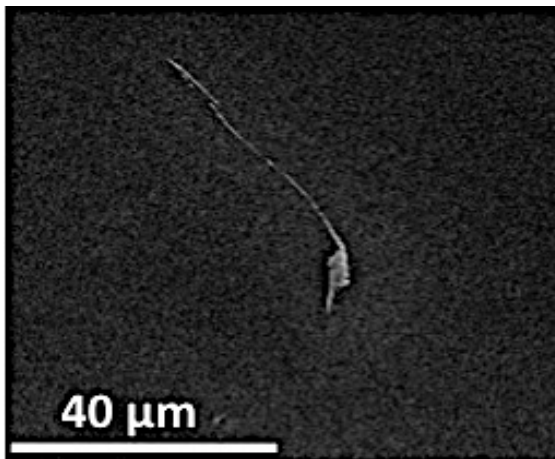
(b)



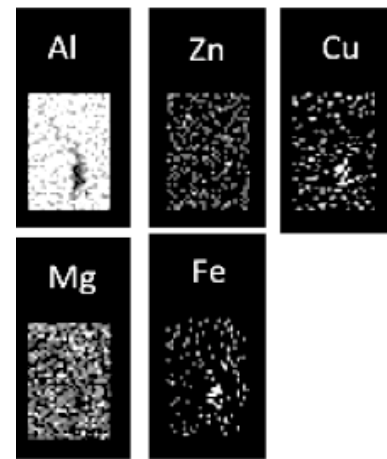
(c)



(d)



(e)



(f)

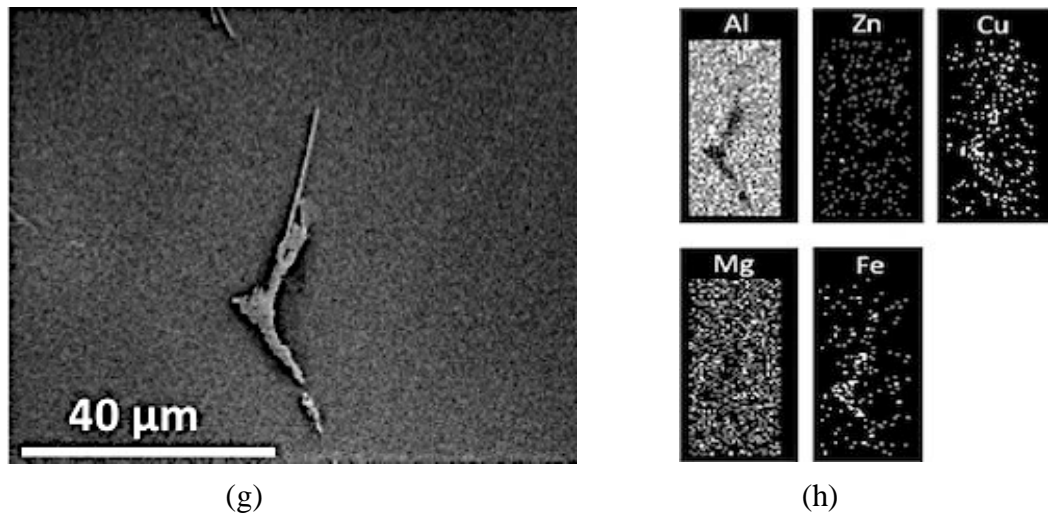


Figure 6–19 SEI on SEM of Fe-bearing intermetallic phases in AA7050 CDS castings in T4 temper; the FeAl_7Cu_2 phases are found to be in different morphologies; in (a), (c), (e) and (g) the bulky or chunky-type shaped Fe-bearing phases are presented alongside with their respective EDS elemental maps in (b), (d), (f) and (h).

6.2.3 Transmission Electron Microscopy (TEM)

The main purpose of this section is to study the particular effect of copper on the ageing process of the Al-7xxx alloys that are cast by the CDS process coupled with the TPGC casting machine. The alloy selection for this study has made in a way to have three levels of total alloying elements, namely, high, medium and low; with a more pronounced effect of copper addition into the alloy composition (Table 6–7).

Table 6–7 The composition of the three alloys from the Al-7xxx that are selected for further TEM investigation in peak age (T6) heat treatment condition according to Table 5–3; the compositions were measured GDOES.

Alloy#	Alloy Designation	Zn (wt.%)	Mg (wt.%)	Cu (wt.%)	Zn+Mg+Cu (wt.%)
1	Al-3.5Zn-0.8Mg-0Cu	3.48	0.79	0.03	4.30
5	Al-3.8Zn-2.18Mg-1.7Cu	3.81	2.18	1.75	7.75
7	Al-5.8Zn-2.2Mg-2.5Cu	5.82	2.22	2.53	10.57

Figure 6–20 (b) to (d) presents Selected Area Diffraction Pattern (SADP) from the Al phase in the $[001]_{\text{Al}}$ zone axis for the Al-7xxx CDS sample alloys in their near peak age (T6) temper. Figure 6–20 (d) presents the schematic representation of the reciprocal space of Al-matrix obtained along the $[001]$ zone axis of the Al-matrix, wherein the positions of the super-lattice reflection of GP clusters/ η' -precipitates are presented to be in a four folded pattern, appearing in the vicinity of the $\{311\}/2$ positions [84,88,89,91]. Further, Figure 6–20 (b) to (d) shows the super-lattice reflection spots of the GP clusters/ η' -phases appearing at positions close to $\{311\}/2$ in the Al matrix reciprocal space.

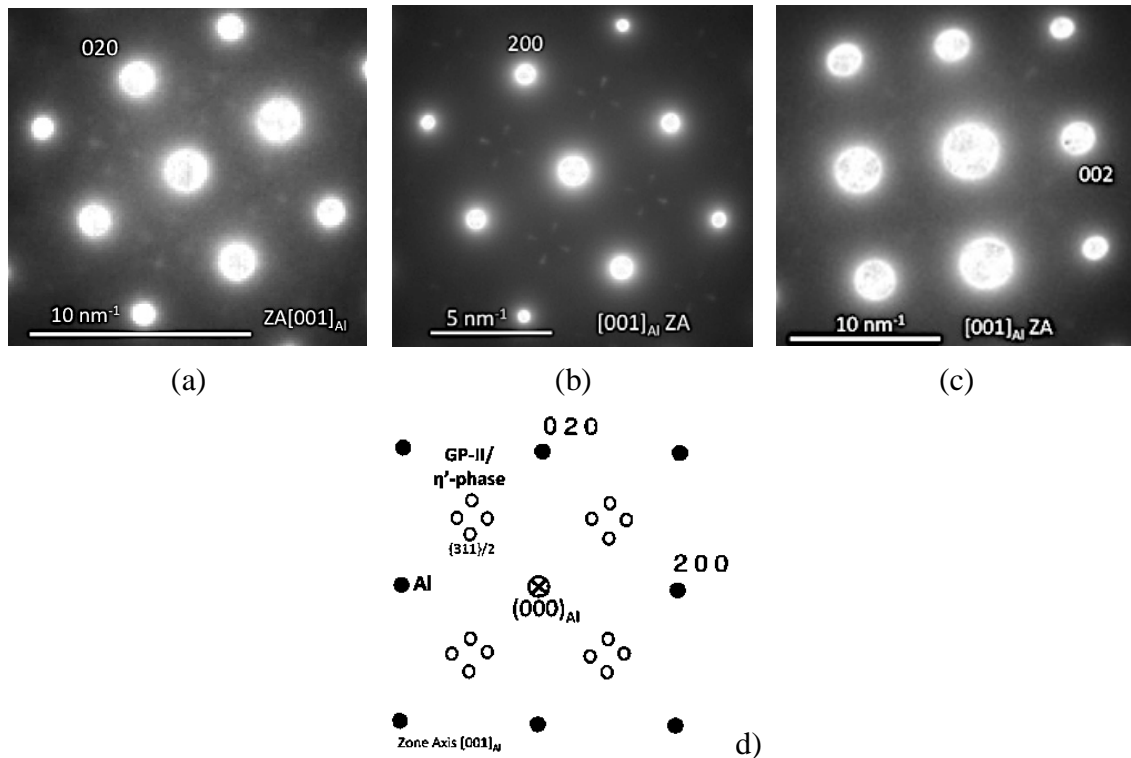


Figure 6–20 SADP patterns of Al matrix brought to $[001]$ -zone axes for samples in T6 temper from (a) Al-5.8Zn-2.2Mg-2.5Cu, (b) Al-3.8Zn-2.2Mg-1.7Cu and (c) Al-3.5Zn-0.8Mg-0Cu alloys. (d) Schematic illustration of observations in (a) to (c).

Figure 6–21 (a) to (c) presents the SADP for the $[111]_{\text{Al}}$ zone axis of the Al matrix for the three Al-7xxx CDS sample alloys in the near peak age (T6) heat treatment condition. Figure 6–21 (d) present the schematics of super-lattice positions in the Al-matrix reciprocal space which are obtained along the $[111]_{\text{Al}}$ axis zone direction of the Al-matrix; wherein the super-lattice reflection of GP clusters/ η' -precipitates appear in the vicinity of the $\{224\}/3$ positions [84,87-89,91,92]; these super lattice reflections are also observed in Figure 6–21 (a) to (c).

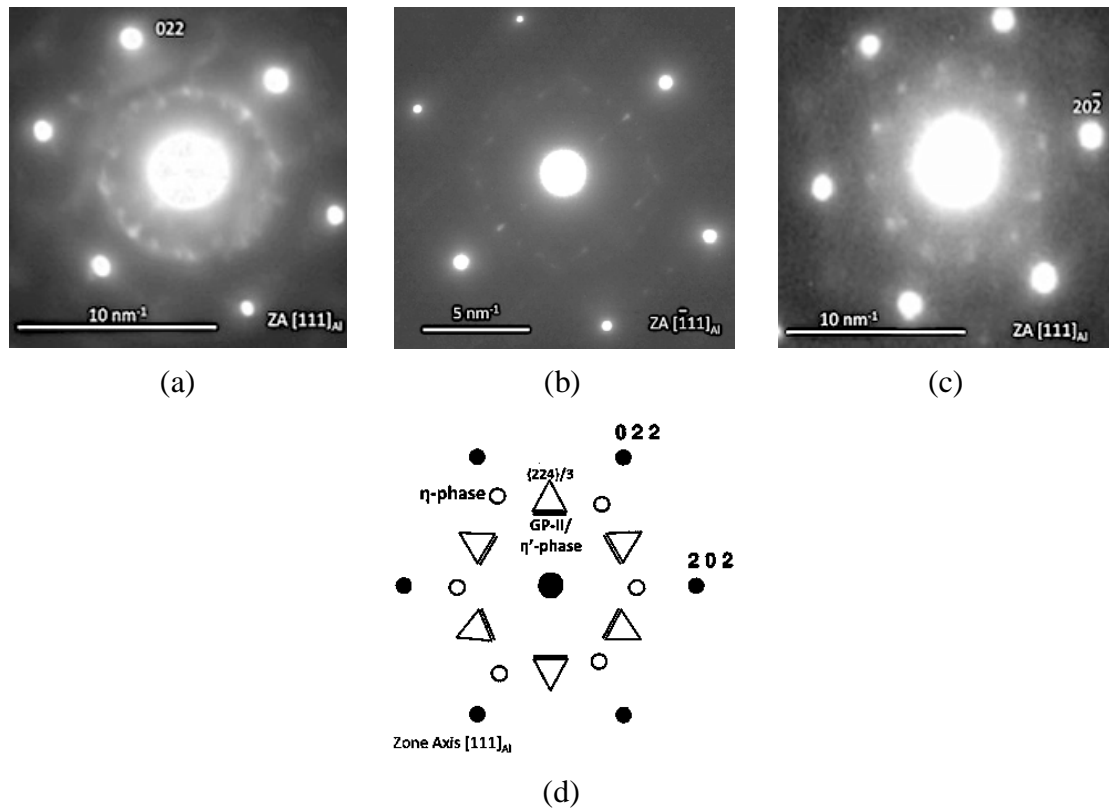


Figure 6-21 SADP patterns of Al matrix brought to $\langle 111 \rangle$ -zone axes for samples in T6 temper from (a) Al-5.8Zn-2.2Mg-2.5Cu, (b) Al-3.8Zn-2.2Mg-1.7Cu and (c) Al-3.5Zn-0.8Mg-0Cu alloys. (d) Schematic illustration of observations in (a) to (c).

Figure 6-22 and Figure 6-23 present the bright field (BF) and dark field (DF) TEM images from the η' -precipitates, forming during the precipitation hardening (T6) process in the three Al-7xxx CDS alloys. It is noticeable from the relatively low magnification bright field TEM images in both Figure 6-22 (a) to (c) and Figure 6-23 (a) to (c) that the number density of η' / η precipitates decreases as the copper content of the Al-7xxx CDS alloy decreases.

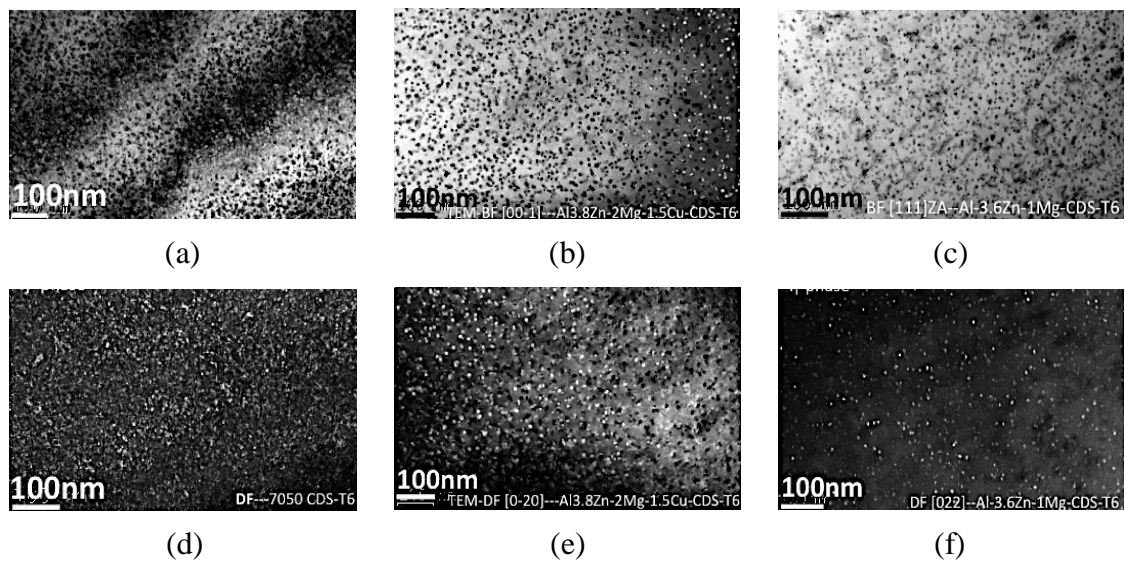


Figure 6-22 TEM Bright-field images along with Dark-field micrographs for T6-aged samples of: (a) and (d) Al-5.8Zn-2.2Mg-2.5Cu; (b) and (e) Al-3.8Zn-2Mg-1.7Cu; (c) and (f) Al-3.5Zn-0.8Mg-0Cu; showing population and size distribution of η' -phase.

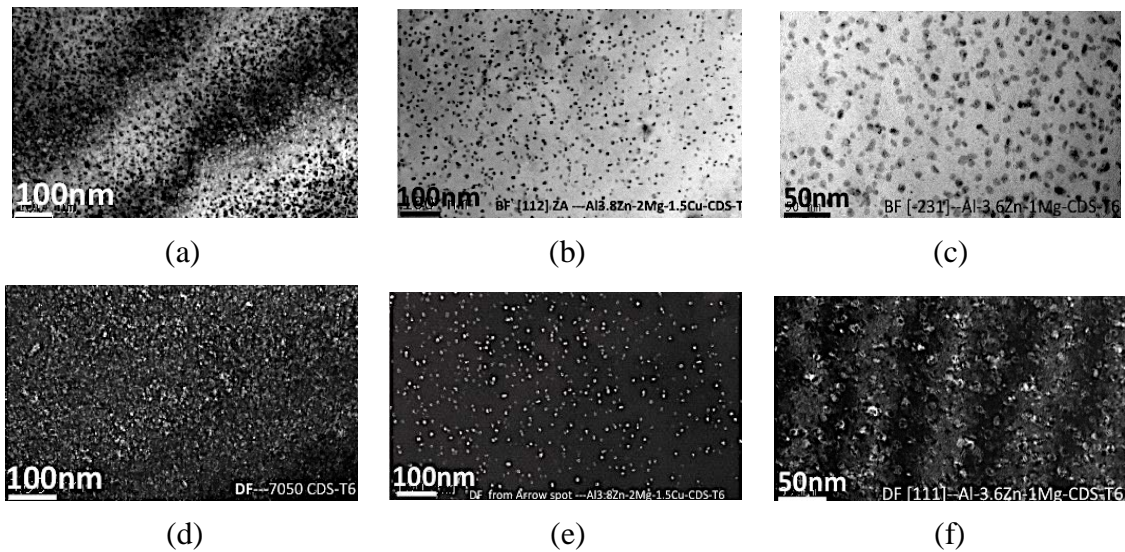


Figure 6–23 TEM Bright-field images along with Dark-field micrographs for T6-aged samples of: (a) and (d) Al-5.8Zn-2.2Mg-2.5Cu; (b) and (e) Al-3.8Zn-2Mg-1.7Cu; (c) and (f) Al-3.5Zn-0.8Mg-0Cu; showing population and size distribution of η' -phase.

Figure 6–24 presents high resolution STEM images obtained both in Dark Field (DF) mode and High Angle Annular Dark Field (HAADF) mode for the Al-3.5Zn-0.8Mg-0Cu and Al-5.8Zn-2.2Mg-2.5Cu alloys from the Al-7xxx family in the near peak age (T6) heat treatment condition, wherein various types of the strengthening precipitates such as GP clusters, η' - and η -phases are distinguishable based on their differences in size, morphology and compositional contrast. Figure 6–24 (a) and (b) present the DF and HAADF STEM images for the Cu free sample alloy (Al-3.5Zn-0.8Mg-0Cu);, respectively; and in Figure 6–24 (c) and (d), the DF and HAADF STEM images for the high Cu sample alloy (Al-5.8Zn-2.2Mg-2.5Cu) are respectively presented. It is notable that the HAADF STEM micrographs are also known as the z-contrast images, which provide information about the composition of the constituents in the micrographs such that the elements with heavier atomic weight appear in brighter color as compared with the lighter atoms. Having said that, one can readily tell apart between different types of strengthening precipitates, namely, GP clusters, η' - and η -phases, by means of comparing the DF and HAADF images for each sample alloy, forming during the ageing process of the Al-7xxx alloys. For instance, in HAADF images of high Cu sample alloy (Al-5.8Zn-2.2Mg-2.5Cu), as shown in Figure 6–24 (d), the η -phases appear as the first brightest spots with an elliptical shape (or elongated spheres); whereas the η' -phases are the second brightest spots (or the grey phases) with a more spherical morphology; and finally the GP clusters are identified as the smallest particles found on HAADF STEM micrographs with the least brightness. By comparing the (b) and (d) images in Figure 6–24, it is noticeable that the high Cu sample alloy (the former image) contains larger number of fine GP clusters as compared with the Cu free sample alloy in the latter image. This is yet another evidence for the participation of the Cu atom in the early stage formation of GP clusters as precursors for the intermediate (η') and the equilibrium (η) precipitates, which in turn accelerate the age hardening rate in the Al-7xxx alloys.

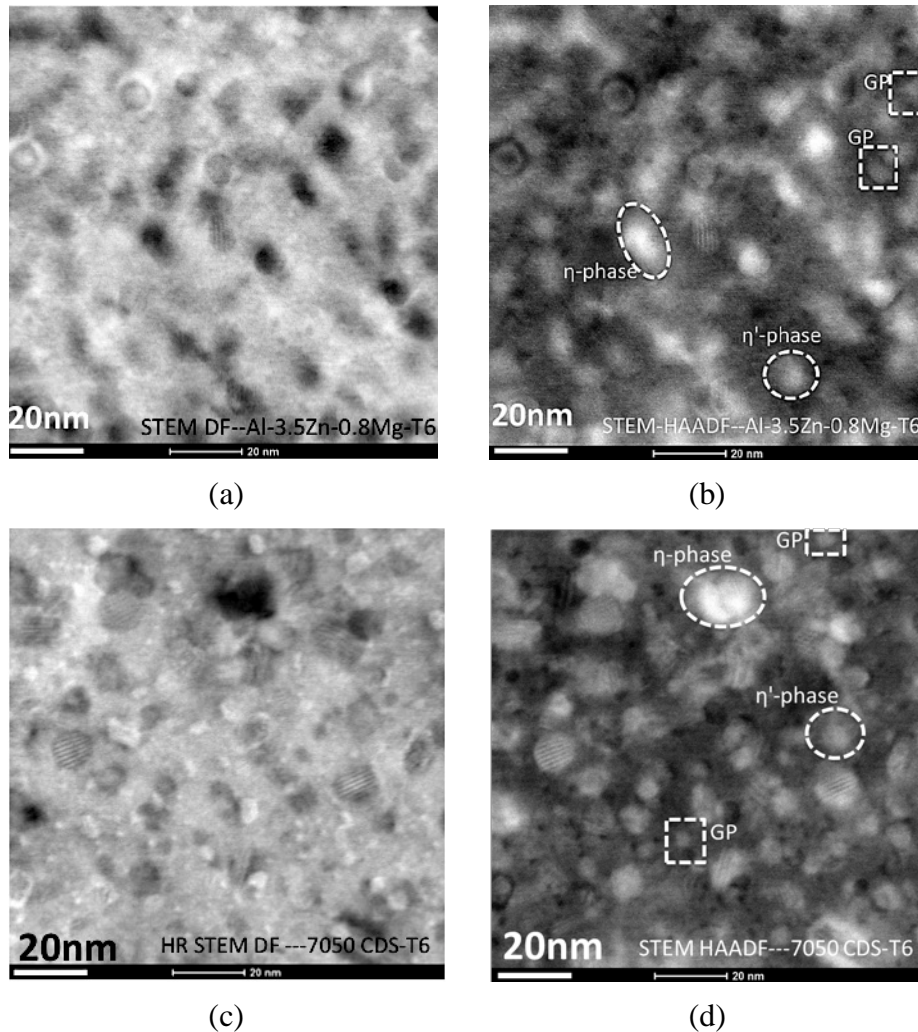


Figure 6–24 HR-STEM images in: (a) and (c) dark field mode; (b) and (d) HAADF (z-contrast) mode, showing the GP zones and η^{\prime} - η -phases precipitating during the age hardening (T6) process of: (a) and (b) Al-3.5Zn-0.8Mg-0Cu; and (c) and (d) Al-5.8Zn-2.2Mg-2.5Cu alloy.

Figure 6–25 part (1), (2) and (3) presents the HAADF in STEM along with the elemental maps obtained from the Al matrix in the three alloy compositions: Al-3.8Zn-0.8Mg, Al-3.8Zn-2Mg-1.7Cu and Al-5.8Zn-2.2Mg-2.5Cu, respectively. Figure 6–26 presents the quantitative metallography results to evaluate the particle size and volume fraction of the precipitates in the three alloys. Figure 6–27 presents the size distribution of the precipitates in the Al matrix for the three alloys showing a near Gaussian distribution; the number percentage of each size category bin.

The salient observations from Figure 6–25 and Figure 6–26 are as follows:

- All the three forms of precipitates such as GP zones, η^{\prime} and η are observed in the Al matrix.
- The volume fraction of the precipitates increases as the Cu content increases.
- The size of the precipitates decreases as the Cu content increases.
- The size of the GP zones decrease while its volume fraction increase as the Cu content increases.
- The Cu dissolved in the precipitates increase as the Cu content in the alloy increases because of the substitution of the Cu atoms to change MgZn_2 to $\text{Mg}(\text{Zn,Cu})_2$. This is observed in the increasing intensity of the Cu elemental map for the three alloys.

All the above-mentioned observations corroborate the observations in the prior-art about the role of Cu in the 7xxx Al alloys during the precipitation reaction during ageing.

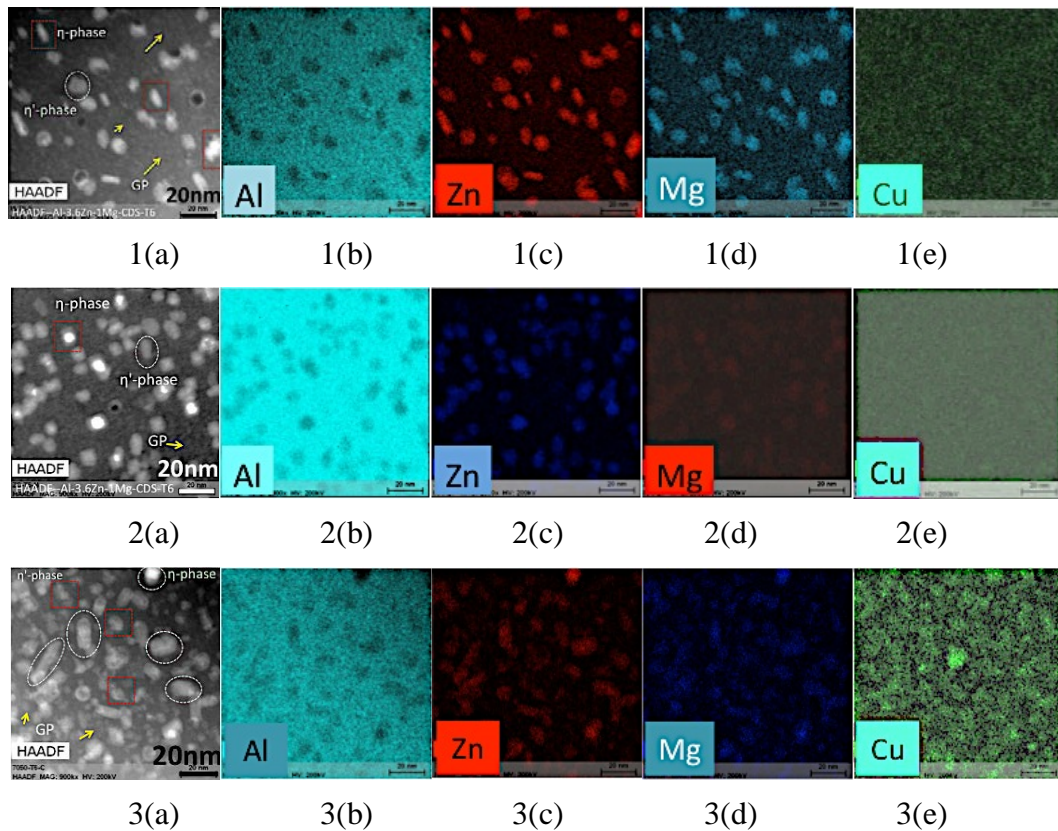


Figure 6–25 Typical HAADF and corresponding elemental maps for the (a) Al-3.5Zn-0.8Mg; (b) Al-3.8Zn-2Mg-1.7Cu; and (c) 5.8Zn-2.2Mg-2.5Cu; showing relative effect of copper on the particle size and distribution of precipitates, η' and η precipitates.

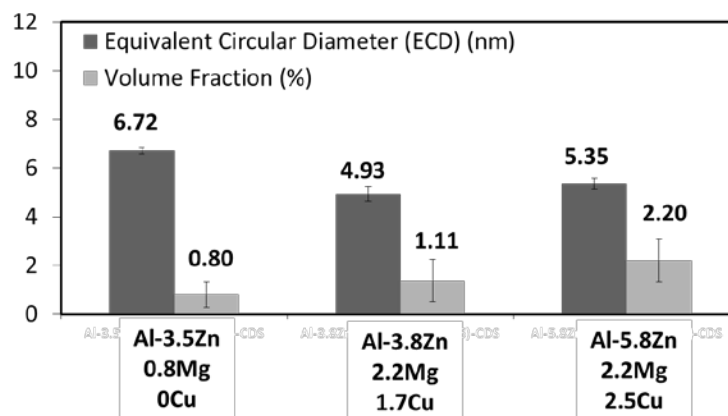


Figure 6–26 Measurements for the particle size and area fraction of precipitates in the three alloys shown in Figure 6–25. The results here show the total for all of GP zones, η' and η precipitates in the respective alloys.

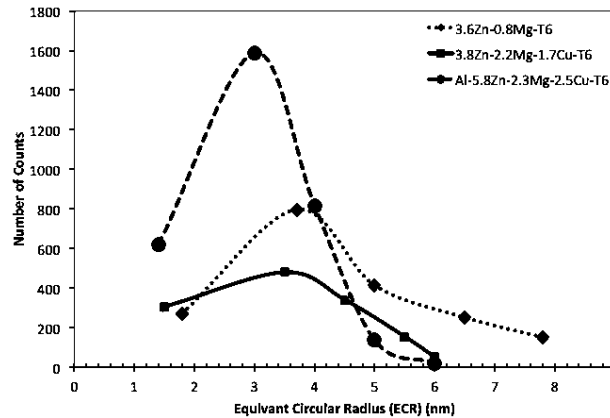


Figure 6–27 Typical distribution of particle size for the precipitate phases in the Al-3.5Zn-0.8Mg; Al-3.8Zn-2Mg-1.7Cu; and Al-5.8Zn-2.2Mg-2.5Cu alloys. The results here show the total for all of GP zones, η' and η precipitates in the respective alloys.

Figure 6–28 (a) and (b) present the STEM micrographs of the Cu-free Al-3.5Zn-0.8Mg-0Cu alloy both in DF and HAADF modes from (1) fine-scale precipitates that are formed in the grain interior areas during the age hardening (T6) process and (2) the coarse precipitates that are formed at grain boundary (GB) areas during the quenching stage from solution heat treatment (T4) [66]. Further, quantitative EDS was carried out on the numbered spots shown in the images in Figure 6–28 and presented in Table 6–8.

The observation from Figure 6–28 and corresponding EDS results in Table 6–8 is that the secondary phases forming at grain boundary areas in Cu-free Al-7xxx alloys such as Al-3.6Zn-0.8Mg (Figure 6–28) are almost entirely Sigma phases ($\text{Mg}(\text{Zn},\text{Cu},\text{Al})_2$); which phases are most probably formed during the quenching stage after the solution heat treatment (T4) [66]. This is important because dissimilar to Cu-bearing Al-7xxx alloys such as Al-7050 (Al-5.8Zn-2.2Mg-2.5Cu) alloy, the secondary phase existing at the grain boundary areas are almost entirely transformed to the S-CuMgAl₂ phase after the solution heat treatment (T4), as shown in (Figure 6–10).

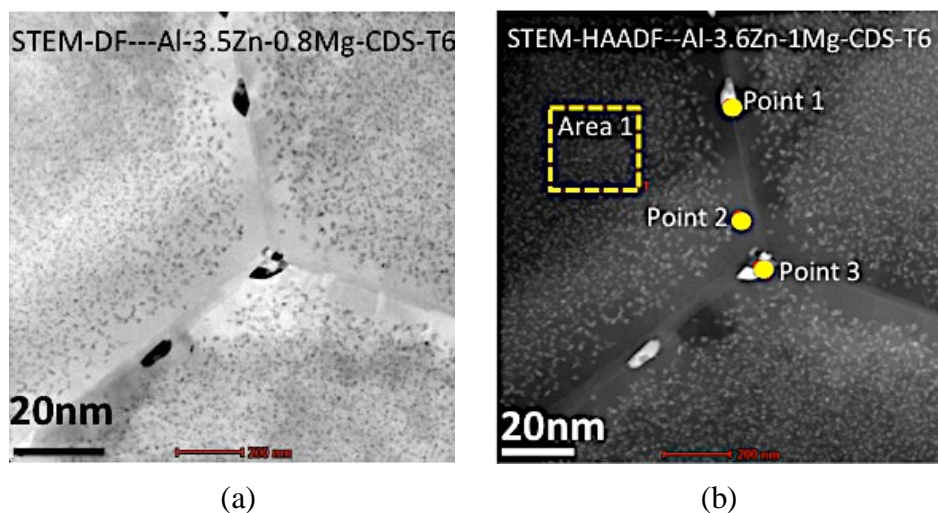


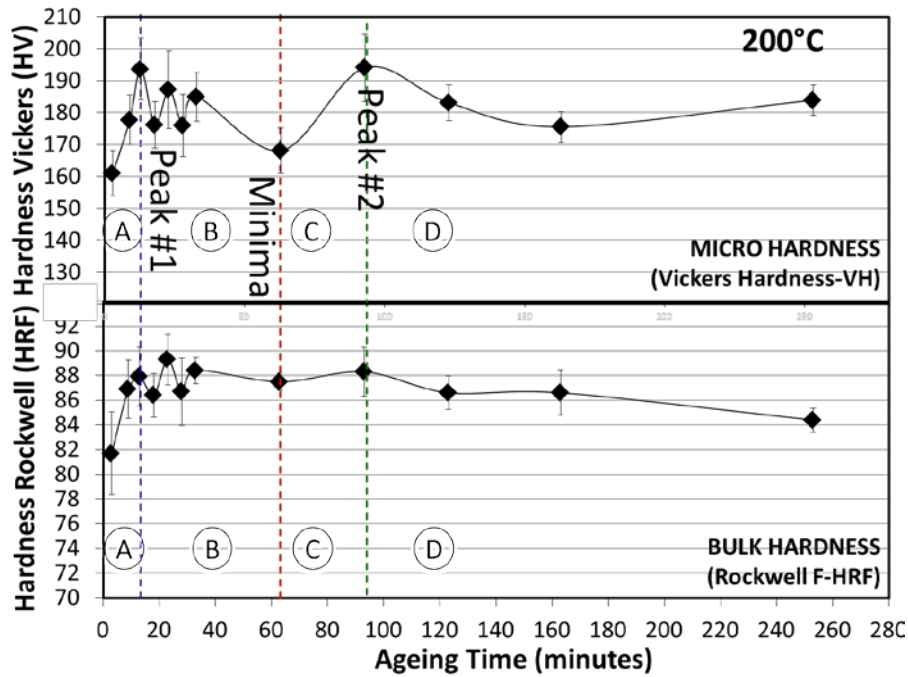
Figure 6–28 Typical STEM micrographs in (a) DF mode and (b) HAADF mode. in the Cu-free Al-3.5Zn-0.8Mg-0Cu alloy.

Table 6–8 EDS elemental analyses of specified area and points that are demarcated in Figure 6–28.

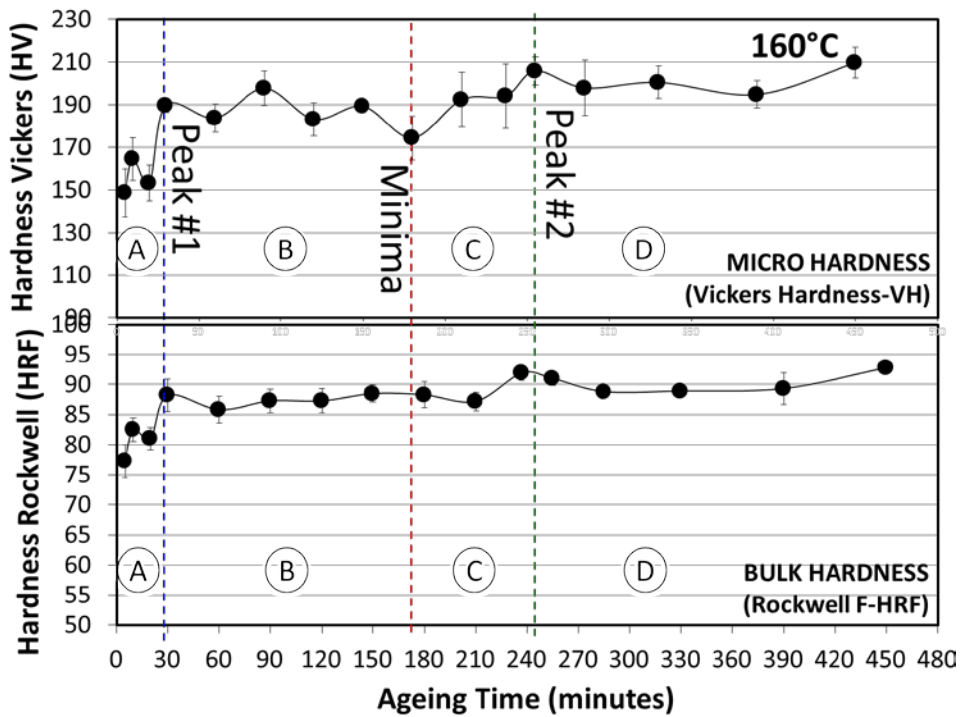
Element Image	Al		Zn		Mg		Cu		Possible phase
	wt.%	at%	wt.%	at%	wt.%	at%	wt.%	at%	
Area1	93.59	95.89	3.95	1.67	1.94	2.21	0.5	0.21	Al matrix grain interior areas containing Sigma (Mg (Zn,Al,Cu) ₂) precipitates
Point 1	63.23	76.61	30.51	15.25	5.91	7.95	0.32	0.16	Sigma (Mg(Zn,Al,Cu) ₂) precipitates
Point 2	95.64	97.29	2.93	1.23	1.23	1.39	0.18	0.07	Precipitate Free Zone (PFZ)
Point 3	41.14	48.17	29.52	14.26	28.64	37.22	0.68	0.34	Sigma (Mg(Zn,Al,Cu) ₂) precipitates

6.3 PRECIPITATION HARDENING

Figure 6–29 (a) to (d) present the micro- and macro-hardness test results for the AA7050 alloy that are obtained during the various artificial ageing processes at elevated temperatures: 70°C, 120°C, 160°C and 200°C, respectively. The hardness measurements shown in Figure 6–29 (a) to (d) were initiated immediately after quenching in water at room temperature from the solutionizing temperature of 477°C. In Figure 6–29, there are two maxima (denoted as Peak #1 and Peak #2) and a local minima (denoted as minima) for hardness data. The maxima represents the competitive precipitation of two distinct types of GP zones forming during the ageing process in the Al-7xxx alloys and the local minima signifies the dissolution of certain GP zones and transformation of the GP zones to the η' phase. The decrease in the hardness prior to the minima signifies more dissolution of GP zones than transformation into η' phase and the increase after the minima signifies the vice-versa. This will be discussed in greater details in the next Chapter (7.1). It is notable that the peak values in hardness curves in various stages of precipitation and the nature of hardness curves in Figure 6–29 for the four ageing temperatures (70°C, 120°C, 160°C and 200°C) are similar. This indicates that the precipitation reaction occurring in the samples at these respective temperatures have similar mechanism while the main effect of temperature is only on the kinetics of the precipitation reaction.



(a)



(b)

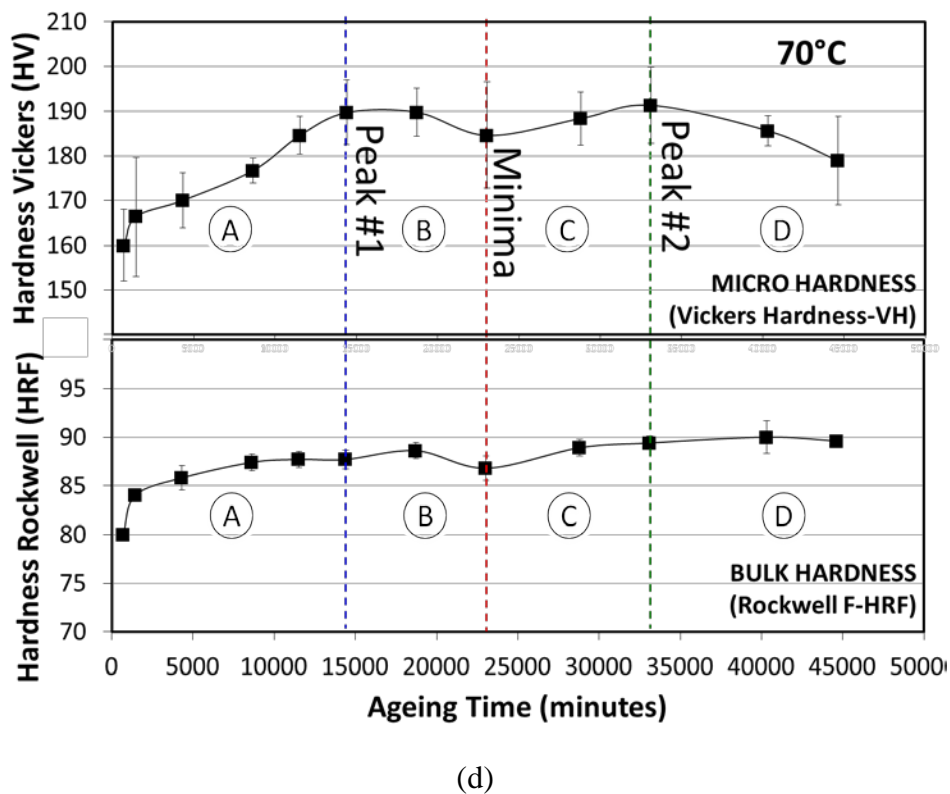
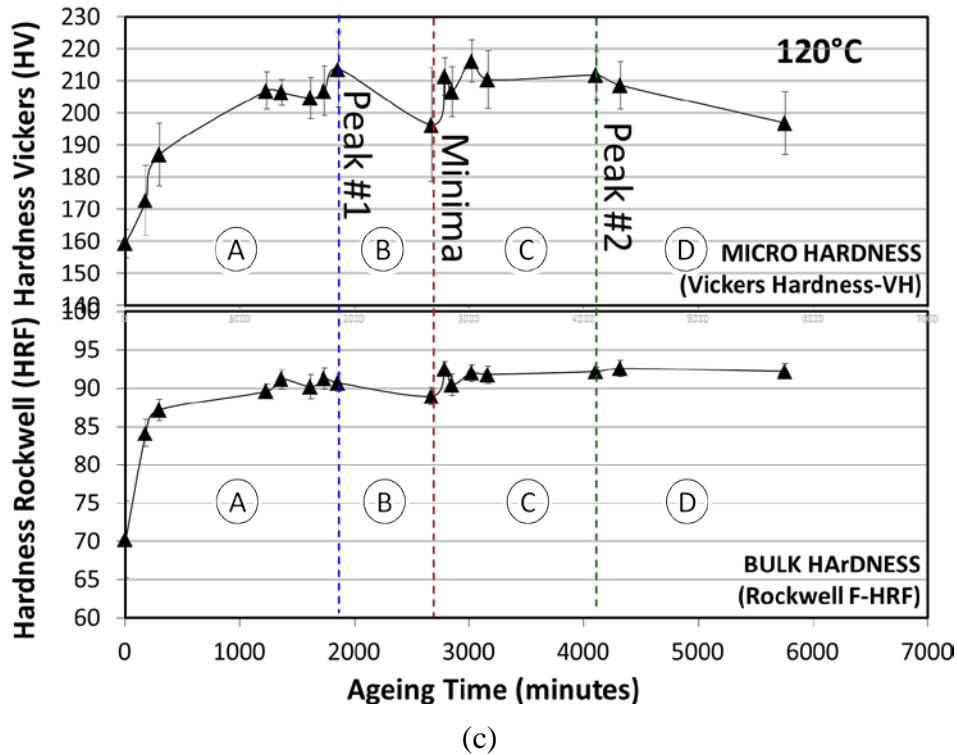


Figure 6–29 Typical micro- and macro-hardness data as a function of time measured from immediately after quenching the samples in water at room temperature after T4 treatment at 477 °C for AA 7050 CDS alloy castings. The isothermal temperature of the samples were (a) 200 °C, (b) 160 °C, (c) 120 °C and (d) 70 °C. The four regions of salient events during the precipitation process are also demarcated.

In Figure 6–29 (a) to (d), two local maximum in the hardness values along with one local minima in-between the two maximum occurs in all the ageing curves for the four different temperatures (70, 120, 160 and 200°C); it is notable that the values of hardness at these salient events are quite similar for all the four temperatures (refer to Figure 6–30). This suggests that the operating mechanisms contributing to the hardness values are similar in all temperatures. Further, the contribution on the hardness by the secondary phases such as eutectics is marginal because the nature of the ageing curve along with the salient features in peaks and minima are identical in both the macro (bulk) and micro hardness measurements shown in Figure 6 30; additionally, the contribution from solid solution of alloying elements in the primary Al matrix at any given thermodynamic event in the ageing curve is constant for all the temperatures, as dictated by the thermodynamics of the precipitation phenomenon in the alloy. The hardness values for all temperatures range between ~150 HV at the beginning of the ageing process and peaks at about ~200 HV; which is consistent with similar data reported in the background literature for the Al-7050 wrought alloys [66]; this suggests that there is no significant difference in the mechanism of precipitation strengthening between wrought alloys and those cast into net shape by the CDS technology and TPGC process.

The general mechanism of the various stages in the ageing curves shown in Figure 6–29 could be summarized as follows:

- Zone (A) → The time scale region demarcated by region (A) denotes the stage of formation of both the GP-I and GP-II zones with a marginal amount of η' phase in the matrix. The thermodynamics of the process at any given temperature will be similar to one another; in other words, the peak hardness value of Peak #1 will be reached when there is the optimum balance between the GP-I and GP-II in the matrix. However, the value of the peak hardness will be further influenced by the size and distribution of these GP zones in the matrix. Prior-art suggests that the GP-II is formed at temperatures above 70 °C from either the existing GP-I transforming or independently formed in the matrix [66]. Both these routes of evolution for GP-II occurs because of the thermally activated process wherein a few layers of Zn atoms simultaneously envelope the self clusters of Mg atoms or GP-I atoms. Hence, the hardness value of Peak #1 is dictated by the balance of the GP zones in the matrix while it is evident from Figure 6–30 that the optimum size and distribution of these two zones for maximum hardness value occurs at 120 °C which incidentally is the most popular temperature adopted by other researchers in the past for this alloy to maximize the effect of precipitate strengthening.
- Zone (B) and (C) → The time scale demarcated by regions (B) and (C) denote the stage when the η' phase evolves in the matrix. The nucleation of the η' phase could occur in one or both of two mechanisms [66,91]: (1) nucleation of η' phase from GP zone type I which requires the disassociation of atoms in the GP (I) zones and reformation of Mg and Zn atoms to form the η' phase, and/or (2) direct transformation from GP (II) zone to η' phase in the Al-matrix. The nucleation of the η' phase is followed by the growth of this phase. Typically the hardness value in a ageing curve will decrease during the nucleation of the η' phase because of the initially dissolution of the GP zones and recombination of atoms in the matrix to nucleate the η' phase; while the hardness value will increase during the growth stage of the η' phase. Hence, between Peak #1 and Peak #2 in Figure 6–30 at all temperatures, there are two competing effects on the hardness value: one decreasing and the other increasing it; the nucleation of the η' phase will precede the growth stage of the phase. At lower temperatures, say at 70 °C, there will be more overlap between the nucleation and growth stages of this phase due to the sluggish kinetics of the process; leading to a shallow dip in the hardness value until a point in time

when all the nucleation is nearly complete and the growth dominates the process of evolution of the η' phase, at which time the hardness will increase again. At higher temperature, say at 200 °C, the accelerated kinetics of the process affected by the thermal energy will result in a notable temporal divide between the nucleation and growth events of the η' phase as the bulk of the GP zone dissolve and nucleate the η' phase followed by the growth of the same. The intermittent temperatures of 120 and 160 °C will have varying degrees of temporal overlaps between the nucleation and growth stages of the η' phase. Figure 6–31 presents the plot of the hardness difference between the Peak #1 and Local Minima at various ageing temperatures from the curves shown in Figure 6–30; showing that there is a continuous and predictable increase in the hardness value for increasing temperatures of ageing; thus verifying the competing effects of nucleation and growth of the η' phase on the hardness value. It is notable that there could be as marginal amount of the incoherent η phase evolving towards the temporal region of peak #2 in the ageing curves; however, our analyses of the microstructure in the T6 (peak age) condition does not show any appreciable formation of this phase which are more plate like in morphology.

- Zone (D) → The time scale denoted by region (D) is when the the semi-coherent η' phases transform to the incoherent η phases resulting in an overageing of the alloy matrix reflected by the decrease in the hardness value of the ageing curve shown in Figure 6–30 for all temperatures.

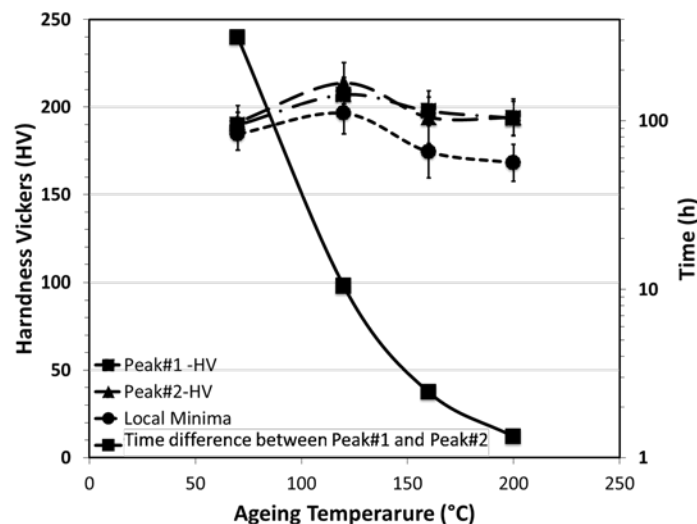


Figure 6–30 Typical variation of the peak micro-hardness values with ageing temperatures for the two distinct peaks observed on the age-hardening curves of AA 7050 CDS alloys measured during the Artificial Age hardening (T6) processes at 70, 120, 160 and 200°C.

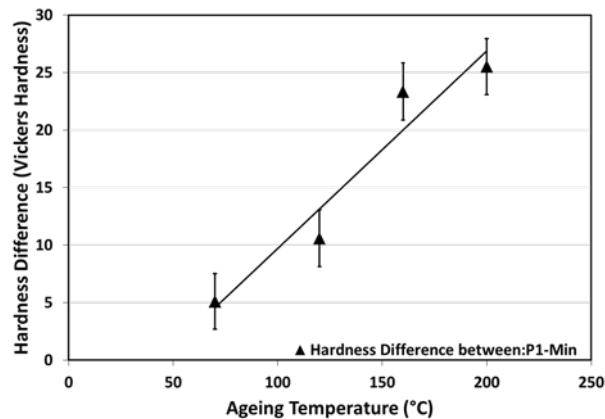


Figure 6–31 Plot of difference between the micro-hardness values at Peak #1 and Local Minima for various temperatures shown in Figure 6–29 (a) to (d).

Further, Figure 6–32 presents the *macro-hardness* test results for various compositions of the Al-7xxx CDS alloys selected for this study. The hardness values were measured during the natural ageing (NA) processes at room temperature, wherein two important features are clearly noticeable: (1) effect of total alloying elements (Zn+Mg+Cu) on the maximum hardness values and (2) effect of Cu content on the hardness and hardening rate during the ageing process. There are two contributions to the hardness value at any given time and the rate of change of the hardness value with time: (1) the total elements existing in as solid solution in the Al matrix and (2) the nature, size and amount of the precipitates in the matrix at any given time. Figure 6–32 shows that the rate of change in the hardness value after about 96 h of ageing seems to have significantly reduced in the various alloys suggesting that most of the significant precipitation reaction event have taken place in the Al matrix prior to 96 h at room temperature (i.e., for the natural ageing process). Hence, in order to enable comparison of mechanical properties amongst these alloys, the uniaxial tensile tests were carried out on all alloy samples after 96 hours of incubation in room temperature following the quenching of the samples after the T4 treatment.

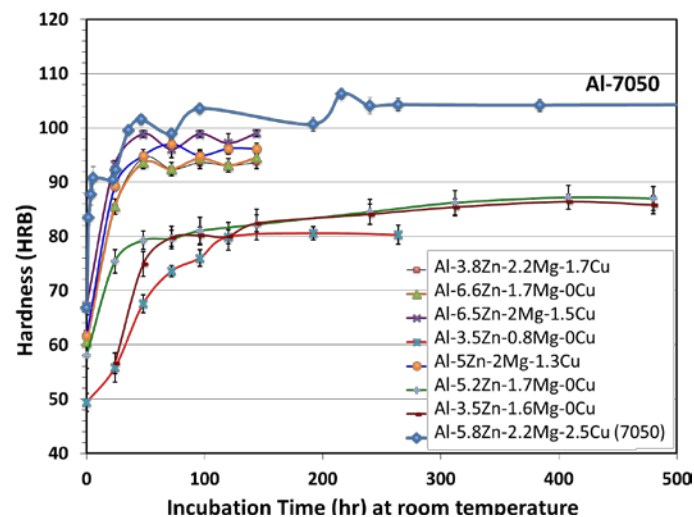


Figure 6–32 Macro-hardness measurement data for various Al-7xxx CDS alloys measured during the natural ageing (NA) process at room temperature following quenching in water at room temperature the solutionizing temperature of 477 °C.

Figure 6–33 presents the optical micrographs of Sigma precipitates in the Al matrix after the annealing (O) treatment. The quantitative metallography results such as Equivalent Circular

Diameter (ECD) and phase fraction (f) of the Sigma phase particles are presented in Figure 6–34 (a) and (b), respectively. The observations are that the ECD for the Sigma phase particles decrease as the Cu content in the alloy increases and the area fraction of the particles increase with increase in the total amount of alloying elements (Zn+Mg+Cu) and increasing Cu content in the alloys, alike.

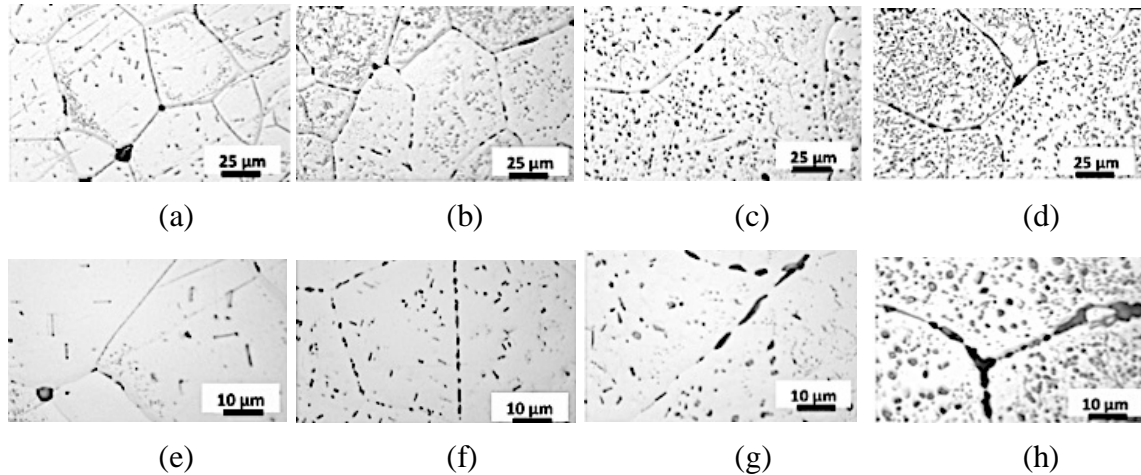


Figure 6–33 Typical optical micrographs in relatively high magnifications for copper free Al-7xxx alloys in annealed (T4+O) condition that are cast for this study by the CDS process coupled with tilt pour gravity cast (TPGC) machine: (a) and (e) Al-3.5Zn-0.8Mg alloy; (b) and (f) Al-3.5Zn-1.6Mg alloy; (c) and (g) Al-5.2Zn-1.7Mg alloy; (d) and (h) Al-6.6Zn-1.7Mg alloy.

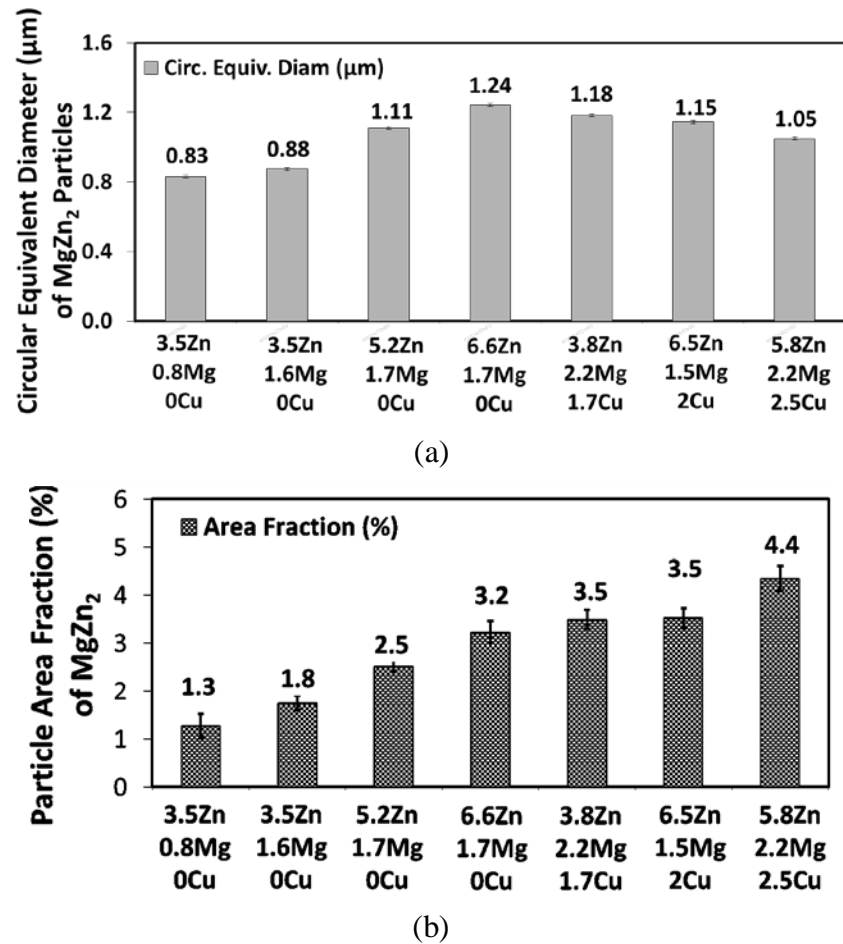


Figure 6–34 Typical comparative bar graphs of (a) size distribution and (b) fraction area (%) of Sigma ($\text{Mg}(\text{Zn},\text{Al},\text{Cu})_2$) phases, precipitating during the annealed (O) heat treatment of the Al-7xxx CDS alloys selected for this study. Note, the effect of total alloying element content on the area fraction (or the number density) and the size distribution of precipitates; and particular effect of Cu content on the size distribution of the precipitates.

6.4 UNIAXIAL TENSILE PROPERTIES

Figure 6–35 summarizes the uniaxial tensile properties of AA 7050 CDS castings under various heat treatment conditions, such as, as-cast (F), solution heat treatment (T4), annealed (O) and optimal peak aged (T6) conditions, all of which are represented by their typical stress-strain curves.

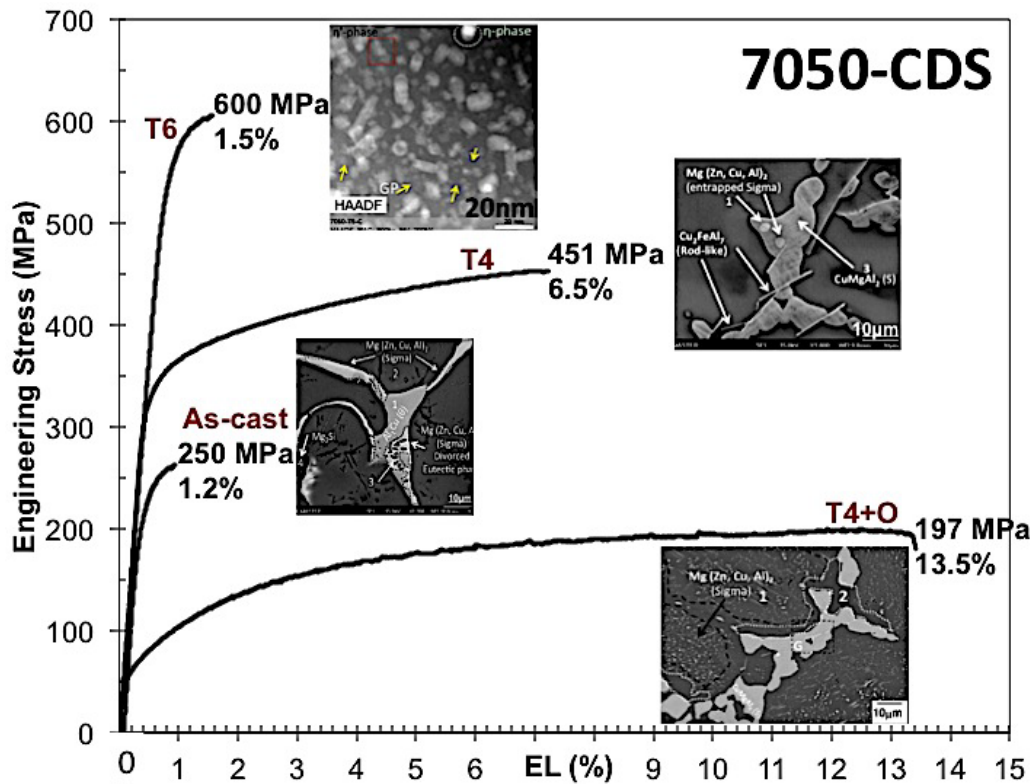


Figure 6–35 Typical stress-strain curves of AA 7050 CDS castings in various heat treatments such as as-cast (F), solution (T4), annealed (O) and near peak aged (T6) conditions.

In the following sections of this chapter, the uniaxial tensile properties of the Al-7xxx CDS cast alloys will be discussed in conjunction with their microstructural evolution during various heat treatment processes.

6.4.1 Effect of heat treatment

Figure 6–36 present the average uniaxial tensile properties along with the respective standard deviations for the AA7050 alloy cast using the CDS technology coupled with TPGC process; in F, T4 and T6 temper conditions. Figure 6–36 presents one typical stress-strain graph obtained during the uniaxial tensile test for the AA7050 CDS and A356.2 (Al-Si-Mg) alloys so as to present a visual comparison of the curves between the alloy in this study and a common heat treatable automotive alloy cast by TPGC process.

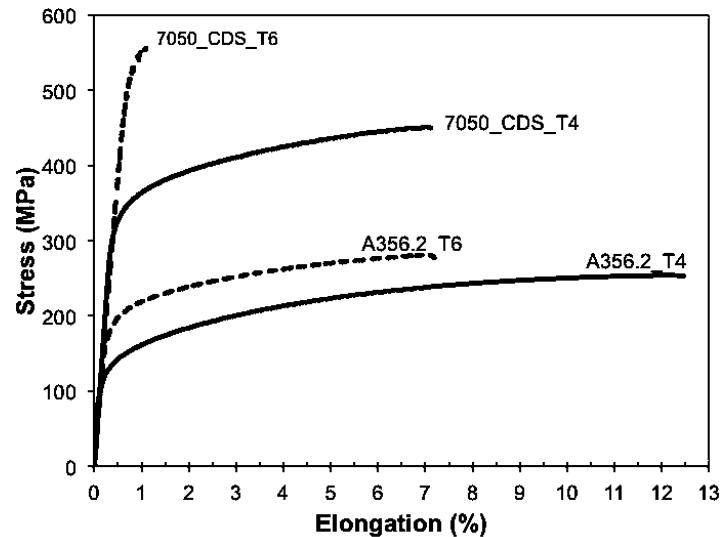


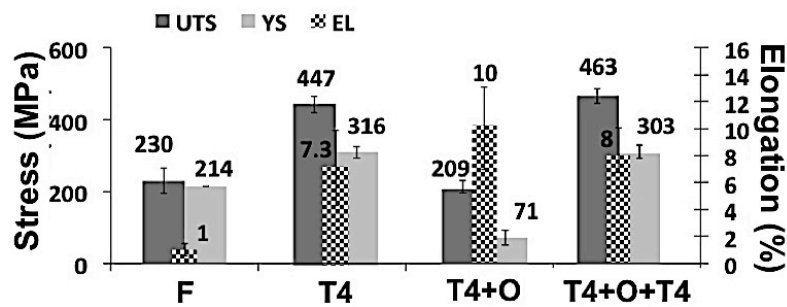
Figure 6–36 Typical stress-strain curve for AA 7050 alloy cast using the CDS technology and AA356.2 alloy; both alloys were cast in the TPGC process. Two heat treatment tempers for each alloy is shown: T4 and T6.

The uniaxial tensile properties for the CDS process shown in Figure 6–37 are in the similar regime of magnitude as that of other products manufactured by this alloy as shown in Table 6–9. However, the elongation obtained in the CDS samples listed in Figure 6–36, after the T6 temper is lower than those obtained for other AA7050 alloy products of manufactured by solid state processes such as forging and extrusion. The T6 temper processes used on the Al-7xxx CDS alloys in this study were obtained from the background literature for the Al 7xxx wrought alloy; the CDS samples in this study are near net shaped castings and hence, there could be a significant variation in the solute redistribution in the as cast and heat treated conditions of these samples as compared to their wrought counterpart products manufactured by conventional forging or extrusion processes which necessitates a new redesign of the heat treatment process for the CDS castings to optimize the parameters of thermal processes which in turn could optimize their tensile properties. It is notable that the tensile properties presented in Table 6–9 are not optimized and is only presented as a starting point of the properties for these castings manufactured by the CDS technology. Optimization of the heat treatment process for the castings in this study would require a critical understanding of the microstructure evolution, nature of solute redistribution and precipitation of strengthening phases during solidification and subsequent stages of the heat treatment process.

The annealing heat treatment (O temper) was carried out to provide a better understanding of the microstructural changes from the as-cast condition to the heat-treated tempers. Carrying out the annealing (O) treatment on the AA7050 castings produced by the CDS process had a significant influence on the mechanical properties as presented in Table 6–9 and graphically shown in both Figure 6–37 and Figure 6–38. Furthermore, Figure 6–39 shows the typical optical micrographs of the different heat-treatment conditions before and after the annealing (O) heat treatment, and illustrates the microstructural evolution during each heat treatment for the purpose of interpreting the correlation between microstructure and mechanical properties.

Table 6–9 Uniaxial tensile test results of CDS samples of AA7050 in different heat treatment combinations between ageing, solutionizing and annealing

Heat Treatment	UTS (MPa)	YS (0.2%) (MPa)	Elongation (%)
F (as-cast)	230.0 ±25	213.9 ±0.7	0.3 ±0.03
F+O	174.1 ±5.04	108.7 ±2.4	2.03 ±0.2
F+O+T4	390.6 ±41.3	261.7 ±30.7	9.1 ±2.1
F+T4	447.5 ±14.3	315.9 ±9.8	7.3 ±1.7
F+T4+T6	551 ±10.1	540 ±20	1.2 ±0.2
F+T4+O	209.0 ±14.2	71.0 ±17.2	10.2 ±2.6
F+T4+O+T4	462.9 ±14.9	303.5 ±13.9	8.0 ±1.2

**Figure 6–37 Comparative bar graph of the tensile properties of the AA7050 CDS cast samples under various heat treatment conditions from the Table 6–9 showing the softening effect of annealing treatment as an intermediate process.**

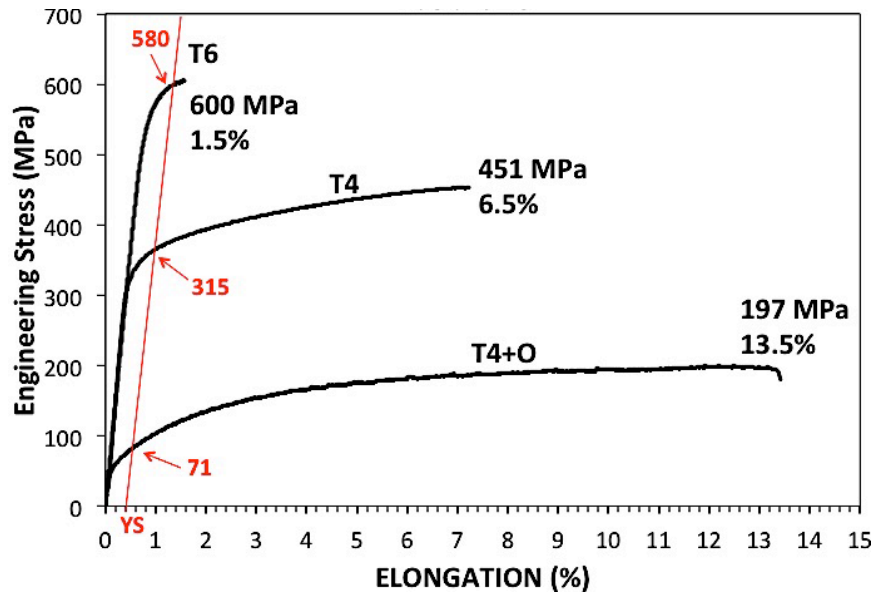


Figure 6–38 Graphical uniaxial tensile testing results for typical samples of the AA7050 alloy cast with the CDS technology, showing the T4, T4+O and T6 tempers.

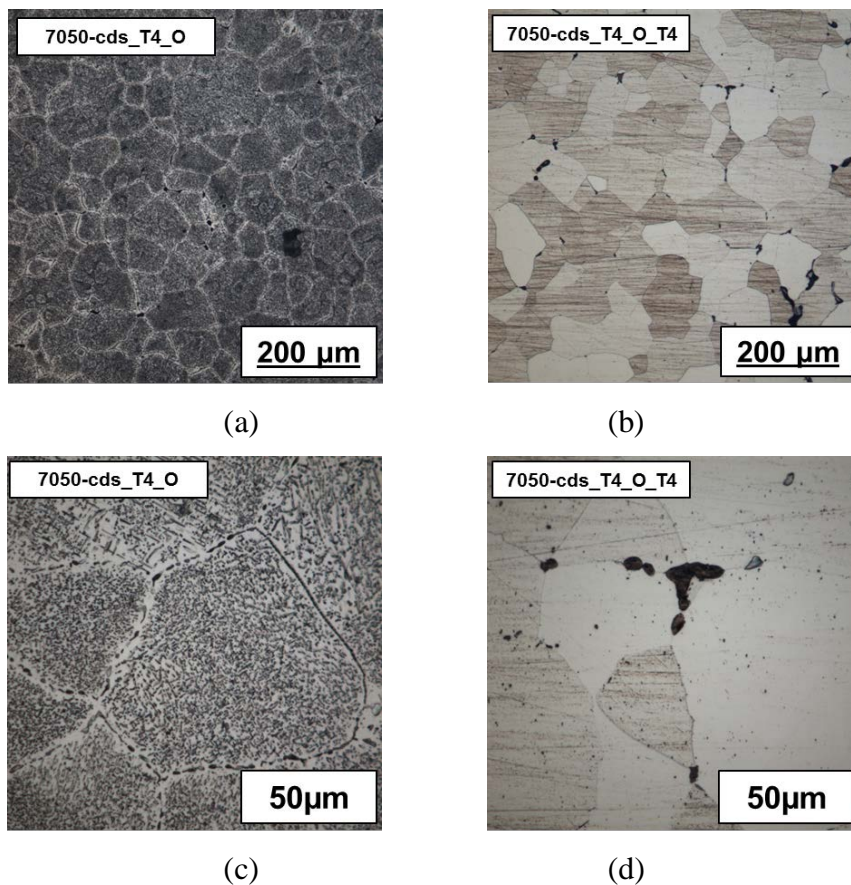


Figure 6–39 Typical light optical micrographs of as-cast samples for AA7050 alloy cast using the TPGC process with CDS technology in high- and low-magnification: (a) and (c) for annealing heat treatment condition (T4+O), and (b) and (d) for solutionizing heat treatment condition (T4), respectively, showing the precipitation within the primary Al matrix.

6.4.2 Effect of alloying elements

Table 6–10 and Table 6–11 present the average values for uniaxial tensile properties of the Al-7xxx family selected for this study, which were produced by the CDS technology using the tilt pour gravity casting (TPGC) machine, and heat treated in two tempers: solution (T4) heat treatment and peak aged (PAC/T6) heat treatment conditions, respectively. Further, the uniaxial tensile properties of the Al-7xxx CDS castings in solution treated (T4) condition and peak aged (T6) condition are graphically plotted in Figure 6–40 and Figure 6–41, respectively. In Figure 6–40, the uniaxial tensile properties such as yield strength (YS), ultimate tensile strength (UTS) and elongation (EL) of Al-7xxx CDS alloys in T4 condition are presented by the typical comparative bar charts; similarly, Figure 6–40 presents the comparative bar graphs of the YS, UTS and EL for the alloys in the near peak age (T6) condition. It is noteworthy that mechanical properties of the two Al-7xxx CDS alloys are excluded from the list presented in the Table 6–10 and Table 6–11 or in Figure 6–40 and Figure 6–41; because the Fe and Si contents in these two alloys are significantly high (Table 5–1) and would contribute to detrimental mechanical properties due to the formation of large amounts of intermetallic phases with these impurity elements.

As shown in Figure 6–40 and Figure 6–41, the increase in the total alloying elements strengthens the materials both in the T4 and T6 conditions, alike. This is partly because of the direct effect of alloying elements on (1) the degree of supersaturation solid solution (SSSS) after the T4 condition; and (2) the amount (volume fraction) of strengthening precipitates in the T6 condition. However, the total alloying elements contents has a counter effect on the ductility (or elongation) response of the Al-7xxx CDS castings under uniaxial tensile test in both T4 and T6 conditions, alike. This is partly attributed to the direct effect of alloying elements on the amount (volume fraction) of eutectic phases, wherein the detrimental phases such as the coarse impurity intermetallic and secondary phases, namely, iron/silicon bearing phases and/or S-phases are most likely to be collectively found.

Table 6–10 Typical uniaxial tensile properties of the Al-7xxx alloys selected for this study, cast by CDS process using Tilt Pour Gravity Castng (TPGC) machine and heat treated in the solution treatment (T4) condition, (24 hours at 477°C followed by water quenching and 96 hour incubation at the ambient temperature).

Alloy Designation	Zn+ Mg+ Cu	Tensile-T4					
		YS(MPa)		UTS(MPa)		El (%)	
Al-3.5Zn-0.8Mg-0Cu	4.6	125.0	±5.0	207.9	±14.2	8.04	±1.76
Al-3.5Zn-1.62Mg-0Cu	5.4	183.8	±24.3	305.3	±30.1	10.8	±2.69
Al-5.2Zn-1.7Mg-0Cu	6.5	200.0	±12.6	291.8	±15.2	5.9	±1.31
Al-6.6Zn-1.7Mg-0Cu	8.5	211.3	±24.2	294.3	±32.5	3.87	±1.74
Al-3.8Zn-2.2Mg-1.7Cu	7.4	222.0	±24.9	344.0	±19.2	11.9	±0.1
Al-6.5Zn-1.5Mg-2Cu	10	255.6	±12.8	367.8	±31.7	9.8	±2.14
Al-5.8Zn-2.2Mg-2.5Cu	10.6	315.9	±9.8	447.5	±14.3	7.3	±1.7

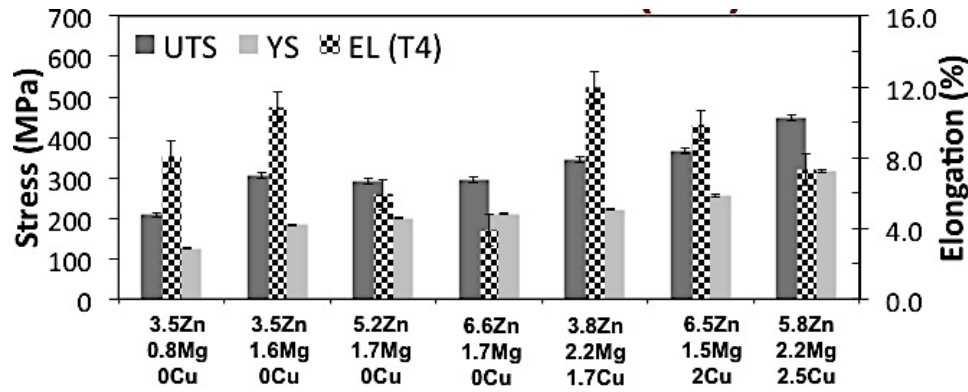


Figure 6–40 Typical comparative bar graphs of uniaxial tensile properties, including yield (YS), ultimate tensile (UTS) strengths and elongation (EL) of Al-7xxx CDS alloys selected for this study, in solution heat treated (T4) condition.

Table 6–11 Typical uniaxial tensile properties of the Al-7xxx CDS alloys selected for this study, obtained in their optimal peak aged (PAC/T6) condition (T4 + 24 hours at 120°C).

Alloy Designation	Zn+ Mg+ Cu	Tensile-T6				
		YS(MPa)	UTS(MPa)	El (%)		
Al-3.5Zn-0.8Mg-0Cu	4.6	279.0 ±13.5	289.6 ±26.1	2.2 ±1.6		
Al-3.5Zn-1.62Mg-0Cu	5.4	351.0 ±12.8	379.0 ±33.4	2.6 ±1.7		
Al-5.2Zn-1.7Mg-0Cu	6.5	346.8 ±9.4	384.0 ±33.4	2.6 ±1.5		
Al-6.6Zn-1.7Mg-0Cu	8.5	375.0 ±61.7	375.0 ±61.7	0.6 ±0.1		
Al-3.8Zn-2.2Mg-1.7Cu	7.4	390.0 ±14.6	396.0 ±17.1	0.8 ±0.2		
Al-6.5Zn-1.5Mg-2Cu	10	463.0 ±0.4	487.6 ±11.7	1.6 ±0.4		
Al-5.8Zn-2.2Mg-2.5Cu	10.6	539.7 ±20	551.2 ±10.8	1.2 ±0.2		

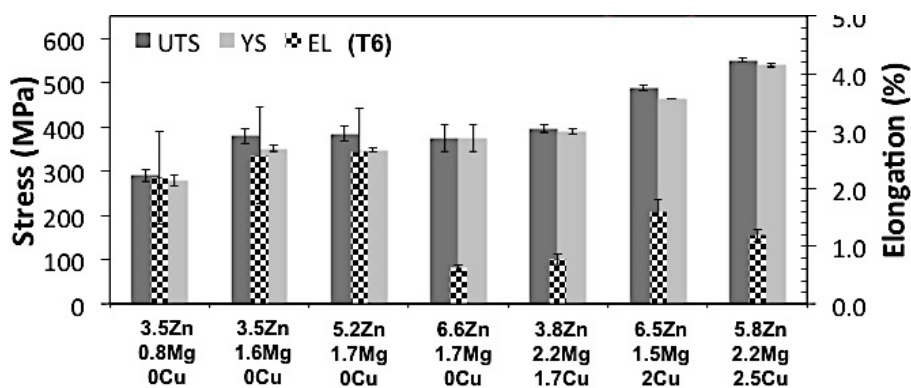


Figure 6–41 Typical comparative bar graphs of uniaxial tensile properties, including yield (YS), ultimate tensile (UTS) strengths and elongation (EL) of Al-7xxx CDS alloys selected for this study, in their optimal peak age hardening (T6) condition.

6.4.2.1 *Effect of copper on uniaxial elongation tensile properties*

Increasing the levels of alloying elements, Zn, Mg and Cu in the Al-Zn-Mg-Cu alloy increases the amount of elements in the super saturated solid solution at the end of the T4 treatment, which contributes to an increase in the yield strength due to the increasing the resistance offered to dislocation movement under tensile load and contributed to a smaller size and subsequently increase the driving force for the evolution of the strengthening precipitates during the ageing process, be it natural or artificial [5,89,91]. Figure 6-42 (a) presents the plot of YS as a function of total alloying element content in the respective alloys of this study in both the T4 and T6 temper conditions, respectively, and Figure 6-43 (b) presents a similar plot for the elongation in the T4 temper condition; these plots are data from both the plots in Figure 6-41 and Figure 6-42. The plot of elongation in the T6 temper is not presented in Figure 6-43 (b) because the values of elongation were quite low in this temper due to the peak age condition of T6 as shown by Table 6-11 and hence, did not present any appreciable trend in data. Although the alloy compositions selected in this study do not lend themselves to clearly elucidate the individual effect of Cu on the uniaxial tensile properties, there appears to be changing in the trend of the YS and elongation when Cu is added to the alloys as shown in Figure 6-42; typically, as the total content of the alloying elements in the Al 7xxx alloy increases, the YS increases and elongation decreases [5] and this trend in changes of YS and elongation seem to be fairly linear. However, when Cu is added to these alloys, there seems to be increase in the slope of this linear trend for the increase in YS with increasing content of alloying elements in the alloy as shown in Figure 6-42 (a); the alloys shown as T4 temper condition in this graph were allowed to naturally age for a minimum of 96 h prior to being tested for uniaxial tensile properties and during this ageing process, certain amount of GP zones and marginal amounts of η' phase may have formed in the Al matrix to increase its strength. It has been well documented in the prior art that the addition of Cu results in accelerating the kinetics of the evolution of the strengthening precipitates in the matrix during natural ageing [5,66,93,180] and results in a smaller and more distributed precipitates in the matrix. This would result in an increase in the YS of the material and increase the slope of the curve shown in Figure 6-42 (a). Further, in the T6 temper condition, it has been shown in Figure 6-23 that the number of strengthening precipitates increases while the size decrease resulting in an increase of YS for alloys with Cu in them. An additional factor that may contribute to the increase in the YS strength due to Cu addition to the alloys would be the change in the nature, size and morphology of the Fe bearing intermetallic phases in the alloy microstructure; addition of Cu to the alloy changes the $\text{Al}_{13}\text{Fe}_4$ phase with a plate-like morphology with high aspect ratio to the $\text{Al}_7\text{Cu}_2\text{Fe}$ phase with a combination of rod like and bulky morphology which would tend to reduce the propensity of defect initiation during tensile testing. This change in the Fe bearing phase may also contribute to the increased elongation observed in Figure 6-43 (b) for the alloys with Cu in them while maintaining the same content of total alloying elements. Further, the reduction of the size of the strengthening precipitates while increasing the number density in the Al matrix will also contribute to a higher elongation for alloys with Cu in them. The trend in elongation shown in Figure 6-43 (b) also shows that there seems to be an increase in the elongation in alloys with Cu as shown by the change in the linear trend of the curve which predicts an increase of about 5% in elongation when Cu is added to the alloy while maintaining the same total content of alloying elements.

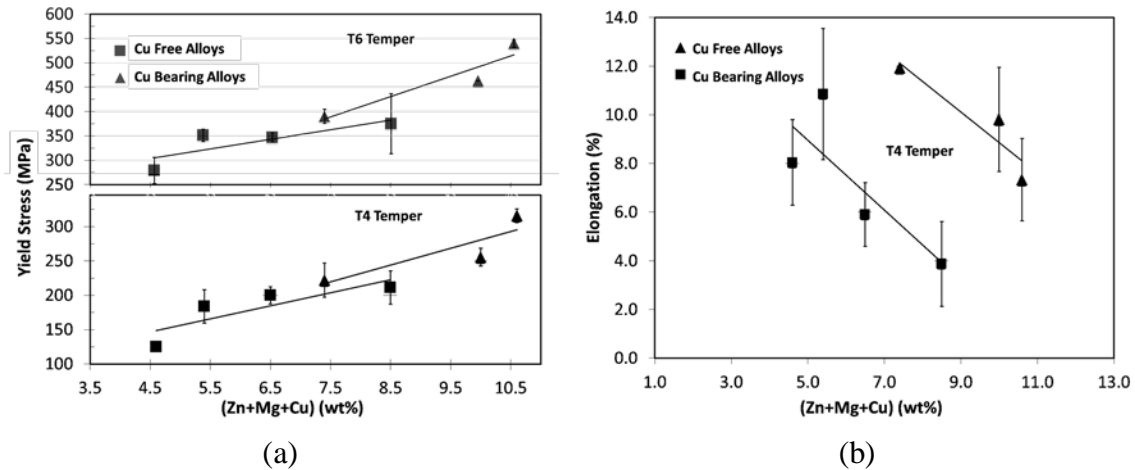


Figure 6–42 Effect of Cu addition on the YS and elongation of the Al 7xxx alloys in this study. (a) plot of YS in both T4 and T6 temper conditions and (b) plot of elongation in the T4 temper conditions.

6.4.3 Effect of grain size

The average grain sizes of various heat treatments of Al-7xxx CDS alloys were measured by the image analysis method according to the ASTM standard number E112–13. The results of measured average grain sizes are presented both in Table 6–12 and Figure 6–43. As it can be seen in Figure 6–43, the average grain sizes are fairly consistent in size distribution in all the alloys. This was a desired result in order to eliminate the effect of grain size variation on the tensile mechanical properties.

Table 6–12 Average grain sizes of the Al-7xxx CDS alloys in various heat treatments.

Average Grain Size (μm)		As Cast	T4	T4+O
1	Al-3.5Zn-0.8Mg-0Cu	53.6 (± 3.9)	62.1 (± 5.8)	59.43 (± 2.5)
2	Al-3.5Zn-1.62Mg-0Cu	63.8 (± 5.1)	71.2 (± 6.8)	75.55 (± 4.3)
3	Al-5.2Zn-1.7Mg-0Cu	57.5 (± 4.0)	69.8 (± 10.5)	74.36 (± 5.7)
4	Al-6.6Zn-1.7Mg-0Cu	68.6 (± 3.7)	74.3 (± 6.6)	69.84 (± 4.7)
5	Al-3.8Zn-2.2Mg-1.7Cu	68.5 (± 4.0)	67.0 (± 7.2)	59.38 (± 4.6)
6	Al-5Zn-2Mg-1.3Cu	64.1 (± 7.1)	63 (± 6)	64.87 (± 2.8)
7	Al-6.5Zn-1.5Mg-2Cu	51.4 (± 4.0)	64.6 (± 5.7)	66.62 (± 5.0)
8	Al-5.8Zn-2.2Mg-2.5Cu	60.5 (± 4.4)	65.4 (± 5.5)	55.21 (± 2.1)
9	Al-9.97Zn-2.4Mg-0.9Cu	58.0 (± 6.4)	73.0 (± 7.2)	69.84 (± 4.7)

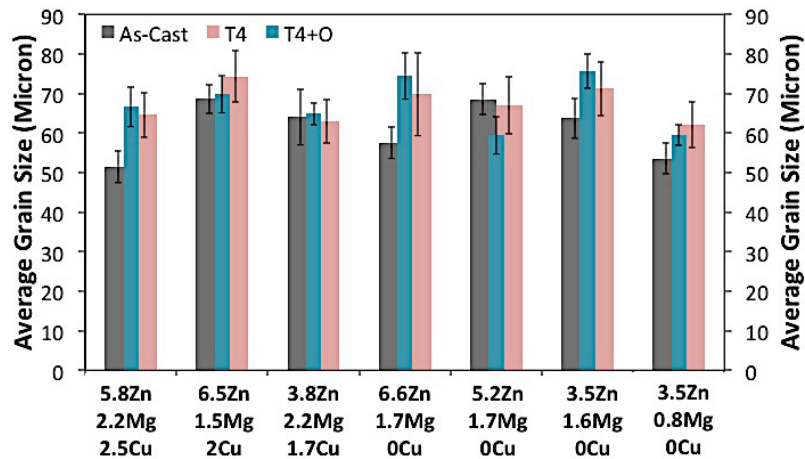


Figure 6–43 The comparative bar graphs representation of the average grain sizes of the Al-7xxx CDS alloys, listed in Table 6–12.

6.4.4 Effect of eutectic phase

The quantified volume fraction of secondary phases evolving during solidification of the various alloys in this study evaluated for the F and T4 tempers is shown in Figure 6–44 along with the predicted volume fraction obtained from phase diagram simulation in Pandat^{*} software under non-equilibrium solidification conditions using the Scheil-Gulliver paradigm. In Figure 6–44, The volume fraction of the phases in the F temper condition is always higher than that predicted by the thermodynamic software and the volume fraction of phases decreases in the T4 temper when compared to the F condition in all the alloys. Further, the deviation in the volume fraction of phase in the F condition from the thermodynamic predictions is larger in alloys with higher element content (Zn+Mg+Cu).

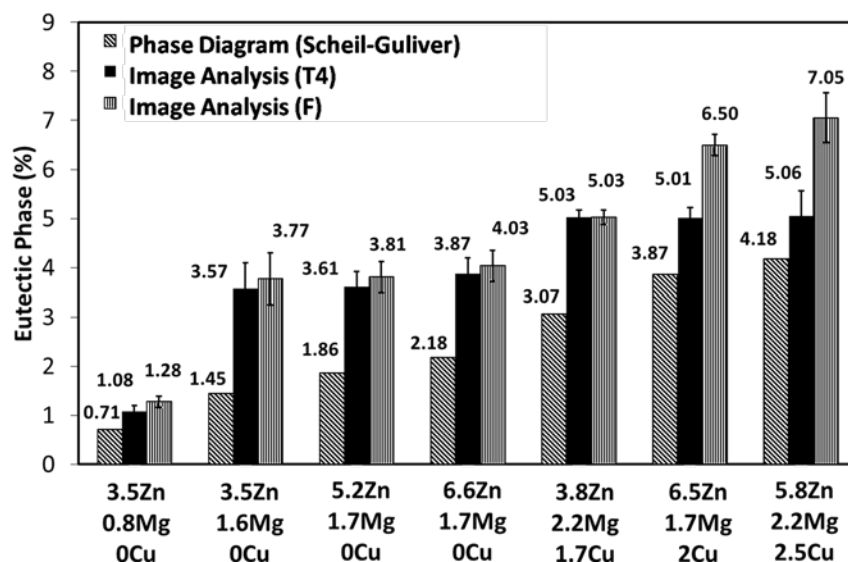


Figure 6–44 Typical comparative bar graphs of fraction area (%) of eutectic phases at grain boundaries, simulated by thermodynamic database (Pandat) and also measured by image analysis on the optical micrographs of the as cast (F) and solution (T4) heat treatments for the Al-7xxx CDS alloys.

* Pan Aluminum Database; CompuTherm LLC, Madison, WI, USA; <http://www.compuTherm.com/>

6.4.5 Effect of porosity content (%)

Figure 6–45 presents the bar chart representation of porosity contents for the Al-7xxx CDS alloys selected for this study, which were evaluated by the density measurements. Also, Figure 6–45 shows that adding Cu to the 7xxx alloys results in an increase in the porosity content of the alloy.

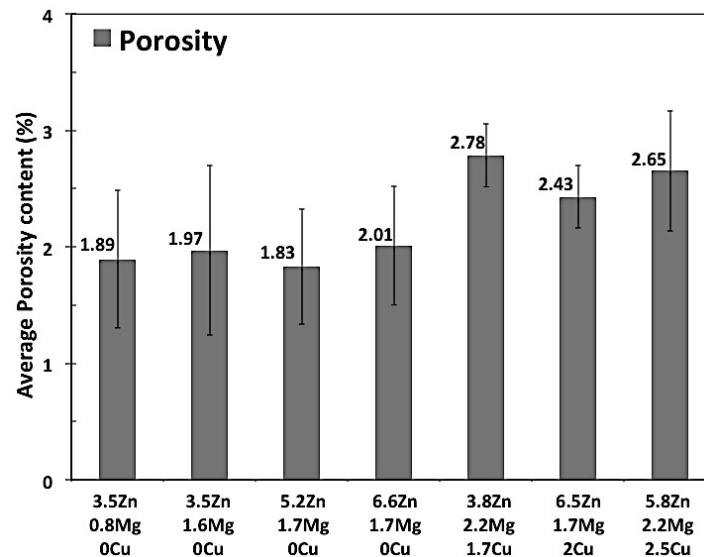


Figure 6–45 The porosity content of the Al-7xxx CDS alloys selected for this study.

Figure 6–46 shows the comparison of the porosity content in the AA7050 alloy cast with the CDS technology and DC cast wrought ingots [181]; the porosity content in the CDS castings are similar to that in as-cast DC cast ingots of the same alloy.

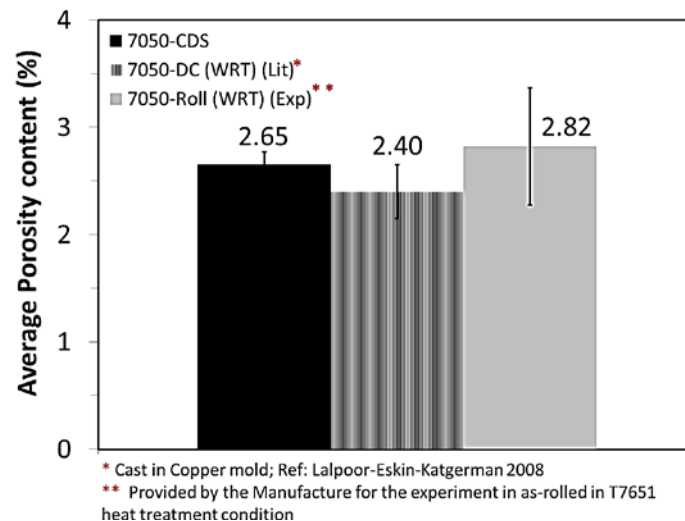


Figure 6–46 Typical comparative bar graphs of porosity content (%) for AA 7050 in CDS and wrought products both from experimental measurements carried out in this study according to standard explained in experimental Chapter 5; it is notable that the wrought samples were provided by the manufacture in T7651 condition. Moreover, the experimental porosity measurements are also compared with that of 7050 found in the background literature (cast in copper mold) [181].

6.4.6 Comparison of AA7050 in CDS Cast and Wrought Conditions

Figure 6–47 presents the uniaxial tensile properties of the CDS and the wrought (rolled) product of the AA 7050 alloy both heat-treated to T4 heat-treated condition (24 hours at 477°C+water quenching+96 hour natural ageing at room temperature). It is noteworthy that the CDS tensile specimens were designed according to ASTM B557 (2-inch gauge length standard size samples with circular cross section); whereas the AA 7050 wrought (rolled) tensile samples were machined out of the 0.25”X6.0” plates in accordance with ASTM E8/E8M–(13a) (flat substandard size with a1.0-inch gauge length), as shown in Figure 5–14 (a) and (b), respectively. In Figure 6–47, the ductility of the CDS castings is lower than that of the wrought products of AA 7050 alloys, which is mainly attributed to the size and morphology difference of intermetallic phases that is more detrimental to ductility properties in the CDS castings than in the wrought products of the AA 7050 alloy.

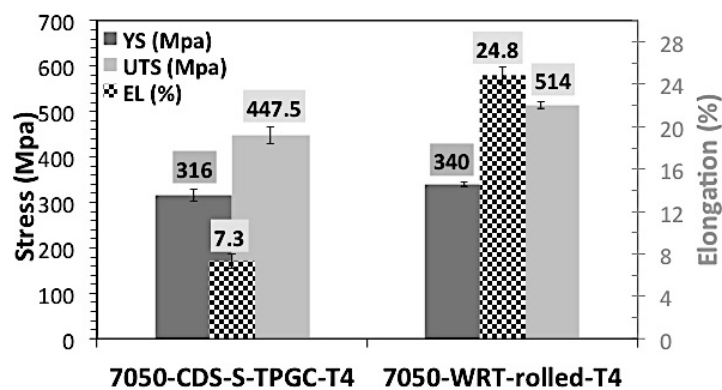


Figure 6–47 Comparative bar graphs of uniaxial tensile properties of AA 7050 alloy produced by two different methods: (1) using the CDS technology and (2) processing with the wrought (rolled*) method. Note that in (a) the uniaxial properties of both CDS and wrought results are reported in an over aged (T7[†]) condition; whereas in (b) they are in solution (T4[‡]) heat treatment condition.

6.5 FRACTOGRAPHY AFTER TENSILE TEST

Figure 6–48 presents low magnification optical stereographs of uniaxial tensile fracture surfaces for the three Al-7xxx alloys cast using CDS and heat treated to the T4 temper: (a) Al-3.5Zn-0.8Mg-0Cu(c) Al-3.8Zn-2.2Mg-1.7Cu (e) Al-5.8Zn-2.2Mg-2.5Cu. In Figure 6–48, the shear lip and fibrous areas on the fracture surface are clearly noticeable indicating ductile fracture. The existence of fibrous area on fracture surface represents the area on which the micro voids nucleate and grow to the extent at which potential slip systems of the bulk material are activated, leading to having a shearing face (also known as “shear lip” area or surface); most of which are aligned at an angle of around 45 ° with respect to uniaxial tensile

* The wrought samples were purchased from the manufacturer, REYNOLDS Inc. (or Alabama Specialty Products, Inc., Munford, AL, USA, www.alspi.com), in the form of hot rolled 0.25”X6” plates according to the ASM 4201B T7651 heat treatment standard.

† The uniaxial tensile data for wrought (rolled) samples in over age (T7) heat treatment condition was used from the manufacture mill certificate.

‡ The wrought (rolled) plates were machined to substandard uniaxial tensile samples according to ASTM E8/E8M–(13a) standard and prior to the tensile tests: the wrought tensile samples were heat treated along with the CDS tensile samples all together in an exactly the same T4 procedure (soaking for 24 hours at 477°C, followed by a water quenching and an 96 hours incubation time at ambient temperature).

loading axis. In the relatively low and high magnification optical images obtained from the cross-section of the fracture surfaces of AA 7050-CDS-alloy in T4 condition, as shown in Figure 6–49, it clearly noticeable that the micro voids were initiated in the vicinity of the insoluble and soluble intermetallic phases at grain boundaries, which further grow alongside of the grain boundaries as the propagation paths. The maximum growth rate of these micro-pores occur in the grain boundaries which are aligned perpendicular to the loading direction in the uniaxial tensile test, as shown in the low and high magnified images of Figure 6–48 (a)-(b) and (d)-(f), respectively.

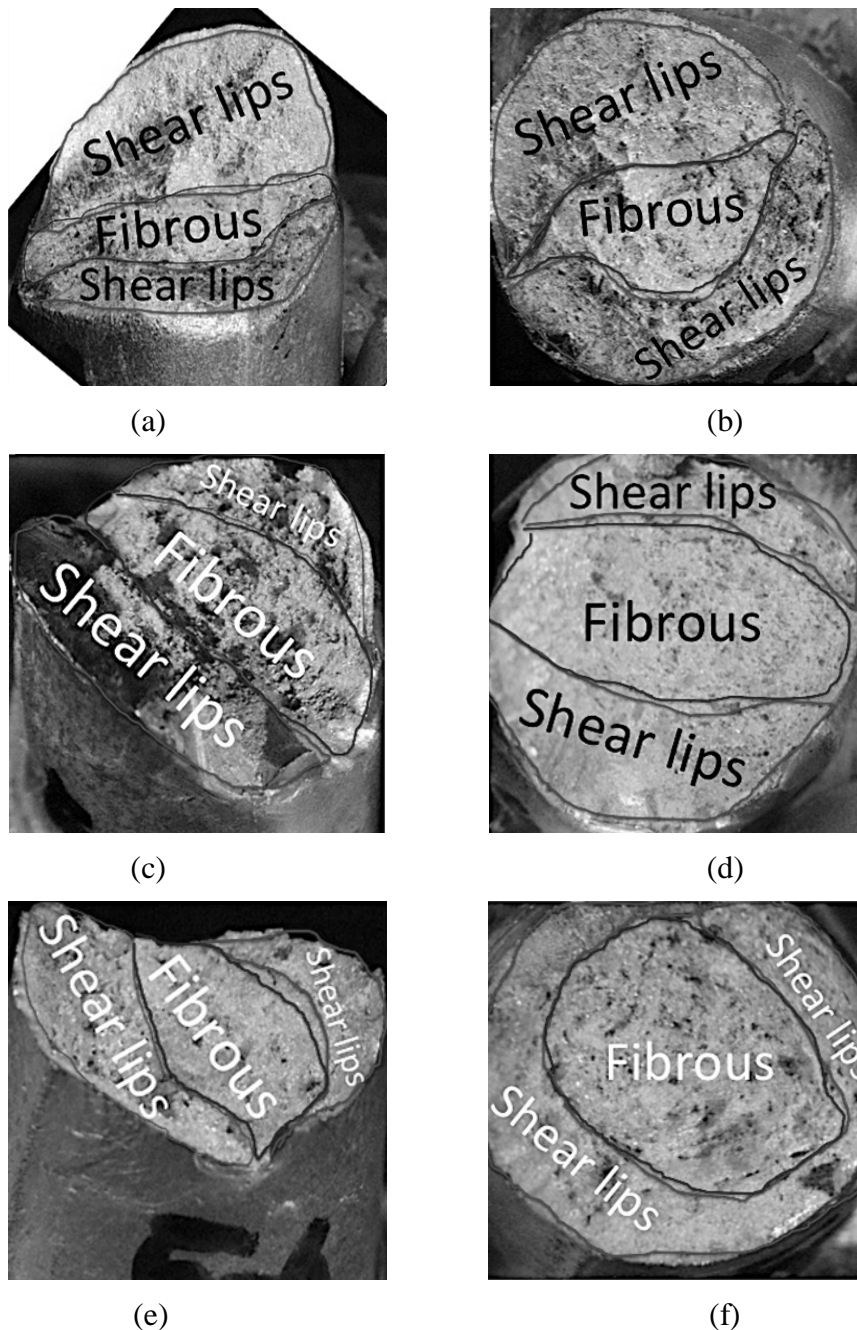


Figure 6–48 Optical stereograph images showing shear lips and fibrous areas on the fraction surfaces (under tension load): (a) Al-3.6Zn-0.8Mg-0Cu (c) Al-3.8Zn-2.2Mg-1.7Cu (e) Al-5.8Zn-2.2Mg-2.5Cu. All the alloys were cast with CDS technology and heat-treated to T4 temper.

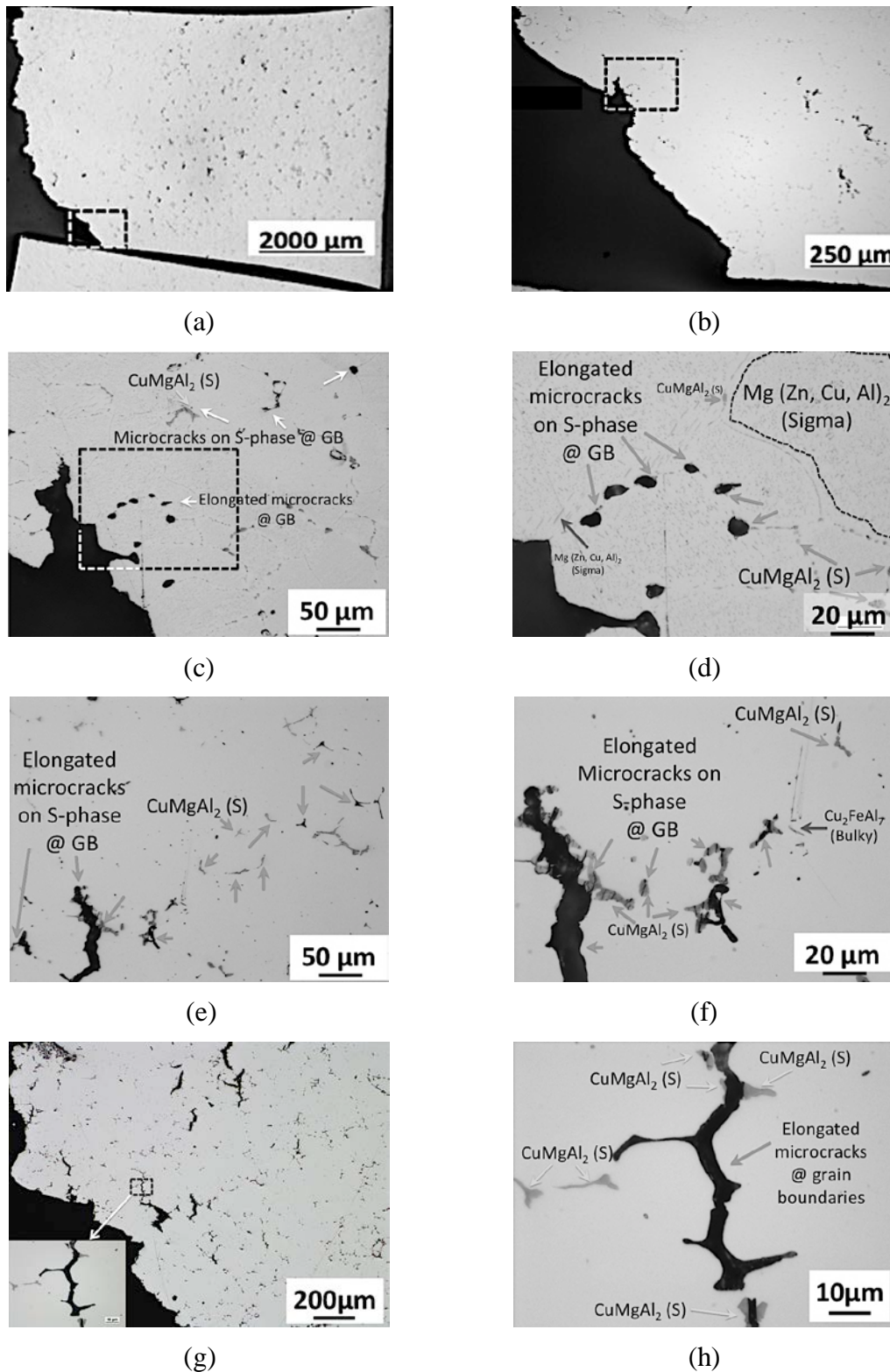
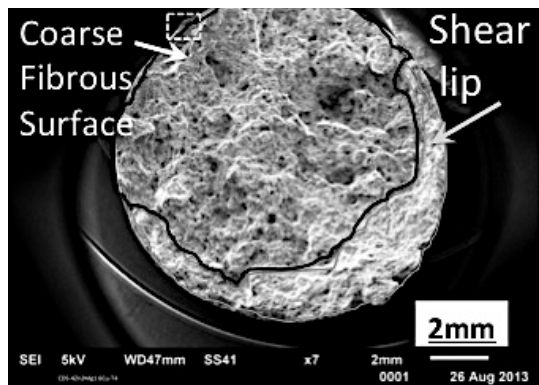


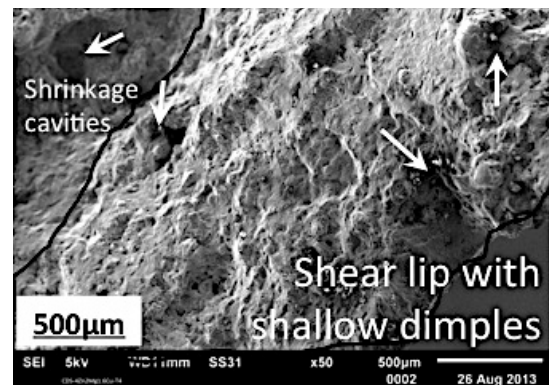
Figure 6-49 Cross sectional image by optical microscopy for Al-5.8Zn-2.2Mg-2.5Cu-CDS samples in annealed (T4+O) heat-treated condition in relatively low and high magnifications; (a) and (b) show crack initiation region; (c) and (d) show existence of micro voids and their coalescence that initiate fracture; (e) to (h) preferred nucleation and growth of the cracks as inter-granular fracture on the interface between the secondary intermetallic phases and primary Al grains.

Figure 6-50 present the SEM micrographs of fracture surface of AA 7050-CDS-T4 samples fractured under the uniaxial tensile load. In the relatively low and high-magnified SEM

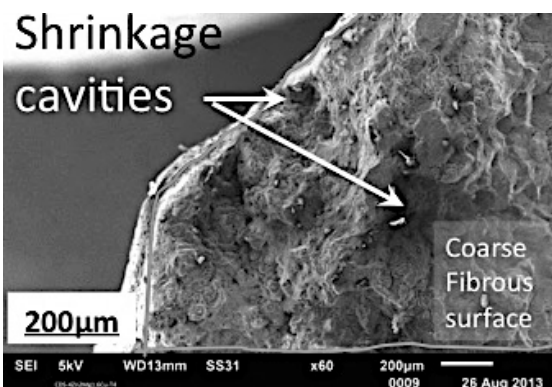
images in Figure 6–50 (a)-(b) and (c)-(d), the shear lip and fibrous areas, respectively, are presented, indicating ductile fracture. In the high-magnified images in Figure 6–50 (e) to (h), the shrinkage cavities with “free surface” are clearly shown on the fracture surface; these are the potential initiation points for the micro cracks. The shrinkage cavities can be characterized by means of “free surface” and “secondary dendritic arms” on the fracture surface, which are clearly shown in the relatively high magnification SEM image of Figure 6–50 (h).



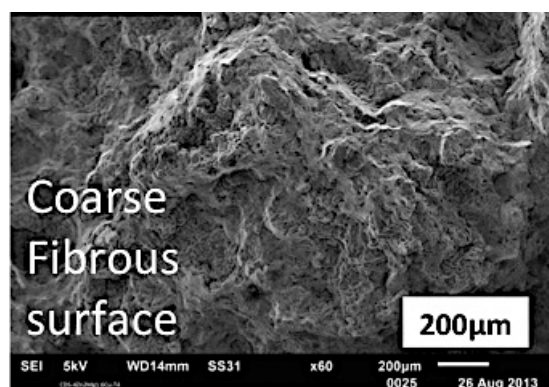
(a)



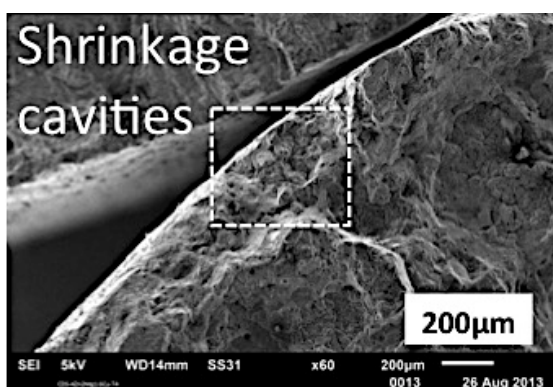
(b)



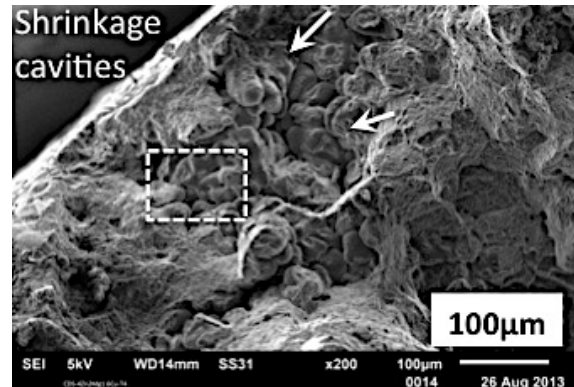
(c)



(d)



(e)



(f)

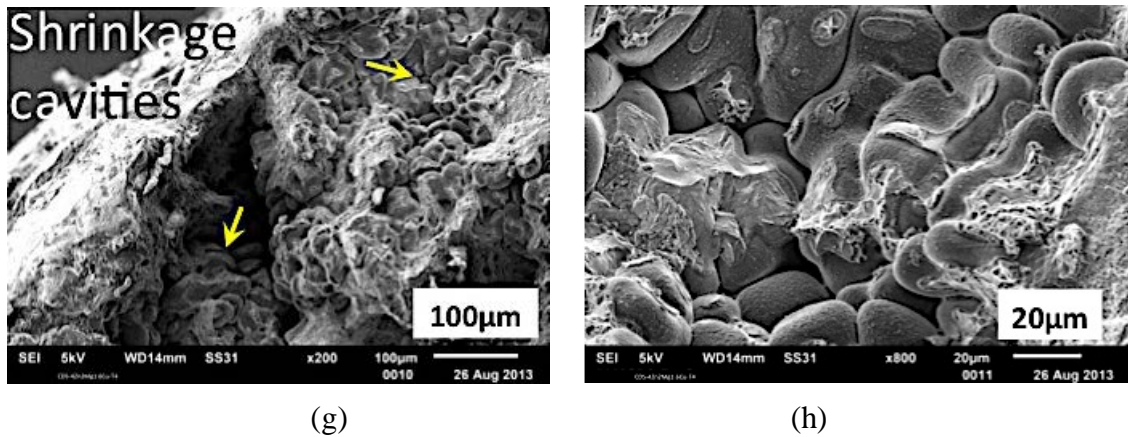
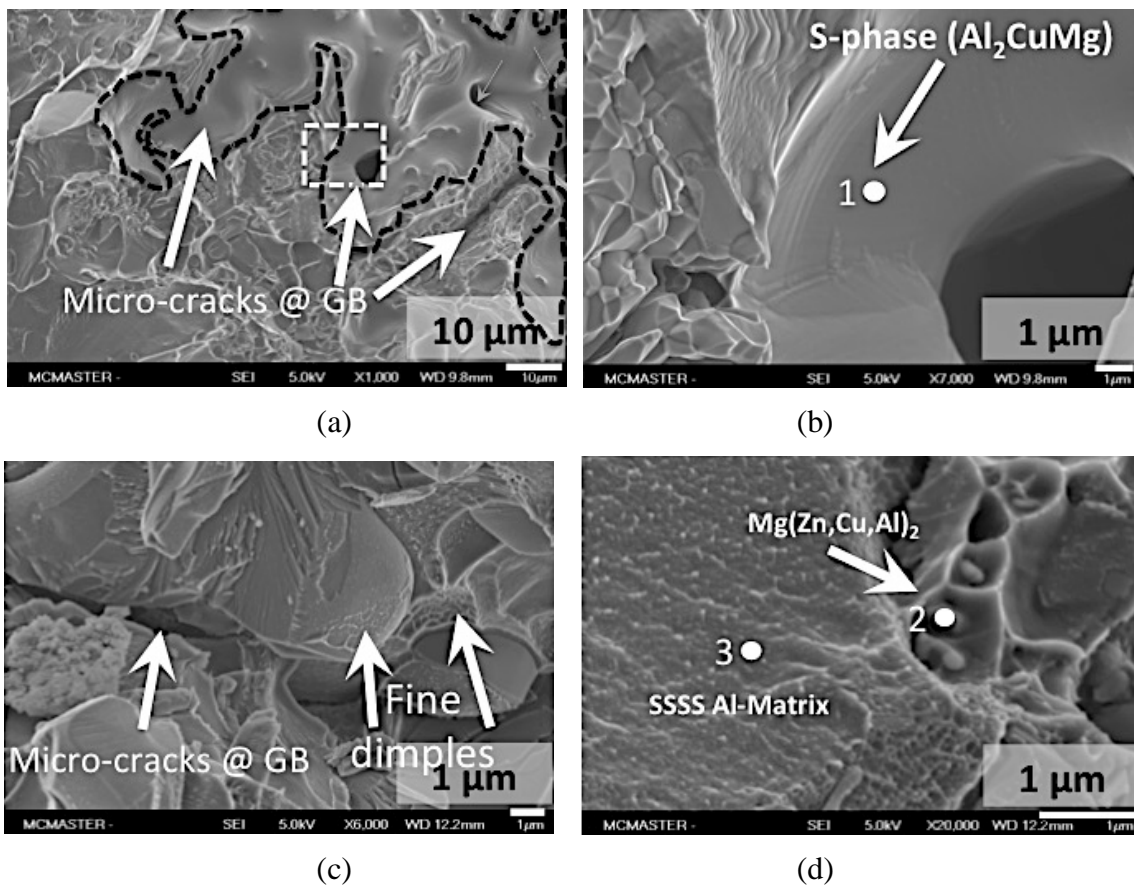


Figure 6-50 SEI on SEM showing the nature of the fracture surface after uniaxial tensile test on Al-5.8Zn-2.2Mg-2.5Cu-CDS samples in T4 temper. (a) and (b) show the fracture surface features; (c) to (h) show the role of shrinkage cavities in the castings on the nature of fracture.

In Figure 6-51, high-magnified SEM images of crack initiation and propagation paths are shown to occur as inter-granular fracture alongside the grain boundary areas at the interface between the secondary intermetallic phases and Al grains; Table 6-13 provides results of the quantitative EDS analyses of the secondary phases alongside the crack; typical phases shown in Table 6-13 are demarcated points such as 1 to 6 in Figure 6-51.



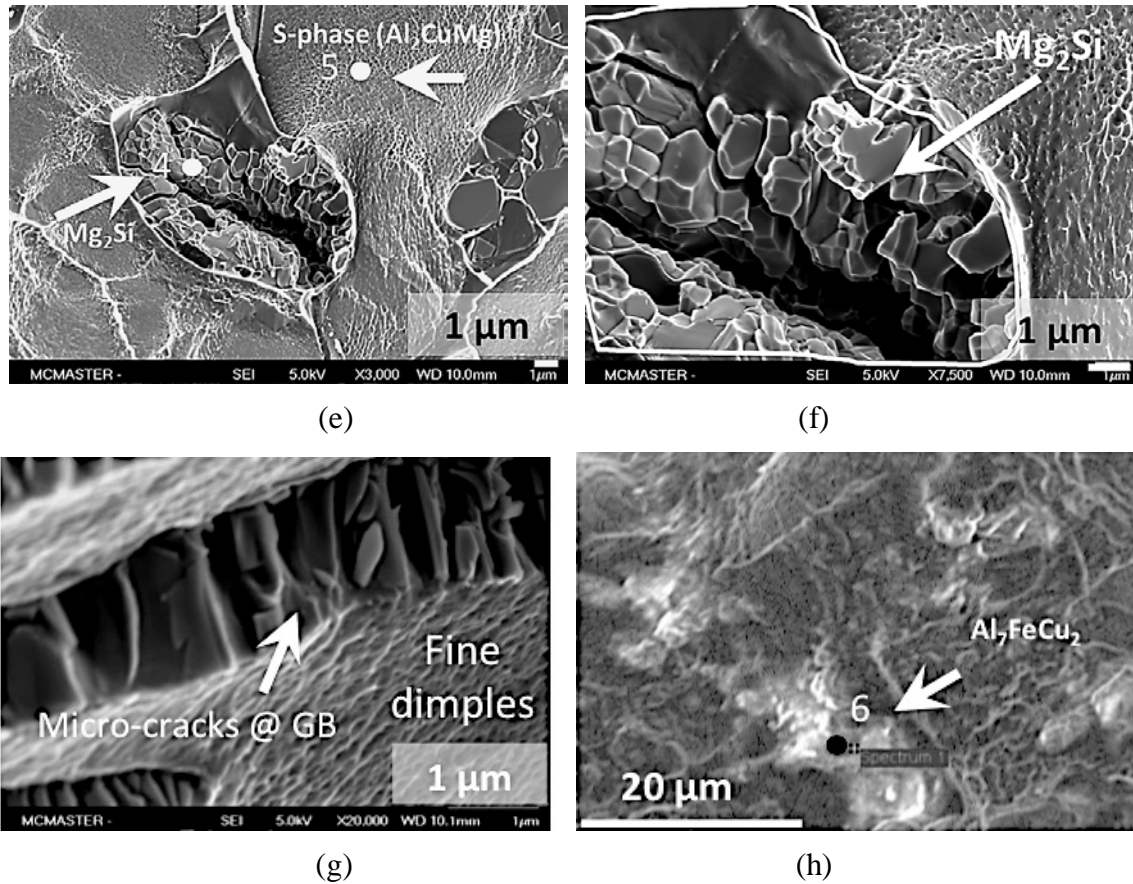


Figure 6-51 Relatively high magnification SEM micrographs showing demarcated points for EDS chemical measurements tabulated in Table 6-13.

Table 6-13 EDS results for point indicated on the fracture surface of in Figure 6-51.

Spot #	Zn-L		Mg-K		Cu-L		Si-K/Fe-K		Al-K		Possible phase
	wt.%	at%	wt.%	at%	wt.%	at%	wt.%	at%	wt.%	at%	
1	23.2	13.1	11.9	18.0	25.0	14.5	-	-	39.7	54.2	S-phase (Al ₂ CuMg)
2	44.3	30.3	16.6	30.5	26.8	18.8	-	-	12.1	20.1	Over aged MgZn ₂ or Mg(Zn,Cu,Al) ₂
3	7.4	3.3	1.6	1.9	4.9	2.2	Fe: 0.7	0.4	85.2	92.0	SSSS Al-Matrix
4	-	-	2.1	3.5	-	-	Si: 37.4	34.4			MgSi ₂
5	9.8	6.1	2.16	3.5	41.7	26.5			38.8	58.1	S-phase (Al ₂ CuMg)
6	2.0	1.2	-	-	37.0	22.3	Fe:13.8	9.5	46.9	66.8	Al ₇ FeCu ₂

7 STRENGTHENING MODEL

Several models to predict the yield strength of the high strength Al alloys that undergo precipitation hardening during heat treatment was presented in Section 4.3.5. In this Chapter, we shall further analyze these models and carry out appropriate evaluation of the parameters in these models using the experiment data in this study and attempt to provide a comparison of the various models and propose one that would be more appropriate for the Al 7xxx alloys cast with the CDS technology in a TPGC process. There are two predictive models discussed in this Chapter: one for the kinetics of the precipitation of the strengthening phases in the Al matrix and the other for the prediction of yield strength of the 7xxx alloy.

7.1 KINETICS OF PRECIPITATION STRENGTHENING

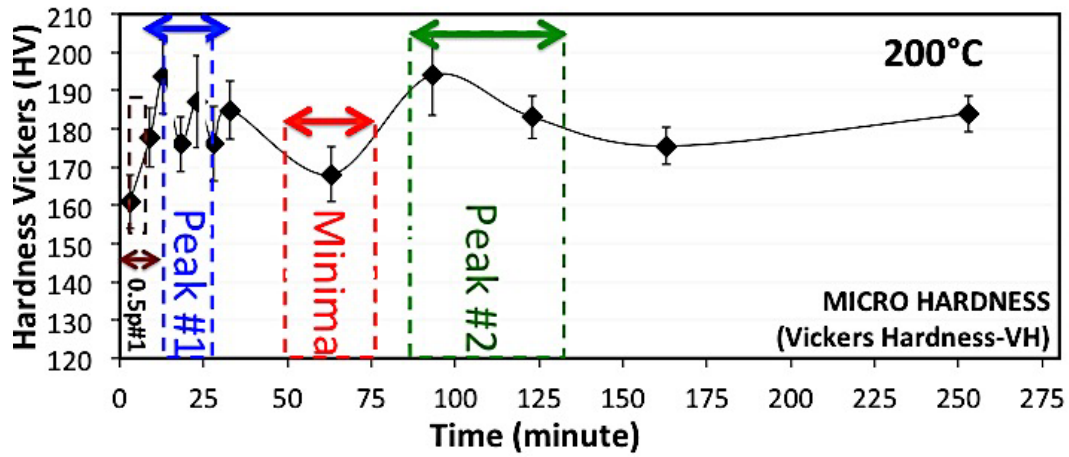
Shercliff and Ashby [121,122] developed a model (Equation 4–13) to predict the yield strength of various families of Al-alloys after various conditions of ageing heat treatment. In doing so, one of the first steps is to be able to determine if the kinetics of the precipitation strengthening reaction during the ageing process is predictable by an appropriate model equation. Shercliff and Ashby [122,123] proposed the model shown in Equation 4–11, which is an Arrhenius type of equation to predict the kinetics of the ageing process; the model to determine the peak age condition of the alloy is shown in Equation 4–12 which is show in Equation 7–1.

$$P_p = \frac{t_p}{T} \exp\left(\frac{-Q_A}{RT}\right) \quad \text{Equation 7-1}$$

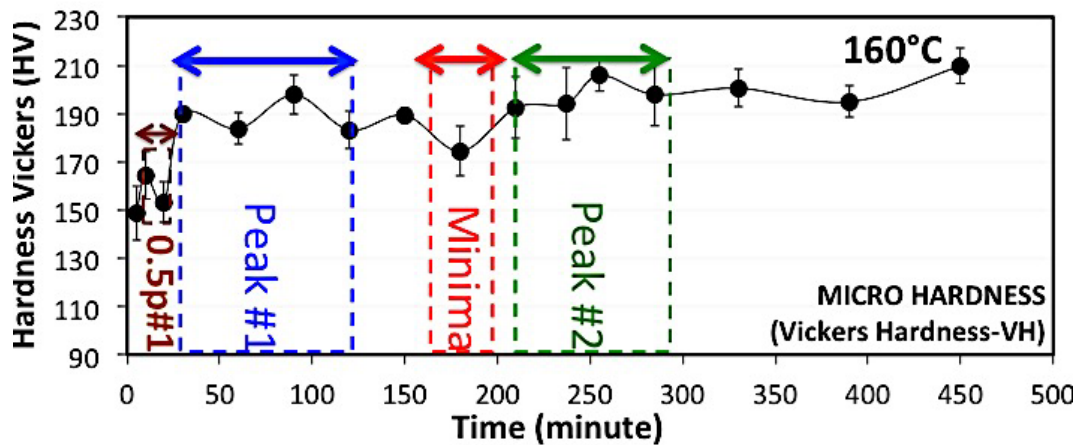
In Equation 7–1, when the validity of its model for the Al7xxx alloy will be determined by plotting $\ln(t_p/T)$ against $1/T$; if this plot yields a straight line then the model shown in Equation 4–12 is valid for the 7xxx alloy family as well. Further, validation of Equation 7–1 would enable the quantification of the temperature corrected peak time parameter, P_p and the activation energy, Q_A .

Figure 6–29 (a) to (d) present the micro- and macro-hardness test results for the Al-5.8Zn-2.2Mg-2.5Cu alloy that are obtained during the various artificial ageing processes at elevated temperatures: 70°C, 120°C, 160°C and 200°C, respectively; the three salient features of the hardness curve are the peak #1, minima and peak #2. In addition to these three salient features in the ageing curve, an additional feature in time taken to reach 50% of the hardness represented by peak #1 was also considered in this study. The identification of the two peaks and the minima in Figure 6–29 (a) to (d) was only carried out as a visual determination of these features to aid an initial qualitative discussion of the subject matter. However, for validating the Equation 7–1, determination of the salient features in the hardness curves in Figure 6–29 must be carried out in a statistically acceptable manner. In order to overcome the limited available resolution of the transient hardness data in Figure 6–29, a range of time scale could be selected for each of the four salient features in each of the four curve, respectively, as shown in Figure 7–1; wherein the four features in presents the time taken to reach 50% of the hardness represented by Peak #1, Peak #1, local Minima and Peak #2 are

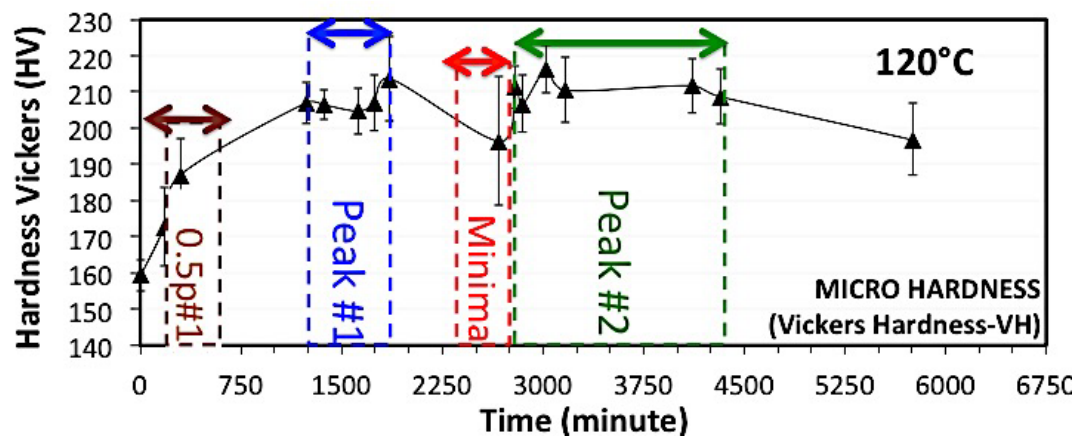
shown by demarcated regions. Figure 7-1 (a) to (d) present the transient hardness data for the four experiment temperatures of 70°, 120°, 160° and 200° C, respectively, for the samples shown in Figure 6-29 (a) to (d).



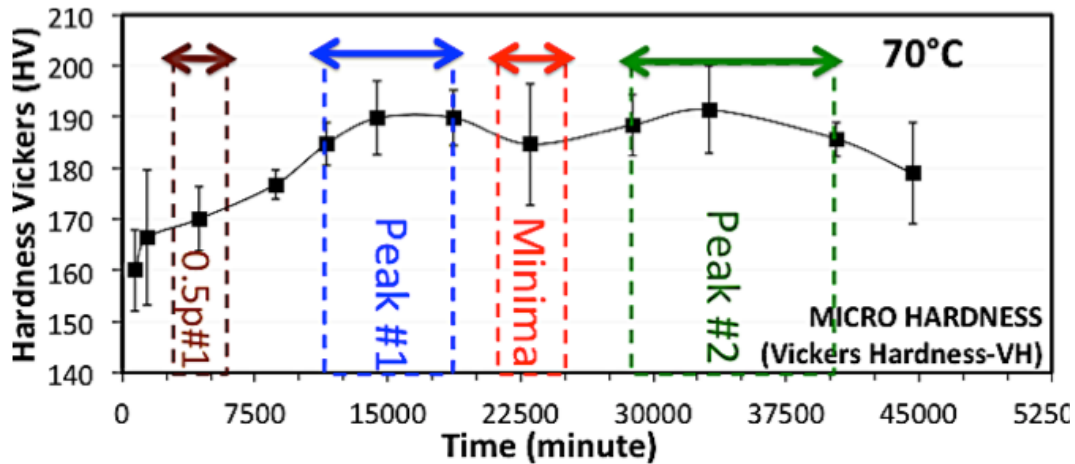
(a)



(b)



(c)



(d)

Figure 7–1 Typical micro-hardness (Vickers Hardness) data as a function of time measured from immediately after quenching the AA 7050 CDS alloy castings samples in water at room temperature after T4 treatment at 477 °C. The subsequent isothermal ageing temperature of the samples were (a) 200 °C, (b) 160 °C, (c) 120 °C and (d) 70 °C. The demarcated regions in each figure represent the selection of these respective features with the assumption that the features could occur in any time location within these respective regions of interest.

A plot of $\ln(t_p/T)$ versus $1/T$ for each of the four regions of interest demarcated in Figure 7–1(a) to (d), respectively is presented in Figure 7–2; wherein, the result of a linear regression analysis weighted least square method for each of the plots in (a) to (d) is also superimposed on the data along with the coefficients of each fit and the R^2 value for the respective fits. Table 7–1 presents the quantified results of the weighted regression analyses shown in Figure 7–2 (a) to (d), respectively.

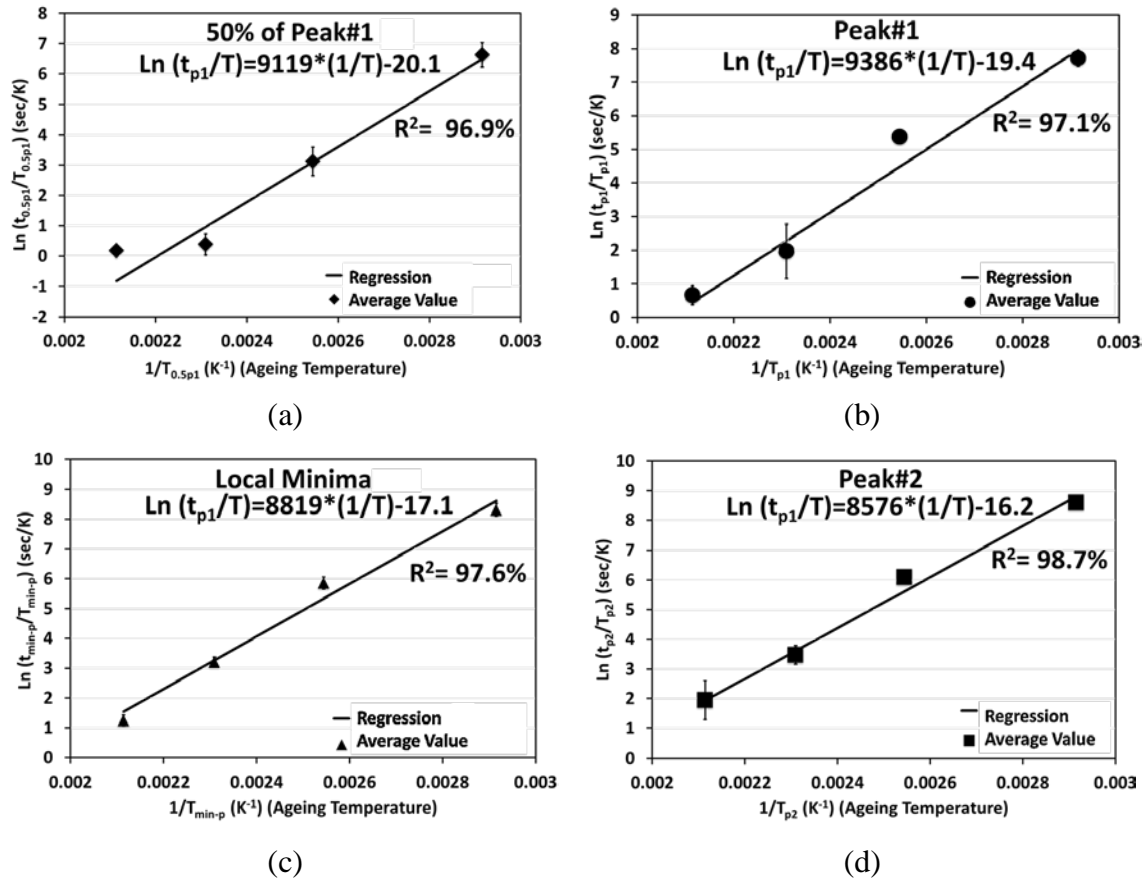


Figure 7–2: The typical graphs of Arrhenius plot of $\ln(t_p/T)$ vs. $1/T$ by which a value for the Q_A (activation energy) is calculated from the slope of the Arrhenius plot. It is noteworthy that. This validity test has been tried for various designated stages presented on the age hardening curves (FIGURE) such as (a) for 50% of the peak hardness value of peak hardness point #1 (Peak#1), (b) for the peak hardness point #1 (Peak#1), (c) for the local minima peak hardness point between the two peak hardness points #1 and #2, and (d) for the peak hardness point #2 (Peak#2).

Table 7–1 Results of the weighted linear regression analysis for each of the curves shown in Figure 7–2 (a) to (d), respectively.

Feature	Parameter	Coefficient	Standard Error	P-value
50% of Peak#1	Constant	-20.08	2.96	0.021
	(1/T)	9119	1158	0.016
Peak#1	Constant	-19.43	2.79	0.020
	(1/T)	9386	1154	0.015
Local Minima	Constant	-17.13	1.98	0.013
	(1/T)	8819	790.2	0.008
Peak#2	Constant	-16.17	1.31	0.006
	(1/T)	8575	557.7	0.004

The standard error term shown in Table 7–1 was used to evaluate the 95% confidence interval for each coefficient and the results for the temperature corrected time parameter, P_p

and Q_A for each of the four salient features in the transient hardness curves are tabulated in Table 7–2.

Table 7–2 Results of P_p and Q_A along with the respective 95% confidence interval for each of the four salient features in the transient hardness curves shown in Figure 7–1 (a) to (d), respectively.

Feature	Activation Energy, Q_A (KJ.mol ⁻¹)		P (x10 ⁻⁸) (Sec.K ⁻¹)
	Mean	95% Confidence Interval	Mean
50% of Peak#1	75.819	±9.6	5.36
Peak#1	71.304	±9.5	2.66
Local Minima	73.324	±6.5	0.267
Peak#2	78.038	±4.6	0.11

The results presented in Figure 7–2 provides a strong evidence that the kinetics of the precipitation strengthening reaction in an AA7050 alloy sample follows the Arrhenius type equation shown in Equation 7–1. Application of the Shercliff and Ashby [122,123] *validity test* on the experiment results shown in Figure 7–1 demonstrates that the constancy of the *temperature-corrected time parameter* (P) and the activation energy Q_A (Figure 7–2) is not only valid for the two distinctive peak-points (i.e., Peak#1 and Peak#2) of the age-hardening (hardness) curves of the Al-7050 CDS alloy at four various ageing temperatures: 70, 120, 160 and 200°C (); but holds true for the other features on the age hardening curves such as the local minima and time for 50% hardness of the Peak#1. These results suggest that the constancy of P and Q_A would be most probably maintained for any particular respective feature in the transient hardness curve.

The constancy of the values of P and Q_A in the 7xxx Al alloy could be a useful design tool to determine the onset of ageing to initiate the various possible T7 type over-ageing heat treatment that are quite commonly carried out in these alloy systems to achieve various degrees of resistance to corrosion from harsh environmental conditions during operation [5].

7.2 ACTIVATION ENERGY (Q_A): AL-7050 CDS CAST SAMPLES AND WROUGHT PRODUCT

The reported values of Q_A of 135 kJ/mol, in the literature [132,146], assuming the mobility of the atoms during the over-aging of the strengthening precipitates in a 7xxx alloy wrought product is entirely from volume diffusion. The value of Q_A in this study is about 75 kJ/mol and this lower than the published value. The scope of this project does not include the elaborate academic work required to provide a mechanistic reason to justify the lesser value for Q_A observed in this study; however, one could hypothesize a general explanation for the same as elaborated below.

It is notable that the experiments carried out to determine the value of 135 kJ/mol in the literature by Dorward [146] were such that the activation energy for the dissolution of overaged strengthening precipitates were evaluated and the mechanism of the dissolution process is almost entirely volume diffusion. The activation energy calculated in this study (~75 KJ/mol) is measured for the process of precipitation from a nearly super saturated solid solution (SSSS) state of the primary Al phase in the solid; which, as amply described in the literature review section of this dissertation, involves large number of intermediate stages encompassing a complex and interdependent set of processes such as such as volume

diffusion of solute atoms, several nucleation mechanisms for the two types of GP zones, three possibilities of phase transformation from GP zones to η' , intermittent preferential dissolution of a few GP zones and precipitates, and growth, impingement and coarsening of precipitates; this level of complexity in the process is unique to the 7xxx Al alloy system and markedly different from the precipitation reactions in most other systems such as the 2xxx system wherein the volume diffusion of solute atoms largely dominate the precipitation mechanism. As further described in the literature review section of this dissertation, the unique dependence of the variable stoichiometry of the precipitates, at every stage of the strengthening process, on the initial composition of the alloy for the 7xxx series of Al alloys further intensifies the complexity of the process mechanism. Notably, there is an agreement amongst the scientists globally that the details of the mechanism of the steps in the strengthening precipitation reaction in the 7xxx Al alloy family is still at-large.

7.3 STRENGTHENING MODEL FOR YIELD STRENGTH PREDICTION

Table 7–3 shows the chemical composition of the three alloys selected to better understand the strengthening mechanisms in the Al 7xxx alloys along with the quantified results of the parameters defining the strengthening precipitates: planar diameter of the precipitate (D_p) or Equivalent Circular Diameter (ECD), average planar free inter-particle spacing (λ) and volume fraction (f_v). Figure 7–3 is a graphical representation of the ECD, λ and f_v shown in Table 7–3.

Table 7–3 Experimental data used in the process models for strengthening mechanisms.

Alloy Designation	Residual Solid Solution in the matrix after T6-precipitation that are calculated by the mass balance.						D_p (nm)	λ (nm)	Fv (%)
	Zn		Mg		Cu				
	wt.%	at%	wt.%	at%	wt.%	at%			
Al-3.5Zn-0.8Mg-0Cu	3.14	1.32	0.42	0.47	0.0		6.7	29.4	0.80
Al-3.8Zn-2.18Mg-1.7Cu	3.21	1.36	1.26	1.43	1.10	0.48	4.9	18.7	1.11
Al-5.8Zn-2.2Mg-2.5Cu	5.07	2.17	1.37	1.57	1.55	0.68	5.4	12.6	2.33

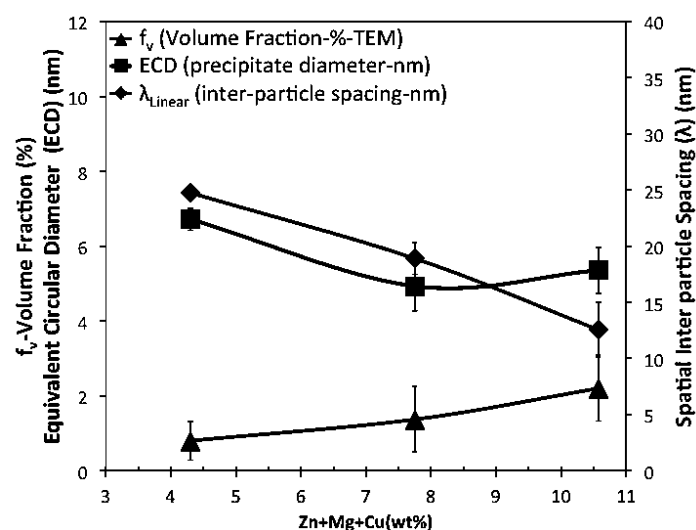


Figure 7–3 Quantitative image analysis on the TEM micrographs for three alloys of the Al-7xxx family selected for this study (Table 6–7).

Table 7–4 presents the mechanical properties of the alloys experimentally evaluated from the uniaxial tensile tests and used as the materials constants in the strengthening process models. Figure 7–4 shows the uniaxial tensile properties of the selected alloys in two heat treatment conditions: T4 and T6.

Table 7–4 Details of the material constants used for application of process models explained earlier for this study.

Alloy Designation	Modulus (E) MPa	Modulus (G or μ) MPa	Burger's Vector (b) nm
		$G=E/(2*(1+\nu))$ Poison's ratio: $\nu=0.3$	
Al-3.5Zn-0.8Mg-0Cu	70000 [5,31]	26923	0.284
Al-3.8Zn-2.18Mg-1.7Cu	70000	26923	0.284
Al-5.8Zn-2.2Mg-2.5Cu	70000	26923	0.284

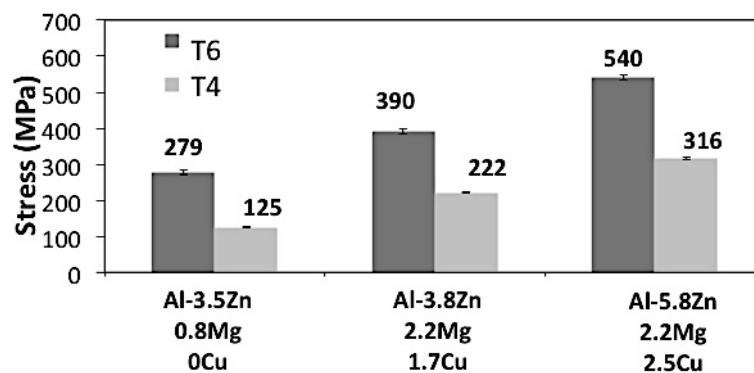


Figure 7–4 Uniaxial Tensile properties in T4 and T6 condition for the three alloys shown in Table 6–7.

There are three approaches from the prior-art to model the strengthening behavior of Al 7xxx alloys: Deschamps and Bre chet (DB) [130,131] Starink and Wang (SW) [137] and Dixit-Mishra-Sankaran (DMS) [149]. All these models are based on a combination of the individual contributors to the yield strength in the alloy as listed in Table 7–5.

Table 7–5 Contributing factors to the total yield strength of Al 7xxx alloys.

Factor	Description	Relevance
σ_a	Intrinsic strength of the nearly pure primary Al matrix devoid of any solid solution.	
σ_{ss}	Solid solution strengthening by alloying elements dissolved in Al matrix.	Active in all heat treatment tempers.
σ_{gb}	Grain boundaries of Al grains (grain size).	
σ_{ppt}	Strengthening precipitates in the Al matrix.	Active in aged condition
σ_{dis}	Dislocations in the Al matrix.	

The DB approach uses the principle stress; σ for the model while SW and DMS approaches uses both σ and τ in the models. The stresses, σ and τ could be used interchangeably and their relationship is show in Equation 7–2; where M is the Taylor factor, which varies between 2 and 3.1 depending on the approach chosen for the model.

$$\sigma = M\tau \quad \text{Equation 7-2}$$

In this section, the models will be represented only by σ along with the value of M to maintain uniformity of presentation; further, the nomenclature of the contributing stresses in Table 7–5 have also been adopted for this purpose.

As discussed in prior-art, the SW and DMS approaches use two difference types of grain sizes in the alloy; fully un-recrystallized and fully recrystallized. It is notable that Al 7xxx in its wrought form would undergo mechanical cold / hot working resulting in recrystallization and growth of Al grains; hence, the assumption of two-grain sizes is valid. However, in the Al 7xxx alloys cast as net shape using the CDS technology coupled with TPGC process, the grains are akin to the fully recrystallized form and there would be no mechanical processing on the cast samples during the heat treatment processes. Hence, in determining the apt model to predict total yield strength in the alloys used in this study, only the *fully recrystallized* assumption for the Al grains will be employed and the grain sizes of the respective alloys were evaluated using quantitative metallography (shown in Table 6–12) as the input data into the models. The parameters shown in Table 7–5 would be further discussed in the following sections.

7.3.1 Intrinsic Strength

The intrinsic strength σ_a is the strength of the primary Al matrix, which is devoid of any solid solution or strengthening precipitates; in other words, it represents the base line strength of the pure Al in the matrix and also referred to as friction stress. Table 7–6 presents the values of the intrinsic strengths from the DB, SW and DMS approaches along with the assumption of intrinsic strength as an average of those in the three approaches; also, shown in this table are the values of M for the three approaches and the assumption of M in this study.

Table 7–6 Values of Intrinsic Strength (σ_a) in various modeling approaches.

Approach	σ_a (MPa)	Taylor Factor (M)
DB [130,131]	10	2
SW [137]	17.85	2.55
DMS [149]	16	3
Present Study	14.5	-

It is notable that the value of intrinsic strength is more than an order of magnitude less than the total yield strength of the material; hence, assuming one value for the σ_a between the two extremes of 10 and 17.85 MPa would only have a marginal effect on the estimation of total yield strength.

7.3.2 Solid Solution Strengthening

All the three approaches (DB, SW and DMS) use the same expression for contribution by the solid solution strength as presented Equation 7–3; where A_{ss} is a constant, C_i is the composition of the element and the subscript i represents each alloying element in the solid solution of the primary Al matrix.

Table 7–7 presents the values of A_{ss} for three approaches and Table 7–8 presents the values of σ_{ss} . Figure 7–5 shows the solid solution strengthening effect on the yield stress for different compositions of the Al-7xxx alloys selected for this study and cast with the CDS process coupled with the TPGC machine including the three alloys used for the application of strengthening models. Using our experimental results, in Figure 7–4, it is shown by the engineering stress-strain curves that the increasing the total alloying elements increases the yield stresses for the Al-7xxx alloys in T4 heat treatment condition.

$$\sigma_{ss} = \sum_i \left\{ (A_{ss})_i \cdot (C_i)^{\left(\frac{2}{3}\right)} \right\} \quad \text{Equation 7-3}$$

Table 7–7 Values of A_{ss} for the various approaches to strengthening modeling.

Approach	A_{ss} (MPa)	Comments
DB [130,131]	840	Composition in atomic fraction [130,131]
SW [149]	924	Composition in atomic fraction. The value of A_{ss} was evaluated by considering 130 MPa for $\sigma_\alpha + \sigma_{ss}$ from Dorward [146].
DMS [137]	$A_{Zn}=3.084$ $A_{Mg}=20.481$ $A_{Cu}=12.431$	Composition in weight percent [149]

Table 7–8 Evaluation of σ_{ss} for the three alloys in this study

Alloy Designation	σ_{ss} (MPa)		
	DB Approach [130,131] (M=2)	SW Approach [149] (M=2.55)	DMS Approach [137] (M=3)
Al-3.5Zn-0.8Mg-0Cu	57.59	63.34	54.33
Al-3.8Zn-2.18Mg-1.7Cu	85.90	94.48	131.76
Al-5.8Zn-2.2Mg-2.5Cu	105.01	115.50	153.09

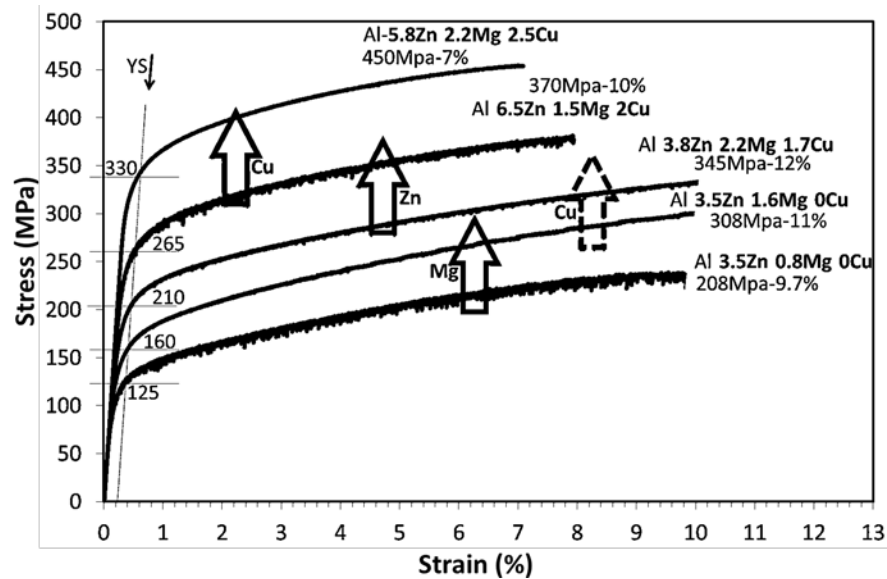


Figure 7-5 Engineering stress-strain curves for different compositions of the Al-7xxx alloys in T4 heat treatment condition, that were selected for this study and cast with the CDS process coupled with the TPGC machine including the three alloys used for the application of strengthening models. It is shown in the figure that increasing the total alloying elements in the composition of the Al-Zn-Mg-Cu alloy increases the yield stress of the material.

7.3.3 Precipitation Strengthening

There are two interactions between the strengthening precipitates in the Al matrix and the moving dislocations during the uniaxial tensile tests: shearing / cutting of the precipitates and by-pass of the same by the dislocations. The DB approach evaluates the critical radius of the precipitate as about 3.5 nm; below which the shearing mode will be active and above which the by-pass mode will be active [130,131]. Hornbogen and Starke [125] have shown that the critical radius for this transition between shearing and by-pass mechanisms is marginally less than 1nm as shown in Figure 4-39. The SW approach of peak and overaged samples indicate that in Al-Zn-Mg-Cu alloy, “It has been shown by several authors that precipitation strengthening in Al-Zn-Mg (-Cu) alloys can be modeled by considering the dislocation bypassing mechanism only.” and assumes that only the by-pass mechanism is the active interaction between the precipitates and dislocation motion [137]. The size distribution of the precipitates in this study is shown in Figure 6-27 which shows that assuming that the dislocation movement around the precipitates in the Al matrix for the three alloys could be safely assumed as mostly being the by-pass mechanism. In this study, the by-pass mechanism for dislocation movement through the precipitates is assumed.

One of critical factors to evaluate the σ_{ppt} is the quantified size, distribution and morphology of the strengthening precipitates: diameter of the precipitate (D_p), average spacing between two precipitates (λ) and aspect ratio of the precipitates. There are two categories of precipitate morphology that is observed in the Al-Zn-Mg- (Cu) system: circular cross-section (spheres or cylindrical rods) and/or plate (also disc) shaped. Typically, in this alloy system, the circular cross section morphology are exhibited by the GP zones and η' precipitates which are predominant around the peak aged condition (T6), while the η precipitates are disc shaped which are predominant in the overaged condition (T7 or O). Typical images of disc shapes and circular morphology are shown in Figure 6-13 and Figure 6-24. The samples used for the models to predict the yield strength of the alloys in this study are all in the T4 and T6 temper conditions which could lead to the assumption of predominantly circular cross-

section (rods or spheres) morphology for the strengthening precipitates as confirmed the TEM images in Figure 6–22 and Figure 6–23. Considering this, there are three main approaches to determine the σ_{ppt} , all of which assume a circular cross-section morphology (rods or spheres) of the precipitates: Table 7–9 presents a summary of these approaches.

Table 7–9 Expressions to evaluate σ_{ppt} in the various approaches to strengthening modeling.

Approach	Expression	Precipitate Morphology	Parameters in the Expressions
Kocks [131]	Equation 4–18	Spherical	
Zhu-Starke [147]	Equation 4–23	Circular cross-section (spheres and/or rods)	$b = 0.284 \text{ nm}$ $v = 0.3$ $r_o = 0.6 \text{ nm}$
Kelly [153]	Equation 4–30	Spherical	

In Equation 4–23, there are two methods to evaluate λ_{cc} , both are from image analyses procedure described in the Section of Image Analysis (5.6) of this dissertation. The first method evaluate the inter-particle distance on a two dimensional (2D) image (as shown in Table 7–3) and the second would be to determine the volume fraction, f_v , of the precipitates (as shown in Table 7–3) in the entire volume of the TEM foil and use Equation 7–4 [134]. The former method presents the inter-particle spacing of the precipitates that are present in a three dimensional (3D) space in the matrix but projected in a 2D area in the measurement image. Hence, the value of λ_{cc} measured from the 2D image will be a lower estimate than reality and the value evaluated from the measurement of f_v as in Equation 7–4 would be more acceptable one as it assumes that the precipitates are distributed in the entire volume (3D).

$$\lambda_{cc} = \left(\frac{\pi}{6f} \right)^{1/2} \cdot \langle D_p \rangle \quad \text{Equation 7–4}$$

The values of λ_{cc} ($=\lambda+D_p$) and D_p are tabulated in Table 7–3, and G and b are shown in Table 7–4. Using these measured parameters and Equation 7–4; and Equation 4–18, Equation 4–23, and Equation 4–30, the evaluations of σ_{ppt} is presented in Table 7–10.

Table 7–10 Evaluation of σ_{ppt} in the various approaches to strengthening modeling.

Modelling Approach	σ_{ppt} (MPa)								
	Zhu-Starke [147]			Kelly [153]			Kocks [131]		
	Taylor Factor (M)								
Alloy Composition	2	2.55	3	2	2.55	3	2	2.55	3
Al-3.5Zn-0.8Mg-0Cu	75	96	113	98	124	146	192	245	288
Al-3.8Zn-2.18Mg-1.7Cu	107	137	161	140	178	209	308	393	462
Al-5.8Zn-2.2Mg-2.5Cu	155	198	233	206	263	309	411	524	616

7.3.4 Dislocation Strengthening

Al 7xxx in wrought condition, when subjected to cold working between heat treatment cycles would create significant number of dislocations in the primary Al matrix which when subjected to a tensile load lead to entanglement as explained in Section 4.3.3 of this dissertation. Equation 4–8 presents an expression to evaluate the shear stress contribution from the dislocation entanglement which leads to significantly higher values of dislocation area density; in a cold work condition the typical density of dislocations in the matrix is in the order of 10^8 to 10^{10} mm^{-2} and that in the fully annealed condition is at 10^3 to 10^4 mm^{-2} [96]; the values of contribution to the yield stress by dislocation network in the matrix would be about 40 MPa in the cold work and 0.13 MPa in the fully annealed conditions. In this study the samples were not subjected to any cold work and the dislocations would only increase through the thermally induced stresses during quenching after T4 treatment which would typically be marginal at best; hence, even with an assumption of 10^6 mm^{-2} for dislocation density in our samples (on the higher side), the contribution to the yield strength is about 4MPa and this value is not a significant contribution. Hence, the contribution to the total yield strength by the dislocation density in the matrix was neglected.

7.3.5 Grain Boundary Strengthening

Table 7–11 presents the values of σ_{gb} for the three alloys as formulated by both SW and DMS approaches.

Table 7–11 Grain boundary strengthening (σ_{gb}) in the DMS approach to strengthening modeling.

Approach	Alloy Designation	DGS (μm)	σ_{gb} (MPa)	
SW [137]	$\sigma_{gb} = \frac{\alpha_2 Gb}{D_{gs}}$	Al-3.5Zn-0.8Mg-0Cu	62.1	0.25
	$\alpha_2 = 2; b = 0.28\text{nm}$	Al-3.8Zn-2.18Mg-1.7Cu	67.0	0.23
		Al-5.8Zn-2.2Mg-2.5Cu	60.5	0.26
DMS [149]	$\sigma_{gb} = \frac{k}{\sqrt{(D_{gs})}}$	Al-3.5Zn-0.8Mg-0Cu	62.1	8.2
	$k = 0.065 \text{ MPa}\cdot\text{m}^{-0.5}$	Al-3.8Zn-2.18Mg-1.7Cu	67.0	7.9
		Al-5.8Zn-2.2Mg-2.5Cu	60.5	8.4

Table 7–11 shows that the contribution by σ_{gb} is negligible in the SW approach; and it is only marginal in the DMS approach; hence, only the DMS approach will be considered for σ_{gb} evaluation.

7.3.6 Total Yield Strength Estimation

The total yield strength of the material is evaluated by including all the above-mentioned contributing factors: intrinsic, solid solution strengthening precipitate strengthening, dislocation and grain boundary effects. Except the intrinsic effect, the others are considered as obstacles for the dislocation movement on the gliding planes [125]. Amongst these contributing stress factors, the ones arising from interaction between dislocations and obstacles in the primary Al matrix are the σ_{ppt} and σ_{dis} . There are two types of obstacles in the matrix: hard and soft. The strengthening precipitates observed in the samples of this study are predominantly hard obstacles as the dislocation only pass them by the looping mechanism and not cut them; the sessile dislocations fall under the hard obstacle category [134]. The combined effect of the interaction between the dislocation that are both types of hard obstacles in the matrix, σ_{ppt} and σ_{dis} could be evaluate by three dependent schemes that are more frequently used by past researchers, as shown in Equation 7–5 (a) to (c)

$$\sigma_y = \sigma_{ppt} + \sigma_{dis} \quad (a)$$

$$\sigma_y^2 = \sigma_{ppt}^2 + \sigma_{dis}^2 \quad (b)$$

$$\sigma_y = \sigma_{ppt} X_{ppt}^{1/2} + \sigma_{dis} X_{dis}^{1/2} \quad (c)$$

Equation 7–5

In Equation 7–5 (c), X represents the number fraction of the particular obstacle type (ppt or dis) in the matrix. Traditionally, researchers have used any one of the three expressions in Equation 7–5 that best fit their experiment data to present as a predictive model. However, computer simulations [134] have shown that the *Pythagorean* summation shown in Equation 7–5 (b) presents the best predictive capability in most cases of continuous distribution of the soft and hard obstacles; however, there is a unique case when the linear model shows a better prediction and that is when the soft obstacles are about 95 % and hard about 5% of the total obstacles in the matrix which may occur in the beginning stages of precipitation reaction such

as during natural ageing [134]. In this study, σ_{dis} contributes to a negligible portion of σ_y ; hence, Equation 7-5 reduces to $\sigma_y = \sigma_{ppt}$. Equation 7-6 presents the expression used in this study to evaluate the total yield strength from the combination of data shown in Table 7-6, Table 7-8, Table 7-10 and Table 7-11.

$$\sigma_y = \sigma_\alpha + \sigma_{ss} + \sigma_{ppt} + \sigma_{gb} \quad \text{Equation 7-6}$$

The value of σ_{gb} (in Table 7-11) evaluated by the DMS approach will be used in Equation 7-6 because the one evaluated by the SW approach is negligible.

The results for the various contributions shown in Table 7-6, Table 7-8, Table 7-10 and Table 7-11 could be combined in a significantly large number of combinations to yield Equation 7-6. A simple logic algorithm was developed to better determine the apt combination of the contributing stresses to evaluate the total yield strength. In Equation 7-6, σ_α and σ_{gb} are 14.5 and 8 MPa, respectively; hence, there are three approaches to evaluate each of σ_{ss} and σ_{ppt} as shown in Table 7-8 and Table 7-10, respectively, resulting in nine (9) combinatorial possibilities for each of the three alloys in Table 7-3. All the nine (9) possible combinations were evaluated for each alloy and the ones that yielded σ_y to be less than 3Σ , 3Σ and 1Σ (27.1MPa, 35.9 MPa and 3.9 MPa) for the alloys Al-3.5Zn-0.8Mg, Al-3.8Zn-2.2Mg-1.7Cu and Al-5.8Zn-2.2Mg-2.5Cu, respectively, were selected and presented in Table 7-12 and plotted in Figure 7-6 along with the experiment data for yield strength. Σ represents the standard deviation of the respective yield strengths from tensile tests. Any other combination of strength factors in Table 7-8, Table 7-10 and Table 7-11, yielded significant deviations greater than 3Σ for the σ_y values for all the three alloys, alike; hence, omitted from being compared to the experiment data for σ_y . The evaluation of σ_y considering several possible combinations of strength contributions mentioned above are presented in the Chapter of APPENDICES (9.3) and in Table 9-1, Table 9-2 and Table 9-3 for the three alloys of Al-3.5Zn-0.8Mg, Al-3.8Zn-2.2Mg-1.7Cu and Al-5.8Zn-2.2Mg-2.5Cu, respectively.

Table 7–12 The models that yielded values of σ_y that were comparable to the experiment data. The Taylor Factor, $M = 2$.

Strength (MPa)		Al-3.5Zn-0.8Mg-0Cu	Al-3.8Zn-2.2Mg-1.7Cu	Al-5.8Zn-2.2Mg-2.5Cu
σ_u		14.5	14.5	14.5
σ_{gb}		8	8	8
σ_{ppt}		192	308	411
σ_{ss}	Model #1	58	86	105
	Model #2	63	95	116
	Model #3	36	88	102
σ_y	Model #1	272	417	539
	Model #2	277	426	550
	Model #3	250	419	536
	Experiment	279(± 13.55)	390(± 14.6)	540(± 20)

In Table 7–12, the σ_{ppt} was determined by the Kocks model with $M = 2$ as shown in Table 7–10; the Model #1, Model #2 and Model #3 represented the DB, SW and DMS approaches in evaluating σ_{ss} , respectively. The important fact that the value of σ_{ppt} that lend itself to be included as a contribution to σ_y for all the three alloys were based on the Kocks approach (Equation 4–18) which assumes a spherical morphology for the strengthening precipitates along with a Taylor Factor of $M=2$ shows the consistency of the predictive model for σ_{ppt} for the three alloys, alike.

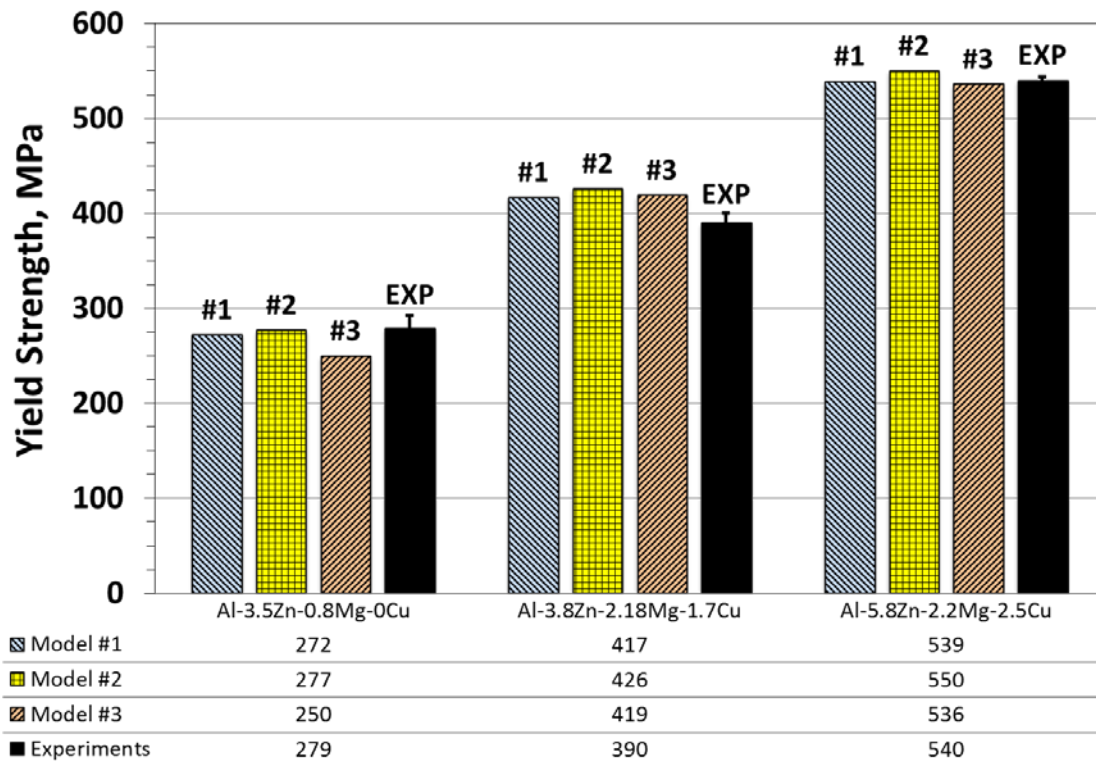


Figure 7–6 Comparison of total Yield Strength, σ_y , for the three models and experiment data. The models are defined in Table 7–12.

In Figure 7–6, any of Models #1, #2 or #3 could be used to predict the yield strength, σ_y for the three alloys without much difference among the predictions; alternately, the σ_{ss} could be determined by any of the three approaches: DB, SW and DMS shown in Table 7–8 with negligible impact on the predictive capability. When σ_{ss} can be evaluated as an average of the three approaches: DB, SW and DMS shown in Table 7–8, a consolidated model could be formulated to predict the yield strength, σ_y for the three alloys, as presented in Table 7–13 and plotted in Figure 7–7 along with the respective experimental σ_y values.

Table 7–13 A consolidated model that yielded values of σ_y , that were comparable to the experiment data. The Taylor Factor, $M = 2$.

Strength (MPa)		Al-3.5Zn-0.8Mg	Al-3.8Zn-2.2Mg-1.7Cu	Al-5.8Zn-2.2Mg-2.5Cu
σ_a		14.5	14.5	14.5
σ_{gb}		8	8	8
σ_{ppt}		192	308	411
σ_{ss}	Consolidated Model	52	90	108
σ_y	Consolidated Model	267	420	542
	Experiment	279(± 13.55)	390(± 14.6)	540(± 20)

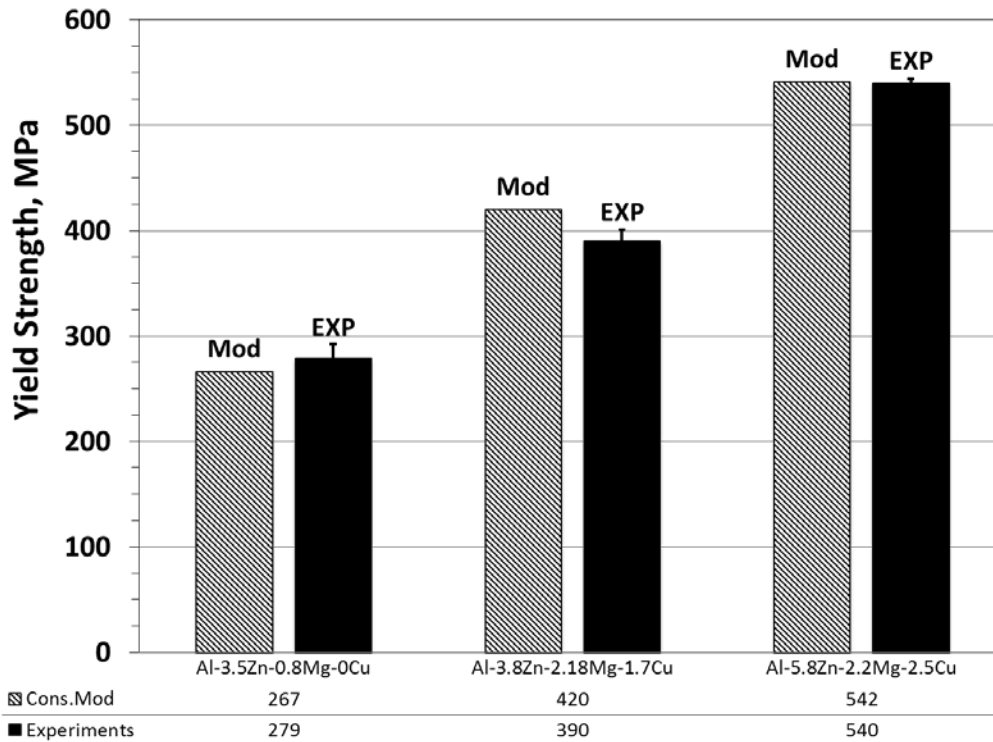


Figure 7–7 Comparison of total Yield Strength, σ_y , for the consolidated models and experiment data.

Figure 7–7 shows that consolidating the σ_{ss} as an average value to use the consolidated model yields a fairly good prediction of the yield strength, σ_y for the three alloys.

The aim of this exercise of correlating the observed values of Yield Strength of the three alloys with a predictive model was merely to demonstrate that these alloys cast using the CDS technology fall within certain predictive capabilities defined by models from the prior-art. The aim was not to develop a predict the YS of these alloys but to show that a summation of intrinsic strength of Al matrix, strength due to solid solution as described by Mott and Labusch [104,105] and strength due to the size and distribution of the strengthening precipitates in the Al matrix as defined by the Kocks statistics [131] present a fairly agreeable prediction of the YS for the three alloys herein. It is notable that the levels of casting defects such as shrinkage and gas porosity in the alloys cast using the CDS technology coupled with the TPGC process is very similar to those obtained in the wrought products of these alloys as shown by Figure 6–45 and Figure 6–46; which demonstrates that within acceptable levels of defects in the component, the strength of the casting with Al 7xxx alloys could be modeled by fundamental physio-mechanical properties of the alloys.

8 CONCLUSIONS

The high-strength, age-hardenable aluminum 7xxx series alloys (Al-Zn-Mg-Cu) in solid-state processed or wrought condition are highly demanded by the aerospace industry. From a designing point of view, the composition and thermos-mechanical solid-state process parameters are very important for the Al-Zn-Mg-(Cu) wrought alloys. This is because of the consequent effect on the microstructure evolution, mechanical and corrosion-resistance properties. The Zn, Mg and Cu elemental additions directly contribute to the strength of these alloys by affecting the formation of strengthening precipitates during the ageing treatment of T6 following the solution heat treatment (T4). The processing of the Al-Zn-Mg-(Cu) alloys by the conventional casting methods is highly complicated even in large sized direct chill (DC) ingots or billets [163]. This is mainly because of the severe segregation of the alloying elements and hot tearing defects that occur during the solidification process, which in turn leads to a significant reduction in the strength, fracture toughness and other mechanical properties of these alloys in the wrought condition [164]. The solidification defects and complications in these alloys worsen in the cases of the near-shape casting methods, which have led these alloys having a limited scope of commercial application which are economical as well.

The motivation for this dissertation was three-fold: to demonstrate the viability of near net shape structural castings of the Al 7xxx alloys while adopting the CDS technology coupled with the Tilt Pour Gravity Casting Process (TPGC), present a quantitative evaluation of the microstructural features and uniaxial tensile properties, and explore the possibility of being able to predict the strength of the castings through existing process strength models in the prior-art.

The originality of this study is to present a viable casting process by which the Al-7xxx family alloys (Al-Zn-Mg-Cu) are presented in cast condition to have an acceptable uniaxial property range that is comparable with their wrought counterparts.

It has been amply demonstrated the casting of the Al 7xxx alloy using the CDS technology coupled with the TPGC process is viable and produces near net shaped casting that exhibit uni-axial tensile properties necessary for structural applications. The castings produced in this study were fairly defect-free with the level of total porosity (shrinkage and gas) similar to those observed in the wrought products. It is notable that the morphology of the primary Al phase in the solidified castings for various alloy compositions within the regime of the Al 7xxx family is always non-dendritic and fairly uniform in size and distribution. The size of the primary Al grains in the alloys cast using the CDS technology is similar to those of the recrystallized grain in the wrought products (~60 μm). The nature, size and distribution of the secondary phases and strengthening precipitate phases evolved during solidification and heat treatment of these alloys in this study is nearly the same as those observed in the wrought counterparts. Furthermore, this study has demonstrated that the existing models to predict the yield strength of these alloys in the wrought condition could also predict the same for the castings in this study. The following paragraphs will further expand on these conclusions in this project while highlight certain nuances in the various observations.

8.1 CDS TECHNOLOGY WITH AL 7XXX ALLOYS

Nine compositions of the alloy that fall within the family of Al-Zn-Mg-Cu (Al 7xxx) were prepared and successfully cast into linear net shaped components of tensile and fatigue test bars using the CDS technology coupled with the TPGC process. The compositions chosen reflect the conditions of lowest and highest acceptable limits of each of Zn, Mg and Cu in the alloy to demonstrate the feasibility of using the CDS technology to repeatedly cast nearly defect free components of this alloy family. Further, the CDS technology involves the use of thermodynamic phase diagram simulations to design the two precursor alloys that enable the process and each of the nine chosen composition would require a unique pair of such precursor alloys that satisfy the required mass ratio of mixing; the design of these precursor alloys were successfully carried out and incorporated in casting the final components.

8.2 MICROSTRUCTURE AND HEAT TREATMENT

The microstructure of the cast components in this study presents a relatively uniform non-dendritic primary Al phase which is realized by the use of the CDS technology; casting that were cast using conventional pouring of superheated liquid metal of the same alloys in a mould yielded a dendritic Al phase and these casting were fraught with defects such as shrinkage porosity and hot tears which rendered the castings ineffective for any commercial application. Notably, the level of combined porosity (shrinkage and gas) in the CDS castings of this study was similar to those reported for the wrought components of these alloys in background literature.

The nature of the secondary phases evolving during solidification of the alloys with various compositions of Zn, Mg and Cu in them was predictable by the commercially available thermodynamic phase diagram simulation software and database showing that there was no deviation from the evolution of these phases due to the introduction of the CDS technology in casting these alloys. The results of quantitative metallography show that there is an increase in the total amount of the secondary phases evolving during solidification from that predicted by the thermodynamic software and such increase in the volume fraction is higher for alloy with higher total content of alloying elements (Zn+Mg+Cu) in them; this may be attributed to the predictable severity of the non-equilibrium solidification conditions (deviation from Scheil-Gulliver solidification paradigm) during the solidification of the castings caused by the increase in the total content of alloying elements. When the castings in this study were heat treated to the T4 temper condition, several of these secondary phases that evolved during solidification under metastable non-equilibrium conditions were dissolved back into the matrix during solutionizing which rendered the volume fraction of such phases back closer to those predicted by the thermodynamic simulations using the Scheil-Gulliver solidification paradigm. Such observations to the microstructure and responses of the same to the heat treatment observed in the casting of this study were akin to those in the wrought products of these alloys. This validates the argument that the use of CDS technology merely alters the morphology of the primary Al phase to more desirable non-dendritic type and has a negligible effect of the evolution of the secondary phases and their transformation during the solutionizing (T4) heat treatment process.

Another notable feature of the casting in this study is that the nature and kinetics of the precipitation of strengthening phases in the primary Al matrix during both the natural and artificial ageing conditions are similar to those observed in the wrought counterparts. The

sequence of precipitation from the coherent GP Zones (GP-I and GP-II) to the semi-coherent η' phase and terminating in the incoherent η phase seems to hold true for the castings from the CDS process as well; this has been demonstrated in this study through the experiments using the Differential Scanning Calorimetry (DSC) and Transmission Electron Microscopy (TEM). Furthermore, the kinetics of the precipitation reaction as measured by the change in the value of both the macro (bulk) hardness in the casting and micro-hardness of the primary Al matrix have shown that the evolution of the precipitates in the castings of this study are similar to those observed in the wrought products of these alloys. A notable contribution of this dissertation is the validation that the Arrhenius type of equation in Equation 4–11 proposed by Ashby and Shercliff [122,123] is valid to predict the kinetics of the precipitation reaction in these alloys and hence, predict the kinetics of the strengthening process in these castings, as well. The values of the constants in Equation 4–11 for the various stages of the precipitation strengthening reaction have been quantified for the Al-5.8Zn-2.2Mg-2.5Cu alloy in this study to enable ease of prediction of peak hardness of these alloys during isothermal ageing at any temperature between 70 and 200 °C. Additionally, several quantified features of the microstructure of these alloys pertaining to the strengthening precipitates in the matrix has been presented in this study for use in future endeavors to hone the predictability models.

8.3 STRENGTHENING MODELS

The prior-art in this topic suggests that the main contribution to the total yield strength in these alloys are intrinsic strength of the pure Al matrix, strength arising from the extent of solid solution in the Al matrix, strength contribution by the nature size, distribution and morphology of the precipitates evolving in the Al matrix during ageing, strength from the density of dislocations in the matrix and strength from the grain size (area of grain boundaries) of the primary Al phase. It has been shown in this dissertation that the contribution of strength from the intrinsic strength, and strength from dislocations and grain size are negligible when compared to that of the solid solution and precipitates in the matrix. Further, the complications reported in several background literatures that arise from choosing a particular scheme for combining the strength contributions from the precipitates and dislocations (linear, Pythagorean, hyperbolic summation schemes) do not apply to the casting made with the CDS technology. In the castings of this study, there is no mechanical deformation of the component within any heat treatment process such as cold working in wrought products; this eliminated the contribution of strength from the dislocations in the matrix; further, this also eliminated the concept of recrystallization of the grains during heat treatment. The casting in this study only have four contributions to the total yield strength: intrinsic, solid solution, precipitates and grain size; these contribution could be combined by linear summation to predict the total yield strength as demonstrated in the preceding Chapter.

The values of intrinsic strength are a constant for all alloy compositions of Al metal. The contribution to the strength from the grain size is also constant for a particular process of casting which yields a predictable size of the Al grains (there is no grain growth during heat treatment); the Hall-Petch relationship presented in Equation 4–5 could be used in evaluating this contribution. The contribution from the solid solution in the Al matrix could be evaluated by the expression proposed by Mott and Labusch [104,105] which requires knowledge of the nature and volume fraction of the individual secondary phases in the T4 temper condition coupled with thermodynamic calculations of elemental mass balance in the Al matrix. The strength contribution from the strengthening precipitates in the Al matrix could be evaluated from the knowledge of the size, distribution and morphology of these

precipitates at the end of the desired ageing process; this would require a detailed study to map the ageing curves shown in Figure 6–29 to the size, distribution and morphology of these precipitates through an experiments and TEM for any desirable alloy composition.

8.4 SUMMARY OF SCIENTIFIC CONTRIBUTIONS IN THIS DISSERTATION

The following is a summary of the salient scientific contribution in this dissertation.

- Establish the feasibility of using the CDS technology to enable sound shaped castings of the Al 7xxx series of alloys with a non-dendritic morphology of the primary Al phase.
- The extensive quantitative characterization of microstructure and mechanical properties in various heat treatment tempers have enabled a metallurgical comparison between the castings from the CDS technology and the wrought counterpart for respective alloys within the Al 7xxx family.
 - The primary difference is the non-dendritic nature of the primary Al phase in the castings using the CDS technology as compared to the regular Al grains with a dendritic morphology in the wrought product
 - There is no significant difference between them in secondary phase evolution during solidification and phase transformations during heat treatment.
 - There is a significant difference between the two in the size, morphology and nature of the intermetallic phases formed during solidification and transformed during subsequent heat treatment. The intermetallic phases that are predominantly detrimental to the ductility of the part were twice as large in the castings using CDS technology as compared to the wrought product counterparts. However, the volume fraction of the intermetallic phases remained the same in both cases.
- The hypothesis in the prior-art describing the complex mechanism of the precipitation hardening process during heat treatment has been further verified through meticulous measurements of transient changes in the macro and micro hardness of the sample. The Arrhenius type of equation describing the hardening process for the Al 6xxx and 2xxx alloys have been shown to be valid for the Al 7xxx alloy castings using the CDS technology.
- Propose a strengthening model that best described and predicts the yield strength of the Al 7xxx type alloys cast using the CDS technology.

9 APPENDICES

9.1 LIST OF PUBLICATIONS

Here the list of papers that are published in journals and the conferences are presented in the following:

- 1) S.Reza Ghiaasiaan, Abbas A. Khalaf, Xiaochun Zeng, and Sumanth Shankar; “*Near Net Shaped Casting of 7050 Al Wrought Alloy By CDS Process: Microstructure And Mechanical Properties*”; TMS 2012; March 10-15, 2012, Orlando, Florida, USA, Copyright © 2012 TMS'14®
- 2) Reza Ghiaasiaan, Xiaochun Zeng, and Sumanth Shankar; “*Near Net Shaped Casting Of Heat treatable Al-Zn-Mg-Cu Wrought Alloy By Controlled Diffusion Solidification (CDS) Process: Microstructure, Mechanical Properties And Heat Treatment*”; Materials Science and Technology (MS&T) 2013; October 27-31, 2013, Montreal, Quebec, Canada Copyright © 2013 MS&T'13®
- 3) Reza Ghiaasiaan, Xiaochun Zeng, Sumanth Shankar; “*Controlled Diffusion Solidification (CDS) of Al-Zn-Mg-Cu (7050): Microstructure, heat treatment and mechanical properties*”; Materials Science & Engineering A, 2014, Vol. 594, pp. 260–277.
- 4) Reza Ghiaasiaan, Diran Apelean and Sumanth Shankar; “*Control Diffusion Solidification (CDS): An Overview of Mechanism and Application*”; TMS 2014; Feb 16-20, 2013, San Diego, California, USA, Copyright © 2014 TMS'14®

9.2 TEM MICRO-GRAPHS OF SECONDARY PHASES IN THE AL-7XXX ALLOYS IN T6 TEMPER

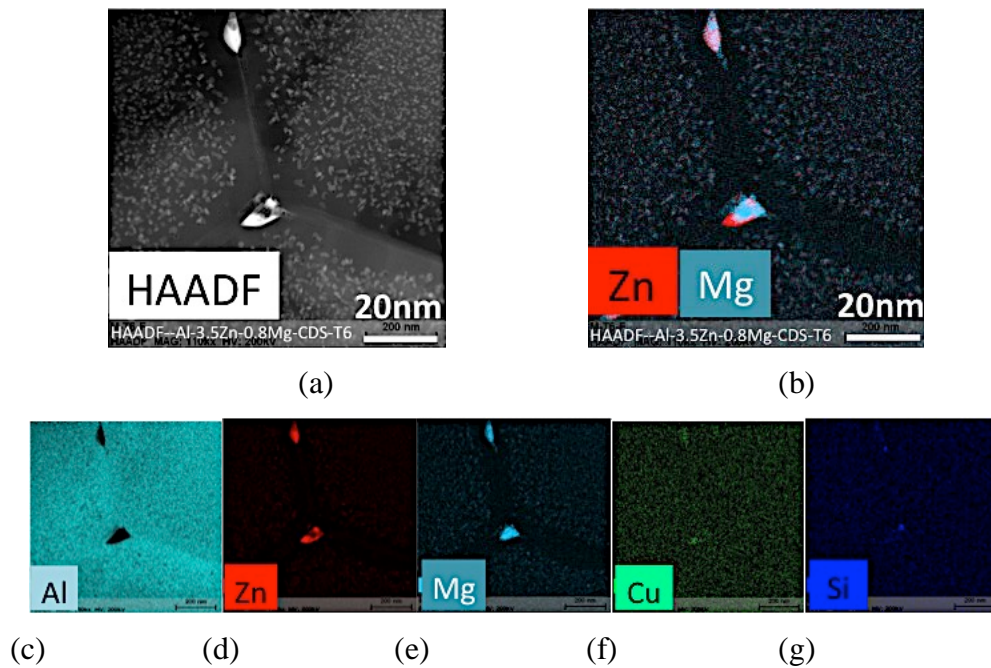


Figure 9–1 STEM micrographs in (a) high angle annular dark field mode of the phases forming at the grain boundary (GB) in the Cu-free alloy of Al-3.5Zn-0.8Mg-0Cu in the T6 temper; along with elemental EDS maps for (b) Zn+Mg, (c) Al, (d) Zn, (e) Mg, (f) Cu, and (g) Si; showing that these GB forming at GB are Sigma ($\text{Mg}(\text{Zn,Al,Cu})_2$) phases in Cu-free Al-7xxx alloys as compared to the S (Al_2CuMg) phases forming in the Cu-bearing Al-7xxx phases that are shown in Figure 9–2.

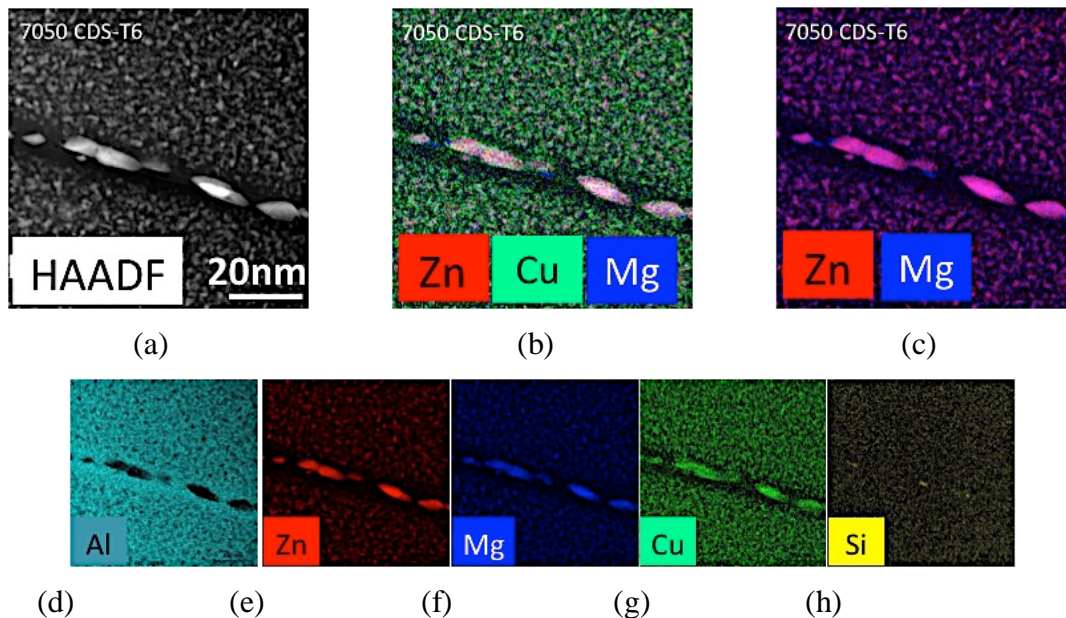


Figure 9–2 STEM micrographs in (a) high angle annular dark field mode of the phases forming at the grain boundary (GB) in the Cu-bearing alloy of Al-5.8Zn-2.2Mg-2.5Cu (7050) in the T6 temper; along with the elemental EDS maps for (b) Zn+Mg+Cu, (c) Zn+Mg, (d) Al, (e) Zn, (f) Mg, (g) Cu, and (h) Si; indicating that these GB phases are the S (Al_2CuMg) phases forming in the Cu-bearing Al-7xxx phases as opposed to the Sigma ($\text{Mg}(\text{Zn,Al,Cu})_2$) phase forming at GB in the Cu-free Al-3.5Zn-0.8Mg-0Cu alloys, as shown in Figure 9–1.

9.3 DETAILS OF THE STRENGTHENING MODELS

Table 9–1, Table 9–2 and Table 9–3 presents the evaluation of σ_y considering several possible combinations of strength contributions mentioned in Chapter of the Strengthening model and the subsection of Total Yield Strength Estimation (7.3.6) for the three alloys used in this study: Al-3.5Zn-0.8Mg, Al-3.8Zn-2.2Mg-1.7Cu and Al-5.8Zn-2.2Mg-2.5Cu, respectively.

Table 9–1 The detail calculations for all and each possible combinations of strengthening contribution to the total yield stress of the Al-3.5Zn-0.8Mg-0Cu alloys as explained in the Section of 7.3.

Composition		Al-3.5Zn-0.8Mg-0Cu (No-Cu)								
Precipitation Hardening Approach		Zhu and Starke [147]			Kelly [153]			Kocks [131]		
Taylor Factor		M			M			M		
		2	2.55	3	2	2.55	3	2	2.55	3
Intrinsic	σ_u	15	15	15	15	15	15	15	15	15
Precipitation	σ_{ppt}	162	207	244	208	265	312	415	529	622
Solid Solution	σ_{ss} (DB)	58	58	58	58	58	58	58	58	58
	σ_{ss} (SW)	63	63	63	63	63	63	63	63	63
	σ_{ss} (DMS)	36	45	54	36	45	54	36	45	54
Precipitation	σ_{ppt}	75	96	113	98	124	146	192	245	288
Total Yield By Model	σ_y (DB)	156	177	194	178	205	227	272	326	369
	σ_y (SW)	161	182	199	183	210	232	277	331	374
	σ_y (DMS)	134	164	190	156	192	223	250	313	365
Experimental Yield	σ_y (Exp.)	279(±13.55)								

Table 9–2 The detail calculations for all and each possible combinations of strengthening contribution to the total yield stress of the Al-3.8Zn-2.2Mg-1.7Cu alloys as explained in the Section of 7.3.

Composition		Al-3.8Zn-2.2Mg-1.7Cu (Mid-Cu)								
Precipitation Hardening Approach		Zhu and Starke [147]			Kelly [153]			Kocks [131]		
Taylor Factor		M			M			M		
		2	2.55	3	2	2.55	3	2	2.55	3
Intrinsic	σ_u	15	15	15	15	15	15	15	15	15
Grain Boundary	σ_{ppt}	8	8	8	8	8	8	8	8	8
Solid Solution	σ_{ss} (DB)	86	86	86	86	86	86	86	86	86
	σ_{ss} (SW)	95	95	95	95	95	95	95	95	95
	σ_{ss} (DMS)	88	110	132	88	110	132	88	110	132
Precipitation	σ_{ppt}	107	137	161	140	178	209	308	393	462
Total Yield By Model	σ_y (DB)	216	246	270	248	287	318	417	501	571
	σ_y (SW)	225	255	279	258	296	327	426	511	580
	σ_y (DMS)	218	269	316	250	311	364	419	525	617
Experimental Yield	σ_y (Exp.)	390(±14.6)								

Table 9–3 The detail calculations for all and each possible combinations strengthening contribution to the total yield stress of the Al-5.8Zn-2.2Mg-2.5Cu alloys as explained in the Section of 7.3.

Composition		Al-5.8Zn-2.2Mg-2.5Cu (Hi-Cu)								
Precipitation Hardening Approach		Zhu and Starke [147]			Kelly [153]			Kocks [131]		
Taylor Factor		M			M			M		
		2	2.55	3	2	2.55	3	2	2.55	3
Intrinsic	σ_{α}	15	15	15	15	15	15	15	15	15
Grain Boundary	σ_{ppt}	8	8	8	8	8	8	8	8	8
Solid Solution	σ_{ss} (GB)	105	105	105	105	105	105	105	105	105
	σ_{ss} (SW)	116	116	116	116	116	116	116	116	116
	σ_{ss} (DMS)	102	128	153	102	128	153	102	128	153
Precipitation	σ_{ppt}	155	198	233	206	263	309	411	524	616
Total Yield By Model	σ_y (DB)	283	326	361	334	391	437	539	652	744
	σ_y (SW)	294	337	372	345	402	448	550	663	755
	σ_y (DMS)	280	348	409	331	413	485	536	674	792
Experimental Yield	σ_y (Exp.)	540(±20)								

10 REFERENCES

-
- [1] L. Cheah, J. Heywood, R. Kirchain, "The Energy Impact of U.S. Passenger Vehicle Fuel Economy Standards", Sustainable Systems and Technology (ISSST), 2010, IEEE International Symposium.
- [2] U.S. Environmental Protection Agency, 2009. Draft Regulatory Impact Analysis: Proposed Rulemaking to Establish Light-Duty Vehicle Greenhouse Gas Emission Standards and Corporate Average Fuel Economy Standards, Assessment and Standards Division, Office of Transportation and Air Quality, EPA-420-D-09-003, September 2009.
- [3] L. W. Cheah, "Cars on a Diet: The Material and Energy Impacts of Passenger Vehicle Weight Reduction in the U.S.", Massachusetts Institute Of Technology (MIT), Massachusetts, USA, 2010.
- [4] S. Logan, Sr. Technical Specialist at Chrysler Group LLC, Materials Engineering Group, Personal Communication.
- [5] J.E. Hatch, Aluminum: properties and physical metallurgy, 1984, American Society for Metals, Ohio, USA.
- [6] R. Ghiaasiaan, S. Shankar, and D. Apelian, "Control Diffusion Solidification (CDS): An Overview of Mechanism and Application", TMS Conference, February 2015, San Diego, California, USA
- [7] Lynette W. Cheah, "Factor of Two: Halving the Fuel Consumption of New U.S. Automobiles By 2035", Masters of Science Thesis, , Massachusetts Institute Of Technology, USA, 2008.
- [8] L. Cheah, C. Evans, A. Bandivadekar, and J. Heywood, "Factor of Two: Halving the Fuel Consumption of New U.S. Automobiles by 2035: Chapter 4 in Reducing Climate Impacts in the Transportation Sector, edited by D. Sperling and J. Cannon, New York: Springer, 2008.
- [9] R. Ghiaasiaan, X. Zeng, and S. Shankar, "Near net shaped casting of heat treatable Al-Zn-Mg-Cu wrought alloy by controlled diffusion solidification (CDS) process: microstructure, mechanical properties and heat treatment", Materials Science and Technology (MS&T) Conference, October 2013, Montreal, Quebec, Canada
- [10] Sumanth Shankar, Private communication, Mechanical Engineering Department, McMaster University, Hamilton, On, Canada L8S 4L7.
- [11] M. Jeyakumar, G. Lui and S. Shankar, "Effect Of Incubation Coupled With Artificial Aging Int6 Heat Treatment Of A356.2 Aluminum Casting Alloy", International Journal of Metal Casting, Fall 2011, pp17: 36.
- [12] J. Grassi, "Ablation Casting", Aluminum Alloys: Fabrication, Characterization and Application, Eds. W. Yin and S. K. Das, The Minerals, Metals and Materials Society (TMS) (2008), pp.73–77.
- [13] G. K. Sigworth, F. DeHart and S. Milhollen, "Use of high strength aluminum casting alloys in automotive applications", in Light Metals, 2001, Métaux Léger, Eds. M. Sahoo and T. Lewis, pp. 313-322.
- [14] D. K. Visser, A. E. Kopper, A. J. Schulz, "Innovations in Marine Propeller Technology: High Ductility Mercalloy™ 366 Alloy", Die Casting Engineer; 2006, Vol. 50, 3; pp. 24-31
- [15] R. J. Donahue et al, "Hypoeutectic Aluminum-Silicon Alloy Having Reduced Microporosity", US Patent #6,923,935B1, August 2, 2005.
- [16] A. Zovi, F. Casarotto, "Silafont-36, the low iron ductile die casting alloy development and applicants", Die Casting, Proceedings of the La Metallurgia Italiana, Milan, Italy, June 2007, pp. 33-38.
- [17] Shimin Li, "Hot Tearing in Cast Aluminum Alloys: Measures and Effects of Process Variables", PhD Thesis, Worcester Polytechnic Institute, Massachusetts, USA, 2010.
- [18] Shan Lin, "A Study of Hot Tearing in Wrought Aluminum Alloys", Master Thesis, Université du Québec à Chicoutimi, Quebec, Canada, 1999.
- [19] D. H. Kirkwood, "Near net shaping by semi-solid metal processing", Materials and Design, 2000, Vol. 21, pp. 387-394

- [20] Anacleto de Figueredo, "Science and Technology of Semi-Solid Metal Processing", Ed. North American Die Casting Association, Rosemont, IL, USA, 2001.
- [21] M. C. Flemings, *Metallurgical Transactions A*, 1991, Vol. 22A, pp. 957.
- [22] G. Kim, M. Koç, R. Mayor and J.Ni, *Journal of Manufacturing Science and Engineering*, 2007, Vol. 129, pp. 237.
- [23] H.V. Atkinson, *Progress in Materials Science*, 2005, Vol. 50, pp. 341–412.
- [24] H. Mirzadeh, B. Niroumand, *Journal of Alloys and Compounds*, 2009, Vo. 474, pp. 257–263.
- [25] D. H. Kirkwood, M. Suéry, P. Kapranos, H. V. Atkinson, K. P. Young, "Semi-solid Processing of Alloys, Springer Series in Material Science No. 124, November 2009.
- [26] www.nrc-cnrc.gc.ca, National Research Council Canada.
- [27] S. Chayong, H.V. Atkinson, P. Kapranos, *Materials Science and Engineering*, 2005, A390, pp. 3–12.
- [28] M.M. Rovira, B.C. Lancini, M.H. Robert *Journal of Materials Processing Technology*, 1999, Vol. 92, pp. 42-49.
- [29] J. G. SIM et al, *ISIJ International*, 2009, Vol. 49, No. 11, pp. 1700–1709.
- [30] J. Jorstad, *High Integrity Die Casting*, Chapter 3, North American Die Casting Association (NADCAL Rosemont, IL, USA, 2008.
- [31] I. Polmear, "Light Alloys: From Tradition Alloys to Nanocrystals", 4th Ed., Elsevier, Oxford, 2006.
- [32] S. Shankar, D. Apelian, "Die soldering: mechanism of the interface reaction between molten Al alloy and tool steel.", *Met. & Mat. Trans.* Vol. 33B, pp. 465-476.
- [33] D-W Suh, S-Y Lee, K-H Lee, S-K Lim, K. H. Oh, "Microstructural evolution of Al–Zn–Mg–Cu–(Sc) alloy during hot extrusion and heat treatments", *Journal of Materials Processing Technology*, 2004, Vol. 155–156, pp. 1330–1336.
- [34] C. Chang, J. Yang, L. Chi, C. Chou, "Optimization of Heat Treatment Parameters with the Taguchi Method for the A7050 Aluminum", *Advanced Materials Research*, 2010, Vol. 139-141, pp. 157-162.
- [35] S. Lin, C. Aliravci, M.O. Pekguleryuz, "Hot-Tear Susceptibility of Aluminum Wrought Alloys and the Effect of Grain Refining", *Met. & Mat. Trans. A*, 2007, Vol. 38A, pp. 1056- 1068.
- [36] T. Marlaud, A. Deschamps, F. Bley, W. Lefebvre, B. Baroux, "Influence of alloy composition and heat treatment on precipitate composition in Al–Zn–Mg–Cu alloys" *Acta Materialia*, 2010, Vol. 58, pp.248–260.
- [37] S. Shankar, Y.W.Riddle , M.M. Makhlof, "Eutectic solidification of Al-Si alloys", *Met. & Mat. Trans. A*, 2004, Vol. 35A, pp. 3038-3043.
- [38] S. Shankar, Y.W. Riddle, M.M. Makhlof, "Nucleation mechanism of the eutectic phases in aluminum–silicon hypoeutectic alloys", *Acta Mat.* , 2004, Vol. 52, No. 15, pp. 4447–4460.
- [39] M.Jeyakumar and S.Shankar, "Rheology of liquid Al, Zn, and Zn-wt7%Al systems", *Mat. Scie. Forum*, 2011, Vol. 690, pp.226-229.
- [40] Kimon Symeonidis PhD thesis, "The Controlled Diffusion Solidification Process: Fundamentals and Principles", Worcester Polytechnic Institute (WPI), Massachusetts, USA, 2009.
- [41] A.A. Khalaf, "Controlled Diffusion Solidification: Process Mechanism and Parameter Study", PhD Thesis, McMaster University, Hamilton, ON, Canada, 2010.
- [42] D. Saha, S. Shankar, D. Apelian and M. M. Makhlof, "Casting of Aluminum-Based Wrought Alloys Using Controlled Diffusion Solidification.", *Metallurgical and Materials Transaction A*, 2004, Vol. 35A, pp. 2174-2180.
- [43] A.A.Khalaf, P. Ashtari, S.Shankar, "Formation of Nondendritic Primary Al Phase in Hypoeutectic alloys in CDS: a hypothesis", *Met. & Mat. Trans. B*, 2009, Vol. 40B, pp. 843-849.
- [44] G.J. Davies, *Solidification and Casting*, John Wiley & sons, New York, 1973.

-
- [45] WA Tiller, KA Jackson, JW Rutter, and B Chalmers, "The redistribution of solute atoms during the solidification of metals", *Acta Metallurgica*, 1953, Vol. 1, pp. 429-437.
- [46] M.Rappaz, J. M. Drezet, and M. Gremaud, *Metall. Mater. Trans. A*, 1999, Vol. 30A, pp. 449-455.
- [47] J. Campbell: *Castings*, Butterworth-Heinemann, Oxford, United Kingdom, 1991.
- [48] A.K. Dahle, M. Suery, *Materials Science Forum*, 2010, Vol. 649, pp. 337-342.
- [49] C.G. Goetzl and J.L. Ellis, U.S. Patent 2,611,443, September 30, 1952
- [50] G. Langford, R. E. Cunningham, *Metallurgical Transactions B*, 1978, Vo. 9B, pp. 5-19
- [51] D. Apelian and G. Langford, "Rapid Cycle Casting of Steel, Final Report", Drexel University, Philadelphia, USA, 1977.
- [52] D. Saha, "Novel Processing Methods and Mechanisms to Control the Cast Microstructure in Al Based Alloys - 390 and Wrought Alloys", PhD Thesis, Worcester Polytechnic Institute, USA, 2005.
- [53] S. Shankar, D. Saha, D. Apelian, M. M. Makhlof, "Casting of Aluminum-Based Wrought Alloys and Aluminum-Based Casting Alloys via Controlled Diffusion Solidification," United States Patent No. 7, 201, 210, April 2007.
- [54] G. Birsan, "Shaped Casting of Aluminum Wrought Alloys by Controlled Diffusion Solidification (CDS) in a Tilt-Pour Gravity Casting process", Master Thesis, Mechanical Engineering Department, McMaster University, Hamilton, Canada, 2009.
- [55] D. Apelian, M.M. Makhlof, and D. Saha, "CDS Method for Casting Aluminum-Based Wrought Alloy Compositions: theoretical framework.", *Materials Science Forum*, 2006, Vol. 519-521, pp. 1771-1776.
- [56] K. Symeonidis, "The Controlled Diffusion Solidification Process: Fundamentals and Principles", PhD thesis, Worcester Polytechnic Institute (WPI), Massachusetts, USA, 2009.
- [57] A. A. Khalaf, P. Ashtari, And S. Shankar, "Formation of Nondendritic Primary Aluminum Phase in Hypoeutectic Alloys in Controlled Diffusion Solidification (CDS): A Hypothesis", *Metallurgical And Materials Transactions B*, 2009, Vol. 40B, pp. 843- 849.
- [58] A. A. Khalaf And S. Shankar, "Favorable Environment for a Nondendritic Morphology in Controlled Diffusion Solidification", *Metallurgical And Materials Transactions A*, 2011, Vol. 42A, pp. 2456-2465.
- [59] A. A. Khalaf and S. Shankar, "Effect of mixing rate on the morphology of primary Al phase in the controlled diffusion solidification (CDS) process", 2012, *J Mater Sci*, Vol. 47, pp. 8153-8166.
- [60] S. Shankar, private communications, Department of Mechanical Engineering, McMaster University, Hamilton, ON, Canada L8S 4L7.
- [61] A.A. Khalaf, P. Ashtari, S. Shankar: *Metall. Mater. Trans. B*, 2009, Vol. 40B, pp. 843-49.
- [62] G. Birsan, P. Ashtari, S. Shankar, "Valid mould and process desing to cast tensile and fatigue test bars in tilt pour casting process", *International Journal Of Cast Metal Research*, 2011, Vol. 24, No.6, pp. 378-384.
- [63] T. Okubo, J. Okamoto and A. Tsuchida, *Colloid Polymer Science*, 2009, Vol. 287, pp. 645-657.
- [64] M.C. Flemings, *Solidification of Castings and Ingots, Solidification Processing*, McGraw-Hill Inc., USA, 1974.
- [65] I. J. Polmear, "Light Alloys From Traditional Alloys to Nanocrystals", Fourth edition 2006, Butterworth-Heinemann is an imprint of Elsevier, Jordan Hill, Oxford, UK, 2006.
- [66] L.F. Mondolfo, "Structure of aluminum:magnesium:zinc alloys. *Metallurgical Reviews*, review 153", 1971, Vol. 95, pp. 94-124.
- [67] H. Löffler, I. Kovacs, J. Lendvai, "Review Decomposition processes in Al-Zn-Mg alloys", *Journal of Mat. Scie.*, 1983, Vol. 18, pp. 2215-2240.
- [68] William D. Calister, Jr. David G. Rethwisch "Material Science and Engineering: An Introduction", 8th Ed., John&Wiley, USA, 2010.

- [69] D.A. Porter, K.E. Easterling, In: Interphase interfaces, pp.152, in "Phase Transformations in Metals And Alloys". 1st Ed. 1981, Von Nostard Reinhold Company, New York, USA, 1981.
- [70] T. Takahashi et al, Mater. Trans., 2002, Vol. 43, No. 2, pp. 232-8.
- [71] J.Manickaraj, G. Liu and S. Shankar, "Effect Of Incubation Coupled With Artificial Aging In T6 Heat Treatment Of A356.2 Aluminum Casting Alloy", International Journal of Metal Casting 2011, pp. 17-36.
- [72] J.D. Robson, Microstructural evolution in aluminum alloy 7050 during processing. Mat. Sci. & Eng. A, 2004, Vo. 382, pp. 112-121.
- [73] X.M. Li and M.J. Starink, "DSC Study on Phase Transitions and Their Correlation with Properties of Overaged Al-Zn-Mg-Cu Alloys", Journal of Materials Engineering and Performance, 2012, Vol. 21, No. 6, pp. 977-84.
- [74] P.N.T. Unwin, G.W. Lorimer and R.B. Nicholson, "The origin of grain boundary precipitation free zones", Acta Metall., 1969, Vol. 17, pp. 1363-1377.
- [75] J.D. Embury and R.B. Nicholson, "The nucleation of precipitates: the system Al-Zn-Mg", Acta Metallurgica., 1965, Vo. 13, pp. 403-417
- [76] J. W. Martin, "Precipitation Hardening," Pergamon Press, New York, 1968.
- [77] D. Godard, P. Archambault, E. Aeby-Gautier, G. Lapasset, "Precipitation sequences during quenching of the AA 7010 alloy", Acta Mater., 2002, Vol. 50, pp. 2319-2329.
- [78] Fanyou Xie et al, "A study of microstructure and microsegregation of aluminum 7050 alloy", Materials Science and Engineering A, 2003, Vol. A355, pp. 144-153.
- [79] J.D. Robson, P.B. Prangnell, "Dispersoid precipitation and process modeling in Zr containing commercial aluminum alloys", Acta Mater., 2001, Vol. 49, pp. 599-613.
- [80] F.X. Gang, J. D. Ming, M. Q. Chang, Z. B. You, W. Tao, "Evolution of eutectic structures in Al-Zn-Mg-Cu alloys during heat treatment", Trans. Nonferrous Met. Soc. China, 2006, Vol. 16, pp. 577-581.
- [81] D. Dumont, A. Deschamps, Y. Brechet, C. Sigli, and Ehrstrom, "Characterisation of precipitation microstructures in aluminum alloys 7040 and 7050 and their relationship to mechanical behavior.", Materials Science and Technology, 2004, Vol. 20, pp. 567-576.
- [82] A. Guinier, Compter Rend., 1938, Vol. 206, pp. 164.
- [83] G. D. Preston, Proc Roy Soc. A, 1938, Vol. 167, pp. 526.
- [84] L. K. Berg, J. Gjønnnes, V. Hansen, X. Z. Li, M. Knutson-Wedel, G. Waterloo, D. Schryvers And L. R. Wallenberg, "GP-Zones in Al-Zn-Mg Alloys and Their Role in artificial ageing", Acta mater., 2001, Vol. 49, pp. 3443-3451.
- [85] A. Naudon and J Guillot, "Comparative Study By Mechanical Electron Microscope And Resistivity Tests of Ageing Of Aluminium Solid Solutions", 1966, Mem. Sci. Rev. Met., Vol. 63, pp. 969.
- [86] H. Schmalzried And V. Gerold, Z. Metallkd., 1954, Vol. 49, pp. 291.
- [87] Li, X. Z., Hansen, V., Gjønnnes, J. and Wallenberg, L. R., Acta mater., 1999, Vol. 47, pp. 2651.
- [88] G. Waterloo, V. Hansen, J. Gjønnnes, S.R. Skjervold, "Effect of predeformation and preaging at room temperature in Al-Zn-Mg-(Cu,Zr) alloys" Materials Science and Engineering, 2001, Vol. A303, pp. 226-233.
- [89] J. Q. Su, "Microstructural investigation of friction stir welded 7050- T651 aluminum", Acta Materialia, 2003, Vol. 51, pp. 713-729.
- [90] G. Sha and A. Cerezo, "Early-stage precipitation in Al-Zn-Mg-Cu alloy (7050)", Acta Materialia, 2004, Vol. 52, pp. 4503-4516.
- [91] K. Stiller, P.J. Warren, V. Hansen, J. Angenete, and J. Gjønnnes, "Investigation of precipitation in an Al-Zn-Mg alloy after two-step ageing treatment at 100° and 150°C", Materials Science and Engineering A, 1999, Vol. A270, pp. 55-63.
- [92] T. Engdahl, V. Hansen, P.J. Warren, K. Stiller, "Investigation of fine scale precipitates in Al-Zn-Mg alloys after various heat treatments", Materials Science and Engineering A, 2002, Vol. A327, pp. 59-64.

-
- [93] N.Q. Chinh, J. Lendvai, D.H. Ping, K. Hono, "The effect of Cu on mechanical and precipitation properties of Al-Zn-Mg alloys, *Journal of Alloys and Compounds*", 2004, Vol. 378, pp. 52–60.
- [94] T. Marlaud, A. Deschamps, F. Bley, W. Lefebvre, B. Baroux, "Influence of alloy composition and heat treatment on precipitate composition in Al-Zn-Mg-Cu alloys", *Acta Materialia*, 2010, Vol. 58, pp. 248–260.
- [95] Luca Sobrin, "Predictions of precipitation reaction mechanisms for 7xxx series aluminum alloys cast by CDS technique", MSc. Thesis, University of Windsor, Windsor, ON, Canada, 2014.
- [96] G.E. Dieter, *Mechanical Metallurgy*, McGraw Hill Book Company (UK) limited, London, UK, 1988.
- [97] E. Schmid, *Z. Elektrochem.*, 1931, Vol. 37, pp. 447.
- [98] J. H. Frye and W. Hume-Rothery, *Proc. R. Soc. London*, 1942, Vol. 181, pp. 1-14.
- [99] D. Hull and D. J. Bacon, "Introduction to Dislocation", Third Ed. 1984, Linacre House, Jordan Hill Oxford, MA, USA, 1984.
- [100] Dilip Chandrasekaran, "Grain Size and Solid Solution Strengthening in Metals: A Theoretical and Experimental Study", PhD Thesis, 2003, Royal University of Sweden, SE-100 44 Stockholm, Sweden, 2003.
- [101] G.P.M. Leyson, W.A. Curtin, "Friedel vs. Labusch: the strong/weak pinning transition in solute strengthened metals", *Philosophical Magazine*, 2013, Vol. 93, No. 19, pp. 2428–2444.
- [102] R. L. Fleischer, "Solution Hardening", *Acta Metallurgica*, 1961, Vol. 9, pp 996-1000.
- [103] Robert L. Fleischer, "Solution Hardening By Tetragonal Distortions: Application To Irradiation Hardening In F.C.C. Crystals", *Acta Metallurgica*, 1962, Vol. 10, pp 835-842.
- [104] R. L. Fleischer, "Substitutional Solution Hardening", *Acta Metallurgica*, 1963, Vol. 11, pp 203-209.
- [105] N.F. Mott and F.R.N. Nabarro, "Report on Conference on the Strength of Solids", 1948, Phys. Soc., London, p. 1
- [106] R. Labusch, "A Statistical Theory of Solid Solution Hardening", *Phys. Stat. Sol.*, 1970, Vol. 41, No. 659, pp. 659-669.
- [107] G. J. Taylor, *J. Inst. Met.*, 1938, Vol. 62, p. 307.
- [108] U. F. Kocks, "The Relation Between Polycrystal Deformation and Single-Crystal Deformation", *Metal. Trans.*, 1970, Vol.1, pp. 1121-1143.
- [109] U. F. Kocks, "Kinetics of Solution Hardening", *Metallurgical Transactions A*, 1985, Vol. 16 A, pp. 2109-2129.
- [110] W. Boas and M. E. Hargreaves, *Proc. R. Soc. London Ser. A*, 1948, Vol. A193, p. 89.
- [111] V. M. Urie and H. L. Wain, *J. Inst. Met.*, 1952, Vol. 81, pp. 153.
- [112] E. O. Hall, *Proc. Phys. Soc. London*, 1951, Vol. 643, pp. 747.
- [113] N. J. Petch, *J. Iron Steel Inst. London*, 1953, Vol. 173, pp. 25.
- [114] J. C. M. Li, *Trans. Metal/. Soc. A/ME*, 1963, Vol. 227, pp. 239-247.
- [115] A.H. Cottrell, "The mechanical properties of matter", John Wiley&Sons Inc., New York, USA, 1964.
- [116] A. Seeger, "Dislocations and Mechanical Properties of Crystals," John Wiley & Sons Inc., New York, USA, 1957.
- [117] U.F. Kocks and H. Mecking, "Physics and phenomenology of strain hardening: the FCC case", *Progress in Materials Science*, 2003, Vol. 48, pp. 171–273.
- [118] J. W. Martin, "Precipitation Hardening," Pergamon Press, New York, USA, 1968.
- [119] E. Orowan, discussion in "Symposium on Internal Stresses," p. 451, Institute of Metals, London, 1947.
- [120] M. F. Ashby, in *Proc. Second Bolton Landing Conf. on Oxide Dispersion Strengthening*. Gordon and Breach, Science Publishers, Inc., New York, 1968.

-
- [121] U. F. Kocks, "The Theory of an Obstacle-controlled Yield Strength -- Report after an International Workshop", *Materials Science and Engineering*, 1977, Vol. 27, pp. 291 – 298.
- [122] H. R. Shercliff and M. F. Ashby, "A Process Model for Age Hardening of Aluminium Alloys--I. The Model", *Acta metall. Mater.* 1990, Vol. 38, No. 10, pp. 1789-1802.
- [123] H. R. Shercliff and M. F. Ashby, "A Process Model for Age Hardening of Aluminium Alloys--II. Applications of The Model", *Acta Metal. Mater.*, 1990, Vol. 38, No. 10, pp. 1803-1812.
- [124] J. C. Ion, K. E. Easterling and M. F. Ashby, "A Second Report on Diagrams of Microstructure and Hardness for Heat Affected Zones in Welds." *Acta metaria.*, 1984, Vol. 32, No. 11, pp. 1949-1962.
- [125] E. Hornbogen and E. A. Starke JR, "Overview No. 102: Theory Assisted Design of High Strength Low Alloy Aluminum", *Acta Metal. Mater.* Vol. 41, 1993, No. 1, pp. 1-16.
- [126] L. F. Mondolfo, *Aluminum Alloys*, p. 69. Butterworths, London, 1979.
- [127] S.K. Maloney, K. Hono, I.J. Polmear, S.P. Ringer, "The effects of a trace addition of silver upon elevated temperature ageing of an Al+Zn+Mg alloy", *Micron*, Vol. 32, (2001), pp. 741-747.
- [128] A. Deschamps, A. Bigot, F. Livet, P. Auger, Y. Bréchet & D. Blavette, "A comparative study of precipitate composition and volume fraction in an Al–Zn–Mg alloy using tomographic atom probe and small-angle X-ray scattering", *Philosophical Magazine*, 2001, Vol.81, No. 10, pp. 2391-2414.
- [129] John A. Wert, "Identification of Precipitates In 7075 After High-Temperature Aging", *Scripta Metallurgica*, 1981, Vol. 15, pp. 445-447.
- [130] A. Deschamps, F. Livet and Y. Bréchet, "Influence of Predeformation on Ageing in an Al-Zn-Mg Alloy-I: Microstructure Evolution and Mechanical Properties", *Acta mater.*, 1999, Vol. 47, No. 1, pp. 281-292.
- [131] A. Deschamps and Y. Bréchet, "Influence of Predeformation and ageing of an Al-Zn-Mg Alloy-II: Modeling of Precipitation Kinetics And Yield Stress", *Acta mater.*, 1999, Vol. 47, No. 1, pp. 293-305.
- [132] X. Li, M.J. Starink, " Analysis of Precipitation and Dissolution of the Overaged 7xxx Aluminum Alloys using DSC", *Materials Science Forum*, 2000, Vol. 331-337, pp. 1071-1076.
- [133] R. Machler, P.J. Uggowitzer, C. Solenthaler, R.M. Pedrazzoli, and M.O. Speidel, "Structure, mechanical properties, and stress corrosion behaviour of high strength spray deposited 7000 series aluminium alloy", *Mater Sci Technol*, 1991, Vol. 7, pp. 447-451.
- [134] A. J. Ardell, "Precipitation Hardening", *Metallurgical Transactions*, 1985, Vol. 16A, December, pp. 2131-2165.
- [135] Kocks, U.F., Argon, A.S. and Ashby, M.F., *Prog. Mater. Sci.*, 1975, Vol.19, pp.1.
- [136] P. Guyot And L. Cottignies, "Precipitation Kinetics, Mechanical Strength and Electrical Conductivity of Al-Zn-Mg-Cu Alloys", *Acta mater.* 1996, Vol. 44, No. 10, pp. 4161-4167.
- [137] M.J. Starink and S.C. Wang, "A model for the yield strength of overaged Al–Zn–Mg–Cu Alloys", *Acta Materialia*, 2003, Vol. 51, pp. 5131–5150.
- [138] K. Marthinsen and E. Nes, "A general model for metal plasticity", *Mater. Sci. Eng. A*, 1997, A234-236, pp. 1095-1098.
- [139] E. Nes and K. Marthinsen, "Modeling the evolution in microstructure and properties during plastic deformation of f.c.c.-metals and alloys – an approach towards a unified model", *Mater. Sci. Eng. A*, 2002, A322, pp.176–193.
- [140] E. Nes, K. Marthinsen, and Y. Brechet, "On the mechanisms of dynamic recovery", *Scripta Materialia*, 2002, Vol. 47, pp. 607–611.
- [141] John A. Wagner and R.N. Shenoy, "The Effect of Copper, Chromium, and Zirconium on the Microstructure and Mechanical Properties of Al-Zn-Mg-Cu Alloys", *Metallurgical Transactions A*, 1991, Vol. 22A, pp. 2809-2818.
- [142] E. Z Sachs *Ver Deutsch Ing*, 1928, pp. 72:734.
- [143] G.I. Taylor *J Inst Metals*, 1938, pp. 62:307.

- [144] J.W. Hutchinson, "Elastic-Plastic Behaviour of Polycrystalline Metals and Composites", Proc R Soc Lond A, 1970, pp. 319:247.
- [145] B. Clausen, T. Lorentzen, and T. Leffers, "Self-Consistent Modelling Of The Plastic Deformation Of F.C.C. Polycrystals and Its Implications For Diffraction Measurements Of Internal Stresses", Acta mater., 1998, Vol. 46, No. 9, , pp. 3087-3098.
- [146] R. C. Dorward, "Precipitate coarsening during overaging of Al–Zn–Mg–Cu alloy", Mater. Sci. Tech., Oct. 1999, Vol. 15, pp. 1133-1138.
- [147] A. W. Zhu and E. A. Starke JR, "Strengthening Effect of Unshearable Particles Of Finite Size: A Computer Experimental Study", Acta mater., 1999, Vol. 47, No. 11, pp. 3263-3269.
- [148] S. D. Harkness-J. J. Hren 1970, "An Investigation of Strengthening by Spherical Coherent G. P. Zones", Met. Trans., 1970, Volume 1, pp. 43-49.
- [149] M. Dixit, R.S. Mishra and K.K. Sankaran, "Structure–property correlations in Al 7050 and Al 7055 high-strength aluminum alloys", Materials Science and Engineering, 2008, A 478, pp. 163–172.
- [150] J.D. Embury, D.J. Lloyd, T.R. Ramachandran, in: A.K. Vasudevan, R.D. Doherty (Eds.), Aluminum Alloys—Contemporary Research and Applications. Treatise on Materials Science and Technology, vol. 31, Academic Press, Inc., Boston, USA, 1989.
- [151] G.E. Totten, D.S. MacKenzie, Handbook of Aluminum, in: Physical Metallurgy and Processes, vol. 1, Marcel Dekker, Inc., New York, 2003.
- [152] R.E. Sanders Jr., S.F. Bauman, H.C. Stumpf, in: E.A. Starke Jr., T.H. Sanders Jr. (Eds.), Aluminum Alloys—Physical and Mechanical Properties, vol. 3, EMAS, West Midlands, UK, 1986.
- [153] P.M. Kelly, "The Effect Of Particle Shape On Dispersion Hardening", Scripta Metallurgica, 1972, Vol. 6, pp. 647-656.
- [154] W. J. Poole, H. R. Shercliff, and T. Castillo, "Process model for two step age hardening of 7475 aluminium alloy", Materials Science and Technology, 1997 Vol. 13, pp. 897.
- [155] J.W. Martin, "Micromechanisms in Particle-Strengthened Alloys", Cambridge University Press, Cambridge, UK, 1980.
- [156] Mill Al 7050 Product data sheet (2013) ALCOA worldwide. <http://www.alcoa.com>
- [157] A.J. Morris, R.F. Rubby, P.D Couch and E. Del los Rois, "A comparison of the damage tolerance of 7010-T7451 and 7050-T7451", Mat. Scie. Forum, 1997, Vol. 242, pp. 181-186.
- [158] Metals Handbook Vol.2 (1990), "Properties and Selection: Nonferrous Alloys and Special-Purpose Materials, ASM International 10th Ed, Vol.2, 1990.
- [159] Zhihui Li, Baiqing Xiong, Yongan Zhang, Baohong Zhu, Feng Wang, and Hongwei Liu, "Ageing behavior of an Al–Zn–Mg–Cu alloy pre-stretched thick plate.", Journal of University of Science and Technology Beijing 2007, Vol. 14, No.3, pp. 246.
- [160] Wang Wei-wei, Jia Bin-bin, Lou Shou-jing, "Effect of heat treatment on mechanical properties of thixoformed 7A09 aluminum alloys." Trans. Nonferrous Met. Soc. China, 2009, Vol. 19, pp. 337-342
- [161] Z. Li, et al., J. Univ. Sci. Technol. Beijing, 2007, Vol. 14, No. 3, pp. 246–250.
- [162] Derek Hull, Fractography, Cambridge University Press, UK, 1999.
- [163] Amin Haghparasta, Masoud Nourimotlaghb, Mohammad Alipour, "Effect of the strain-induced melt activation (SIMA) process on the tensile properties of a new developed super high strength aluminum alloy modified by Al₅Ti₁B grain refiner"; Materials Characterization, 2012, Vol. 71, pp. 6–18.
- [164] D. Godard, P. Archambault, E. Aeby-Gautier, G. Lapasset, Acta Mater., 2002, Vol. 50, pp. 2319–2329.
- [165] X.M. Li, M.J. Starink, "Identification and analysis of intermetallic phases in overaged Zr-containing and Cr-containing Al–Zn–Mg–Cu alloys", Journal of Alloys and Compounds, 2011, Vol. 509, pp. 471–476.
- [166] ASM Handbook committee, Metals Handbook, Metallographic, Structure and Phase diagram, Vol. 8, 8th Edition, American Society for Metals, 1973.

- [167] C. W. Corti, P. Cotterill and G. Fitzpatrick, "The Evaluation of the Interparticle Spacing in Dispersion Alloys", *Int. Metallurgical Review*, 1974, Vol. 19, pp. 77-88.
- [168] G. A. Botton, G. L'esperance, C. E. Gallerneault & M. D. Ball, "Volume fraction measurement of dispersoids in a thin foil by parallel energy-loss spectroscopy: development and assessment of the technique", *Journal of Microscopy*, 1995, Vol. 180, pp. 217-229.
- [169] J.C. Werenskiold, A. Deschamps, Y. Brechet: *Mater. Sci. Eng. A*, 2000, Vol. 293A, pp. 267-74.
- [170] M. Nicolas, A. Deschamps, *Acta Materialia*, 2003, Vol. 51, pp. 6077-94.
- [171] M. Dumont, W. Lefebvre, B. Doisneau-Cottignies, A. Deschamps : *Acta Materialia*, 2005, Vol. 53, pp. 2881-92.
- [172] J. Buha, R.N. Lumley, and A.G. Crosky: *Mater. Sci. Eng. A*, 2008, Vol. 492A, pp. 1-10.
- [173] R.N. Lumley, I.J. Polmear: *Scripta Mater.*, 2004, Vol. 50, pp. 1227-31.
- [174] R. Ferragut, A. Dupasquier, C.E. Macchi, A. Somoza, R.N. Lumleyd and I.J. Polmear: *Scripta Materialia*, 2009, Vol. 60, pp. 137-40.
- [175] A. Deschamps, Y. Brechet: *Acta mater.*, 1999, Vol. 47, No. 1, pp. 293-305.
- [176] Nonjabuliso E. Mazibuko, Ulyate A. Curle, *Materials Science Forum*, 2011, Vol. 690, pp. 343-346.
- [177] Frank Czerwinski , "Magnesium Injection Molding", *Spring Scinece+Business Medai, LLC, New York, USA*, 2008.
- [178] Warren L. McCabe, Julian C. Smith, Peter Harriot, "Unit Operation of Chemical Engineering, International Editions 1993", Fifth Ed., Chapter 28, McGraw Hill Chemical Engineering Series, Printed in Singapore; pp.
- [179] Reza Ghiaasiaan, Xiaochun Zeng, Sumanth Shankar, "Controlled Diffusion Solidification (CDS) of Al-Zn-Mg-Cu (7050): Microstructure, heat treatment and mechanical properties, *Materials Science & Engineering A*, 2014, Vol. 594, pp. 260-277.
- [180] A. Deschamps, Y. Bre´chet, and F. Livet, "Influence of copper addition on precipitation kinetics and hardening in Al-Zn-Mg alloy", *Materials Science and Technology*, September 1999, Vol. 15, pp. 993-1000
- [181] M. Lalpoora, D.G. Eskina, L. Katgerman, "Fracture behavior and mechanical properties of high strength aluminum alloys in the as-cast condition", *Materials Science and Engineering A*, 2008, Vol. 497A, pp. 186-194.